



저작자표시-비영리-변경금지 2.0 대한민국

이용자는 아래의 조건을 따르는 경우에 한하여 자유롭게

- 이 저작물을 복제, 배포, 전송, 전시, 공연 및 방송할 수 있습니다.

다음과 같은 조건을 따라야 합니다:



저작자표시. 귀하는 원저작자를 표시하여야 합니다.



비영리. 귀하는 이 저작물을 영리 목적으로 이용할 수 없습니다.



변경금지. 귀하는 이 저작물을 개작, 변형 또는 가공할 수 없습니다.

- 귀하는, 이 저작물의 재이용이나 배포의 경우, 이 저작물에 적용된 이용허락조건을 명확하게 나타내어야 합니다.
- 저작권자로부터 별도의 허가를 받으면 이러한 조건들은 적용되지 않습니다.

저작권법에 따른 이용자의 권리는 위의 내용에 의하여 영향을 받지 않습니다.

이것은 [이용허락규약\(Legal Code\)](#)을 이해하기 쉽게 요약한 것입니다.

[Disclaimer](#)

공학박사학위논문

리튬 및 소듐 이온 배터리를 위한 불화인산염
양극물질 연구

**Tailoring fluorophosphate cathode materials for
high-performance sodium and lithium ion battery**

2015년 2월

서울대학교 대학원

재료공학부 하이브리드재료전공

박 영 욱

리튬 및 소듐 이온 배터리를 위한 불화인산염 양극물질 연구

Tailoring fluorophosphate cathode materials for high-
performance sodium and lithium ion battery

지도교수 강 기 석

이 논문을 공학 박사학위논문으로 제출함

2015년 2월

서울대학교 대학원

재료공학부 하이브리드재료전공

박 영 옥

박영옥의 박사학위논문을 인준함

2014년 12월

위 원 장 홍 성 현 (인)

부 위 원 장 강 기 석 (인)

위 원 한 승 우 (인)

위 원 이 윤 성 (인)

위 원 윤 원 섭 (인)

Abstract

Tailoring fluorophosphate cathode materials for high-performance sodium and lithium ion battery

Park, Young-Uk

Department of Materials Science and Engineering

The Graduate School

Seoul National University

Large-scale electric energy storage is a key enabler for the use of renewable energy. Low-cost and highly durable battery chemistry is required in affordable large-scale storage applications. In this respect, the room-temperature Na-ion battery (NIB) has been re-highlighted recently as a low-cost alternative technology to lithium-ion battery (LIB). A cheap and earth-abundant element, Na, will be advantageous if a large amount of material is demanded for renewable energy solutions. However, significant challenges such as energy density and long term stability must be addressed. In Chap. 2, a novel cathode material for Na-ion battery, $\text{Na}_{1.5}\text{VPO}_{4.8}\text{F}_{0.7}$, is introduced. This new material provides a high energy density of $\sim 600 \text{ Wh kg}^{-1}$, originating from both the multi-electron redox reaction (1.2 e^- per formula unit) and high potential ($\sim 3.8 \text{ V}$ vs. Na^+/Na) of the tailored vanadium redox couple ($\text{V}^{3.8+}/\text{V}^{5+}$). Furthermore, an outstanding cycle life ($\sim 95\%$ capacity retention for 100 cycles) could be achieved, which is attributed to small volume change (2.9%) upon cycling. The open crystal framework with two-dimensional Na diffusion paths leads to low activation barriers for Na diffusion, enabling excellent rate capability.

In Chap. 3, the first successful synthesis of a series of $\text{Na}_3(\text{VO}_{1-x}\text{PO}_4)_2\text{F}_{1+2x}$ ($0 \leq x \leq 1$) compounds is introduced, which is a new family of high-performance cathode materials

for NIB. The $\text{Na}_3(\text{VO}_{1-x}\text{PO}_4)_2\text{F}_{1+2x}$ series can function as high-performance cathodes for NIB with high energy density and good cycle life, although the redox mechanism varies depending on the composition. The combined first-principles calculations and experimental analysis revealed the detailed structural and electrochemical mechanisms of the various compositions in solid solutions of $\text{Na}_3(\text{VOPO}_4)_2\text{F}$ and $\text{Na}_3\text{V}_2(\text{PO}_4)_2\text{F}_3$. The comparative data for the $\text{Na}_y(\text{VO}_{1-x}\text{PO}_4)_2\text{F}_{1+2x}$ electrodes showed a clear relationship among $\text{V}^{3+}/\text{V}^{4+}/\text{V}^{5+}$ redox reactions, Na^+-Na^+ interactions, and Na^+ intercalation mechanisms in NIB.

Lithium-ion battery (LIB), which has been widely used to power portable electronic devices, is on the verge of being applied to new automobile applications. To expand this emerging market, however, an electrode that combines fast charging capability, long-term cycle stability, and high energy density is needed. In Chap. 4, a novel layered lithium vanadium fluorophosphate, $\text{Li}_{1.1}\text{Na}_{0.4}\text{VPO}_{4.8}\text{F}_{0.7}$, is introduced as a promising positive electrode contender. This new material has two-dimensional lithium pathways and is capable of reversibly releasing and reinserting $\sim 1.1 \text{ Li}^+$ ions at 4 V (vs. Li^+/Li) to give a capacity of $\sim 156 \text{ mAh g}^{-1}$ (energy density of 624 Wh kg^{-1}). Moreover, outstanding capacity retentions of 98% and 96% after 100 cycles were achieved at 60°C and room temperature, respectively. Unexpectedly high rate capability was delivered for both charge and discharge despite the large particle size (a few microns), which promises further enhancement of power density with proper nano-engineering.

Keywords: sodium ion battery, lithium ion battery, cathode materials, fluorophosphates, multi-electron redox reaction, ion-exchange reaction

Student Number: 2011-30785

Table of Contents

Abstract	3
Table of Contents	5
List of Figures	7
List of Tables	12

Chapter 1. Introduction	15
--------------------------------------	-----------

Chapter 2. A High-Energy Cathode for a Na-Ion Battery with High Stability

2.1. Introduction	25
2.2. Experimental and Computational Details	27
2.3. Results and Discussion	
2.3.1. Material Characterization of $\text{Na}_{1.5}\text{VPO}_{4.8}\text{F}_{0.7}$	31
2.3.2. Electrochemical Properties of $\text{Na}_{1.5}\text{VPO}_{4.8}\text{F}_{0.7}$	37
2.3.3. Structural Evolution of the $\text{Na}_x\text{VPO}_{4.8}\text{F}_{0.7}$ Electrode upon Cycling	46
2.3.4. Kinetics of the $\text{Na}_x\text{VPO}_{4.8}\text{F}_{0.7}$ Electrode	56
2.3.5. Charge/Discharge Mechanism of the $\text{Na}_x\text{VPO}_{4.8}\text{F}_{0.7}$ Electrode	68
2.4. Summary	71

Chapter 3. A Family of Cathodes for Na-ion Batteries, $\text{Na}_3(\text{VO}_{1-x}\text{PO}_4)_2\text{F}_{1+2x}$

3.1. Introduction	72
3.2. Experimental and Computational Details	74
3.3. Results and Discussion	
3.3.1. Characterization of a Family of $\text{Na}_3(\text{VO}_{1-x}\text{PO}_4)_2\text{F}_{1+2x}$ Compounds	78

3.3.2. Electrochemical Mechanisms of $\text{Na}_y(\text{VO}_{1-x}\text{PO}_4)_2\text{F}_{1+2x}$ Electrodes -----	106
3.3.3. Possibility of Multi-Electron Transfer in $\text{Na}_y(\text{VO}_{1-x}\text{PO}_4)_2\text{F}_{1+2x}$ System -----	134
3.4. Summary -----	137

Chapter 4. Tailoring a Fluorophosphate as a 4 V Cathode for Li-Ion Batteries

4.1. Introduction -----	138
4.2. Experimental and Computational Details -----	140
4.3. Results and Discussion	
4.3.1. Fluorination of the Pristine Na Phase of $\text{Na}_{1.5}\text{VPO}_5\text{F}_{0.5}$ -----	145
4.3.2. Evidence for Reduced Oxidation State of Vanadium in $\text{Na}_{1.5}\text{VPO}_{4.8}\text{F}_{0.7}$ -----	154
4.3.3. Na^+/Li^+ Ion-Exchange for Lithium Derivative of $\text{Na}_{1.5}\text{VPO}_{4.8}\text{F}_{0.7}$ -----	160
4.3.4. Electrochemical Properties of $\text{Li}_{1.1}\text{Na}_{0.4}\text{VPO}_{4.8}\text{F}_{0.7}$ -----	174
4.3.5. The Origin of the Fast Charging and Discharging -----	186
4.4. Summary -----	193

Chapter 5. Conclusion ----- 194

References ----- 198

Abstract in Korean ----- 203

Curriculum Vitae ----- 205

List of Figures

Figure 1-1. Comparison of operating voltages and gravimetric capacities of various cathode and anode materials for Na-ion batteries.

Figure 1-2. Galvanostatic charge/discharge curve of the 1st cycle (top) and cycle lives (bottom) for hard-carbon electrodes in a) EC, b) PC, and c) BC solution containing 1 mol dm⁻³ NaClO₄ tested at 25 mA g⁻¹ in beaker-type cells.

Figure 1-3. A schematic representation of two kinds of NASICON-type structures.

Figure 1-4. Comparison of V⁴⁺/V⁵⁺ redox potentials in oxides, phosphates, and fluorophosphates.

Figure 2-1. Powder XRD pattern of Na_{1.5}VPO_{4.8}F_{0.7}.

Figure 2-2. Crystal structure of Na_{1.5}VPO_{4.8}F_{0.7} and two local environments for vanadium ions.

Figure 2-3. Formation energy plot of Na_xVPO₅F_{0.5} from first-principle calculations.

Figure 2-4. Comparison of voltage *vs.* composition curves from experiments and calculations.

Figure 2-5. Space group change from *P*4₂/*mnm* to *I*4/*mmm* for Na_xVPO_{4.8}F_{0.7}.

Figure 2-6. Charge/discharge profile at a C/10 rate for Na_{1.5}VPO_{4.8}F_{0.7} cathode.

Figure 2-7. Vanadium K-edge XANES spectra of the Na_xVPO_{4.8}F_{0.7} electrodes.

Figure 2-8. Energy density comparison of various cathode materials for NIBs and LIBs.

Figure 2-9. *Ex situ* XRD patterns of the Na_xVPO_{4.8}F_{0.7} electrodes.

Figure 2-10. Detailed *Ex situ* study on the Na_xVPO_{4.8}F_{0.7} electrodes.

Figure 2-11. Evolution of (220) and (113) reflections of the *ex situ* XRD patterns at different SOC in regions I and II during charging.

Figure 2-12. Changes in lattice parameters *a* and *c* as a function of Na content (*x*)

in the $\text{Na}_x\text{VPO}_{4.8}\text{F}_{0.7}$ electrodes during charging.

Figure 2-13. Comparison of volume changes on charging in various cathodes for NIBs.

Figure 2-14. Cycle life of the $\text{Na}_{1.5}\text{VPO}_{4.8}\text{F}_{0.7}$ electrode at room (25°C; bottom) and high (60°C; top) temperatures.

Figure 2-15. XRD pattern of the $\text{Na}_{1.5}\text{VPO}_{4.8}\text{F}_{0.7}$ electrode in the discharged state after 515 cycles at a 1C cycling rate at room temperature (top red line).

Figure 2-16. Capacity recovery by reassembling a multi-cycled electrode into another electrochemical cell using fresh Na metal and electrolyte.

Figure 2-17. GITT curve of the carbon-coated $\text{Na}_{1.5}\text{VPO}_{4.8}\text{F}_{0.7}$ electrode in charge and discharge modes at room temperature.

Figure 2-18. Rate capability of the $\text{Na}_{1.5}\text{VPO}_{4.8}\text{F}_{0.7}$ cathode.

Figure 2-19. Ragone plot for the $\text{Na}_{1.5}\text{VPO}_{4.8}\text{F}_{0.7}$ cathode and other cathodes materials for NIBs.

Figure 2-20. Arrhenius plot of electrical conductivities of $\text{Na}_{1.5}\text{VPO}_{4.8}\text{F}_{0.7}$ (red triangles) and $\text{Na}_{1.0}\text{VPO}_{4.8}\text{F}_{0.7}$ (blue circles) pellets at various temperatures.

Figure 2-21. EIS study on the $\text{Na}_{1.5}\text{VPO}_{4.8}\text{F}_{0.7}$ and $\text{Na}_{1.0}\text{VPO}_{4.8}\text{F}_{0.7}$ pellets.

Figure 2-22. *In situ* EIS measurement during a charge process in GITT mode.

Figure 2-23. The origin of the fast kinetics of the $\text{Na}_x\text{VPO}_{4.8}\text{F}_{0.7}$ electrode.

Figure 2-24. Trajectory for Na hopping along path 2 in the $\text{Na}_x\text{VPO}_5\text{F}_{0.5}$ phase.

Figure 2-25. Change in d_{hkl} values of $\text{Na}_x\text{VPO}_5\text{F}_{0.5}$ from first-principle calculations.

Figure 3-1. XRD patterns of $\text{Na}_3(\text{VO}_{1-x}\text{PO}_4)_2\text{F}_{1+2x}$ ($x = 0.0, 0.2, 0.5, 0.8,$ and 1.0) powders.

Figure 3-2. EDS and ICP analyses for the $\text{Na}_3(\text{VO}_{1-x}\text{PO}_4)_2\text{F}_{1+2x}$ ($x = 0.0, 0.2, 0.5, 0.8,$ and 1.0) powders.

Figure 3-3. SEM images of the $\text{Na}_3(\text{VO}_{1-x}\text{PO}_4)_2\text{F}_{1+2x}$ samples.

Figure 3-4. Bright-field TEM images (left) and the SAED patterns (right).

Figure 3-5. ND patterns of the $\text{Na}_3(\text{VO}_{1-x}\text{PO}_4)_2\text{F}_{1+2x}$ ($x = 0.0, 0.2, 0.5, 0.8$, and 1.0) powders and their Rietveld refinements.

Figure 3-6. Synchrotron XRD patterns of $\text{Na}_3(\text{VO}_{1-x}\text{PO}_4)_2\text{F}_{1+2x}$ powders.

Figure 3-7. Structural change with the fluorine content in $\text{Na}_3(\text{VO}_{1-x}\text{PO}_4)_2\text{F}_{1+2x}$ ($0 \leq x \leq 1$).

Figure 3-8. Variation of h and d with x in $\text{Na}_3(\text{VO}_{1-x}\text{PO}_4)_2\text{F}_{1+2x}$ ($0 \leq x \leq 1$).

Figure 3-9. ^{23}Na MAS NMR study for $\text{Na}_3(\text{VO}_{1-x}\text{PO}_4)_2\text{F}_{1+2x}$ system ($0 \leq x \leq 1$).

Figure 3-10. Voltage-composition curves of the $\text{Na}_y(\text{VO}_{1-x}\text{PO}_4)_2\text{F}_{1+2x}$ electrodes for $x = 0.0$ (blue), 0.2 (red), and 0.5 (green).

Figure 3-11. Voltage-composition curves of the $\text{Na}_y(\text{VO}_{1-x}\text{PO}_4)_2\text{F}_{1+2x}$ electrodes for $x = 0.8$ (red) and 1.0 (blue).

Figure 3-12. Change in average voltages of the $\text{Na}_y(\text{VO}_{1-x}\text{PO}_4)_2\text{F}_{1+2x}$ ($x = 0.0, 0.2, 0.5, 0.8$, and 1.0) electrodes.

Figure 3-13. Evolution of Na-vacancy ordering in the $\text{Na}_y(\text{VO}_{1-x}\text{PO}_4)_2\text{F}_{1+2x}$ ($0 \leq x \leq 1$) electrodes from $y = 3.0$ to $y = 2.0$.

Figure 3-14. ^{23}Na MAS NMR study on Na-vacancy ordering in $\text{Na}_3(\text{VOPO}_4)_2\text{F}$ ($x = 0$) phase.

Figure 3-15. XRD patterns of $\text{Na}_y(\text{VOPO}_4)_2\text{F}$ powders for $y = 3.00$ and 2.08 .

Figure 3-16. Derivative dV/dy analysis of the $\text{Na}_y(\text{VO}_{1-x}\text{PO}_4)_2\text{F}_{1+2x}$ electrodes for $x = 0$ (red) and $x = 1$ (blue).

Figure 3-17. Formation energy curve of $\text{Na}_y\text{V}_2(\text{PO}_4)_2\text{F}_3$ ($x = 1$) from first-principles calculations.

Figure 3-18. Calculated formation energies of some Na configurations for the $\text{Na}_y(\text{VO}_{1-x}\text{PO}_4)_2\text{F}_{1+2x}$ system.

Figure 3-19. Intra-unit Na^+-Na^+ repulsion in Na layer of $\text{Na}_3(\text{VO}_{1-x}\text{PO}_4)_2\text{F}_{1+2x}$ ($0 \leq x \leq 1$).

Figure 3-20. Na-vacancy configuration on the Na layer of $\text{Na}_y(\text{VO}_{1-x}\text{PO}_4)_2\text{F}_{1+2x}$ ($x = 1$; $y = 2.5$).

Figure 3-21. Two possible unit-unit Na configurations by Na3 site occupation at $y = 2.5$.

Figure 3-22. Size variation of the main voltage step at $y \approx 2.0$ for the $\text{Na}_y(\text{VO}_{1-x}\text{PO}_4)_2\text{F}_{1+2x}$ ($0 \leq x \leq 1$) electrodes with increasing fluorine content (x).

Figure 3-23. Derivative dV/dy curves for the first charge cycle of the $\text{Na}_y(\text{VO}_{1-x}\text{PO}_4)_2\text{F}_{1+2x}$ electrodes at 25°C and 60°C.

Figure 3-24. ND and XRD patterns of $\text{Na}_y(\text{VOPO}_4)_2\text{F}$ ($x = 0$; $1.0 \leq y \leq 3.0$) powders.

Figure 3-25. Lattice parameter changes with decreasing Na content (y) in $\text{Na}_y(\text{VOPO}_4)_2\text{F}$ ($x = 0$).

Figure 3-26. *Ex-situ* XRD patterns of the $\text{Na}_y\text{V}_2(\text{PO}_4)_2\text{F}_3$ ($x = 1$) electrode for the region of $2.0 \leq y \leq 3.0$.

Figure 3-27. XRD patterns of fully charged states of the $\text{Na}_y(\text{VO}_{1-x}\text{PO}_4)_2\text{F}_{1+2x}$ electrodes ($x = 0.8$ and 0.5).

Figure 3-28. Variation in discharge capacity of the $\text{Na}_3(\text{VO}_{1-x}\text{PO}_4)_2\text{F}_{1+2x}$ ($x = 0.0, 0.2, 0.5, 0.8,$ and 1.0) electrodes for 150 cycles.

Figure 3-29. Variation in Columbic efficiency of the $\text{Na}_3(\text{VO}_{1-x}\text{PO}_4)_2\text{F}_{1+2x}$ ($x = 0.0, 0.2, 0.5, 0.8,$ and 1.0) electrodes for 150 cycles.

Figure 3-30. Voltage–composition curves for the $\text{Na}_y(\text{VO}_{1-x}\text{PO}_4)_2\text{F}_{1+2x}$ ($0 \leq x \leq 1$; $0 \leq y \leq 3$) electrodes from first-principles calculations.

Figure 4-1. Crystal structure of the pristine Na phase ($\text{Na}_{1.5}\text{VPO}_5\text{F}_{0.5}$).

Figure 4-2. Search for the optimum fluorine substitution in $\text{Na}_{1.5}\text{VPO}_{5-\delta}\text{F}_{0.5+\delta}$.

Figure 4-3. Structural characterization of the fluorinated $\text{Na}_{1.5}\text{VPO}_{4.8}\text{F}_{0.7}$.

Figure 4-4. Comparison of P2p binding energies in XPS spectra of the pristine sodium phase ($\text{Na}_{1.5}\text{VPO}_5\text{F}_{0.5}$) and the fluorinated phase ($\text{Na}_{1.5}\text{VPO}_{4.8}\text{F}_{0.7}$).

Figure 4-5. ^{23}Na and ^7Li MAS NMR spectra of vanadium fluorophosphates.

Figure 4-6. Photographs representing the experimental procedure of the double titration method.

Figure 4-7. EPR spectra of sodium vanadium fluorophosphates and lithium vanadium phosphates.

Figure 4-8. Material characterization of the ion-exchanged $\text{Li}_{1.1}\text{Na}_{0.4}\text{VPO}_{4.8}\text{F}_{0.7}$.

Figure 4-9. TEM study for $\text{Li}_{1.1}\text{Na}_{0.4}\text{VPO}_{4.8}\text{F}_{0.7}$.

Figure 4-10. Local environments of Li and Na sites in $\text{Li}_{1.1}\text{Na}_{0.4}\text{VPO}_{4.8}\text{F}_{0.7}$.

Figure 4-11. The configuration of Na^+ ions on *ab* plane in $\text{Na}_{1.5}\text{VPO}_{4.8}\text{F}_{0.7}$.

Figure 4-12. ^6Li and ^{23}Na MAS NMR spectra of $\text{Li}_{1.1}\text{Na}_{0.4}\text{VPO}_{4.8}\text{F}_{0.7}$.

Figure 4-13. Schematic representation for several types of $\text{Na } 3s - \text{O } 2p (\text{F } 2p) - \text{V } t_{2g}$ interactions in $\text{Na}_{1.5}\text{VPO}_{4.8}\text{F}_{0.7}$ and $\text{Li}_{1.1}\text{Na}_{0.4}\text{VPO}_{4.8}\text{F}_{0.7}$.

Figure 4-14. Temperature-controlled XRD patterns of $\text{Li}_{1.1}\text{Na}_{0.4}\text{VPO}_{4.8}\text{F}_{0.7}$.

Figure 4-15. GITT curve during charge and discharge of $\text{Li}_{1.1}\text{Na}_{0.4}\text{VPO}_{4.8}\text{F}_{0.7}$ at 60°C .

Figure 4-16. Charge/discharge curves and cyclability of $\text{Li}_{1.1}\text{Na}_{0.4}\text{VPO}_{4.8}\text{F}_{0.7}$.

Figure 4-17. Rate capability of the $\text{Li}_{1.1}\text{Na}_{0.4}\text{VPO}_{4.8}\text{F}_{0.7}$ electrode.

Figure 4-18. XRD patterns of the lithium phase and fully delithiated phase.

Figure 4-19. Ground-state structures for the lattice parameter calculations.

Figure 4-20. XRD patterns of the $\text{Li}_{1.1}\text{Na}_{0.4}\text{VPO}_{4.8}\text{F}_{0.7}$ electrode in the pristine and 100th discharged states.

Figure 4-21. Top view (*ab* plane) of the alkali metal layer in $\text{Li}_{1.1}\text{Na}_{0.4}\text{VPO}_{4.8}\text{F}_{0.7}$.

Figure 4-22. Initial configurations of alkali ions for the NEB calculations.

Figure 4-23. NEB calculations for path 1 in $\text{Na}_{1.5}\text{VPO}_5\text{F}_{0.5}$ and $\text{LiNa}_{0.5}\text{VPO}_5\text{F}_{0.5}$.

Figure 4-24. NEB calculations for path 2 in $\text{Na}_{1.5}\text{VPO}_5\text{F}_{0.5}$ and $\text{LiNa}_{0.5}\text{VPO}_5\text{F}_{0.5}$.

List of Tables

Table 3-1. Lattice parameters of the $\text{Na}_3(\text{VO}_{1-x}\text{PO}_4)_2\text{F}_{1+2x}$ samples ($x = 0.0, 0.2, 0.5, 0.8$, and 1.0) from the combined ND and XRD refinement.

Table 3-2. Lattice parameters and cell volumes for $\text{Na}_3(\text{VOPO}_4)_2\text{F}$ ($x = 0$) from the ND refinement.

Table 3-3. Atomic positions for $\text{Na}_3(\text{VOPO}_4)_2\text{F}$ ($x = 0$) from the ND refinement.

Table 3-4. Anisotropic atomic displacement (thermal) parameters for Na sites in $\text{Na}_3(\text{VOPO}_4)_2\text{F}$ ($x = 0$) from the ND refinement.

Table 3-5. Lattice parameters and cell volumes for $\text{Na}_3(\text{VO}_{0.8}\text{PO}_4)_2\text{F}_{1.4}$ ($x = 0.2$) from the ND refinement.

Table 3-6. Atomic positions for $\text{Na}_3(\text{VO}_{0.8}\text{PO}_4)_2\text{F}_{1.4}$ ($x = 0.2$) from the ND refinement.

Table 3-7. Anisotropic atomic displacement (thermal) parameters for Na sites in $\text{Na}_3(\text{VO}_{0.8}\text{PO}_4)_2\text{F}_{1.4}$ ($x = 0.2$) from the ND refinement.

Table 3-8. Lattice parameters and cell volumes for $\text{Na}_3(\text{VO}_{0.5}\text{PO}_4)_2\text{F}_{2.0}$ ($x = 0.5$) from the ND refinement.

Table 3-9. Atomic positions for $\text{Na}_3(\text{VO}_{0.5}\text{PO}_4)_2\text{F}_{2.0}$ ($x = 0.5$) from the ND refinement.

Table 3-10. Anisotropic atomic displacement (thermal) parameters for the Na1 site in $\text{Na}_3(\text{VO}_{0.5}\text{PO}_4)_2\text{F}_{2.0}$ ($x = 0.5$) from the ND refinement.

Table 3-11. Lattice parameters and cell volumes for $\text{Na}_3(\text{VO}_{0.2}\text{PO}_4)_2\text{F}_{2.6}$ ($x = 0.8$) from the ND refinement.

Table 3-12. Atomic positions for $\text{Na}_3(\text{VO}_{0.2}\text{PO}_4)_2\text{F}_{2.6}$ ($x = 0.8$) from the ND refinement.

Table 3-13. Anisotropic atomic displacement (thermal) parameters for Na sites in $\text{Na}_3(\text{VO}_{0.2}\text{PO}_4)_2\text{F}_{2.6}$ ($x = 0.8$) from the ND refinement.

Table 3-14. Lattice parameters and cell volumes for $\text{Na}_3\text{V}_2(\text{PO}_4)_2\text{F}_3$ ($x = 1$) from the ND refinement.

Table 3-15. Atomic positions for $\text{Na}_3\text{V}_2(\text{PO}_4)_2\text{F}_3$ ($x = 1$) from the ND refinement.

Table 3-16. Anisotropic atomic displacement (thermal) parameters for Na sites in $\text{Na}_3\text{V}_2(\text{PO}_4)_2\text{F}_3$ ($x = 1$) from the ND refinement.

Table 3-17. Bond distances of V–O(F) bonds, Baur’s distortion indices (Δ), and octahedral volumes of VO_5F ($x = 0$) and VO_4F_2 ($x = 1$) octahedra.

Table 3-18. Bond angles for various Na–O(F)–V interactions in $\text{Na}_3(\text{VOPO}_4)_2\text{F}$ ($x = 0$).

Table 4-1. Lattice parameters and cell volumes for $\text{Na}_{1.5}\text{VPO}_{4.8}\text{F}_{0.7}$.

Table 4-2. Atomic positions for $\text{Na}_{1.5}\text{VPO}_{4.8}\text{F}_{0.7}$.

Table 4-3. Average oxidation state of vanadium (AV) for various vanadium-containing compounds determined by the double titration method.

Table 4-4. Comparison of the degree of Na^+/Li^+ ion-exchange (i.e., the exchanged amount) for a variety of experimental conditions.

Table 4-5. Lattice parameters and cell volumes for $\text{Li}_{1.1}\text{Na}_{0.4}\text{VPO}_{4.8}\text{F}_{0.7}$.

Table 4-6. Atomic positions for $\text{Li}_{1.1}\text{Na}_{0.4}\text{VPO}_{4.8}\text{F}_{0.7}$.

Table 4-7. Lattice parameters of $\text{Li}_{1.1}\text{Na}_{0.4}\text{VPO}_{4.8}\text{F}_{0.7}$ and $\text{Na}_{0.4}\text{VPO}_{4.8}\text{F}_{0.7}$.

Table 4-8. Lattice parameters predicted by first-principles calculations.

Chapter 1. Introduction

1.1. Li-ion battery (LIB) and Na-ion battery (NIB)

Since SONY successfully commercialized Li-ion battery (LIB) in the 1990s, LIB technologies have been closely related to human life. They were first applied in mobile devices and are on the verge of a new application in electric vehicles. With increasing importance of renewable energy, LIB technologies related to large-scale electric energy storage are being investigated as well. However, the high price and unstable supply of lithium resource prevent the large-scale application of the LIB technology.^{1,2} Therefore, low-cost and highly durable battery chemistry is required in affordable large-scale storage applications. In this respect, the room-temperature Na-ion battery (NIB) has been re-highlighted recently as a low-cost alternative technology to LIB.^{1,2} The abundance and low cost of Na in the earth will be advantageous when a large amount of material is demanded for renewable energy solutions, which will eventually be beneficial in large-scale storage applications.^{1,2} However, despite the recent rigorous search for high-performance NIB electrode materials,¹⁻⁷ their overall electrochemical performance remains inferior to Li chemistry. The less negative redox potential of Na^+/Na compared with Li^+/Li (-2.71 and -3.04 V vs. standard hydrogen electrode) reduces the operating voltage, leading to a generally lower energy density.^{1,2} The larger Na^+ ion compared with the Li^+ ion (1.02 vs. 0.59 Å) causes greater change in the host structure upon insertion or removal, which often results in poorer cycle life or even sluggish diffusion.^{1,2}

1.2. Current status of the research on Na-ion battery

Recently, the study on cathode materials for Na rechargeable batteries was the first to be activated because they share a lot of similarities with those for Li-ion batteries and hold the key to a high energy density for the success of electric vehicles.^{1,2} The class and feature of available cathodes for Na-ion batteries are not far different from those for Li-ion batteries. In the early studies, polyanion-based sodium phases have been most vigorously explored as cathode materials for Na-ion batteries. Most studies were focused on phosphates such as NaFePO_4 , $\text{Na}_3\text{V}_2(\text{PO}_4)_3$, $\text{Na}_3\text{V}_2(\text{PO}_4)_2\text{F}_3$, $\text{Na}_2\text{FeP}_2\text{O}_7$, $\text{Na}_2\text{FePO}_4\text{F}$, and alluaudites, and some of them showed promising electrochemical properties.¹⁻⁷ Operating voltages and specific capacities of those cathode materials are shown in **Figure 1-1**. More recently, a kind of layered oxides, P2-type $\text{Na}_x[\text{Fe}_{1/2}\text{Mn}_{1/2}]\text{O}_2$, has been reported as a high-capacity cathode composed of earth-abundant elements.⁸ The energy density of the electrode exceeded 500 Wh kg^{-1} , which was the highest value at that time.

New anode materials for Na-ion batteries have been vigorously studied, because metallic sodium has safety issues due to dendrite formation and lower melting point compared to metallic lithium (97.7 vs. 180.5 °C).^{1,2} In LIB chemistry, cheap graphite is commercially used as a negative electrode. Unfortunately, graphite is known to be electrochemically inactive in a Na-ion cell. For this reason, other carbonaceous materials such as hard carbon, amorphous carbon, and petroleum coke were first explored. Their voltage range was from 0.5 to 1.0 V (vs. Na^+/Na) as shown in **Figure 1-1**. Among them, the hard carbon exhibited the highest specific capacity of $\sim 300 \text{ mAh g}^{-1}$ and reasonable cycle life (**Figure 1-2**).⁹

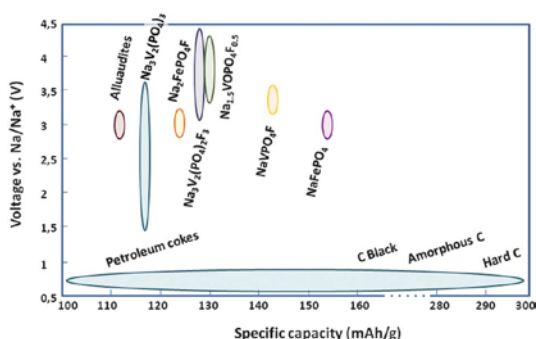


Figure 1-1. Comparison of operating voltages and gravimetric capacities of various cathode and anode materials for Na-ion batteries. Reproduced from [V. Palomares *et al.*, *Energy Environ. Sci.*, 5, 5884-5901 (2012); DOI: 10.1039/C2EE02781J] with permission of The Royal Society of Chemistry.

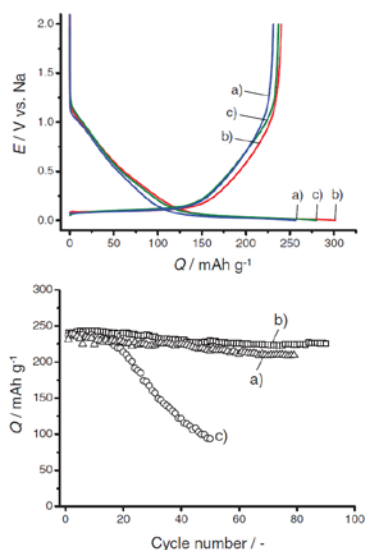


Figure 1-2. Galvanostatic charge/discharge curve of the 1st cycle (top) and cycle lives (bottom) for hard-carbon electrodes in a) EC, b) PC, and c) BC solution containing 1 mol dm⁻³ NaClO₄ tested at 25 mA g⁻¹ in beaker-type cells. Used with permission from [S. Komaba *et al.*, *Adv. Funct. Mater.*, **21**, 3859-3867 (2011); DOI: 10.1002/adfm.201100854]. Copyright 2011 Wiley.

1.3. Limitation of current cathodes for Na-ion battery

The classes and features of cathodes available for NIBs share common aspects with those of LIBs.^{1,4,5,10} As the first successful Li battery cathode was layered oxides such as LiCoO_2 , layered Na transition metal oxides have been studied extensively as NIB cathodes.^{4,8,11-14} Recently, Komaba and coworkers succeeded in synthesizing P2-type layered $\text{Na}_x[\text{Fe}_{1/2}\text{Mn}_{1/2}]\text{O}_2$ as a new high-capacity cathode for NIBs which showed the highest energy density (520 Wh kg^{-1}) of an NIB cathode to date.⁸ Polyanion-based Na phases are also being explored as new cathode materials for NIBs. Various Na-intercalation materials have been suggested,^{1,2,5,15-28} inspired by works on polyanion-based Li phases such as LiFePO_4 or earlier works on NASICONs (sodium super ionic conductors) such as $\text{Na}_3\text{V}_2(\text{PO}_4)_3$. More recently, unconventional approaches for NIB cathodes such as a bipolar porous organic electrode (BPOE) have been undertaken,^{29,30} proposing a new possible NIB chemistry with a high energy density that can approach 500 Wh kg^{-1} .

In spite of the current rigorous search for high-performance NIB electrode materials, their overall electrochemical performance remains inferior to Li chemistry. The less negative redox potential of Na^+/Na compared with Li^+/Li (-2.71 and $-3.04 \text{ V vs. standard hydrogen electrode}$) reduces the operating voltage. Moreover, heavier Na atom than Li ($22.99 \text{ vs. } 6.94 \text{ g mol}^{-1}$) lowers the gravimetric capacity, leading to a generally lower energy density. The larger Na^+ ion compared with the Li^+ ion ($1.02 \text{ vs. } 0.59 \text{ \AA}$) causes greater change in the host structure upon insertion or removal, which often results in poorer cycle life or even sluggish diffusion. Such fundamental disadvantages must be overcome to advance NIBs and their wide application as an alternative to LIBs.

1.4. NASICON (sodium super ionic conductors) structure

NASICON (sodium super ionic conductors) structure are basically composed of MO_6 octahedral unit (M = transition metals) and XO_4 tetrahedral units (X = P, S, Si, W, As, or Mo).^{31,32} By corner-sharing of the units, an open framework of $M_2(XO_4)_3$ is constructed, allowing fast conduction of mobile ions such as Li^+ and Na^+ ions in the framework.^{31,32} This type of material can bring superior rate capability of a positive electrode for Na-ion batteries that suffer from sluggish kinetics due to big Na^+ ions. For this reason, $Na_{1.5}VOPO_4F_{0.5}$ with NASICON structure was chosen as a starting material because its open framework is advantageous to fast kinetics.²⁷

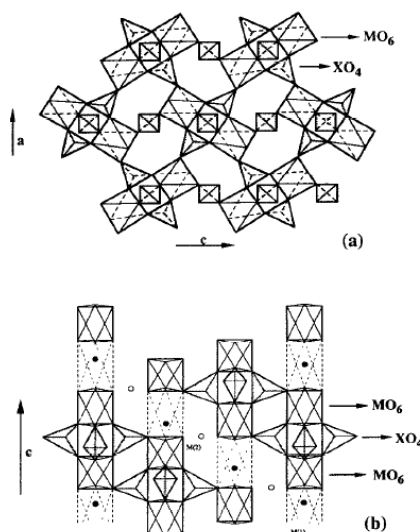


Figure 1-3. A schematic representation of two kinds of NASICON-type structures. (a) Monoclinic and (b) rhombohedral forms. Reprinted from [*Solid State Ionics*, Volume 92, K.S. Nanjundaswamy *et al.*, Synthesis, redox potential evaluation and electrochemical characteristics of NASICON-related-3D framework compounds, Pages 1-10, Copyright 1996, with permission from Elsevier.

1.5. Strategy for solving the limitation of NIB cathodes

As part of an effort to overcome such inherent disadvantages of NIB, I tried to design novel cathode materials with high operating voltage, high specific capacity, and fast kinetics for Na diffusion. To screen a lot of candidates, I used a systematic approach for each property. First of all, to get higher specific capacity, compounds with multivalent transition metal ions were preferentially searched. For example, the valence state of vanadium ions is known to be various so that more than one electron can be supplied by a vanadium redox couple in some cases. If there is more than one Na^+ ion per vanadium ion in a compound, it is theoretically possible to increase the specific capacity of an electrode twice.

In the case of the operating voltage of the electrode, changing the kind of redox couple was the most common approach. In this work, however, I focused on the interesting fact that the redox potential of a certain redox couple substantially varies with the kind of anion group in the compound.³¹ For example, the potentials of $\text{V}^{4+}/\text{V}^{5+}$ redox couples in oxides, phosphates, and fluorophosphates are known to be ~3.0 V, ~3.6 V, and ~4.0 V (vs. Li^+/Li), respectively, as shown in **Figure 1-4**.³³ In this regard, I preferentially searched fluorophosphates-based compounds which can provide high voltage.

Since the kinetics of Na diffusion depends on the crystal structure, I tried to find a certain crystal framework which allows fast Na^+ ion conduction. Fortunately, lots of studies on NASICONs (sodium super ionic conductors) have been executed, and I found that some vanadium-containing fluorophosphates adopted the NASICON structure with an open framework. $\text{Na}_{1.5}\text{VOPO}_4\text{F}_{0.5}$ was one of the most dramatic examples. This compound was reported as a new cathode for NIB by Sauvage *et al.*

in 2006, but they could not show good electrochemical properties.²⁷ Nonetheless, I recognized the potential of this material as a high-performance cathode for NIB due to aforementioned reasons.

In the first part, I tried to extend V^{n+} redox range in $Na_{1.5}VOPO_4F_{0.5}$ via a novel anion-substitution. By replacing some O^{2-} ions by less negative F^- ions, I reduced the oxidation state of vanadium ions from +4 to +3.8. This modification extended V^{n+} redox range from V^{4+}/V^{5+} to $V^{3.8+}/V^{5+}$, enabling multi-electron redox reaction. As expected, high operating voltage (~ 3.8 V) and an increase capacity (~ 140 mAh g^{-1}) were obtained. Using this novel approach, I could demonstrate for the first time that the performance of an NIB can rival and even excel that of an LIB. The new electrode material, $Na_{1.5}VPO_{4.8}F_{0.7}$, can function as an excellent cathode for rechargeable Na batteries with a high energy density that excels the state-of-the-art P2-type layered oxide, which has the highest energy density at that time.⁸ Most electrochemical properties of this material such as power capability and long-term cycle life outperform those of existing cathodes for the NIB and even rival those of LIB cathodes such as olivine $LiFePO_4$ and spinel $LiMn_2O_4$.

In the second part, the works of the first part were expanded by exploring wide anion compositions. I enriched the chemistry of vanadium-based fluorophosphates by discovering a new family of compounds, $Na_3(VO_{1-x}PO_4)_2F_{1+2x}$ ($0 \leq x \leq 1$), which exhibited promising electrochemical performance in NIBs. Also, I showed the first successful synthesis of the full solid solution for $Na_3(VO_{1-x}PO_4)_2F_{1+2x}$ compounds and discussed their potential as a new cathode group for NIBs. The $Na_y(VO_{1-x}PO_4)_2F_{1+2x}$ electrodes delivered an energy density (~ 520 Wh kg^{-1}) among the highest reported for NIB cathodes with ultrahigh stability, placing this family of compounds in the category of outstanding cathodes. I also performed an extensive

structural analysis of the new series of $\text{Na}_y(\text{VO}_{1-x}\text{PO}_4)_2\text{F}_{1+2x}$ via a combined first-principles and experimental study. The electrochemical mechanisms and structural evolution during battery operation were determined. The results showed different behaviors depending on the composition, even though the compounds belong to the same crystal framework.

In the final part, I designed a novel cathode material for LIB using the sodium compounds studied in the previous parts. To prepare lithium-containing version maintaining most merits of the sodium compounds, I focused on the soft chemistry which is known to be efficient to make metastable phase without structural change. Chemical ion-exchange process, a kind of the soft chemistry, was applied to synthesis a Li-version of the $\text{Na}_3(\text{VO}_{1-x}\text{PO}_4)_2\text{F}_{1+2x}$ compounds. As a result, a novel cathode material for lithium-ion batteries, $\text{Li}_{1.1}\text{Na}_{0.4}\text{VPO}_{4.8}\text{F}_{0.7}$, was successfully prepared. It was the highest-performing positive electrode material among ever reported lithium transition metal fluorophosphates. It exhibited high theoretical energy density (624 Wh kg^{-1}) with an operating voltage of $\sim 4 \text{ V}$ (vs. Li^+/Li) and a capacity of $\sim 156 \text{ mAh g}^{-1}$. Also, it showed excellent capacity retentions and an outstanding rate capability in spite of the micron-sized particles. Such a high rate capability had never been reported for any fluorophosphate-based electrodes at that time.

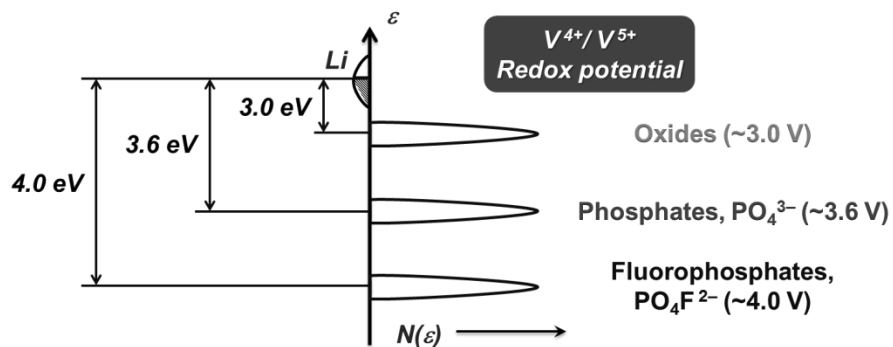


Figure 1-4. Comparison of V^{4+}/V^{5+} redox potentials in oxides, phosphates, and fluorophosphates.

1.6. The main objective and novelty of this work

The main objective of this work was to develop new high-performance cathode materials for Na-ion batteries. The quantitative target of energy density was above 600 Wh kg^{-1} , which was achieved in this work. Another goal was to find the effect of anion substitution on electrochemical properties of a newly discovered cathode group of $\text{Na}_3(\text{VO}_{1-x}\text{PO}_4)_2\text{F}_{1+2x}$ ($0 \leq x \leq 1$), which was systematically studied via a combined theoretical and experimental approach.

One of the new ideas in this work was to use anion-substitution as a way to tune redox reactions of a redox couple. Because anion group plays a role of a backbone in a crystal framework, it is known to be very challenging to modify the anion group substantially. Conventionally, cation doping is used to control redox reaction. However, in this work, I tried to modify the anion group to widen the redox range of vanadium redox couple maintaining the crystal structure. With this approach, I could make a redox couple capable of providing more than one electron. Moreover, for the first time, I found a solid-solution of sodium vanadium fluorophosphates. Also, I suggested many other options to tailor the redox couple and increase the theoretical capacity of the electrode via the first-principle calculations.

Another important finding in this work was the discovery of high-performance cathode materials for both NIB and LIB. A combined theoretical and experimental approach was used for an efficient and systematic exploration. Furthermore, rich information on newly discovered compounds was provided in this dissertation by using a variety of advanced analytical tools. I believe that my works on developing new electrode materials will pave a way for post Li-ion batteries as well as the current battery technologies.

Chapter 2. A High-Energy Cathode for a Na-Ion Battery with High Stability

(The content of this chapter has been published in *Journal of the American Chemical Society*. Reprinted with permission from [Y.-U. Park *et. al.*, *J. Am. Chem. Soc.*, **135**, 13870-13878 (2013); DOI: 10.1021/ja406016j]. Copyright 2013 American Chemical Society.)

2.1. Introduction

Establishing a sustainable energy solution is one of the most important issues in efforts to achieve a sustainable society. Alternative energies such as solar, wind and geothermal energy do not produce electricity coincident with consumption times. Thus, a large-scale energy storage system is essential to deal with such discrepancy. High-energy Li-ion batteries (LIBs) are expected to contribute in part to the solution; however, their high cost and low stability prohibit wide application in this area. Recently, attention has been refocused on room-temperature Na-ion batteries (NIBs) as a low-cost alternative technology compared with LIBs.^{1,2,4,5,8,10,15} The abundance and low cost of Na in the earth will become advantageous when a large amount of material is demanded for renewable energy solutions. Moreover, because rechargeable Na batteries share many similarities with LIBs, opportunities for fast-advancing NIB research can be found in state-of-the-art LIB technologies.

The classes and features of cathodes available for NIBs share common aspects with those of LIBs.^{1,4,5,10} As the first successful Li battery cathode was layered oxides such as LiCoO₂, layered Na transition metal oxides have been studied extensively as NIB cathodes.^{4,8,11-14} Recently, Komaba and coworkers succeeded in

synthesizing P2-type layered $\text{Na}_x[\text{Fe}_{1/2}\text{Mn}_{1/2}]\text{O}_2$ as a new high-capacity cathode for NIBs which showed the highest energy density (520 Wh kg^{-1}) of an NIB cathode to date.⁸ Polyanion-based Na phases are also being explored as new cathode materials for NIBs. Various Na-intercalation materials have been suggested,^{1,2,5,15-28} inspired by works on polyanion-based Li phases such as LiFePO_4 or earlier works on NASICONs (sodium super ionic conductors) such as $\text{Na}_3\text{V}_2(\text{PO}_4)_3$. More recently, unconventional approaches for NIB cathodes such as a bipolar porous organic electrode (BPOE) have been undertaken,^{29,30} proposing a new possible NIB chemistry with a high energy density that can approach 500 Wh kg^{-1} .

Despite the current rigorous search for high-performance NIB electrode materials, their overall electrochemical performance remains inferior to Li chemistry. The less negative redox potential of Na^+/Na compared with Li^+/Li (-2.71 and $-3.04 \text{ V vs. standard hydrogen electrode}$) reduces the operating voltage, leading to a generally lower energy density. The larger Na^+ ion compared with the Li^+ ion (1.02 vs. 0.59 \AA) causes greater change in the host structure upon insertion or removal, which often results in poorer cycle life or even sluggish diffusion. Such fundamental demerits must be overcome to advance NIBs and their wide application as an alternative to LIBs.

In this study exploring a new NIB cathode, I attempted to counterbalance these limitations by searching for a material chemistry with a high redox potential and a rigid open framework that is less sensitive to the volume change from the guest ion insertion. In this regard, I focused on polyanion-based open crystal frameworks with vanadium redox couples. Recent studies have demonstrated that vanadium redox can exhibit high voltage in a Na cell. A relatively high average voltage of $\sim 3.4 \text{ V (vs. Na}^+/\text{Na)}$ was achieved for $\text{Na}_3\text{V}_2(\text{PO}_4)_3$.^{15,26} The $\text{V}^{3+}/\text{V}^{4+}$ redox couple

in $\text{Na}_3\text{V}_2(\text{PO}_4)_2\text{F}_3$ showed an even higher average voltage (~ 3.9 V) in a Na cell,¹⁷ although its specific capacity remained limited due to the relatively heavy polyanion group. Moreover, I demonstrated that multi-electron transfer of a vanadium redox couple is possible in certain polyanion frameworks maintaining its high potential. In my previous work,³⁴ I reported a new electrode material, $\text{Li}_{1.1}\text{Na}_{0.4}\text{VPO}_{4.8}\text{F}_{0.7}$, for LIBs by tailoring the polyanion group of the crystal and expanded the redox range to $\text{V}^{3.8+}/\text{V}^{5+}$ in the high-voltage region. The tuned redox couple provided an additional 0.2 electrons per formula unit, compared with the one electron transfer reaction of $\text{V}^{4+}/\text{V}^{5+}$.

In this chapter, I show that $\text{Na}_{1.5}\text{VPO}_{4.8}\text{F}_{0.7}$, the precursor of $\text{Li}_{1.1}\text{Na}_{0.4}\text{VPO}_{4.8}\text{F}_{0.7}$, can function as an excellent cathode for rechargeable Na batteries with a high energy density. It exceeds the state-of-the-art P2-type layered oxide. Surprisingly, most electrochemical properties of this material such as its power capability and long-term cycle life outperform those of existing cathodes for NIBs and even rival those of LIB cathodes such as olivine LiFePO_4 and spinel LiMn_2O_4 . The origin of the high battery performance is discussed through an analysis using combined theoretical and experimental tools.

2.2. Experimental and Computational Details

2.2.1. Materials synthesis. $\text{Na}_{1.5}\text{VPO}_{4.8}\text{F}_{0.7}$ and $\text{Na}_{1.5}\text{VPO}_5\text{F}_{0.5}$ powders were prepared by solid-state reaction using stoichiometric amounts of VOPO_4 , VPO_4 , NaF (Sigma-Aldrich, 99%) and Na_2CO_3 (Sigma-Aldrich, 99%), as described in my previous report.³⁴ To obtain Na-deficient $\text{Na}_x\text{VPO}_{5-\delta}\text{F}_{0.5+\delta}$ phases ($x < 1.5$, $\delta = 0$ and

0.2) with various Na contents, the $\text{Na}_{1.5}\text{VPO}_{5-\delta}\text{F}_{0.5+\delta}$ powders were chemically oxidized using a stoichiometric amount of NO_2BF_4 (Sigma-Aldrich, 95%) in acetonitrile solvent (Sigma-Aldrich, 99.8%) at room temperature. Following reaction for 6–15 h, the powders were washed, centrifuged several times with acetonitrile and ethanol, and then dried in a vacuum oven at 70°C overnight. The atomic ratios of Na, V, and P were determined by ICP spectroscopy (Polyscan 60E; Thermo Jarrell Ash, USA).

2.2.2. SEM, XRD, and XANES. SEM images were obtained using a SUPRA 55VP FE-SEM (Carl Zeiss, Germany) at an operating voltage of 2 kV. Powder XRD patterns were recorded using an X-ray diffractometer (D8 Advance; Bruker, Germany) using Ni-filtered $\text{Cu-K}\alpha$ radiation ($\lambda_1 = 1.54059 \text{ \AA}$, $\lambda_2 = 1.54431 \text{ \AA}$) in the 2θ range of 10–60°. The room temperature XRD data were refined using the Rietveld method and FullProf software.³⁵ All $\text{Na}_x\text{VPO}_{5-\delta}\text{F}_{0.5+\delta}$ phases cited in the text ($x \leq 1.5$, $\delta = 0$ and 0.2) were refined with the same space group of $P4_2/mnm$. X-ray absorption near-edge structure (XANES) spectra were recorded at room temperature at the 8C XAFS beamline in PLS-II using photons with a storage ring energy of 2.5 GeV and a current of 125 mA in top-up mode. They were collected in the transmission mode at the vanadium K-edge.

2.2.3. Electrochemical tests. A slurry of 70 wt% $\text{Na}_{1.5}\text{VPO}_{4.8}\text{F}_{0.7}$, 20 wt% carbon black, and 10 wt% polyvinylidene fluoride (Sigma-Aldrich) dispersed in *N*-methyl-2-pyrrolidone (Sigma-Aldrich) was prepared and cast on aluminum foil. The electrode was dried at 120°C, and the loading of the active material on the electrode was *ca.* 2–3 mg cm^{-2} . Electrochemical cells were assembled into CR2032-type coin cells in an Ar-filled glove box (MBraun, Germany). Na metal (Sigma-Aldrich) and a glass microfiber filter (grade GF/F; Whatman, USA) were

used as a counter electrode and separator, respectively. Unless otherwise noted, 1 M NaClO₄ in propylene carbonate (PC, Sigma-Aldrich) was used as an electrolyte, and all electrochemical tests were performed at room temperature using a potentiostat/galvanostat (WBCS 3000; WonA Tech, Korea). To prepare the Na_xVPO_{4.8}F_{0.7} electrodes for the *ex situ* XRD experiment, the electrochemical cells were galvanostatically charged or discharged at a C/10 rate and disassembled at various states of charge and depths of discharge. Prior to XRD experiments, the electrodes were washed with PC and dried overnight in a vacuum oven at 70°C. Based on one electron transfer, 1C was calculated to correspond to 129.7 mA g⁻¹. For GITT measurement, the electrochemical cells were rested for 2 h after each hour-long charging or discharging at a C/10 rate. Combined GITT and electrochemical impedance spectroscopy (EIS) measurement was carried out for the first charge process. An electrochemical cell comprising the Na_{1.5}VPO_{4.8}F_{0.7} cathode was charged for 11 min in galvanostatic mode at a C/5 rate and rested for 1 h. EIS spectra were recorded at the end of each rest step between 1 MHz and 1 Hz, with a sinus amplitude of 10 mV. This sequence was repeated when the operating voltage reached 4.5 V (vs. Na⁺/Na) using a multichannel potentiostat/galvanostat with EIS (VSP-300; Bio-Logic, France). For the room-temperature rate capability test, the Na_{1.5}VPO_{4.8}F_{0.7} powder was subjected to a dry carbon-coating process; 20 wt% carbon black was blended, and the mixture was ball-milled for 24 h. In this test, the total active content in the electrode was 72 wt%, and the voltage window was 1.5–4.6 V (vs. Na⁺/Na).

2.2.4. Electrical conductivity (a.c.) measurements. Na_{1.5}VPO_{4.8}F_{0.7} and Na_{1.0}VPO_{4.8}F_{0.7} powders were pressed into pellets with 15-mm diameters and ~1 mm thicknesses using a uniaxial press (400 kg cm⁻²). They were further compacted

at 200 MPa for 6 min by cold isostatic press; a compactness of ~70% of the pellet was obtained without sintering. 50-nm-thick platinum layers were deposited on both sides of the pellets by sputtering. The bulk conductivities of the pellets were measured using two-probe a.c. impedance spectroscopy (models 1260 and 1296; Solatron, UK) and the ZView electrochemical impedance software (Scribner Associates, USA). EIS data were recorded from 1 MHz to 100 mHz with a voltage perturbation of 1 V. Bulk conductivities (a.c.) were calculated from both the geometries of the pellets and bulk resistance values which were obtained by one-circle fitting of the high-frequency region in the EIS spectra. Finally, activation energies (a.c.) were obtained using linear interpolation of the conductivity values at various temperatures by the Arrhenius equation: $\sigma T = \sigma_0 \exp(-E_a/k_B T)$, where σ is conductivity, T is temperature, E_a is activation energy, and k_B is the Boltzmann constant. Room-temperature conductivities were estimated by linear extrapolation of the measured data points.

2.2.5. Computational details. First-principle calculations were performed using the Perdew–Burke–Ernzerhof exchange-correlation parameterization to density functional theory (DFT) with the spin-polarized generalized gradient approximation (GGA).³⁶ A plane-wave basis set and the projector-augmented wave (PAW) method was used as implemented in the Vienna *ab initio* simulation package (VASP).³⁷ Hubbard parameters (GGA+U)³⁸ were added to correct the incomplete cancellation of the self-interaction of GGA. A U value of 5.0 eV (the on-site coulomb term) and J value of 1.0 eV (the exchange term) were used for the vanadium ions.^{17,39} To study $\text{Na}_x\text{VPO}_5\text{F}_{0.5}$ phases, all possible Na-vacancy orderings were considered within the unit cell of $\text{Na}_x\text{VPO}_5\text{F}_{0.5}$ ($0.5 \leq x \leq 1.5$) generated with the CASM program.⁴⁰ Among them, 30 Na-vacancy orderings were

picked up with the lowest electrostatic energy at each composition through the Ewald summation method³² and then calculated their energies with GGA+U. Their formation energies were plotted as a function of Na content. The voltage profile of $\text{Na}_x\text{VPO}_5\text{F}_{0.5}$ in a Na cell was also determined using following equation:

$$\langle V \rangle = -[E(\text{Na}_{x_1}\text{VPO}_5\text{F}_{0.5}) - E(\text{Na}_{x_2}\text{VPO}_5\text{F}_{0.5}) - (x_1 - x_2) \times E(\text{Na})] / [(x_1 - x_2) \times F],$$

where E is the DFT energy of the most stable structure and F is the Faraday constant. Activation energies for Na vacancy diffusion in $\text{Na}_x\text{VPO}_{5-\delta}\text{F}_{0.5+\delta}$ ($x \approx 1.5$) were calculated using the nudged-elastic-band (NEB) method.⁴¹ In these calculations, the Na^+ ions were allowed to move in the unit cell of $\text{Na}_{23/16}\text{VPO}_5\text{F}_{0.5}$. Five or seven replicate systems were used as the starting points for the NEB method, with linear interpolation between the initial and final states of the plausible diffusion pathways. All lattice parameters were fixed at the $\text{Na}_{1.5}\text{VPO}_5\text{F}_{0.5}$ states, but all internal degrees of freedom were relaxed during the NEB calculations. The bond valence mismatch map was calculated using the 3DBVSMAPPER program⁴² and drawn using VESTA program.⁴³

2.3. Results and Discussion

2.3.1. Material Characterization of $\text{Na}_{1.5}\text{VPO}_{4.8}\text{F}_{0.7}$

Phase-pure $\text{Na}_{1.5}\text{VPO}_{4.8}\text{F}_{0.7}$ with no notable impurity was obtained successfully (**Figure 2-1**). The composition and oxidation state of vanadium ions of $\text{Na}_{1.5}\text{V}^{3.8+}\text{PO}_{4.8}\text{F}_{0.7}$ were confirmed by multiple lines of evidence in the previous report.³⁴ The fluorinated $\text{Na}_{1.5}\text{VPO}_{4.8}\text{F}_{0.7}$ phase was isostructural to both $\text{Na}_{1.5}\text{VPO}_5\text{F}_{0.5}$ and $\text{Na}_3\text{V}_2(\text{PO}_4)_2\text{F}_3$ (or $\text{Na}_{1.5}\text{VPO}_4\text{F}_{1.5}$), with a space group of

$P4_2/mnm$. Refinement of the crystal structure of $\text{Na}_{1.5}\text{VPO}_{4.8}\text{F}_{0.7}$ indicated that the corner-sharing between PO_4 tetrahedral and $\text{VO}_5\text{F}/\text{VO}_4\text{F}_2$ octahedral units constructs a three-dimensional open framework where Na^+ ions can be inserted into the interstitial sites (**Figure 2-2**). The overall crystal framework can also be described as a pseudo-layered structure because the intercalant Na^+ ions form Na layers on the ab plane in the structure. The sizes of $\text{Na}_{1.5}\text{VPO}_{4.8}\text{F}_{0.7}$ particles ranged from 1 to 5 μm (**Figure 2-1**, inset).

As a result of fluorination, two types of vanadium local environment, VO_5F and VO_4F_2 octahedra, were generated. This also led to the mixed valence state of vanadium (*i.e.*, coexistence of V^{4+} and V^{3+} ions) in $\text{Na}_{1.5}\text{VPO}_{4.8}\text{F}_{0.7}$, which was confirmed previously by the double titration method and electron paramagnetic resonance (EPR) experiments.³⁴

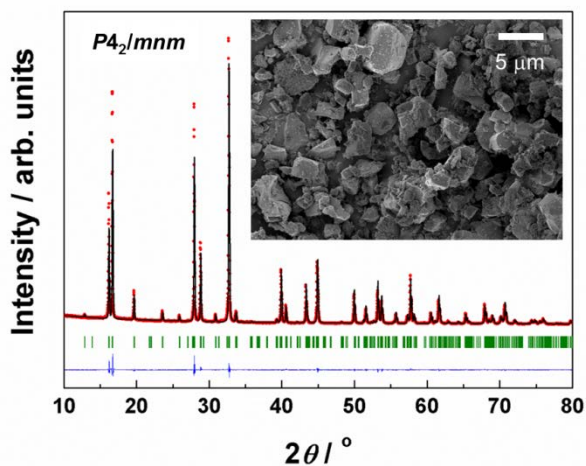


Figure 2-1. Powder XRD pattern of $\text{Na}_{1.5}\text{VPO}_{4.8}\text{F}_{0.7}$. Rietveld refinement with observed data points (red dots), calculated pattern (black line), difference curve (blue line), and Bragg positions (green bars); lattice parameters in the space group of $P4_2/mnm$ were $a = b = 9.03057(9) \text{ \AA}$, $c = 10.6282(1) \text{ \AA}$, and $V = 866.74(2) \text{ \AA}^3$. The inset shows an SEM image (magnification: $\times 5,000$). Reprinted with permission from [Y.-U. Park *et. al.*, *J. Am. Chem. Soc.*, **135**, 13870-13878 (2013); DOI: 10.1021/ja406016j]. Copyright 2013 American Chemical Society.

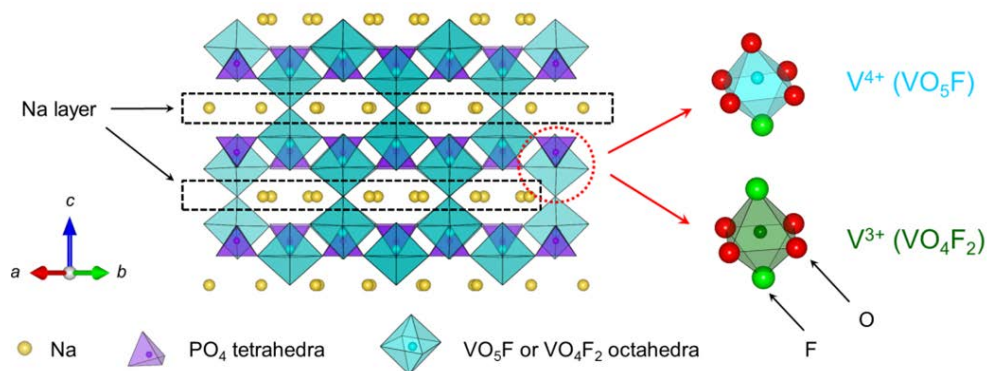


Figure 2-2. Crystal structure of $\text{Na}_{1.5}\text{VPO}_{4.8}\text{F}_{0.7}$ and two local environments for vanadium ions. The Na, V, P, O, and F atoms are depicted as yellow, cyan, purple, red, and green spheres, respectively. The Na layers are denoted as dashed boxes. Reprinted with permission from [Y.-U. Park *et. al.*, *J. Am. Chem. Soc.*, **135**, 13870-13878 (2013); DOI: 10.1021/ja406016j]. Copyright 2013 American Chemical Society.

2.3.2. Electrochemical Properties of $\text{Na}_{1.5}\text{VPO}_{4.8}\text{F}_{0.7}$

Prior to electrochemical tests in Na batteries, the Na extraction behavior of $\text{Na}_{1.5}\text{VPO}_{4.8}\text{F}_{0.7}$ was monitored *via* first-principle calculations on a simpler isostructural $\text{Na}_{1.5}\text{VPO}_5\text{F}_{0.5}$ system. **Figure 2-3** shows the calculated formation energies of $\text{Na}_x\text{VPO}_5\text{F}_{0.5}$ with various Na-vacancy configurations for selected Na contents. The energy plot shows a minimum at $x = 1.0$, implying the strong tendency for a stable intermediate phase at this composition. The existence of the intermediate phase at this composition was identified by *ex situ* XRD study, which will be discussed later. Generally, intermediate phases are often observed in Na-intercalation compounds.^{11,44} $\text{Na}^+ - \text{Na}^+$ electrostatic repulsion, as well as the interaction between Na^+ and transition metal ions, leads to strong Na-vacancy ordering at certain Na concentrations, forming a stable intermediate phase, as recently demonstrated for P2- Na_xCoO_2 .^{11,44} Similarly, the intermediate phase (at $x = 1.0$) in the $\text{Na}_x\text{VPO}_{5-\delta}\text{F}_{0.5+\delta}$ system likely originated from Na-vacancy ordering.

First-principle calculations suggested the most energetically plausible Na-vacancy configurations in the stable phases of $\text{Na}_x\text{VPO}_{5-\delta}\text{F}_{0.5+\delta}$ ($x = 1.5, 1.0$, and 0.5 ; **Figure 2-4**, inset). The as-prepared material ($x = 1.5$) contained three Na^+ ions per basic unit of the Na layer (indicated in a red box in **Figure 2-4**, right panel), while there are four crystallographically equivalent Na sites per basic unit. Each basic unit contained the same number (three) of Na^+ ions, without segregation into two and four Na^+ ion occupations in two basic units, which is attributable to $\text{Na}^+ - \text{Na}^+$ repulsion inside the basic units of the Na layers. Due to the strong $\text{Na}^+ - \text{Na}^+$ repulsion, Na^+ ions do not occupy the centers of the interstitial sites, but have shifted positions. The number of Na^+ ions per basic unit (n) is a fingerprint of each phase; $n = 3, 2$, and 1 for $x = 1.5, 1.0$, and 0.5 , respectively. Note that no mixture of

$n = 3$ and 1 occurred in the intermediate phase ($x = 1.0$).

When 0.5 Na⁺ ions were extracted from the material, the repulsive force could be greatly relieved by Na-vacancy reordering through the diagonal configuration ($x = 1.0$; **Figure 2-4**, inset). This change accompanied the increased symmetry of the intermediate phase. Indeed, I later observed in the experimental structure characterization that Na_{1.0}VPO_{4.8}F_{0.7} transformed from $P4_2/mnm$ to the higher-symmetry space group of $I4/mmm$ (see **Figure 2-5**). The diagonal Na-vacancy configuration that minimizes electrostatic repulsion is believed to stabilize the Na_{1.0}VPO₅F_{0.5} intermediate phase relative to the mixture of two-end members (*i.e.*, Na_{1.5}VPO₅F_{0.5} and Na_{0.5}VPO₅F_{0.5}). It causes a voltage gap at the composition of $x = 1.0$ (**Figure 2-4**, blue profile), which is in good agreement with the experiment, as indicated by the red profile in **Figure 2-4**. The calculated operating voltages for two regions (3.62 and 3.90 V) yielded an average voltage of 3.76 V (*vs.* Na⁺/Na) which was also comparable to the experimental value (**Figure 2-4**, red profile) of 3.8 V measured in a Na half-cell using a Na metal anode. The average voltage of Na_{1.5}VPO_{4.8}F_{0.7} (~3.8 V *vs.* Na⁺/Na) is an impressively high value for a cathode material for NIBs. The high voltage of Na_{1.5}VPO_{4.8}F_{0.7} electrode can be attributed to the high redox potential of the vanadium couple, aided by the large inductive effect of the fluorophosphate group.

Galvanostatic measurement at a C/10 rate revealed that the specific capacity could be enhanced *via* the multi-electron redox reaction of vanadium ($V^{3.8+} \leftrightarrow V^{5+}$) in a Na cell (**Figure 2-6**). The discharge capacity (~134 mAh g⁻¹) at a C/10 rate simply exceeded the theoretical capacity (129.7 mAh g⁻¹), based on one electron transfer for both charging and discharging, which is consistent with my observations for Li_{1.1}Na_{0.4}VPO_{4.8}F_{0.7}.³⁴ It should be noted that the additional

V^{3+}/V^{4+} redox reaction from the widened redox range in $Na_{1.5}V^{3.8+}PO_{4.8}F_{0.7}$ does not exhibit voltage well below that of V^{4+}/V^{5+} , but is rather comparable to the V^{3+}/V^{4+} redox potential of ~ 3.9 V (vs. Na^+/Na) in $Na_3V_2(PO_4)_2F_3$ (or $Na_{1.5}V^{3+}PO_4F_{1.5}$).¹⁷ For $Na_{1.5}VPO_{4.8}F_{0.7}$, the additional fluorination that induces V^{3+} formation is considered to create a local environment of $V^{3+}O_4F_2$ similar to $Na_3V_2(PO_4)_2F_3$, sustaining the reasonably high voltage for the V^{3+}/V^{4+} redox reaction. Cycling at a C/10 rate showed two peaks at 3.61 and 4.02 V (vs. Na^+/Na) in the dQ/dV curve (**Figure 2-6**, inset), implying two different reactions, which will be discussed later.

The evolution of the vanadium oxidation state in $Na_xVPO_{4.8}F_{0.7}$ electrodes could be clearly identified by XANES analysis of the vanadium K-edge during charging and discharging process (**Figure 2-7**). During charging, the edge of the spectrum shifted toward a higher energy, indicating oxidation of the vanadium ion. During the reverse reaction, it completely returned to the initial state, implying that the vanadium redox reaction is fully reversible. A clearer change was observed in the pre-edge region, where the pre-edge peak reversibly arose at a higher energy region during cycling, which is consistent with previous reports.^{45,46}

Based on the average voltage of 3.8 V (vs. Na^+/Na), the theoretical energy density of the $Na_{1.5}VPO_{4.8}F_{0.7}$ cathode can reach 600 Wh kg^{-1} with the $V^{3.8+}/V^{5+}$ redox couple. It should be noted that the $Na_{1.5}VPO_{4.8}F_{0.7}$ cathode exhibits the highest energy density among cathode materials for NIBs (**Figure 2-8**). The energy densities of polyanion-based cathodes such as $NaFePO_4$, Na_2FePO_4F , and $Na_3V_2(PO_4)_3$ hover around 400 Wh kg^{-1} , and only a few cathode materials such as the P2-type $Na_x[Fe_{1/2}Mn_{1/2}]O_2$ and BPOE have been reported to have energy densities approaching 500 Wh kg^{-1} .^{8,15,21,22,24-30} The energy density of the

$\text{Na}_{1.5}\text{VPO}_{4.8}\text{F}_{0.7}$ cathode ($\sim 600 \text{ Wh kg}^{-1}$) holds a unique position among cathode materials for NIBs with a high operating voltage. Moreover, it can rival state-of-the-art LIB cathode materials such as LiFePO_4 (theoretical energy density of 580 Wh kg^{-1}) and LiMn_2O_4 (480 Wh kg^{-1}), indicating the promise of its application as an alternative chemistry to LIB.

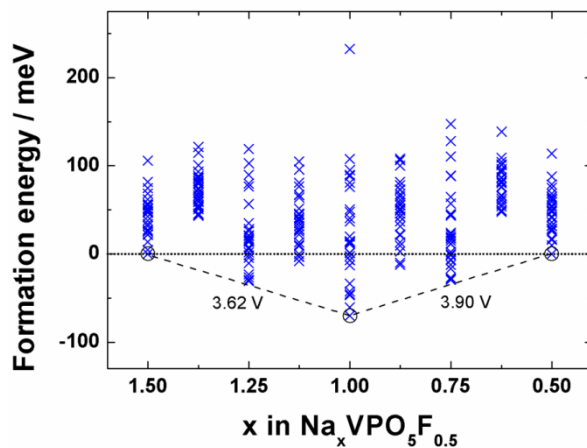


Figure 2-3. Formation energy plot of $\text{Na}_x\text{VPO}_5\text{F}_{0.5}$ from first-principle calculations. Reprinted with permission from [Y.-U. Park *et. al.*, *J. Am. Chem. Soc.*, 135, 13870-13878 (2013); DOI: 10.1021/ja406016j]. Copyright 2013 American Chemical Society.

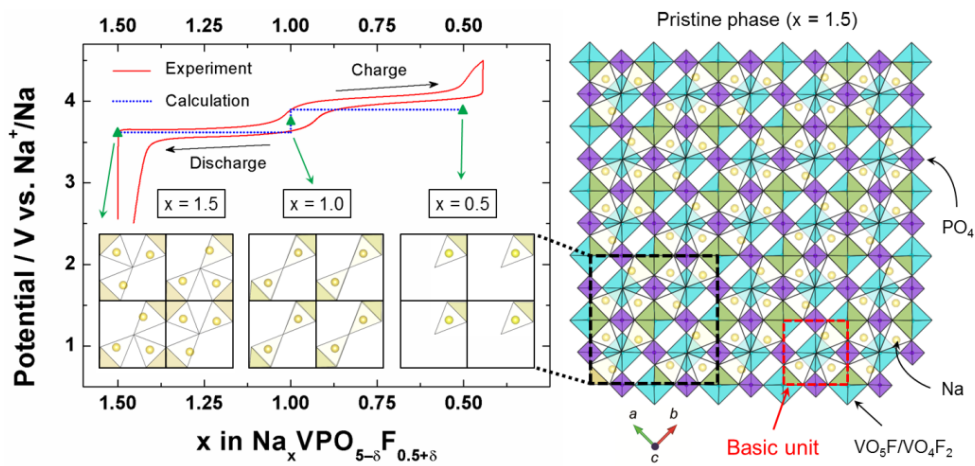


Figure 2-4. Comparison of voltage vs. composition curves from experiments and calculations. The inset shows the most stable Na-vacancy configuration in the Na layer (on the *ab* plane) for each Na content ($x = 1.5$, 1.0 , and 0.5) in the calculations. Complete crystal structure on the *ab* plane of the pristine phase ($x = 1.5$) is shown on the right side, where a basic unit (*i.e.*, the smallest unit for defining the Na-vacancy ordering in the Na layer) is denoted as a red dashed box. Reprinted with permission from [Y.-U. Park *et. al.*, *J. Am. Chem. Soc.*, **135**, 13870-13878 (2013); DOI: 10.1021/ja406016j]. Copyright 2013 American Chemical Society.

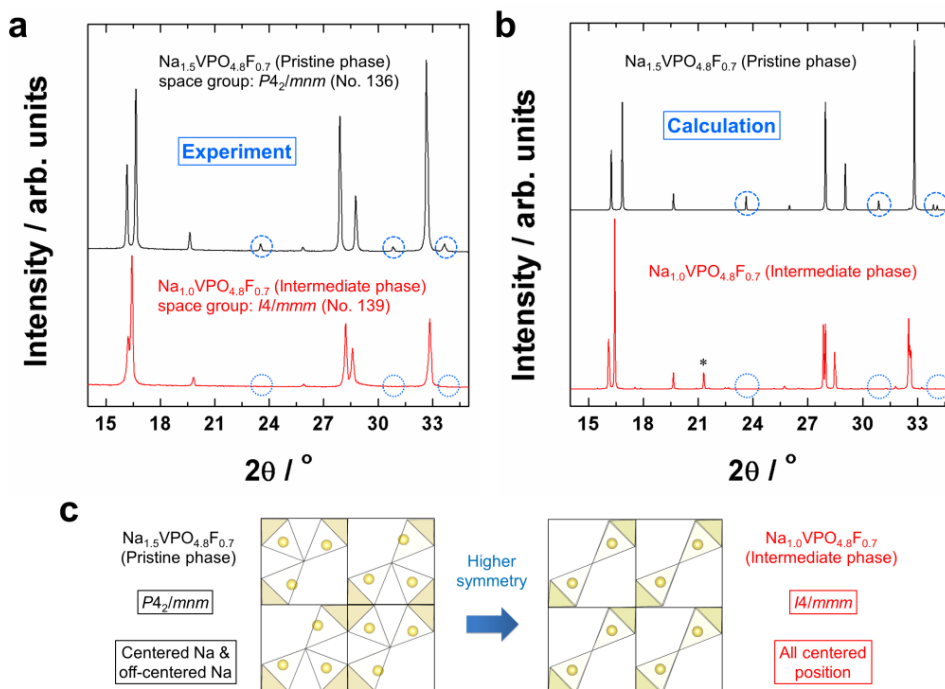


Figure 2-5. Space group change from $P4_2/mnm$ to $I4/mmm$ for Na_xVPO_{4.8}F_{0.7}.

(a) Experimental X-ray diffraction (XRD) patterns of Na_{1.5}VPO_{4.8}F_{0.7} (top) and Na_{1.0}VPO_{4.8}F_{0.7} (bottom). The former has a space group of $P4_2/mnm$ (No. 136), and the latter has a higher symmetry of $I4/mmm$ (No. 139). The reflections denoted as dashed circles in the top spectrum are allowed only for $P4_2/mnm$; they are forbidden for a higher symmetry of $I4/mmm$ (see dotted circles in the bottom spectrum).

(b) Simulated XRD patterns of Na_{1.5}VPO_{4.8}F_{0.7} (top) and Na_{1.0}VPO_{4.8}F_{0.7} (bottom) based on the most stable structures from the first-principle calculations. The absence of the superstructure peaks (denoted as circles) in the latter was consistently observed in the calculations as well. A reflection at $\sim 21^\circ$ (denoted as

an asterisk) in the simulated XRD pattern of $\text{Na}_{1.0}\text{VPO}_{4.8}\text{F}_{0.7}$ (**Figure 2-5b**; bottom) was not observed in the experiment (**Figure 2-5a**; bottom), which is attributable to the layer-layer Na-vacancy disordering in the real system.

(c) Correlation between the change in the Na-vacancy configuration in the Na layer and the symmetry change. I believe that this symmetry change is strongly related to the Na-vacancy configuration. Because $\text{Na}^+ - \text{Na}^+$ repulsion in the pristine phase is severe, some Na^+ ions lie in off-centered positions at Na sites, leading to distortion of the framework (left). In contrast, in the intermediate phase, all Na^+ ions can lie in the center positions at Na sites because $\text{Na}^+ - \text{Na}^+$ repulsion is greatly relieved by the diagonal Na configuration (right). This situation may remove distortion of the framework and result in the increased symmetry ($P4_2/mnm \rightarrow I4/mmm$).

(*) Reprinted with permission from [Y.-U. Park *et. al.*, *J. Am. Chem. Soc.*, 135, 13870-13878 (2013); DOI: 10.1021/ja406016j]. Copyright 2013 American Chemical Society.

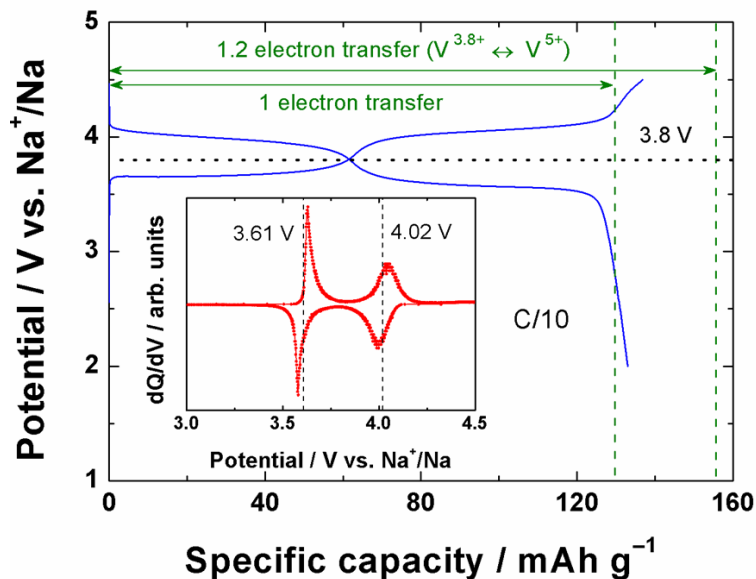


Figure 2-6. Charge/discharge profile at a C/10 rate for $\text{Na}_{1.5}\text{VPO}_{4.8}\text{F}_{0.7}$ cathode.

The average voltage (3.8 V vs. Na^+/Na) is represented as a horizontal dotted line. The capacities based on 1 electron transfer (129.7 mAh g^{-1}) and 1.2 electron transfer (155.6 mAh g^{-1}) are shown as vertical dashed lines, respectively. The 1C rate corresponds to 129.7 mA g^{-1} . The inset shows the corresponding dQ/dV curve. Reprinted with permission from [Y.-U. Park *et. al.*, *J. Am. Chem. Soc.*, 135, 13870-13878 (2013); DOI: 10.1021/ja406016j]. Copyright 2013 American Chemical Society.

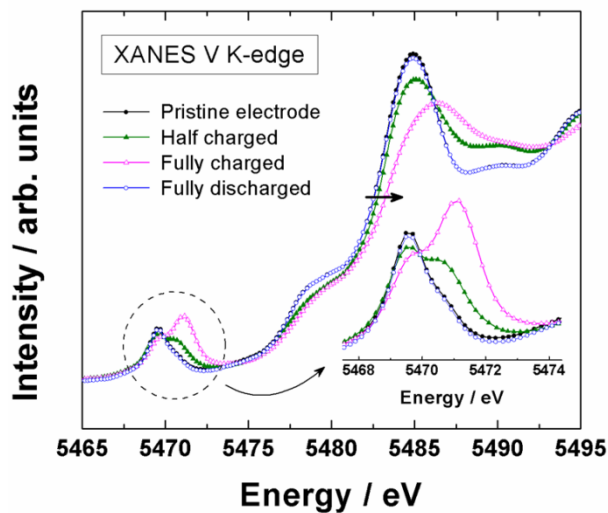


Figure 2-7. Vanadium K-edge XANES spectra of the $\text{Na}_x\text{VPO}_{4.8}\text{F}_{0.7}$ electrodes.

The inset shows an enlarged graph of a pre-edge region. Reprinted with permission from [Y.-U. Park *et. al.*, *J. Am. Chem. Soc.*, 135, 13870-13878 (2013); DOI: 10.1021/ja406016j]. Copyright 2013 American Chemical Society.

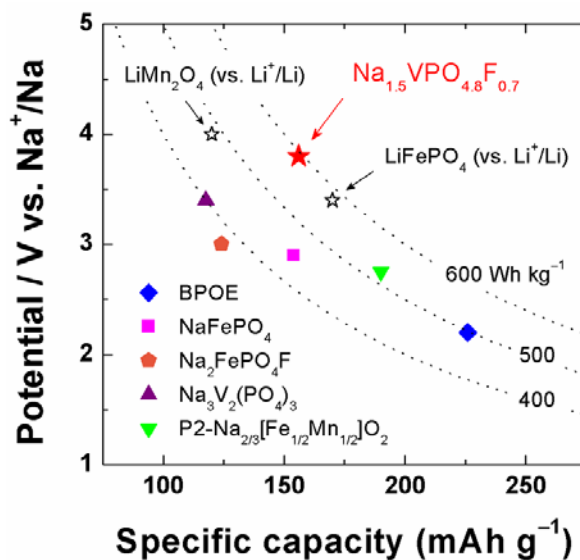


Figure 2-8. Energy density comparison of various cathode materials for NIBs and LIBs. The average voltages were used to calculate the energy densities of the cathodes. Reprinted with permission from [Y.-U. Park *et. al.*, *J. Am. Chem. Soc.*, 135, 13870-13878 (2013); DOI: 10.1021/ja406016j]. Copyright 2013 American Chemical Society.

2.3.3. Structural Evolution of the $\text{Na}_x\text{VPO}_{4.8}\text{F}_{0.7}$ Electrode upon Cycling

To understand the charge/discharge mechanism of the $\text{Na}_x\text{VPO}_{4.8}\text{F}_{0.7}$ electrode in Na batteries, *ex situ* XRD experiments were carried out (**Figure 2-9**; see **Figure 2-10** for more complete pictures). Overall, a continuous peak shift was observed, implying a widespread solid-solution region. However, closer examination of the *ex situ* XRD patterns in **Figure 2-11** revealed that two phases coexisted in the first half of the charge (*i.e.*, region I), indicating the existence of the stable intermediate phase at $x = 1.0$. Conversely, signs of a biphasic reaction were difficult to identify in region II, implying a widespread miscibility gap. After a cycle, the XRD pattern returned to the pristine state, suggesting structural reversibility.

Figure 2-12 shows the changes in lattice parameters of $\text{Na}_x\text{VPO}_{4.8}\text{F}_{0.7}$ phases during charging: a continuous decrease in lattice parameter a and increase in lattice parameter c with decreasing Na content. The reduction of lattice parameter a is attributed to the contraction of vanadium octahedra with the oxidation of V^{n+} ions. On the other hand, lattice parameter c increased due to the developing electrostatic repulsion between O^{2-} layers, as the Na layers that screen the electrostatic repulsion between O^{2-} layers became empty with charging. Interestingly, the same tendency is typically observed in layered oxides such as Na_xCoO_2 and Li_xCoO_2 , which reminds that the $\text{Na}_{1.5}\text{VPO}_{4.8}\text{F}_{0.7}$ crystal can be described as a pseudo-layered structure. The discussion on the charge/discharge mechanism of the $\text{Na}_x\text{VPO}_{4.8}\text{F}_{0.7}$ electrode will be continued in the later part.

The opposite trends of the two lattices with de/sodiation were three-dimensionally counterbalanced, resulting in a surprisingly small volume change (2.9%) upon cycling. Usually, Na^+ ion intercalation accompanies a large volumetric

change due to the larger ionic size of the Na^+ ion compared with the Li^+ ion, which often leads to limited cycle stability and practical capacity.^{8,12,14,16} However, $\text{Na}_{1.5}\text{VPO}_{4.8}\text{F}_{0.7}$ undergoes one of the smallest volume changes with full charge/discharge among cathode materials for NIBs (**Figure 2-13**).^{8,13,15,21,24,28,47} The 2.9% volume change is comparable to that predicted from the first-principle calculations ($\Delta V = 3.1\%$) in my previous work.³⁴ The exceptionally small volume change gives rise to excellent cyclability of the $\text{Na}_{1.5}\text{VPO}_{4.8}\text{F}_{0.7}$ cathode at room and high (60°C) temperatures (**Figure 2-14**). 95% of the initial capacity was retained after 100 cycles. Furthermore, more than 83% and 84% of the initial capacity were maintained after extended 500 cycles at room and high temperatures, respectively. I believe that this outstanding cycle life is due to the low volume change of the rigid polyanion framework that is less sensitive to Na insertion/extraction. Even after 515 cycles, no trace of structural deterioration in the electrode was observed, implying a remarkably stable charge/discharge process (*see* **Figure 2-15**). The correlation between the small volume change and stable cycle property is reminiscent of the well-known zero-strain $\text{Li}_4\text{Ti}_5\text{O}_{12}$ electrode for LIBs, indicating the importance of the small volume change in achieving high cycle stability.⁴⁸ It was also found that after ~300 cycles, the electrode recovered most of the initial capacity when reassembled into another electrochemical cell using new Na metal foil and fresh electrolyte (**Figure 2-16**). This result indicates that the observed capacity fading is mainly due to the oxidation of Na metal or the decomposition of the electrolyte during cycling, rather than the degradation of the material.

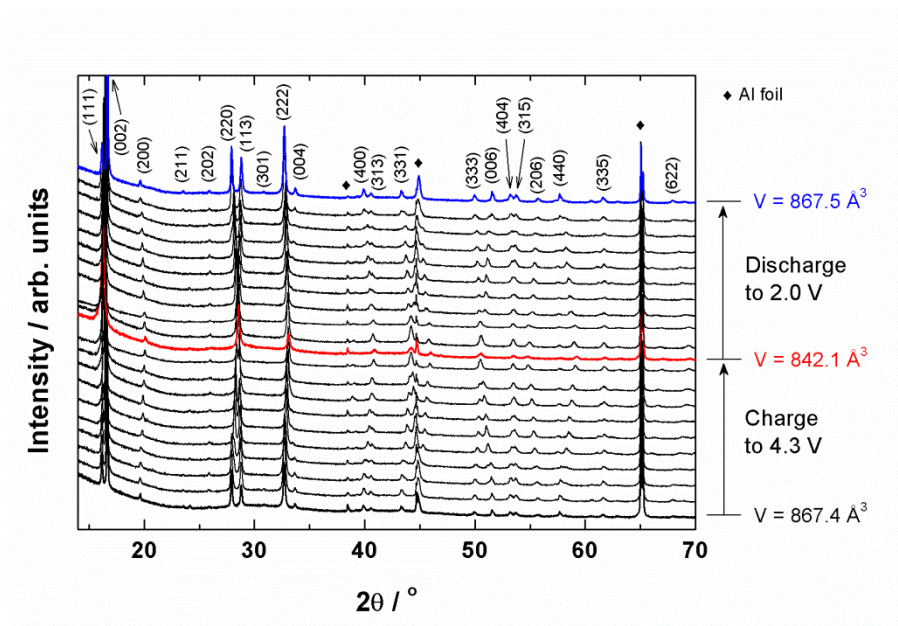


Figure 2-9. *Ex situ* XRD patterns of the $\text{Na}_x\text{VPO}_{4.8}\text{F}_{0.7}$ electrodes. The intervals were identical (10%). The XRD patterns of the fully charged state (at 4.3 V vs. Na^+/Na) and the fully discharged state (at 2.0 V vs. Na^+/Na) were denoted as red and blue colors, respectively. The refined unit cell volumes of the pristine, fully charged, and fully discharged phases were 867.4, 842.1, and 867.5 \AA^3 , respectively. The Rietveld refinements and the indexing of the reflections were based on the space group of $P4_2/mnm$. Peaks marked with diamonds are from aluminum foil in the electrodes. Reprinted with permission from [Y.-U. Park *et. al.*, *J. Am. Chem. Soc.*, 135, 13870-13878 (2013); DOI: 10.1021/ja406016j]. Copyright 2013 American Chemical Society.

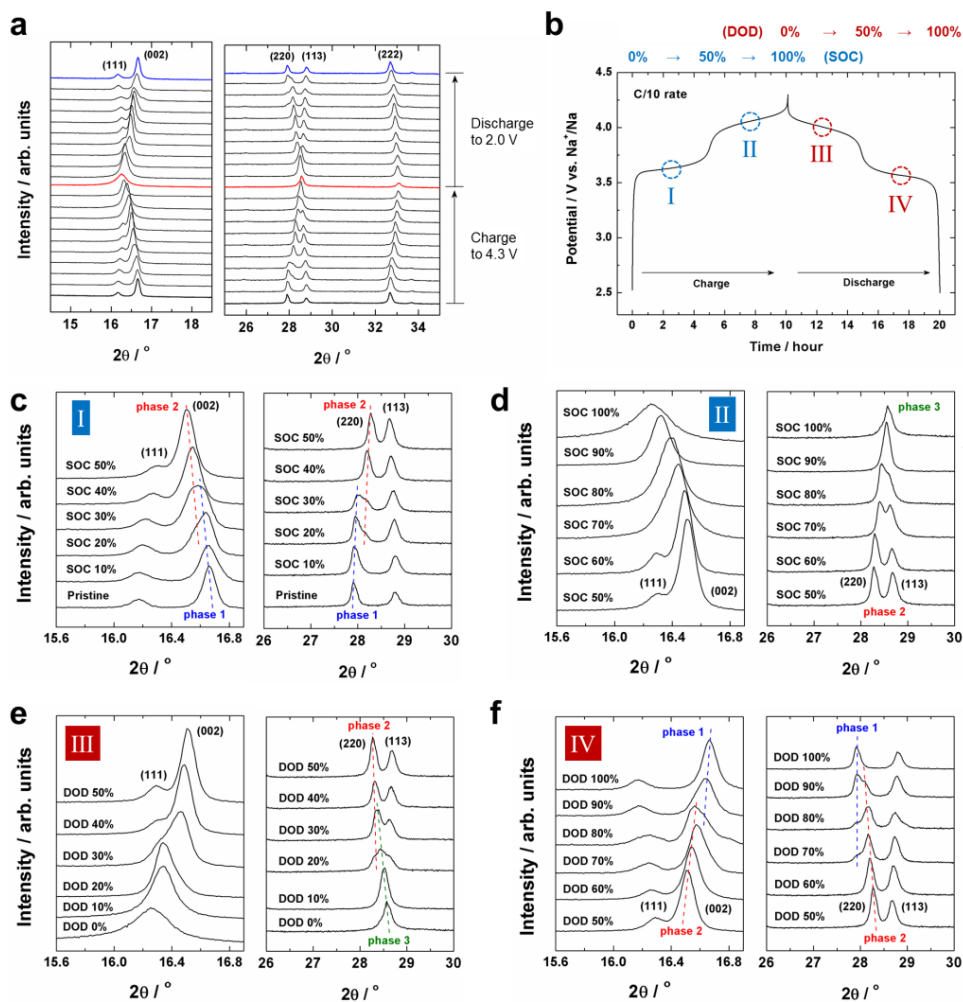


Figure 2-10. Detailed *Ex situ* study on the Na_xVPO_{4.8}F_{0.7} electrodes. (a) *Ex situ* XRD spectra of the Na_{1.5}VPO_{4.8}F_{0.7} electrode upon cycling. (b) Charge/discharge profile for the Na_{1.5}VPO_{4.8}F_{0.7} electrode at a C/10 rate. (c–f) Enlarged XRD spectra for various states of charge (SOCs) and depths of discharge (DODs) whose intervals were identical (10%). Reprinted with permission from [Y.-U. Park *et al.*, *J. Am. Chem. Soc.*, 135, 13870-13878 (2013); DOI: 10.1021/ja406016j]. Copyright 2013 American Chemical Society.

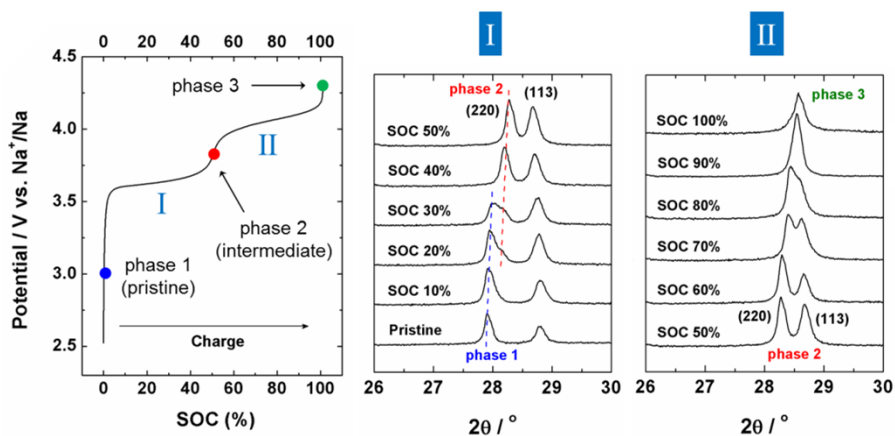


Figure 2-11. Evolution of (220) and (113) reflections of the *ex situ* XRD patterns at different SOC in regions I and II during charging. The left panel shows a typical voltage profile of the $\text{Na}_{1.5}\text{VPO}_{4.8}\text{F}_{0.7}$ electrode as a function of SOC; the regions I and II correspond to the low-voltage and high-voltage regions, respectively. Phases 1 (blue), 2 (red), and 3 (green) represent the pristine phase ($\text{Na}_{1.5}\text{VPO}_{4.8}\text{F}_{0.7}$), the intermediate phase ($\text{Na}_{1.0}\text{VPO}_{4.8}\text{F}_{0.7}$), and the fully charged phase, respectively. Reprinted with permission from [Y.-U. Park *et. al.*, *J. Am. Chem. Soc.*, 135, 13870-13878 (2013); DOI: 10.1021/ja406016j]. Copyright 2013 American Chemical Society.

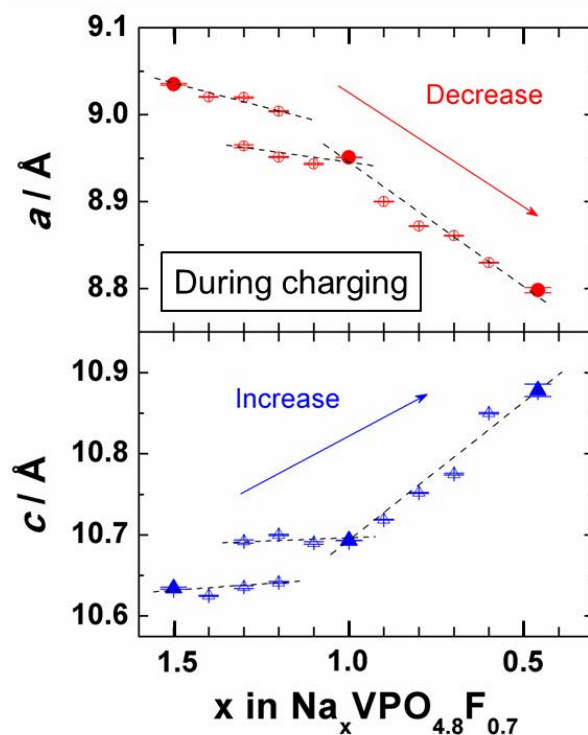


Figure 2-12. Changes in lattice parameters a and c as a function of Na content (x) in the $\text{Na}_x\text{VPO}_{4.8}\text{F}_{0.7}$ electrodes during charging. Reprinted with permission from [Y.-U. Park *et. al.*, *J. Am. Chem. Soc.*, 135, 13870-13878 (2013); DOI: 10.1021/ja406016j]. Copyright 2013 American Chemical Society.

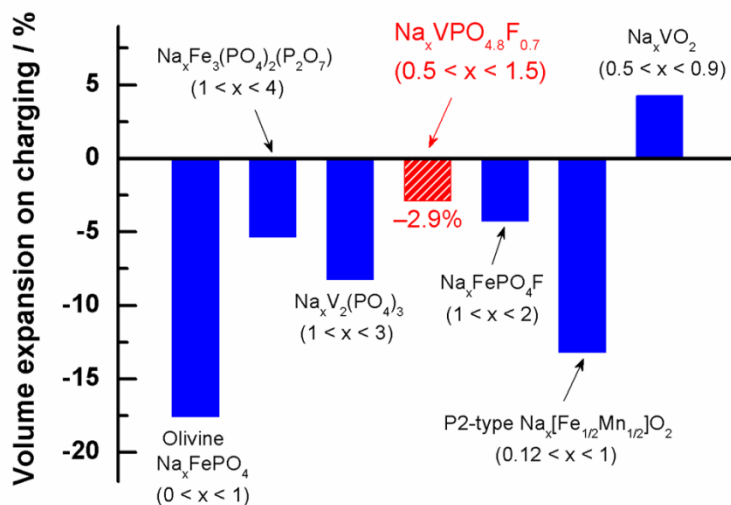


Figure 2-13. Comparison of volume changes on charging in various cathodes for NIBs. Reprinted with permission from [Y.-U. Park *et. al.*, *J. Am. Chem. Soc.*, 135, 13870-13878 (2013); DOI: 10.1021/ja406016j]. Copyright 2013 American Chemical Society.

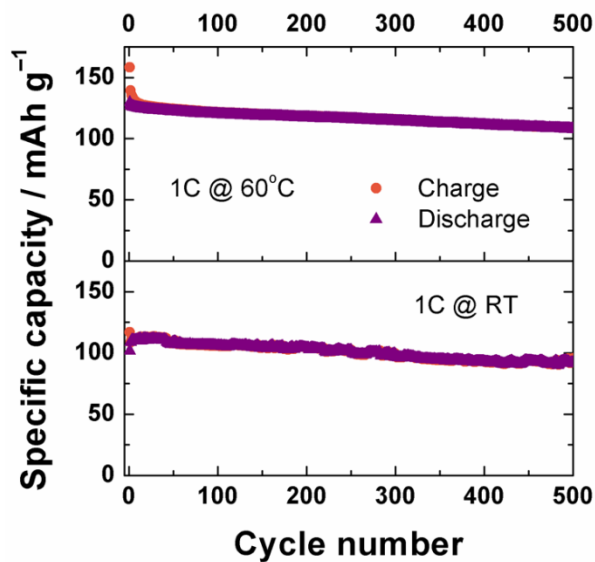


Figure 2-14. Cycle life of the $\text{Na}_{1.5}\text{VPO}_{4.8}\text{F}_{0.7}$ electrode at room (25°C; bottom) and high (60°C; top) temperatures. The electrochemical cells were cycled at a 1C rate with a voltage window of 2.0–4.7 V using the electrolyte of NaBF_4 in a mixture of ethyl carbonate and propylene carbonate (1:1 v/v). Reprinted with permission from [Y.-U. Park *et. al.*, *J. Am. Chem. Soc.*, 135, 13870-13878 (2013); DOI: 10.1021/ja406016j]. Copyright 2013 American Chemical Society.

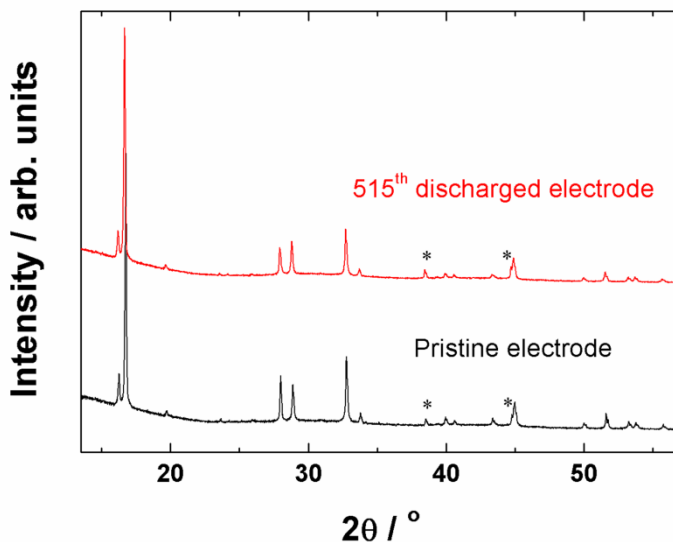


Figure 2-15. XRD pattern of the $\text{Na}_{1.5}\text{VPO}_{4.8}\text{F}_{0.7}$ electrode in the discharged state after 515 cycles at a 1C cycling rate at room temperature (top red line). The bottom black line shows the XRD pattern of the pristine electrode for comparison. Reflections from aluminum foil are denoted by asterisks. Reprinted with permission from [Y.-U. Park *et. al.*, *J. Am. Chem. Soc.*, 135, 13870-13878 (2013); DOI: 10.1021/ja406016j]. Copyright 2013 American Chemical Society.

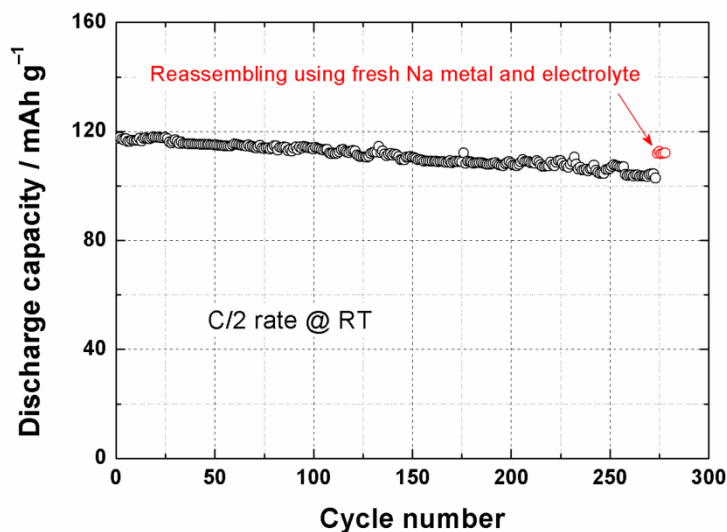


Figure 2-16. Capacity recovery by reassembling a multi-cycled electrode into another electrochemical cell using fresh Na metal and electrolyte. First, the $\text{Na}_{1.5}\text{VPO}_{4.8}\text{F}_{0.7}$ electrode was cycled at a C/2 rate with a voltage window of 2.0–4.7 V (vs. Na^+/Na) at room temperature using the counter electrode of Na metal and the electrolyte of NaBF_4 in a mixture of ethyl carbonate (EC) and propylene carbonate (PC) (1:1 v/v). After 273 cycles, the electrochemical cell was disassembled and the electrode was washed with PC and dried under inert atmosphere. After reweighing, the electrode was reassembled into another electrochemical cell using new Na foil and fresh electrolyte. The cell was cycled again under the same conditions. Reprinted with permission from [Y.-U. Park *et. al.*, *J. Am. Chem. Soc.*, 135, 13870-13878 (2013); DOI: 10.1021/ja406016j]. Copyright 2013 American Chemical Society.

2.3.4. Kinetics of the $\text{Na}_{1.5}\text{VPO}_{4.8}\text{F}_{0.7}$ Electrode

The kinetic behavior of the $\text{Na}_{1.5}\text{VPO}_{4.8}\text{F}_{0.7}$ electrode was first examined using the galvanostatic intermittent titration technique. The negligible overpotential values (~ 20 mV) throughout the whole charge/discharge process implied potentially fast kinetics of the electrode (**Figure 2-17**). In effect, high power capabilities during charging and discharging were observed in the rate tests of the $\text{Na}_{1.5}\text{VPO}_{4.8}\text{F}_{0.7}$ electrode in the Na cell (**Figure 2-18**). From 0.2C to 1C, only negligible capacity reduction was detected with a remarkably small polarization. Even at the 20C rate, the charge/discharge exhibited reasonably small polarization with a high capacity. A capacity more than 100 mAh g^{-1} could be delivered at a 3-min charge/discharge rate (20C rate). Notably, the particle sizes of $\text{Na}_{1.5}\text{VPO}_{4.8}\text{F}_{0.7}$ ranged from 1 to 5 μm with no special treatment. This result is in contrast to conventional polyanion-based cathodes such as $\text{Na}_3\text{V}_2(\text{PO}_4)_3$ and LiFePO_4 which must be fabricated with nano-morphology with proper conductive coatings to achieve a high power capability. The Ragone plot in **Figure 2-19** depicts the trade-off between energy and power density of the $\text{Na}_{1.5}\text{VPO}_{4.8}\text{F}_{0.7}$ electrode in comparison with the performance of various state-of-the-art NIB electrodes whose power capabilities have been reported. According to the plot, the $\text{Na}_{1.5}\text{VPO}_{4.8}\text{F}_{0.7}$ electrode showed the highest energy density throughout a wide range of charge and discharge rates.^{22,25,26,29,49}

Despite this high power capability, EIS experiments revealed a relatively low electrical conductivity of pristine $\text{Na}_{1.5}\text{VPO}_{4.8}\text{F}_{0.7}$ ($\sim 2.4 \times 10^{-12} \text{ S cm}^{-1}$ at room temperature; **Figure 2-20**). However, the low activation energy (E_a) of ~ 350 meV hinted at its fast kinetics (*see* **Figure 2-21** for the EIS spectra at various temperatures), which is lower than those of other polyanion-based cathodes for

LIBs such as LiFePO_4 (~ 600 meV)⁵⁰ and LiFeSO_4F (~ 990 meV)⁵¹. Interestingly, it was found that electrical conductivity increased dramatically, by five orders of magnitude, in the $\text{Na}_{1.0}\text{VPO}_{4.8}\text{F}_{0.7}$ phase ($\sim 1.2 \times 10^{-7}$ S cm^{-1} at room temperature; **Figure 2-20**). Compared to room-temperature electrical conductivities of other polyanion-based LIB cathodes such as LiFePO_4 ($\sim 10^{-9}$ S cm^{-1})⁵⁰ and LiFeSO_4F ($\sim 10^{-11}$ S cm^{-1})⁵¹, the conductivity of $\sim 10^{-7}$ S cm^{-1} is much higher. More interestingly, its E_a (~ 130 meV) was remarkably low and far less than that of the NASICON-type $\text{Na}_3\text{Zr}_2\text{Si}_2\text{PO}_{12}$ (~ 330 meV) and most Na^+ ion-conducting solid electrolytes.^{52,53} The substantial increase in conductivity upon the change of guest ion concentration is reminiscent of the behavior of $\text{Li}_4\text{Ti}_5\text{O}_{12}$ which is an insulator in the pristine state but becomes conductive, exhibiting very high power capability.⁵⁴ Because the intermediate phase, $\text{Na}_{1.0}\text{VPO}_{4.8}\text{F}_{0.7}$, is related to the phase reactions of all regions (**Figure 2-10**), a fast electrode reaction is believed to be possible except for in the very initial state. Indeed, I observed rapidly improved kinetics of the charge transfer reaction with decreasing Na content of the $\text{Na}_x\text{VPO}_{4.8}\text{F}_{0.7}$ cathode in successive EIS measurements (*see* Supplementary **Figure 2-22** for the evolution of EIS spectra).

The first-principle calculations indicated that the rapid Na ionic diffusion is possible in the *ab* plane with low activation barriers for $\text{Na}_{1.5-y}\text{VPO}_{4.8}\text{F}_{0.7}$. **Figure 2-23** shows that two Na diffusion paths exist in the *ab* plane. The activation barriers for path 1 and 2 were about 30 and 310 meV, respectively,³⁴ indicating that path 2 is a rate-determining step for the successive diffusion of Na^+ ions in the bulk, while path 1 provides ultrafast hopping of Na, even at room temperature. The activation barrier of ~ 300 meV is comparable with those of layered Li transition metal oxide cathodes for LIBs, including LiNiO_2 and LiCoO_2 .⁵⁵ This result indicates that Na

diffusion in the electrode for NIBs is not necessarily slow, despite its larger ionic size, and it is more dominantly affected by its host crystal structure. The two-dimensional nature of Na diffusion can also be beneficial for high power. In a one-dimensional diffuser such as LiFePO_4 , Li migration can be sensitively retarded by small amounts of defects; thus, a large particle size that can contain defects with higher probability is not suitable.⁵⁶ In contrast, the $\text{Na}_{1.5}\text{VPO}_{4.8}\text{F}_{0.7}$ cathode exhibited facile Na migration despite the micron-sized particles. Possible structural defects in the bulk $\text{Na}_x\text{VPO}_{4.8}\text{F}_{0.7}$ hardly obstructed Na migration because Na^+ ions could bypass them easily *via* the two-dimensional diffusional pathways. The high power electrode with micron-sized particles that does not require nanosizing would be beneficial in compensating for a generally low volumetric energy density of polyanion-based electrode materials.

Finally, it is noteworthy that an abnormally low E_a value was observed, despite the high oxidation states of vanadium in the Na-deficient $\text{Na}_x\text{VPO}_{5-\delta}\text{F}_{0.5+\delta}$ phases. NEB calculations for Na diffusion kinetics in $\text{Na}_x\text{VPO}_{5-\delta}\text{F}_{0.5+\delta}$ ($0.5 \leq x \leq 1.5$) revealed that Na^+ ions can move very quickly, regardless of the state of charge. This finding contrasts sharply with the large activation barriers for Li motion (~490 meV) in some layered oxides in highly charged states.⁵⁷ In the intermediate state of Li hopping, Li^+ gets too close to the high-valent transition-metal ions, with large electrostatic repulsion leading to a high activation barrier.⁵⁷ However, the $\text{Na}^+-\text{V}^{n+}$ distance in $\text{Na}_x\text{VPO}_{5-\delta}\text{F}_{0.5+\delta}$ does not shorten, even in the intermediate state of path 2, over the trajectory of Na hopping; rather, it increases, as evidenced from NEB calculations (**Figure 2-24**). Because the stability of the intermediate state during ion hopping is greatly affected by the electrostatic repulsion between cations, less $\text{Na}^+-\text{V}^{n+}$ repulsion during Na migration is expected to lower the activation barrier.

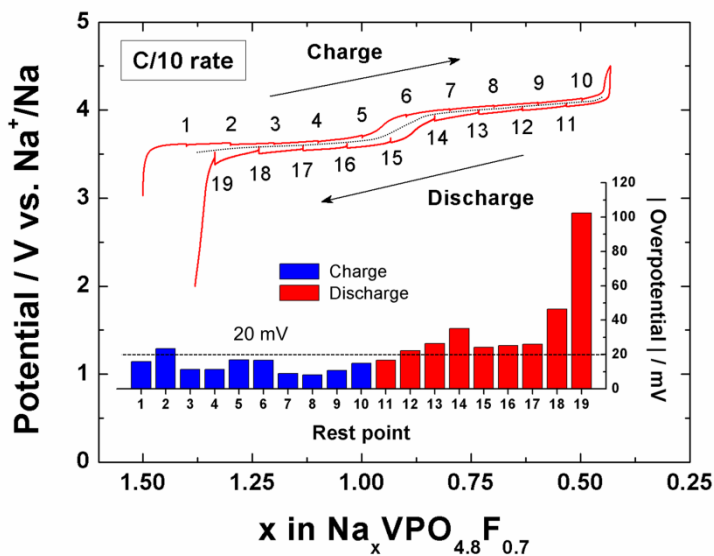


Figure 2-17. GITT curve of the carbon-coated $\text{Na}_{1.5}\text{VPO}_{4.8}\text{F}_{0.7}$ electrode in charge and discharge modes at room temperature. The electrochemical cells were rested for 2 h after each hour-long charging or discharging at a C/10 rate (voltage window: 2.0–4.5 V). 1C corresponds to 129.7 mA g^{-1} , which was calculated based on one electron transfer. The inset shows absolute overpotential values for all rest points (1–19). Most exhibit very small overpotential values less than 20 mV. Reprinted with permission from [Y.-U. Park *et. al.*, *J. Am. Chem. Soc.*, 135, 13870-13878 (2013); DOI: 10.1021/ja406016j]. Copyright 2013 American Chemical Society.

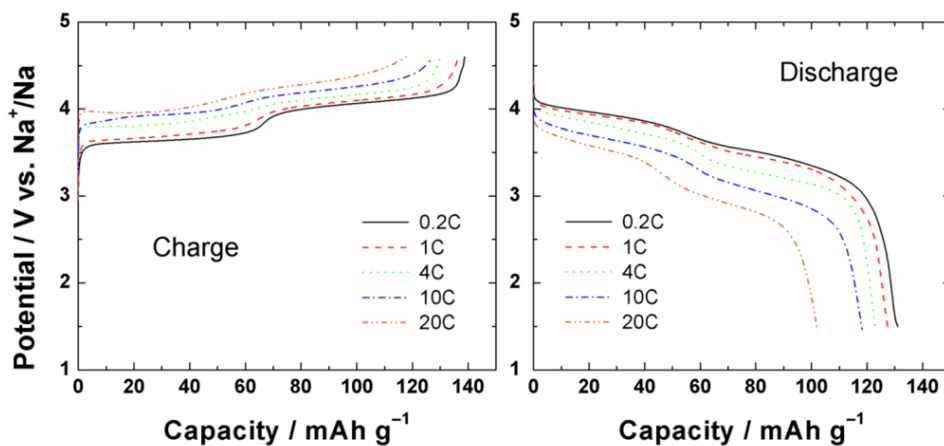


Figure 2-18. Rate capability of the $\text{Na}_{1.5}\text{VPO}_{4.8}\text{F}_{0.7}$ cathode. Charge (left) and discharge (right) profiles of the $\text{Na}_{1.5}\text{VPO}_{4.8}\text{F}_{0.7}$ cathode at various C rates. Reprinted with permission from [Y.-U. Park *et. al.*, *J. Am. Chem. Soc.*, 135, 13870-13878 (2013); DOI: 10.1021/ja406016j]. Copyright 2013 American Chemical Society.

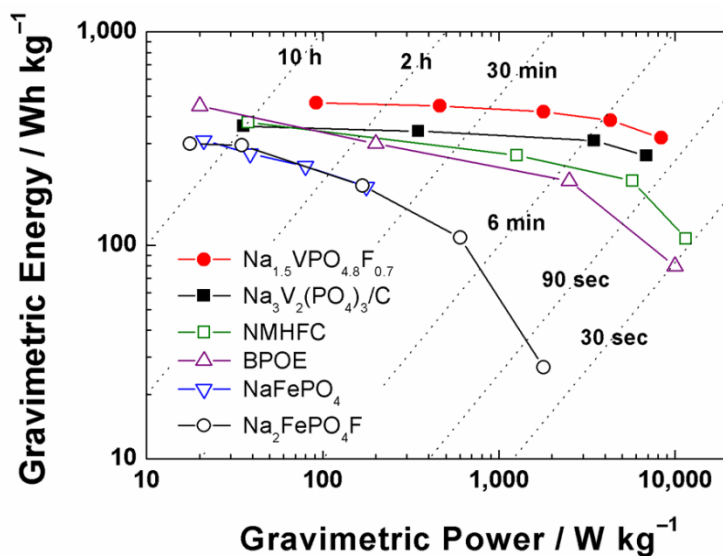


Figure 2-19. Ragone plot for the Na_{1.5}VPO₄F_{0.7} cathode and other cathode materials for NIBs. Reprinted with permission from [Y.-U. Park *et. al.*, *J. Am. Chem. Soc.*, 135, 13870-13878 (2013); DOI: 10.1021/ja406016j]. Copyright 2013 American Chemical Society.

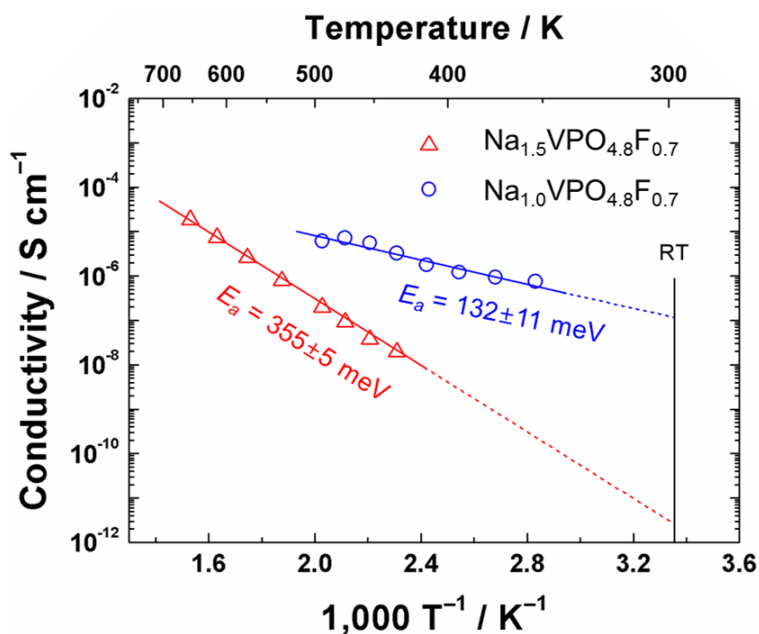


Figure 2-20. Arrhenius plot of electrical conductivities of $\text{Na}_{1.5}\text{VPO}_{4.8}\text{F}_{0.7}$ (red triangles) and $\text{Na}_{1.0}\text{VPO}_{4.8}\text{F}_{0.7}$ (blue circles) pellets at various temperatures. Activation energies (E_a) were calculated from the slopes of the fitted lines. E_a for the former and the latter were 355 ± 5 and 132 ± 11 meV, respectively. Room-temperature (RT) conductivities were estimated by linear extrapolation of the measured data points. Good linearity was observed for the two Arrhenius plots. Reprinted with permission from [Y.-U. Park *et. al.*, *J. Am. Chem. Soc.*, 135, 13870-13878 (2013); DOI: 10.1021/ja406016j]. Copyright 2013 American Chemical Society.

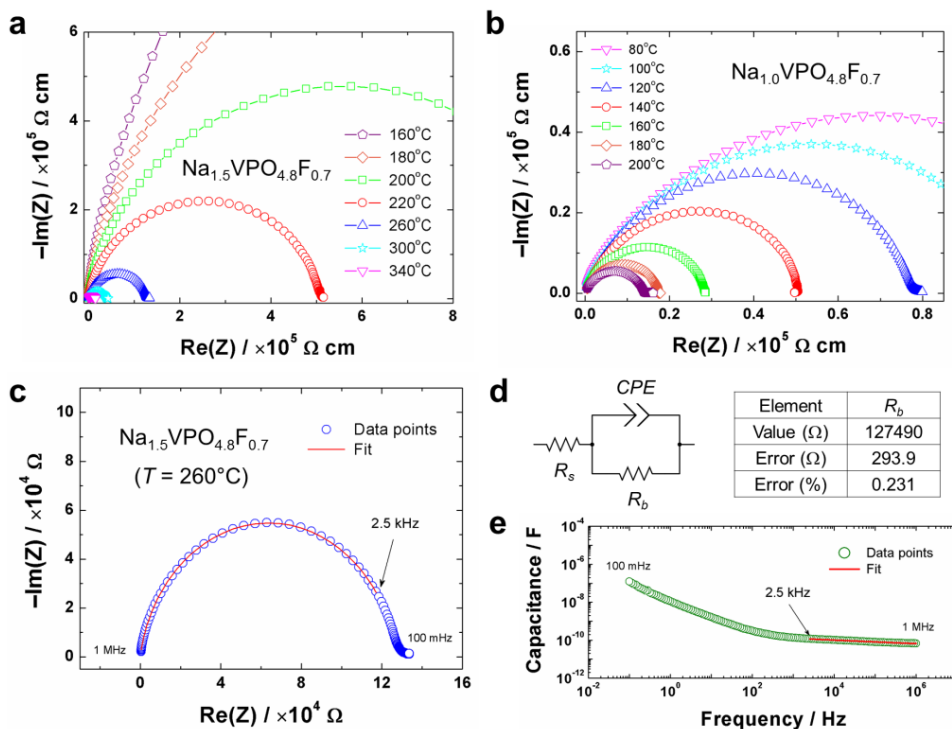


Figure 2-21. EIS study on the $\text{Na}_{1.5}\text{VPO}_{4.8}\text{F}_{0.7}$ and $\text{Na}_{1.0}\text{VPO}_{4.8}\text{F}_{0.7}$ pellets.

EIS spectra of (a) $\text{Na}_{1.5}\text{VPO}_{4.8}\text{F}_{0.7}$ and (b) $\text{Na}_{1.0}\text{VPO}_{4.8}\text{F}_{0.7}$ for various temperatures.

(c) EIS spectrum of $\text{Na}_{1.5}\text{VPO}_{4.8}\text{F}_{0.7}$ (260°C) and the fitted curve. Only the high-frequency (HF) region was fitted (2.5 kHz – 1 MHz in this case).

(d) An equivalent circuit for the fitting; R_s and CPE represent ohmic resistance and constant phase element, respectively. The bulk resistance (R_b) values were obtained by one-circle fitting of the EIS data with the equivalent circuit using the ZView program. The table shows the fitted R_b value and error for the EIS spectrum of $\text{Na}_{1.5}\text{VPO}_{4.8}\text{F}_{0.7}$ at 260°C . The fitting of R_b for all spectra was almost perfect (< 1% error).

(e) Variation of capacitance with frequency of the EIS spectrum of $\text{Na}_{1.5}\text{VPO}_{4.8}\text{F}_{0.7}$ at 260°C. Only data points in the constant capacitance region (*i.e.*, the HF region) were used for fitting; constant capacitance means that the region contains only one component, which validates this one-circle fitting with the frequency range of 2.5 kHz – 1 MHz. Generally, HF semicircles are known to be attributable to bulk contributions, whereas low-frequency (LF) semicircles originate from grain boundary contributions.⁵⁰ Because I was interested only in bulk resistance, one-circle fitting for the HF region was sufficient to obtain R_b values of the material. For EIS spectra of $\text{Na}_{1.0}\text{VPO}_{4.8}\text{F}_{0.7}$, two-circle fittings using double CPE- R_b sets were carried out due to the greater distortions of semicircles.

(*) Reprinted with permission from [Y.-U. Park *et. al.*, *J. Am. Chem. Soc.*, 135, 13870-13878 (2013); DOI: 10.1021/ja406016j]. Copyright 2013 American Chemical Society.

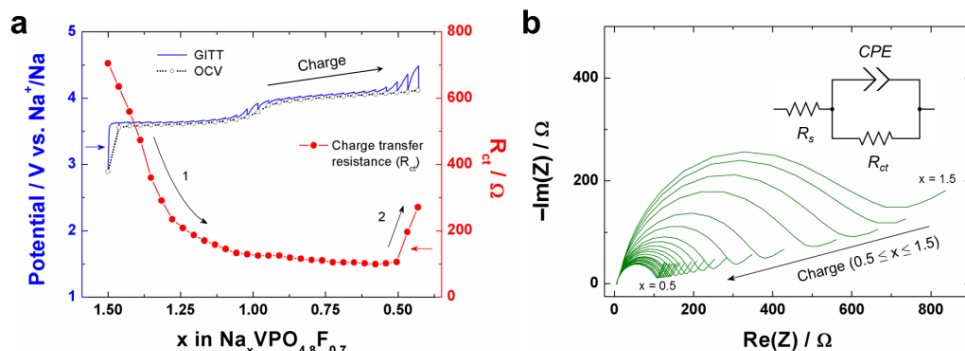


Figure 2-22. *In situ* EIS measurement during a charge process in GITT mode.

(a) For GITT measurement, an electrochemical cell comprising the $\text{Na}_{1.5}\text{VPO}_{4.8}\text{F}_{0.7}$ cathode was charged for 11 min in galvanostatic mode (C/5 rate) and rested for 1 h. EIS spectra were recorded at the end of each rest step between 1 MHz and 1 Hz, with a sinus amplitude of 10 mV. This sequence was repeated when the operating voltage reached 4.5 V (vs. Na^+/Na). **Figure 2-22a** shows the GITT curve and open circuit voltage (OCV) for each rest point. The charge transfer resistance (R_{ct}) in the electrochemical cell decreased with Na content; it dropped abruptly in the early charge stage (arrow 1) and was saturated after $x = 1.0$, suggesting that the reaction kinetics improved rapidly as more Na vacancies were generated in the structure. Beyond $x = 0.5$, the charge transfer resistance increased again (arrow 2) due to higher electrode/electrolyte resistance, which could be due to the onset of electrolyte decomposition around 4.5 V (vs. Na^+/Na).

(b) Changes in EIS spectra as the electrochemical cell was charged. The size of the high-frequency semicircle systematically decreased with Na content (from $x = 1.5$ to $x = 0.5$). The inset shows the equivalent circuit for the one-circle fitting of the EIS spectra. R_s , R_{ct} , and CPE represent ohmic resistance, charge transfer resistance, and constant phase element, respectively.

(*) Reprinted with permission from [Y.-U. Park *et. al.*, *J. Am. Chem. Soc.*, 135, 13870-13878 (2013); DOI: 10.1021/ja406016j]. Copyright 2013 American Chemical Society.

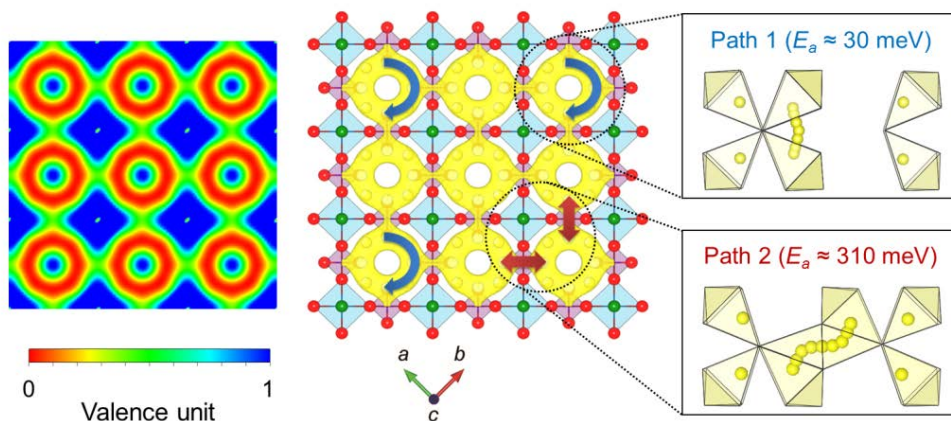


Figure 2-23. The origin of the fast kinetics of the $\text{Na}_x\text{VPO}_{4.8}\text{F}_{0.7}$ electrode. Bond valence mismatch map for Na in the $\text{Na}_{1.5}\text{VPO}_{5-\delta}\text{F}_{0.5+\delta}$ crystal structure (left). The spatial distribution of the bond valence mismatch on the ab plane is represented. The colors represent bond valence mismatches ranging from 0 (red) to 1 (blue). Yellow isosurfaces (isovalued = ± 0.45 valence unit) represent the possible two-dimensional Na diffusional pathways on the ab plane (right figures). Enlarged figures show the trajectories and activation barriers for Na hopping for path 1 (blue arrows) and path 2 (red arrows). Reprinted with permission from [Y.-U. Park *et. al.*, *J. Am. Chem. Soc.*, 135, 13870-13878 (2013); DOI: 10.1021/ja406016j]. Copyright 2013 American Chemical Society.

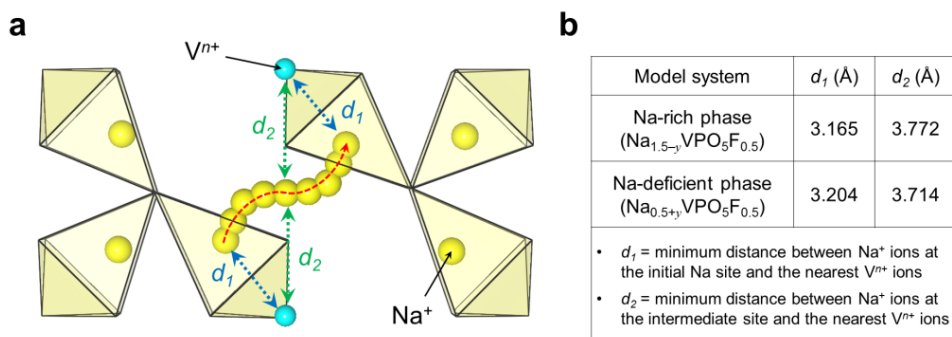


Figure 2-24. Trajectory for Na hopping along path 2 in the $\text{Na}_x\text{VPO}_5\text{F}_{0.5}$ phase.

(a) Trajectory for Na hopping along path 2 (red dashed arrow) from the NEB calculations in the Na-rich $\text{Na}_{1.5-y}\text{VPO}_5\text{F}_{0.5}$ phase; d_1 (blue dotted arrows) indicates the minimum distance between Na^+ ions at the initial Na site and the nearest V^{n+} ions, and d_2 (green dotted arrows) indicates the minimum distance between Na^+ ions at the intermediate Na site and the nearest V^{n+} ions.

(b) d_1 and d_2 values for Na-rich ($\text{Na}_{1.5-y}\text{VPO}_5\text{F}_{0.5}$) and Na-deficient ($\text{Na}_{0.5+y}\text{VPO}_5\text{F}_{0.5}$) phases from NEB calculations. For both model systems, the $\text{Na}^+-\text{V}^{n+}$ distances rather increased when Na^+ ions moved from the initial site to the intermediate site, suggesting less $\text{Na}^+-\text{V}^{n+}$ repulsion during Na migration along path 2.

(*) Reprinted with permission from [Y.-U. Park *et. al.*, *J. Am. Chem. Soc.*, 135, 13870-13878 (2013); DOI: 10.1021/ja406016j]. Copyright 2013 American Chemical Society.

2.3.5. Charge/Discharge Mechanism of the $\text{Na}_x\text{VPO}_{4.8}\text{F}_{0.7}$ Electrode

The charge/discharge mechanism of the $\text{Na}_{1.5}\text{VPO}_{4.8}\text{F}_{0.7}$ cathode is worth describing in greater detail. Despite the apparent two-phase reaction in the electrochemical profile, evidence of the second phase in the *ex situ* XRD data was not as clear. It is because two end-members of the region have different Na configurations in the basic units on the *ab* plane and do not involve significant structural change. Note that phases 1, 2, and 3 have different Na-vacancy orderings in the same framework (**Figure 2-4**, inset). Although the Na-vacancy ordering within basic units was relatively strong, interaction among the basic units was weak, as revealed from the first-principle calculations. This situation may easily allow disorder in the long-range Na-vacancy ordering at ambient temperature keeping the short-range ordering in the basic units. Local segregation of two different Na configurations in the material can result in a relatively clear electrochemical footprint of a two-phase reaction, although XRD may be insensitive to it.¹¹ The continuous lattice parameter change in the two-phase regions ($1.5 \geq x \geq 1.0$; **Figure 2-12**) could be a consequence of the combination of the coherent interface and the lack of the long-range Na-vacancy ordering, which may result in mosaic-type phase distribution. First, if coherent interfaces between the two phases are present, gradual lattice variation may occur near the interface due to lattice strain. According to a general alloy theory, the coherent interface can be stable at levels below a lattice mismatch between two phases of ~5%.⁵⁸ The critical lattice mismatch for incoherent interfaces has also been shown to be ~5% for the olivine LiMPO_4 ($M = \text{Fe}, \text{Mn}, \text{and/or Co}$).^{59,60} In the $\text{Na}_x\text{VPO}_{4.8}\text{F}_{0.7}$ system, the lattice misfits in regions I and II were less than 2%, implying the possibility of fully coherent interfaces. Second, when the two phases exist as a mosaic type with

an extremely small domain size due to weak long-range interactions, the effect of the coherent interface cannot be neglected. Gradual lattice variation in the interface will significantly affect the overall lattice parameter, eventually leading to continuous lattice parameter change.

Closer examination of the XRD data revealed a hint of a two-phase reaction in the high-voltage region, also evident from the *ex situ* XRD data in **Figure 2-10**. Peak splitting for (220) reflection was clearly observed in this region, particularly during discharge (*see Figure 2-10e*). These results indicate that local segregation of two Na configurations (*i.e.*, the occurrence of biphasic domains) also occurred in the high-voltage region, although it was much weaker. Interestingly, in the XRD evolution, all reflections except for the (002) and (220) families showed no trace of peak splitting; instead, they continuously shifted throughout the whole region. This phenomenon can be understood by the opposite trends of changes in the *a* and *c* lattice parameters. Due to the canceling of the reduction and increase, much less change in lattice spacing such as d_{222} and d_{113} was observed compared with d_{220} and d_{002} with indices of *hk0* or *00l* (**Figure 2-25**). Except for *hk0* or *00l*, the Δd_{hkl} is so small that clear resolution with XRD is likely to be difficult. Similarly, the ambiguous biphasic behavior in the high-voltage region is speculated to originate from: (i) (220) and (113) reflections becoming very close in the highly charged state of the material, and (ii) the broad nature of the (002) reflection of phase 3 (*i.e.*, the fully charged phase), which likely obscured the peak splitting.

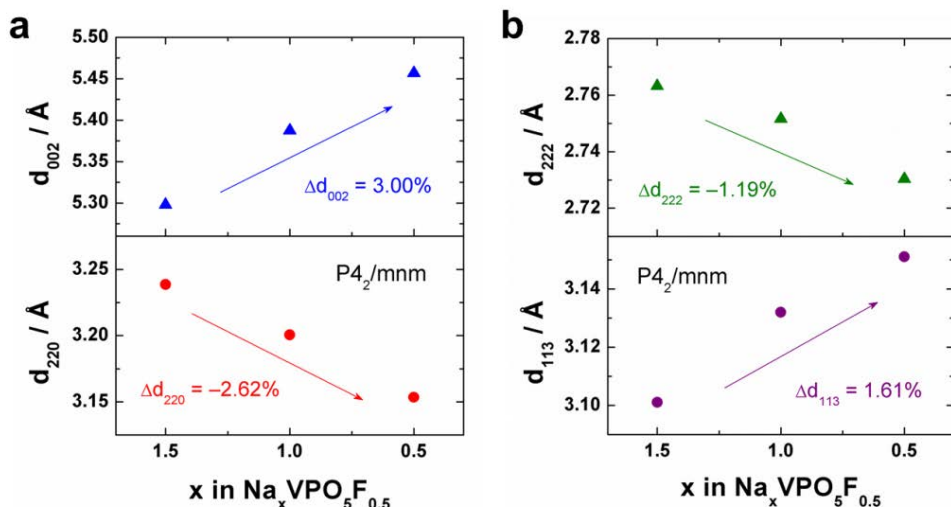


Figure 2-25. Change in d_{hkl} values of $\text{Na}_x\text{VPO}_5\text{F}_{0.5}$ from first-principle calculations.

(a) Changes in d_{002} and d_{220} values of $\text{Na}_x\text{VPO}_5\text{F}_{0.5}$ as Na content (x) decreases.

(b) Changes in d_{222} and d_{113} values of $\text{Na}_x\text{VPO}_5\text{F}_{0.5}$ as Na content decreases. All values were from first-principle calculations and the indices were based on the space group of $P4_2/mnm$.

(*) Reprinted with permission from [Y.-U. Park *et. al.*, *J. Am. Chem. Soc.*, 135, 13870-13878 (2013); DOI: 10.1021/ja406016j]. Copyright 2013 American Chemical Society.

2.4. Summary

In this chapter, I introduced a novel $\text{Na}_{1.5}\text{VPO}_{4.8}\text{F}_{0.7}$ cathode with outstanding electrochemical performance for rechargeable Na batteries. It exhibited a high voltage of ~ 3.8 V (vs. Na^+/Na), giving a large theoretical energy density of ~ 600 Wh kg^{-1} . This originated from both the multi-electron redox reaction ($1.2 e^-$ per formula unit) and high potential (~ 3.8 V vs. Na^+/Na) of the tailored vanadium redox couple ($\text{V}^{3.8+}/\text{V}^{5+}$). The cycling of the material was exceptionally stable (*i.e.*, $\sim 95\%$ capacity retention for 100 cycles and $\sim 84\%$ for extended 500 cycles) compared with other cathodes for NIBs, which was attributed to the low volume change (2.9%) during charge/discharge. The open framework of $\text{Na}_{1.5}\text{VPO}_{4.8}\text{F}_{0.7}$ allowed fast conduction of Na^+ ions through two-dimensional diffusional pathways, which resulted in excellent rate capability. I believe that my study of this novel $\text{Na}_{1.5}\text{VPO}_{4.8}\text{F}_{0.7}$ cathode with fascinating electrochemical properties can provoke stimulating discussions about the next-generation NIB and its potential new applications.

Chapter 3. A Family of Cathodes for Na-ion Batteries,

$\text{Na}_3(\text{VO}_{1-x}\text{PO}_4)_2\text{F}_{1+2x}$

(The essence of this chapter has been published in *Advanced Function Materials*. Used with permission from [Y.-U. Park *et. al.*, *Adv. Funct. Mater.*, **24**, 4603-4614 (2014); DOI: 10.1002/adfm.201400561]. Copyright 2014 Wiley.)

3.1. Introduction

Sustainable energy production is an important advancement toward a sustainable society. The rapid depletion of fossil fuels and growing environmental concerns have stimulated the utilization of renewable energy sources, which is critical to a sustainable energy supply. However, challenges remain, including cost reduction and the efficient storage of energy. In particular, large-scale energy-storage systems (ESSs) are necessary for efficient utilization of renewable energies, such as solar and wind energy, whose production time does not correspond with consumption rates.^{1,2,4} Li-ion batteries (LIBs), a candidate for ESSs, rely on limited and potentially expensive lithium resources; thus, LIBs may not be able to satisfy the demand for rapidly increasing renewable energy production.^{1,2,4} On the other hand, room-temperature Na-ion batteries (NIBs) have recently been revisited as a possible alternative due to unlimited sodium resources from seawater.^{1-7,61} Moreover, the close similarity between LIBs and NIBs has advanced the development of NIBs.

So far, many oxides^{8,11,16} and polyanion-based compounds^{15,17,20,22,24,27,47,62-66} have been studied as NIB cathode materials. These materials primarily determine the

performance of NIBs and account for a substantial part of the cost. Among cathode materials with promising electrochemical properties, recent studies have shown that sodium–vanadium fluorophosphates are outstanding due to their high energy densities ($>500 \text{ Wh kg}^{-1}$) and the potential for multi-electron transfer of the vanadium redox couple.^{67,68} The fluorophosphate framework provides a stable host with a low volumetric change during Na insertion/extraction.^{34,67,69} These properties are particularly advantageous for NIBs, which typically undergo a large volumetric change with Na intercalation due to the larger ionic size of Na compared to Li, leading to poor cycle life. Additionally, while NIBs have exhibited a relatively low energy density due to the low potential of NIB cathodes, the inductive effects of both $(\text{PO}_4)^{3-}$ and F^- anions allow a high working potential in sodium–vanadium fluorophosphates.^{34,67-70} Thus, the investigation of sodium–vanadium fluorophosphate chemistry is expected to advance the development of cathode materials that are well suited for NIBs.

To date, only a few sodium–vanadium fluorophosphates, including $\text{Na}_{1.5}\text{VOPO}_4\text{F}_{0.5}$,^{27,70,71} NaVPO_4F ,^{64,66,72} $\text{Na}_3\text{V}_2(\text{PO}_4)_2\text{F}_3$,^{17-19,62,73,74} and $\text{Na}_3\text{V}_2\text{O}_2(\text{PO}_4)_2\text{F}$,⁶⁵ have been independently reported as minerals or cathode materials for electrochemical systems. Around the same time, our group^{34,67} and the Rojo group^{17,70} first recognized that some of these compounds belong to the same crystallographic system of $\text{Na}_3(\text{VO}_{1-x}\text{PO}_4)_2\text{F}_{1+2x}$, where $x = 0$ corresponds to $\text{Na}_{1.5}\text{VOPO}_4\text{F}_{0.5}$ and $x = 1$ corresponds to $\text{Na}_3\text{V}_2(\text{PO}_4)_2\text{F}_3$. Although the Rojo group attempted to synthesize $\text{Na}_3(\text{VO}_{1-x}\text{PO}_4)_2\text{F}_{1+2x}$ ($0 \leq x \leq 1$),⁶⁸⁻⁷⁰ and I recently succeeded in doping fluorine into $\text{Na}_{1.5}\text{VOPO}_4\text{F}_{0.5}$ ($x \approx 0.2$),^{34,67} attempts to synthesize the solid solution frequently resulted in phases close to either $\text{Na}_3(\text{VOPO}_4)_2\text{F}$ ($x = 0$) or $\text{Na}_3\text{V}_2(\text{PO}_4)_2\text{F}_3$ ($x = 1$). Until now, the full solid solution

of $\text{Na}_3(\text{VO}_{1-x}\text{PO}_4)_2\text{F}_{1+2x}$ could not be obtained.

In this chapter, I will show the successful synthesis of a family of $\text{Na}_3(\text{VO}_{1-x}\text{PO}_4)_2\text{F}_{1+2x}$ ($0 \leq x \leq 1$) and demonstrate their potential as new cathode materials for NIBs. It will be also shown that each compound of the $\text{Na}_3(\text{VO}_{1-x}\text{PO}_4)_2\text{F}_{1+2x}$ series can function as a high-performance cathode for NIBs with high energy density and good cycle life. Interestingly, the redox mechanism and phase reactions significantly varied depending on the composition, even though the compounds belong to the same crystal framework. I used a combined theoretical and experimental approach to find the detailed reaction mechanisms of the $\text{Na}_3(\text{VO}_{1-x}\text{PO}_4)_2\text{F}_{1+2x}$ electrodes and revealed that their behavior varied with fluorine content. Finally, I will propose a strategy for further improvement of the energy density of the $\text{Na}_3(\text{VO}_{1-x}\text{PO}_4)_2\text{F}_{1+2x}$ electrodes by activating the multi-electron transfer of the vanadium redox couple.

3.2. Experimental and Computational Details

3.2.1. Materials synthesis. $\text{Na}_3(\text{VO}_{1-x}\text{PO}_4)_2\text{F}_{1+2x}$ ($x = 0.0, 0.2, 0.5, 0.8$, and 1.0) powders were prepared by a solid-state reaction using stoichiometric amounts of VOPO_4 , VPO_4 , NaF (Sigma-Aldrich, 99%), and Na_2CO_3 (Sigma-Aldrich, 99%) as precursors. Because the oxidation state of vanadium and the fluorine content simultaneously changed in this system due to the charge balance, I controlled the ratio of V^{3+} to V^{5+} precursors (*i.e.*, VPO_4 and VOPO_4) rather than simply changing the amount of the fluorine precursor to prepare the $\text{Na}_3(\text{VO}_{1-x}\text{PO}_4)_2\text{F}_{1+2x}$ ($0 \leq x \leq 1$)

compounds. The reaction is as follows: “ $(1-x)\text{V}^{5+}\text{OPO}_4 + x\text{V}^{3+}\text{PO}_4 + (0.5+x)\text{NaF} + [(1-x)/2]\text{Na}_2\text{CO}_3 \rightarrow \frac{1}{2}\text{Na}_3(\text{VO}_{1-x}\text{PO}_4)_2\text{F}_{1+2x} + \text{gases}$ ”. Blending of the precursors was performed by high-energy ball-milling at 300 rpm for 24 hours; the resulting mixtures were pelletized and sintered at 750°C for 1.5 hours under flowing argon. To prepare VOPO_4 powder, a stoichiometric amount of V_2O_5 (Sigma-Aldrich, 99%) and $\text{NH}_4\text{H}_2\text{PO}_4$ (Sigma-Aldrich, 99%) was mixed by high-energy ball-milling at 300 rpm for 24 hours; the mixture was then pelletized and heat-treated at 750°C for 4 hours in air. To synthesize VPO_4 powder, a stoichiometric mixture of V_2O_5 and $\text{NH}_4\text{H}_2\text{PO}_4$, including 20 mol% Super P, was mixed by high-energy ball-milling, also at 300 rpm for 24 hours; the mixture was then pelletized and heat-treated at 850°C for 2 hours under Ar flow. To obtain $\text{Na}_y(\text{VOPO}_4)_2\text{F}$ ($x = 0$) powders with various Na contents ($1.0 \leq y \leq 3.0$), the $\text{Na}_3(\text{VOPO}_4)_2\text{F}$ ($x = 0$) powders were chemically oxidized using a stoichiometric amount of NO_2BF_4 (Sigma-Aldrich, 95%) in acetonitrile (Sigma-Aldrich, 99.8%) at room temperature. After reacting for 16 hours, the powders were washed, centrifuged several times with acetonitrile and ethanol, and then dried in a vacuum oven at 70°C.

3.2.2. Elemental analysis and morphology. The atomic ratios of sodium, vanadium, and phosphorus in the series of samples were determined by ICP spectroscopy (Polyscan 60E; Thermo Jarrell Ash, USA). SEM images were obtained using a SUPRA 55VP FE-SEM (Carl Zeiss, Germany) at an operating voltage of 2 kV. Fluorine contents in the $\text{Na}_3(\text{VO}_{1-x}\text{PO}_4)_2\text{F}_{1+2x}$ ($0 \leq x \leq 1$) samples were further verified using EDS (X-Flash spectrometer; Bruker, Germany) at an operating voltage of 15 kV. TEM images were acquired using a Tecnai F20 (FEI, USA) and JEM-3000F/JEM-2100F (JEOL, Japan) at an accelerating voltage of 200 kV.

3.2.3. Global and local structure of Na₃(VO_{1-x}PO₄)₂F_{1+2x}. ND data were collected over the 2θ range of 0–180° with a step size of 0.05°, and a wavelength of $\lambda = 1.83429$ Å was supplied by a Ge(331) single-crystal monochromator on a high-resolution powder diffractometer (HRPD) at the Hanaro facility of the Korea Atomic Energy Research Institute. XRD spectra were obtained using an X-ray diffractometer (D8 Advance; Bruker, Germany) with Ni-filtered Cu K α radiation ($\lambda = 1.5406$ Å) over the 2θ range of 10–60°. High-resolution XRD using synchrotron radiation was carried out at beam line 9B at the Pohang Accelerator Laboratory (PAL) with an average wavelength of 1.5475 Å. The room-temperature ND/XRD data were refined using the Rietveld method and Fullprof software.³⁵ The crystal structures were drawn using the VESTA program.⁴³ XANES spectra were recorded at room temperature at beam line 7D at the PAL using photons with a storage ring energy of 2.5 GeV and a current range of 100–140 mA. The spectra were collected in the transmission mode at the vanadium K-edge. Solid-state ²³Na MAS NMR spectroscopy experiments were performed using a Bruker Avance 400 MHz 9.4 T wide-bore spectrometer (4 mm probe) at a Larmor frequency of 105.8 MHz. The shifts were referenced to 0.1 M NaCl (0 ppm). All spectra were obtained using a 90° pulse of 1 μ s and a recycle time of 0.5 s with a MAS frequency of either 15 or 17 kHz at room temperature.

3.2.4. Electrochemical characterization. Slurries of 70 wt% Na₃(VO_{1-x}PO₄)₂F_{1+2x} ($x = 0.0, 0.2, 0.5, 0.8,$ and 1.0) powders, 20 wt% carbon black, and 10 wt% polyvinylidene fluoride (PVDF, Sigma-Aldrich) dispersed in *N*-methyl-2-pyrrolidone (NMP, Sigma-Aldrich) were prepared, cast on Al foil, and dried at 120°C for the electrode fabrication. The loadings of the active material on the electrodes were ~ 3 mg cm⁻². Electrochemical cells were assembled into CR2032-

type coin cells in an Ar-filled glove box (MBraun, Germany). Na metal (Sigma-Aldrich) and a glass microfiber filter (grade GF/F; Whatman, USA) were used as a counter electrode and separator, respectively. All electrochemical tests were performed using a potentiostat/galvanostat (WBCS 3000; WonA Tech, Korea) with an electrolyte of 1 M NaBF_4 in a mixture of ethyl carbonate (EC) and propylene carbonate (PC) (1:1 v/v). To prepare the $\text{Na}_y(\text{VO}_{1-x}\text{PO}_4)_2\text{F}_{1+2x}$ ($x = 0.0, 0.2, 0.5, 0.8$, and 1.0) electrodes for *ex-situ* experiments, the electrochemical cells were galvanostatically charged or discharged at a $C/10$ rate and disassembled at various states of charge (SOC). Prior to the *ex-situ* experiments, the electrodes were washed with PC and dried overnight in vacuum at 70°C . Based on one-electron transfer, 1C rates were calculated to correspond to $\sim 130 \text{ mA g}^{-1}$ for the $\text{Na}_y(\text{VO}_{1-x}\text{PO}_4)_2\text{F}_{1+2x}$ ($x = 0.0, 0.2, 0.5, 0.8$, and 1.0) electrodes.

3.2.5. Computational details. First-principles calculations were carried out using the Perdew–Burke–Ernzerhof exchange-correlation parameterization to DFT with the spin-polarized GGA.³⁶ A plane-wave basis set and the projector-augmented wave (PAW) method was used, as implemented in the Vienna *ab initio* simulation package (VASP).³⁷ Hubbard parameters (GGA+ U)³⁸ were added to correct the incomplete cancellation of the self-interaction of GGA. Redox potentials of $\text{V}^{4+}/\text{V}^{5+}$ in $\text{Na}_y(\text{VOPO}_4)_2\text{F}$ ($x = 0$) and $\text{V}^{3+}/\text{V}^{4+}$ in $\text{Na}_y\text{V}_2(\text{PO}_4)_2\text{F}_3$ ($x = 1$) were calculated with various U values. The calculated redox potentials for both compounds were in the best agreement with the experimental values when U value was 4.0 eV, thus this U value was used for vanadium ions of the family of $\text{Na}_3(\text{VO}_{1-x}\text{PO}_4)_2\text{F}_{1+2x}$ ($0 \leq x \leq 1$). To study the $\text{Na}_y(\text{VO}_{1-x}\text{PO}_4)_2\text{F}_{1+2x}$ ($x = 0.0, 0.5$, and 1.0) electrodes, all possible Na-vacancy orderings were considered within the unit cell of $\text{Na}_y(\text{VO}_{1-x}\text{PO}_4)_2\text{F}_{1+2x}$ ($0 \leq y \leq 3$) generated with the CASM program.⁴⁰

From the results, thirty Na-vacancy orderings were selected with the lowest electrostatic energy at each composition through the Ewald summation method⁷⁵ and then their energies with GGA+ U were calculated. A plane wave basis set was used with sampling the Monkhorst-Pack $4 \times 4 \times 4$ k -point mesh. The double-sized supercells containing 8 formula units were additionally explored to determine the energies of the intermediate phases at $y = 2.5$ and 1.5 because long-range $\text{Na}^+ - \text{Na}^+$ interactions in the larger supercell may further stabilize the structure. Voltage profiles of the $\text{Na}_y(\text{VO}_{1-x}\text{PO}_4)_2\text{F}_{1+2x}$ ($0 \leq y \leq 3$; $x = 0.0, 0.5$, and 1.0) electrodes were determined using the following equation: $\langle V \rangle = -[E(\text{Na}_{y_1}(\text{VO}_{1-x}\text{PO}_4)_2\text{F}_{1+2x}) - E(\text{Na}_{y_2}(\text{VO}_{1-x}\text{PO}_4)_2\text{F}_{1+2x}) - (y_1 - y_2) \times E(\text{Na})] / [(y_1 - y_2) \times F]$, where E is the DFT energy of the structure and F is the Faraday constant.

3.3. Results and Discussion

3.3.1. Characterization of a Family of $\text{Na}_3(\text{VO}_{1-x}\text{PO}_4)_2\text{F}_{1+2x}$ Compounds.

Substantial changes in the anion composition in a crystal generally result in the formation of impurities or second phases because the anions are usually the main building blocks of crystals. Moreover, substitution with aliovalent anions accompanies a simultaneous change in the oxidation states of the cations, which often complicates the synthesis of pure phases. Nevertheless, I found that a series of $\text{Na}_3(\text{VO}_{1-x}\text{PO}_4)_2\text{F}_{1+2x}$ compounds can be obtained in the same crystal framework with a full range of $0 \leq x \leq 1$. The similar XRD patterns of $\text{Na}_3(\text{VO}_{1-x}\text{PO}_4)_2\text{F}_{1+2x}$ powders ($x = 0.0, 0.2, 0.5, 0.8$, and 1.0) indicate that they belong to an isostructural system (**Figure 3-1**). The continuous peak shift with varying composition of

$\text{Na}_3(\text{VO}_{1-x}\text{PO}_4)_2\text{F}_{1+2x}$ ($0 \leq x \leq 1$) also implies a complete solid solution over this composition range (**Figure 3-1a**, insets). I also confirmed that the fluorine content in $\text{Na}_3(\text{VO}_{1-x}\text{PO}_4)_2\text{F}_{1+2x}$ changed linearly with the targeted composition (x) from the EDS and ICP analyses (see **Figure 3-2**). The particle sizes and morphologies of the $\text{Na}_3(\text{VO}_{1-x}\text{PO}_4)_2\text{F}_{1+2x}$ powders ($x = 0.0, 0.2, 0.5, 0.8$, and 1.0) were examined by SEM and TEM. The SEM images showed particle sizes in the range of 1–5 μm (see **Figure 3-3**), and the TEM images and corresponding SAED data suggested that all the micron-sized particles were single-crystalline with the same tetragonal symmetry (**Figure 3-4**).

To closely monitor the crystal structure of isostructural $\text{Na}_3(\text{VO}_{1-x}\text{PO}_4)_2\text{F}_{1+2x}$ ($0 \leq x \leq 1$) compounds, I carried out ND (**Figure 3-5**) and synchrotron XRD (**Figure 3-6**) experiments for the samples ($x = 0.0, 0.2, 0.5, 0.8$, and 1.0). Based on the combined ND and XRD refinements of each sample, the lattice parameters continuously changed with increasing fluorine content in $\text{Na}_3(\text{VO}_{1-x}\text{PO}_4)_2\text{F}_{1+2x}$ ($0 \leq x \leq 1$) (see **Table 3-1** to **Table 3-16** for the detailed results of the combined ND and XRD refinements). **Figure 3-7** show that lattice parameter a increased slightly, whereas lattice parameter c and volume V increased significantly with increasing fluorine content. The continuous lattice change confirmed the formation of the solid solution. The asymmetric lattice variations with the fluorine content (a vs. c) can be understood as follows. Lattice parameter c results from the sum of the height (h) of V^{n+} octahedra and the distance (d) between terminal anions, as shown in **Figure 3-7e**. When x increases from 0 to 1, h increases due to the larger V^{3+} octahedra relative to V^{4+} . On the other hand, d decreases due to the increase in fluorine content, which exhibits weaker $\text{F}^- - \text{F}^-$ repulsion compared to $\text{O}^{2-} - \text{O}^{2-}$ repulsion (see **Figure 3-8** for the variation of h and d with increasing x). However,

the increase in h is much more pronounced than the reduction of d , because the expansion of vanadium octahedra from V^{4+} to V^{3+} leads to a greater elongation along the c -axis (the direction of h) than the a - or b -axis. This anisotropic change is attributable to the distorted characteristics of V^{4+} octahedra. As Whittingham *et al.* noted,⁷⁶ V^{4+} ions usually form a distorted octahedron due to the exceptionally short vanadyl bond, unlike V^{3+} ions, which are prone to form a regular octahedron. In my samples, the refinement results in **Table 3-17** showed a very short vanadyl V1–O4 bond (~ 1.63 Å) along the c -axis for $\text{V}^{4+}\text{O}_5\text{F}$ octahedra ($x = 0$; **Figure 3-7f**) compared to V–O(F) bonds (~ 2.0 Å) for $\text{V}^{3+}\text{O}_4\text{F}_2$ octahedra ($x = 1$; **Figure 3-7g**). Baur's distortion indices⁷⁷ (Δ) in **Table 3-17** also confirm that the $\text{V}^{4+}\text{O}_5\text{F}$ octahedra were much more distorted than the $\text{V}^{3+}\text{O}_4\text{F}_2$ octahedra. As x increased, changes in the octahedral volume were accommodated by the recovery of the V–O(F) bond length from the short vanadyl bond along the c -axis, leaving the lattice parameter a nearly constant.

The variation in the fluorine content of $\text{Na}_3(\text{VO}_{1-x}\text{PO}_4)_2\text{F}_{1+2x}$ ($0 \leq x \leq 1$) shifted the oxidation state of vanadium, which eventually affected the electrochemical reaction mechanism. According to XANES analysis of the vanadium K-edge (**Figure 3-7h**), the vanadium oxidation state continuously changed with fluorine content (x). As x increased from 0 to 1, the edge of the spectrum shifted toward lower energy, indicating the reduction of the vanadium ion. A clearer change was observed in the pre-edge region (**Figure 3-7h**, inset), where the pre-edge peak gradually became smaller with increasing x and finally disappeared at $x = 1$. This observation agrees with previous XANES work for compounds containing V^{4+} and V^{3+} ions.^{45,46} Compounds with distorted V^{4+} octahedra generally exhibit a large pre-edge peak, whereas those with V^{3+} octahedra show a negligible pre-edge peak due

to the much weaker $1s \rightarrow 3d$ transition.^{45,76} The gradual disappearance of the pre-edge peak with increasing x agrees with the structural analysis, which showed that $\text{V}^{4+}\text{O}_5\text{F}$ octahedra were much more distorted than $\text{V}^{3+}\text{O}_4\text{F}_2$ octahedra.

Further atomic analysis of series of $\text{Na}_3(\text{VO}_{1-x}\text{PO}_4)_2\text{F}_{1+2x}$ ($0 \leq x \leq 1$) was done using NMR. In paramagnetic compounds, unpaired electron spins of transition metals are transferred to other nearby atoms by the so-called *Fermi-contact interaction*. This can be used for probing oxidation states of transition metals because the resulting NMR shift (*i.e.*, Fermi-contact shift) is highly sensitive to the number of unpaired electrons in transition metals.⁷⁸⁻⁸⁰ This phenomenon can be clearly observed for sodium and phosphorus atoms in $\text{Na}_3(\text{VO}_{1-x}\text{PO}_4)_2\text{F}_{1+2x}$ because they have no direct bonding to paramagnetic V^{n+} ions, which leads to severe peak broadening. Therefore, I performed solid-state ^{23}Na MAS NMR experiments for the $\text{Na}_3(\text{VO}_{1-x}\text{PO}_4)_2\text{F}_{1+2x}$ samples ($0 \leq x \leq 1$) to determine the distribution of V^{3+} and V^{4+} ions in the crystal structure.

Figure 3-9 shows ^{23}Na MAS NMR spectra of $\text{Na}_3(\text{VO}_{1-x}\text{PO}_4)_2\text{F}_{1+2x}$ ($x = 0.0, 0.2, 0.5, 0.8, \text{ and } 1.0$). According to the modified Goodenough–Kanamori rules,^{79,80} unpaired electron spins of V^{4+} ions ($t_{2g}^1 e_g^0$) or V^{3+} ions ($t_{2g}^2 e_g^0$) are transferred to Na $3s$ orbitals *via* O $2p$ (or F $2p$) orbitals; thus, large and positive Fermi-contact shifts are expected in ^{23}Na MAS NMR spectra, as illustrated in **Figure 3-9a**. Na ions can receive unpaired electron spins from four adjacent vanadium ions *via* seven neighboring anions (O1, O3, O4, or F1 $2p$ orbitals), and most angles for the Na–O(F)–V interactions were around 90° (see **Table 3-18**). This type of interaction can transfer a large amount of electron spin density (strong interactions; denoted by blue arrows), whereas an interaction deviating from 90° , such as the Na–O4–V interaction, can transfer only a small amount of the electron spin density of V^{4+}

ions (weak interactions; denoted by orange arrows). Consequently, most of the transferred electron density of a Na atom was not from corner-sharing VO_5F octahedra but from face-sharing $\text{V}_2\text{O}_{10}\text{F}$ bioctahedra. This enabled a partial view of the distribution of V^{3+} and V^{4+} ions in the structure.

The ^{23}Na MAS NMR spectra in **Figure 3-9b** show single, strong Fermi-contact shifts (71 and 136 ppm) for two end members of $\text{Na}_3(\text{VOPO}_4)_2\text{F}$ ($x = 0$) and $\text{Na}_3\text{V}_2(\text{PO}_4)_2\text{F}_3$ ($x = 1$), respectively, indicating a single valence state for the vanadium ions. The gap between the two Fermi-contact shifts was *ca.* 65 ppm, mainly due to the difference in the number of unpaired electrons in V^{4+} (d^1) and V^{3+} (d^2) ions. This difference is similar to the gap between ^7Li NMR shifts of $\text{LiV}^{3+}\text{PO}_4\text{F}$ and $\text{Li}_2\text{V}^{2+}\text{PO}_4\text{F}$, which is known to be 60–70 ppm.⁸¹ For intermediate fluorine contents ($x = 0.2, 0.5$, and 0.8), more than two isotropic resonances were observed. In the case of $\text{Na}_3(\text{V}^{3.8+}\text{O}_{0.8}\text{PO}_4)_2\text{F}_{1.4}$ ($x = 0.2$), two major Fermi-contact shifts were detected at 70 and 112 ppm, indicating that two types of paramagnetic sources having a different number of unpaired electrons coexisted in the crystal. V^{3+} ions cause a larger positive Fermi-contact shift due to the greater paramagnetic nature relative to V^{4+} ions; thus, the two peaks centered at 70 and 112 ppm are attributable to Na neighboring V^{4+} and V^{3+} ions, respectively.

Further explanations for the two peaks (70 and 112 ppm; see **Figure 3-9b**) of $\text{Na}_3(\text{V}^{3.8+}\text{O}_{0.8}\text{PO}_4)_2\text{F}_{1.4}$ ($x = 0.2$) are possible by interpreting electron spin transfer mechanisms. **Figure 3-9a** schematically shows several types of $\text{Na } 3s - \text{O } 2p - \text{V } t_{2g}$ and $\text{Na } 3s - \text{F } 2p - \text{V } t_{2g}$ interactions in $\text{Na}_3(\text{VOPO}_4)_2\text{F}$ ($x = 0$). The corresponding bond angles are tabulated in **Table 3-18**. Between the two types of spin transfer mechanisms, spin delocalization or hybridization (causing positive spin densities) is generally dominant compared to spin polarization (causing

negative spin densities).⁷⁹ Moreover, in the case of $\text{Na}_3(\text{VO}_{1-x}\text{PO}_4)_2\text{F}_{1+2x}$ ($0 \leq x \leq 1$), there exists only 90° delocalization ($t_{2g} - p_\pi - s$ hybridization) because 180° delocalization ($e_g - p_\sigma - s$ hybridization) is forbidden due to the empty e_g level of V^{4+} ions ($t_{2g}^1 e_g^0$) and V^{3+} ions ($t_{2g}^2 e_g^0$). Thus, as the Na–O(F)–V bond angles deviate from 90° , less transferred electron spin density (*i.e.*, less positive NMR shift) is expected.

The mixed valences of V^{3+} and V^{4+} led to three types of local environments for strong 90° interactions between Na and vanadium bioctahedra in the intermediate compositions of $\text{Na}_3(\text{VO}_{1-x}\text{PO}_4)_2\text{F}_{1+2x}$ ($x = 0.2, 0.5$, and 0.8), as shown in **Figure 3-9c**. Assuming that the V^{4+} and V^{3+} ions are homogeneously mixed in the crystal with a ratio of 4:1 for $\text{Na}_3(\text{V}^{3.8+}\text{O}_{0.8}\text{PO}_4)_2\text{F}_{1.4}$ ($x = 0.2$),³⁴ the abundance ratios are expected to be 64, 32, and 4% for the three environments. The observed intensity ratio of about 3:1 for the peaks at 70 and 112 ppm suggests that the Fermi-contact shift at 70 ppm is most likely due to the interaction between Na and $(\text{V}^{4+})_2\text{O}_{10}\text{F}$ bioctahedra. Interestingly, the peak related to V^{3+} ions had a considerably less positive NMR shift ($x = 0.2$; 112 ppm) compared to that of $\text{Na}_3\text{V}_2(\text{PO}_4)_2\text{F}_3$ ($x = 1$; 136 ppm). This suggests that most of the Na atoms affected by V^{3+} ions (d^2) had at least one weak interaction with V^{4+} ions (d^1) and implies that V^{4+} and V^{3+} ions were rather randomly mixed at the atomic level in the crystal. A similar explanation is also valid for $\text{Na}_3(\text{V}^{3.2+}\text{O}_{0.2}\text{PO}_4)_2\text{F}_{2.6}$ ($x = 0.8$) having two Fermi-contact shifts at 138 ppm (related to V^{3+} ions) and 87 ppm (related to V^{4+} ions) with an intensity ratio of 3:1. The peak related to V^{4+} ions had a considerably more positive NMR shift ($x = 0.8$; 87 ppm) compared to that of $\text{Na}_3(\text{VOPO}_4)_2\text{F}$ ($x = 0$; 71 ppm), also implying similar distribution of V^{4+} and V^{3+} ions at the atomic level.

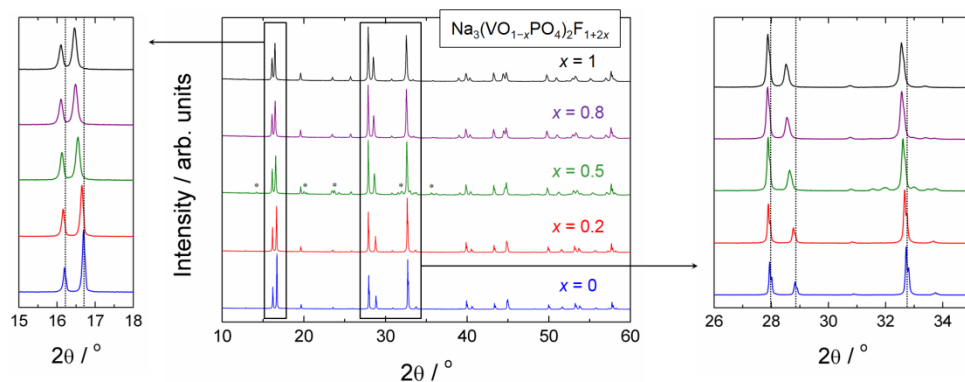


Figure 3-1. XRD patterns of $\text{Na}_3(\text{VO}_{1-x}\text{PO}_4)_2\text{F}_{1+2x}$ ($x = 0.0, 0.2, 0.5, 0.8$, and 1.0) powders. Reflections denoted by asterisks are from the rhombohedral $\text{Na}_3\text{V}_2(\text{PO}_4)_3$, which is an impurity in $x = 0.5$. Used with permission from [Y.-U. Park *et. al.*, *Adv. Funct. Mater.*, **24**, 4603-4614 (2014); DOI: 10.1002/adfm.201400561]. Copyright 2014 Wiley.

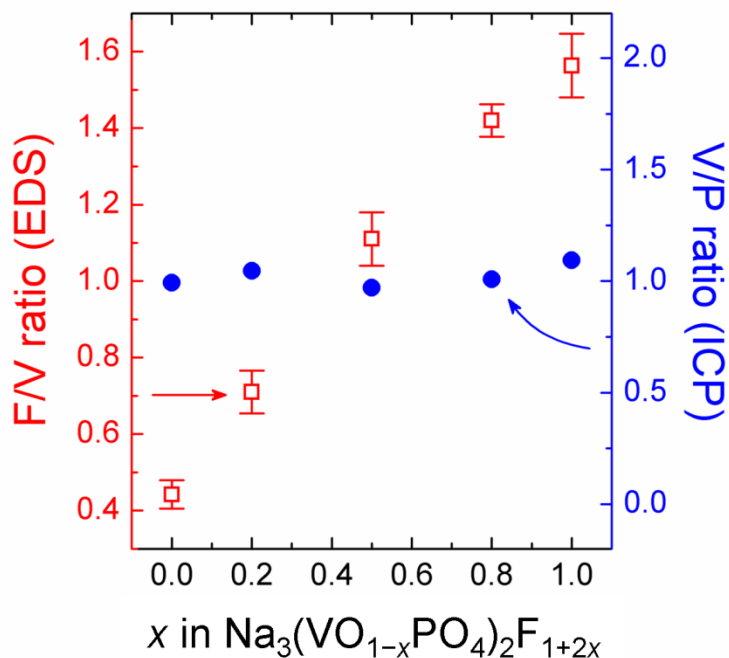


Figure 3-2. EDS and ICP analyses for the $\text{Na}_3(\text{VO}_{1-x}\text{PO}_4)_2\text{F}_{1+2x}$ ($x = 0.0, 0.2, 0.5, 0.8$, and 1.0) powders. Their F/V ratios were obtained by averaging several EDS measurements. Their V/P ratios were obtained by ICP measurements. Used with permission from [Y.-U. Park *et. al.*, *Adv. Funct. Mater.*, **24**, 4603-4614 (2014); DOI: 10.1002/adfm.201400561]. Copyright 2014 Wiley.

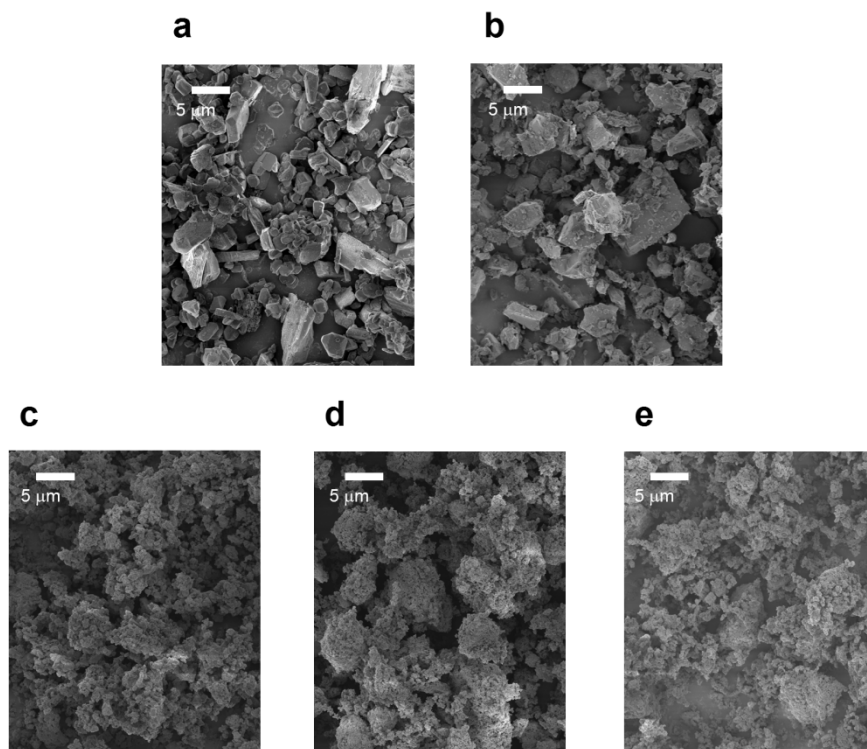


Figure 3-3. SEM images of the $\text{Na}_3(\text{VO}_{1-x}\text{PO}_4)_2\text{F}_{1+2x}$ samples.

(a) $x = 0.0$, (b) $x = 0.2$, (c) $x = 0.5$, (d) $x = 0.8$, and (e) $x = 1.0$.

(*) Used with permission from [Y.-U. Park *et. al.*, *Adv. Funct. Mater.*, **24**, 4603-4614 (2014); DOI: 10.1002/adfm.201400561]. Copyright 2014 Wiley.

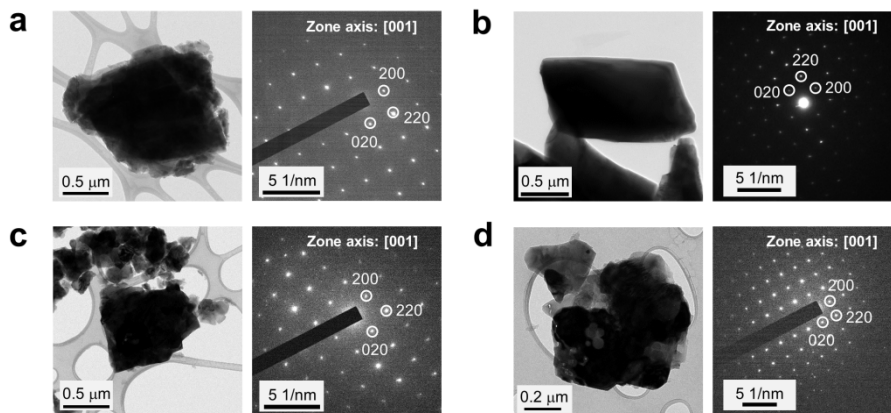


Figure 3-4. Bright-field TEM images (left) and the SAED patterns (right).

(a) $x = 0.0$, (b) $x = 0.2$, (c) $x = 0.8$, and (d) $x = 1.0$.

(*) Used with permission from [Y.-U. Park *et. al.*, *Adv. Funct. Mater.*, **24**, 4603-4614 (2014); DOI: 10.1002/adfm.201400561]. Copyright 2014 Wiley.

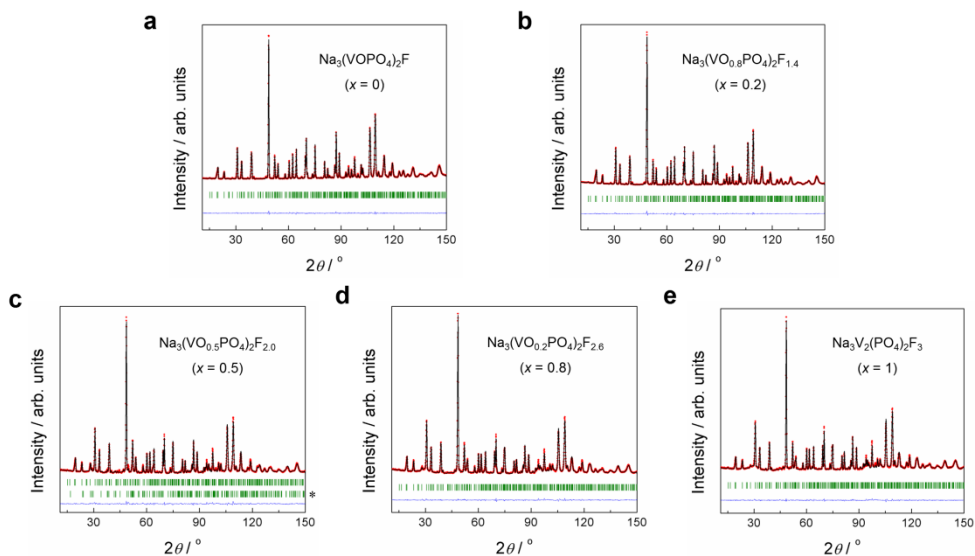


Figure 3-5. ND patterns of the $\text{Na}_3(\text{VO}_{1-x}\text{PO}_4)_2\text{F}_{1+2x}$ ($x = 0.0, 0.2, 0.5, 0.8$, and **1.0**) powders and their Rietveld refinements. Rietveld refinements with observed data points (red dots), the calculated pattern (black line), the difference curve (blue line), and the Bragg positions (green bars). Additional Bragg positions for $x = 0.5$ (denoted by an asterisk) are for the rhombohedral $\text{Na}_3\text{V}_2(\text{PO}_4)_3$ phase.

(a) $x = 0.0$, (b) $x = 0.2$, (c) $x = 0.5$, (d) $x = 0.8$, and (e) $x = 1.0$.

(*) Used with permission from [Y.-U. Park *et. al.*, *Adv. Funct. Mater.*, **24**, 4603-4614 (2014); DOI: 10.1002/adfm.201400561]. Copyright 2014 Wiley.

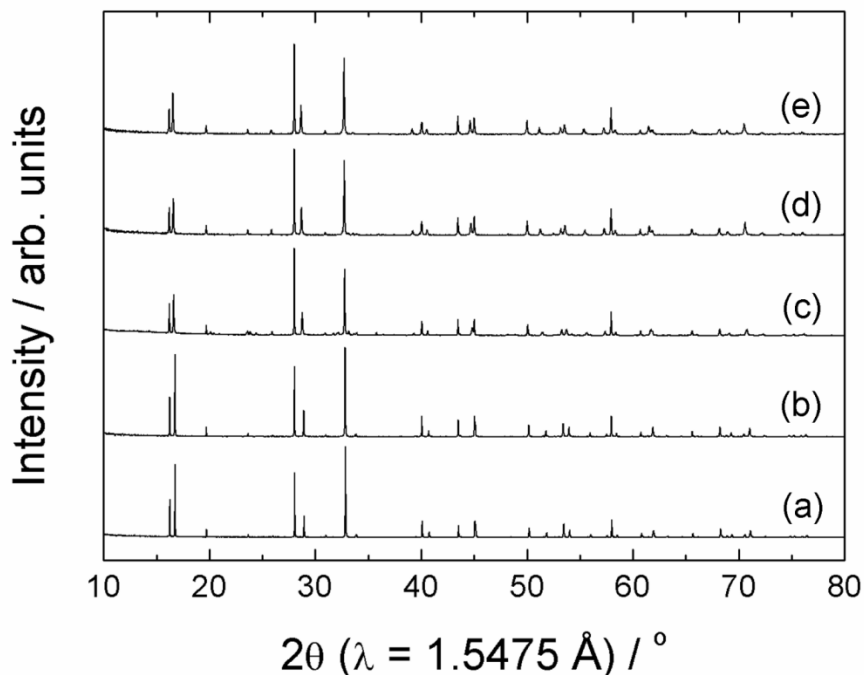


Figure 3-6. Synchrotron XRD patterns of $\text{Na}_3(\text{VO}_{1-x}\text{PO}_4)_2\text{F}_{1+2x}$ powders.

(a) $x = 0.0$, (b) $x = 0.2$, (c) $x = 0.5$, (d) $x = 0.8$, and (e) $x = 1.0$. There are some preferred orientations originating from their platelet morphologies. The position and the displacement (thermal) parameter of the vanadium atom were determined from the XRD refinement because its nuclei hardly scatter neutrons.⁸² Positions, thermal parameters, and occupancies of the other atoms were investigated by ND refinement.

(*) Used with permission from [Y.-U. Park *et. al.*, *Adv. Funct. Mater.*, **24**, 4603-4614 (2014); DOI: 10.1002/adfm.201400561]. Copyright 2014 Wiley.

Table 3-1. Lattice parameters of the $\text{Na}_3(\text{VO}_{1-x}\text{PO}_4)_2\text{F}_{1+2x}$ samples ($x = 0.0, 0.2, 0.5, 0.8,$ and 1.0) from the combined ND and XRD refinement.

x	ND or XRD	a (Å)	c (Å)	V (Å ³)
0.0	ND	9.02257(13)	10.61358(18)	864.02(2)
	XRD ^a	9.02726(1)	10.61877(3)	865.340(3)
0.2	ND	9.03330(11)	10.63004(16)	867.42(2)
	XRD ^a	9.03404(4)	10.63059(6)	867.603(7)
0.5	ND	9.0326(2)	10.6917(3)	872.32(4)
	XRD ^a	9.03433(6)	10.69451(7)	872.877(9)
0.8	ND	9.0341(2)	10.7299(4)	875.73(4)
	XRD ^a	9.03725(9)	10.73107(12)	876.427(16)
1.0	ND	9.03635(9)	10.74843(14)	877.670(17)
	XRD ^a	9.0350(2)	10.7408(3)	876.79(4)

(^a: synchrotron X-ray source)

Table 3-2. Lattice parameters and cell volumes for $\text{Na}_3(\text{VOPO}_4)_2\text{F}$ ($x = 0$) from the ND refinement.

<i>Space Group</i>	<i>P4₂/mmn</i>
<i>Cell parameters</i>	
a (Å)	9.02257(13)
b (Å)	9.02257(13)
c (Å)	10.61358(18)
α (°)	90(-)
β (°)	90(-)
γ (°)	90(-)
Volume (Å ³)	864.02(2)
<i>Agreement factors</i>	
R_p (%)	3.21
R_{wp} (%)	4.21
R_F (%)	2.78
R_I (%)	3.13

Table 3-3. Atomic positions for $\text{Na}_3(\text{VOPO}_4)_2\text{F}$ ($x = 0$) from the ND refinement.

<i>Label</i>	<i>Atom</i>	<i>Site</i>	<i>x</i>	<i>y</i>	<i>z</i>	<i>Occupancy</i>	<i>B_{iso}</i> (\AA^2)
Na1	Na	8i	0.5081(10)	0.239(2)	0 (-)	0.878(7)	-
Na2	Na	8i	0.793(2)	0.0325(13)	0 (-)	0.622(7)	-
V1	V	8j	0.2492(3) [§]	0.2492(3) [§]	0.19944(11) [§]	1	0.47(3) [§]
P1	P	4d	0 (-)	½ (-)	¼ (-)	1	0.63(3)
P2	P	4e	0 (-)	0 (-)	0.2577(6)	1	0.63(3)
O1	O	16k	0.1003(5)	0.4064(5)	0.1648(4)	1	0.83(8)
O2	O	8j	0.0953(5)	0.0953(5)	0.1679(6)	1	1.28(9)
O3	O	8j	0.4058(5)	0.4058(5)	0.1549(5)	1	1.28(9)
O4	O	8j	0.2463(4)	0.2463(4)	0.35323(15)	1	1.34(3)
F1	F	4f	0.2481(6)	0.2481(6)	0 (-)	1	0.97(4)

(§: from XRD refinement)

Table 3-4. Anisotropic atomic displacement (thermal) parameters for Na sites in $\text{Na}_3(\text{VOPO}_4)_2\text{F}$ ($x = 0$) from the ND refinement.

<i>Label</i>	<i>U₁₁</i> (\AA^2)	<i>U₂₂</i> (\AA^2)	<i>U₃₃</i> (\AA^2)	<i>U₁₂</i> (\AA^2)	<i>U₁₃</i> (\AA^2)	<i>U₂₃</i> (\AA^2)
Na1	0.0072(11)	0.0182(15)	0.0018(6)	-0.005(3)	0 (-)	0 (-)
Na2	0.020(3)	0.0051(14)	0.0010(9)	0.0074(17)	0 (-)	0 (-)

Table 3-5. Lattice parameters and cell volumes for $\text{Na}_3(\text{VO}_{0.8}\text{PO}_4)_2\text{F}_{1.4}$ ($x = 0.2$) from the ND refinement.

<i>Space Group</i>	<i>$P4_2/mnm$</i>
<i>Cell parameters</i>	
a (Å)	9.03330(11)
b (Å)	9.03330(11)
c (Å)	10.63004(16)
α (°)	90(-)
β (°)	90(-)
γ (°)	90(-)
Volume (Å ³)	867.42(2)
<i>Agreement factors</i>	
R_p (%)	2.63
R_{wp} (%)	3.54
R_F (%)	2.33
R_I (%)	2.79

Table 3-6. Atomic positions for $\text{Na}_3(\text{VO}_{0.8}\text{PO}_4)_2\text{F}_{1.4}$ ($x = 0.2$) from the ND refinement.

<i>Label</i>	<i>Atom</i>	<i>Site</i>	<i>x</i>	<i>y</i>	<i>z</i>	<i>Occupancy</i>	<i>B_{iso}</i> (\AA^2)
Na1	Na	8i	0.5137(10)	0.236(2)	0 (-)	0.892(3)	-
Na2	Na	8i	0.795(2)	0.0322(14)	0 (-)	0.608(3)	-
V1	V	8j	0.2487(5) [§]	0.2487(5) [§]	0.1965(2) [§]	1	0.43(5) [§]
P1	P	4d	0 (-)	½ (-)	¼ (-)	1	0.59(3)
P2	P	4e	0 (-)	0 (-)	0.2584(5)	1	0.59(3)
O1	O	16k	0.0989(5)	0.4065(5)	0.1644(4)	1	0.73(7)
O2	O	8j	0.0955(5)	0.0955(5)	0.1687(5)	1	1.28(8)
O3	O	8j	0.4051(5)	0.4051(5)	0.1559(5)	1	1.28(8)
O4	O	8j	0.2473(4)	0.2473(4)	0.35509(14)	0.8	1.53(3)
F1	F	4f	0.2507(6)	0.2507(6)	0 (-)	1	0.94(4)
F2	F	8j	0.2473(4)	0.2473(4)	0.35509(14)	0.2	1.53(3)

(§: from XRD refinement)

Table 3-7. Anisotropic atomic displacement (thermal) parameters for Na sites in $\text{Na}_3(\text{VO}_{0.8}\text{PO}_4)_2\text{F}_{1.4}$ ($x = 0.2$) from the ND refinement.

<i>Label</i>	<i>U₁₁</i> (\AA^2)	<i>U₂₂</i> (\AA^2)	<i>U₃₃</i> (\AA^2)	<i>U₁₂</i> (\AA^2)	<i>U₁₃</i> (\AA^2)	<i>U₂₃</i> (\AA^2)
Na1	0.0044(10)	0.0162(14)	0.0020(6)	-0.001(2)	0 (-)	0 (-)
Na2	0.027(4)	0.011(2)	0.0001(9)	0.0105(19)	0 (-)	0 (-)

Table 3-8. Lattice parameters and cell volumes for $\text{Na}_3(\text{VO}_{0.5}\text{PO}_4)_2\text{F}_{2.0}$ ($x = 0.5$) from the ND refinement.

<i>Space Group</i>	<i>P4₂/mmn</i>
<i>Cell parameters</i>	
a (Å)	9.0326(2)
b (Å)	9.0326(2)
c (Å)	10.6917(3)
α (°)	90(-)
β (°)	90(-)
γ (°)	90(-)
Volume (Å ³)	872.32(4)
<i>Agreement factors</i>	
R_p (%)	4.43
R_{wp} (%)	5.78
R_F (%)	4.73
R_I (%)	5.45

Table 3-9. Atomic positions for $\text{Na}_3(\text{VO}_{0.5}\text{PO}_4)_2\text{F}_{2.0}$ ($x = 0.5$) from the ND refinement.

<i>Label</i>	<i>Atom</i>	<i>Site</i>	<i>x</i>	<i>y</i>	<i>z</i>	<i>Occupancy</i>	<i>B_{iso}</i> (\AA^2)
Na1	Na	<i>8i</i>	0.5184(11)	0.250(2)	0 (-)	0.978(6)	-
Na2	Na	<i>8i</i>	0.8158(17)	0.045(2)	0 (-)	0.522(6)	0.605
V1	V	<i>8j</i>	0.2488(4) [§]	0.2488(4) [§]	0.18923(14) [§]	1	0.91(4) [§]
P1	P	<i>4d</i>	0 (-)	½ (-)	¼ (-)	1	0.58(6)
P2	P	<i>4e</i>	0 (-)	0 (-)	0.2481(13)	1	0.58(6)
O1	O	<i>16k</i>	0.0981(6)	0.4077(6)	0.1596(4)	1	0.24(8)
O2	O	<i>8j</i>	0.0944(7)	0.0944(7)	0.1592(7)	1	1.21(9)
O3	O	<i>8j</i>	0.4030(7)	0.4030(7)	0.1761(5)	1	1.21(9)
O4	O	<i>8j</i>	0.2470(9)	0.2470(9)	0.3632(3)	0.5	1.29(6)
F1	F	<i>4f</i>	0.2513(11)	0.2513(11)	0 (-)	1	0.35(7)
F2	F	<i>8j</i>	0.2470(9)	0.2470(9)	0.3632(3)	0.5	1.29(6)

(§: from XRD refinement)

Table 3-10. Anisotropic atomic displacement (thermal) parameters for the Na1 site in $\text{Na}_3(\text{VO}_{0.5}\text{PO}_4)_2\text{F}_{2.0}$ ($x = 0.5$) from the ND refinement.

<i>Label</i>	U_{11} (\AA^2)	U_{22} (\AA^2)	U_{33} (\AA^2)	U_{12} (\AA^2)	U_{13} (\AA^2)	U_{23} (\AA^2)
Na1	0.0086(18)	0.014(2)	0.0044(8)	0.016(3)	0 (-)	0 (-)

Table 3-11. Lattice parameters and cell volumes for $\text{Na}_3(\text{VO}_{0.2}\text{PO}_4)_2\text{F}_{2.6}$ ($x = 0.8$) from the ND refinement.

<i>Space Group</i>	<i>P4₂/mmn</i>
<i>Cell parameters</i>	
a (Å)	9.0341(2)
b (Å)	9.0341(2)
c (Å)	10.7299(4)
α (°)	90(-)
β (°)	90(-)
γ (°)	90(-)
Volume (Å ³)	875.73(4)
<i>Agreement factors</i>	
R_p (%)	3.35
R_{wp} (%)	4.42
R_F (%)	3.60
R_I (%)	3.80

Table 3-12. Atomic positions for $\text{Na}_3(\text{VO}_{0.2}\text{PO}_4)_2\text{F}_{2.6}$ ($x = 0.8$) from the ND refinement.

<i>Label</i>	<i>Atom</i>	<i>Site</i>	<i>x</i>	<i>y</i>	<i>z</i>	<i>Occupancy</i>	<i>B_{iso}</i> (\AA^2)
Na1	Na	8i	0.5255(15)	0.2355(15)	0 (-)	0.969(5)	-
Na2	Na	8i	0.792(5)	0.063(3)	0 (-)	0.531(5)	-
V1	V	8j	0.2480(6) [§]	0.2480(6) [§]	0.1859(2) [§]	1	0.68(6) [§]
P1	P	4d	0 (-)	½ (-)	¼ (-)	1	0.91(5)
P2	P	4e	0 (-)	0 (-)	0.2558(11)	1	0.91(5)
O1	O	16k	0.0984(7)	0.4087(7)	0.1595(3)	1	1.10(3)
O2	O	8j	0.0959(7)	0.0959(7)	0.1632(7)	1	1.10(3)
O3	O	8j	0.4043(7)	0.4043(7)	0.1734(5)	1	1.10(3)
O4	O	8j	0.2442(6)	0.2442(6)	0.3663(2)	0.2	1.369(1)
F1	F	4f	0.2524(10)	0.2524(10)	0 (-)	1	0.936(2)
F2	F	8j	0.2442(6)	0.2442(6)	0.3663(2)	0.8	1.369(1)

(§: from XRD refinement)

Table 3-13. Anisotropic atomic displacement (thermal) parameters for Na sites in $\text{Na}_3(\text{VO}_{0.2}\text{PO}_4)_2\text{F}_{2.6}$ ($x = 0.8$) from the ND refinement.

<i>Label</i>	<i>U₁₁</i> (\AA^2)	<i>U₂₂</i> (\AA^2)	<i>U₃₃</i> (\AA^2)	<i>U₁₂</i> (\AA^2)	<i>U₁₃</i> (\AA^2)	<i>U₂₃</i> (\AA^2)
Na1	0.0067(14)	0.018(3)	0.0054(9)	-0.0102(18)	0 (-)	0 (-)
Na2	0.15(2)	0.015(6)	0.012(3)	0.059(10)	0 (-)	0 (-)

Table 3-14. Lattice parameters and cell volumes for $\text{Na}_3\text{V}_2(\text{PO}_4)_2\text{F}_3$ ($x = 1$) from the ND refinement.

<i>Space Group</i>	<i>P4₂/mnm</i>
<i>Cell parameters</i>	
a (Å)	9.0350(2)
b (Å)	9.0350(2)
c (Å)	10.7408(3)
α (°)	90(-)
β (°)	90(-)
γ (°)	90(-)
Volume (Å ³)	876.79(4)
<i>Agreement factors</i>	
R_p (%)	4.02
R_{wp} (%)	5.32
R_F (%)	6.90
R_I (%)	5.38

Table 3-15. Atomic positions for $\text{Na}_3\text{V}_2(\text{PO}_4)_2\text{F}_3$ ($x = 1$) from the ND refinement.

<i>Label</i>	<i>Atom</i>	<i>Site</i>	<i>x</i>	<i>y</i>	<i>z</i>	<i>Occupancy</i>	<i>B_{iso}</i> (\AA^2)
Na1	Na	8i	0.5236(15)	0.236(3)	0 (-)	0.993(6)	-
Na2	Na	8i	0.810(5)	0.059(3)	0 (-)	0.507(6)	-
V1	V	8j	0.2477(5) [§]	0.2477(5) [§]	0.1854(2) [§]	1	0.36(6) [§]
P1	P	4d	0 (-)	½ (-)	¼ (-)	1	0.48(5)
P2	P	4e	0 (-)	0 (-)	0.2591(9)	1	0.48(5)
O1	O	16k	0.1011(8)	0.4072(7)	0.1683(3)	1	0.69(6)
O2	O	8j	0.0957(7)	0.0957(7)	0.1633(6)	1	0.69(6)
O3	O	8j	0.4071(7)	0.4071(7)	0.1558(5)	1	0.82(18)
F1	F	4f	0.2462(12)	0.2462(12)	0 (-)	1	0.59(8)
F2	F	8j	0.2461(8)	0.2461(8)	0.3672(2)	1	1.34(6)

(§: from XRD refinement)

Table 3-16. Anisotropic atomic displacement (thermal) parameters for Na sites in $\text{Na}_3\text{V}_2(\text{PO}_4)_2\text{F}_3$ ($x = 1$) from the ND refinement.

<i>Label</i>	<i>U₁₁</i> (\AA^2)	<i>U₂₂</i> (\AA^2)	<i>U₃₃</i> (\AA^2)	<i>U₁₂</i> (\AA^2)	<i>U₁₃</i> (\AA^2)	<i>U₂₃</i> (\AA^2)
Na1	0.012(2)	0.024(3)	0.0071(12)	-0.015(3)	0 (-)	0 (-)
Na2	0.049(9)	-0.001(3)	0.006(2)	0.016(4)	0 (-)	0 (-)

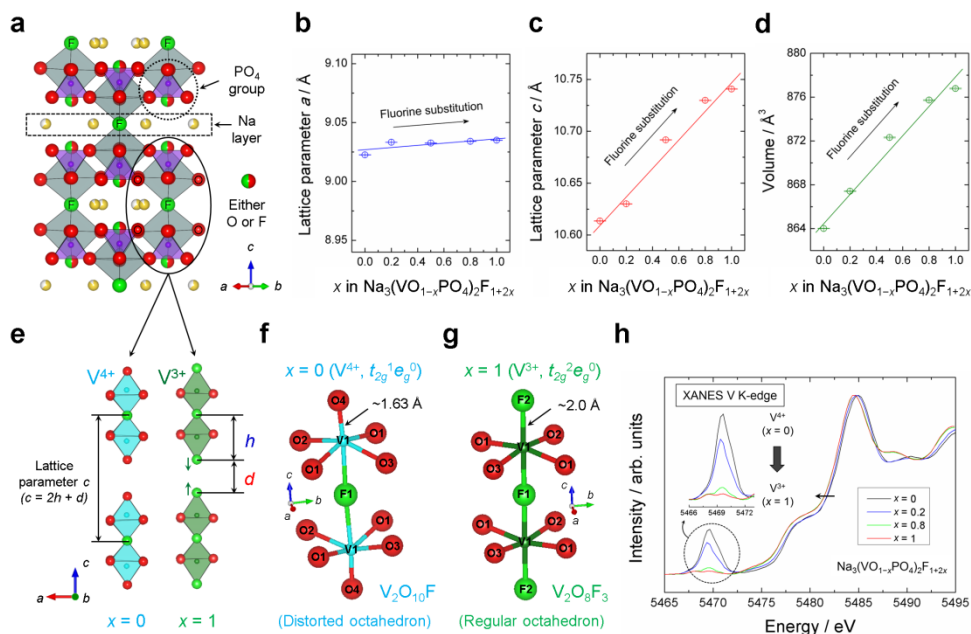


Figure 3-7. Structural change with the fluorine content in $\text{Na}_3(\text{VO}_{1-x}\text{PO}_4)_2\text{F}_{1+2x}$ ($0 \leq x \leq 1$). (a) Crystal structure of $\text{Na}_3(\text{VO}_{1-x}\text{PO}_4)_2\text{F}_{1+2x}$. Oxygen and fluorine ions are shown as red and green spheres, respectively. (b–d) Lattice parameter change of $\text{Na}_3(\text{VO}_{1-x}\text{PO}_4)_2\text{F}_{1+2x}$ based on the ND data; (b) lattice parameter a , (c) lattice parameter c , (d) unit cell volume. (e) Components of lattice parameter c . (f) Geometry of the $\text{V}_2\text{O}_{10}\text{F}$ bioctahedron for $x=0$ (V^{4+} , $t_{2g}^1 e_g^0$). (g) Geometry of the $\text{V}_2\text{O}_8\text{F}_3$ bioctahedron for $x=1$ (V^{3+} , $t_{2g}^2 e_g^0$). (h) Vanadium K-edge XANES spectra of the $\text{Na}_3(\text{VO}_{1-x}\text{PO}_4)_2\text{F}_{1+2x}$ samples with different fluorine contents; $x = 0.0$ (black), $x = 0.2$ (blue), $x = 0.8$ (green), and $x = 1.0$ (red). The inset shows an enlarged graph of the pre-edge region. Used with permission from [Y.-U. Park *et al.*, *Adv. Funct. Mater.*, **24**, 4603–4614 (2014); DOI: 10.1002/adfm.201400561]. Copyright 2014 Wiley.

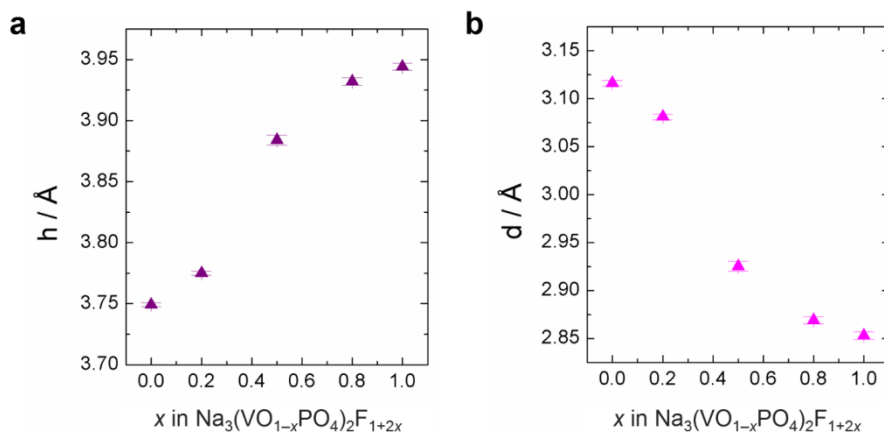


Figure 3-8. Variation of h and d with x in $\text{Na}_3(\text{VO}_{1-x}\text{PO}_4)_2\text{F}_{1+2x}$ ($0 \leq x \leq 1$).

Variation of (a) the height (h) of V^{n+} octahedron and (b) the distance (d) between terminal O^{2-} or F^- ions of $\text{V}_2\text{O}_{10-2x}\text{F}_{1+2x}$ ($0 \leq x \leq 1$) bioctahedra with increasing fluorine content (x) in the $\text{Na}_3(\text{VO}_{1-x}\text{PO}_4)_2\text{F}_{1+2x}$ ($0 \leq x \leq 1$) system. The data were from the combined ND and XRD refinement results.

(*) Used with permission from [Y.-U. Park *et. al.*, *Adv. Funct. Mater.*, **24**, 4603-4614 (2014); DOI: 10.1002/adfm.201400561]. Copyright 2014 Wiley.

Table 3-17. Bond distances of V–O(F) bonds, Baur’s distortion indices (Δ), and octahedral volumes of VO_5F ($x = 0$) and VO_4F_2 ($x = 1$) octahedra.

x	Type of bioctahedron (or octahedron)	Electronic configuration of V^{n+} ions	V–O(F) Bonds	Bond distance (Å)	Baur’s distortion index (Δ)	Octahedral volume (Å ³)
0	$\text{V}_2\text{O}_{10}\text{F}$ (VO_5F)	$\text{V}^{4+} (t_{2g}^1 e_g^0)$	V1–O1 (×2) V1–O2 (×1) V1–O3 (×1) V1–F1 (×1) V1–O4 (×1)	1.988(6) 1.992(6) 2.053(6) 2.11682(5) 1.6327(16)	0.05592	9.6670
1	$\text{V}_2\text{O}_8\text{F}_3$ (VO_4F_2)	$\text{V}^{3+} (t_{2g}^2 e_g^0)$	V1–O1 (×2) V1–O2 (×1) V1–O3 (×1) V1–F1 (×1) V1–F2 (×1)	1.966(9) 1.957(8) 2.061(8) 1.991(3) 1.953(4)	0.01482	10.2295

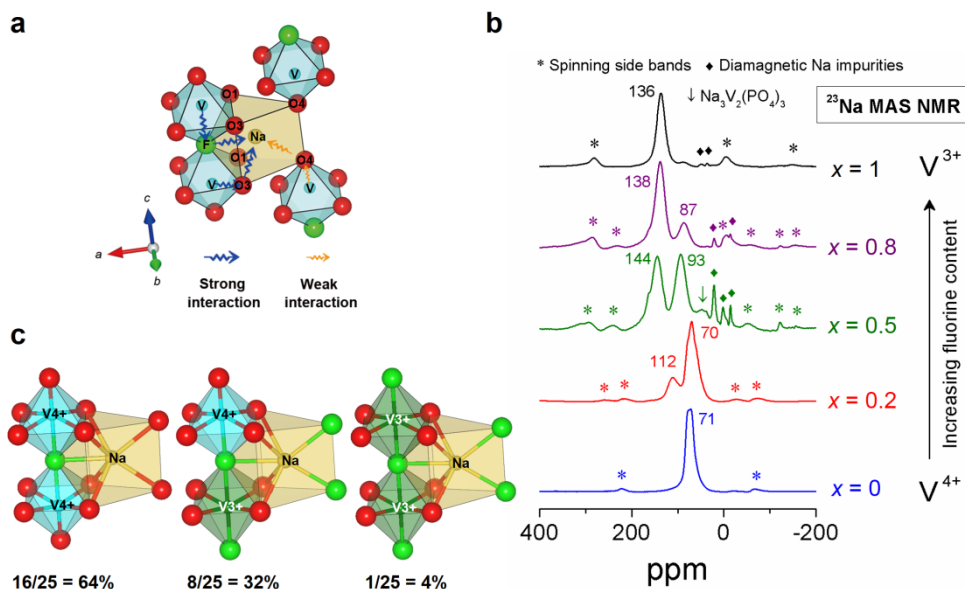


Figure 3-9. ^{23}Na MAS NMR study for $\text{Na}_3(\text{VO}_{1-x}\text{PO}_4)_2\text{F}_{1+2x}$ system ($0 \leq x \leq 1$).

(a) Schematic representing various types of Na–O(F)–V interactions in the crystal structure of $\text{Na}_3(\text{VOPO}_4)_2\text{F}$ ($x = 0$).

(b) ^{23}Na MAS NMR spectra of the $\text{Na}_3(\text{VO}_{1-x}\text{PO}_4)_2\text{F}_{1+2x}$ samples with different fluorine contents ($x = 0.0, 0.2, 0.5, 0.8$, and 1.0) at a MAS spinning speed of 15 kHz; spinning side bands are marked with asterisks. Diamagnetic Na impurities are denoted by diamonds. A broad peak at ~45 ppm for $x = 0.5$ (denoted by an arrow) may originate from an impurity phase of $\text{Na}_3\text{V}_2(\text{PO}_4)_3$.

(c) Three types of possible local environments for vanadium bi-octahedra for $x = 0.2$ and their expected abundance ratio when the ratio of V^{4+} to V^{3+} ions is 4:1.

(*) Used with permission from [Y.-U. Park *et al.*, *Adv. Funct. Mater.*, **24**, 4603–4614 (2014); DOI: 10.1002/adfm.201400561]. Copyright 2014 Wiley.

Table 3-18. Bond angles for various Na–O(F)–V interactions in $\text{Na}_3(\text{VOPO}_4)_2\text{F}$ ($x = 0$).

<i>Na site</i>	<i>Occupancy</i>	<i>Na–O(F)–V interaction</i>	<i>Bond angle, θ (°)</i>	<i>Strength of the interaction</i>
Na1	0.878	Na1–F1–V1 (×2)	89.74(14)	Strong
		Na1–O1–V1 (×2)	93.25(18)	Strong
		Na1–O3–V1 (×2)	89.48(19)	Strong
		Na1–O4–V1 (×2)	126.7(3)	Weak
Na2	0.622	Na2–F1–V1 (×2)	90.30(2)	Strong
		Na2–O1–V1 (×2)	86.90(19)	Strong
		Na2–O2–V1 (×2)	99.8(3)	Strong
		Na2–O4–V1 (×2)	126.28(10)	Weak

3.3.2. Electrochemical Mechanisms of $\text{Na}_y(\text{VO}_{1-x}\text{PO}_4)_2\text{F}_{1+2x}$ Electrodes.

Figure 3-10 and **Figure 3-11** show the voltage–composition curves of the $\text{Na}_y(\text{VO}_{1-x}\text{PO}_4)_2\text{F}_{1+2x}$ ($x = 0.0, 0.2, 0.5, 0.8$, and 1.0) electrodes. It is noteworthy that all the $\text{Na}_y(\text{VO}_{1-x}\text{PO}_4)_2\text{F}_{1+2x}$ electrodes showed the similar average voltage of 3.8–3.9 V (vs. Na^+/Na) and the capacity of 120–130 mAh g^{-1} . The notably smaller charge capacity and larger irreversible capacity of the first cycle for $x = 0.5$ may be due to various impurity phases in the sample which can trigger some kinds of side reactions upon cycling. Also, all the $\text{Na}_y(\text{VO}_{1-x}\text{PO}_4)_2\text{F}_{1+2x}$ electrodes exhibited roughly similar voltage-composition profiles regardless of fluorine content. However, while electrodes with lower x values ($x = 0.0, 0.2$, and 0.5) in **Figure 3-10** showed two voltage plateaus with a step at $y \approx 2.0$, those with higher x values ($x = 0.8$ and 1.0) in **Figure 3-11** exhibited four voltage plateaus; the two additional steps at $y \approx 2.43$ and 1.55 are shown more closely in the inset of **Figure 3-11**. The presence of the voltage steps suggests multiple phase transitions due to Na contents in $\text{Na}_y(\text{VO}_{1-x}\text{PO}_4)_2\text{F}_{1+2x}$, and the difference in electrochemical steps implies the sensitive influence of fluorine content on the phase reaction.

Notably, similar average voltages were observed despite the different redox couples of $\text{V}^{3+}/\text{V}^{4+}$ and $\text{V}^{4+}/\text{V}^{5+}$. While the end members of $\text{Na}_3(\text{VO}_{1-x}\text{PO}_4)_2\text{F}_{1+2x}$ had either only the $\text{V}^{4+}/\text{V}^{5+}$ redox couple for $x = 0$ or only the $\text{V}^{3+}/\text{V}^{4+}$ redox couple for $x = 1$, the $\text{V}^{4+}/\text{V}^{5+}$ redox potential of the former (~ 3.77 V vs. Na^+/Na) was lower than the $\text{V}^{3+}/\text{V}^{4+}$ redox potential of the latter (~ 3.9 V vs. Na^+/Na) by ~ 0.13 V, as shown in **Figure 3-12**. This indicates that the strong inductive effect of fluorine ions in fluorine-rich samples could raise the $\text{V}^{3+}/\text{V}^{4+}$ redox potential substantially. Typically, the redox potential of $\text{V}^{3+}/\text{V}^{4+}$ is lower than that of $\text{V}^{4+}/\text{V}^{5+}$ by ~ 0.66 V under standard conditions.⁸³ However, this difference could be counterbalanced by

the voltage gain from the stronger inductive effect. Furthermore, this cancellation resulted in a net voltage gain of +0.13 V. **Figure 3-12** shows that the average voltage changed linearly over the full range of fluorine contents ($0 \leq x \leq 1$).

All the samples showed distinct voltage steps at $y \approx 2.0$ in the electrochemical profile, indicating the presence of a stable intermediate phase for this composition. The phase stabilization at $y \approx 2.0$ is believed to originate from the significantly relieved $\text{Na}^+ - \text{Na}^+$ repulsion at this particular Na composition, as schematically shown in **Figure 3-13**. The reduction in $\text{Na}^+ - \text{Na}^+$ repulsion at $y \approx 2.0$ occurs *via* (i) Na extraction [$n = 3 \rightarrow 2$; blue arrows] and (ii) Na-vacancy re-ordering [$n = 2$ (*cis*) $\rightarrow 2$ (*trans*); red arrows]. The diagonal Na configuration (*i.e.*, *trans* configuration), minimizing the electrostatic repulsion, is possible at this composition and is believed to stabilize the intermediate phase.⁶⁷ A similar phenomenon has been observed for $x = 0.2$ in my previous work.⁶⁷

Off-centered Na^+ ions shifted significantly to more centered positions upon Na extraction ($n = 3 \rightarrow 2$; see **Figure 3-13**), indicating strong $\text{Na}^+ - \text{Na}^+$ repulsion in the initial state ($y = 3$). The coexistence of centered and off-centered Na^+ ions in the pristine phase ($y = 3$) was supported by ^{23}Na MAS NMR and diffraction data. **Figure 3-14** shows the ^{23}Na MAS NMR spectrum of $\text{Na}_3(\text{VOPO}_4)_2\text{F}$ ($x = 0$), where the main Fermi-contact shift at 71 ppm (**Figure 3-9b**) could be deconvoluted into two peaks at 70 and 80 ppm having comparable intensities (**Figure 3-14a**). These two peaks are attributable to two different Na sites in $\text{Na}_3(\text{VOPO}_4)_2\text{F}$. According to the refinement results (**Table 3-3**), $\text{Na}_3(\text{VOPO}_4)_2\text{F}$ possesses two different Na sites (*i.e.*, Na1 and Na2) with similar occupancies. Na^+ ions in the Na1 site are located in the center of the prism, whereas those in the Na2 site are in an off-centered position, as shown in **Figure 3-14b**, resulting in the slightly different bond angles and

distances of the Na–O(F)–V interactions. The change in the Na–O(F)–V bonding nature is thought to cause the distinct Fermi-contact shifts for the two Na sites.

Another notable change in the electrochemical profile of $\text{Na}_y(\text{VO}_{1-x}\text{PO}_4)_2\text{F}_{1+2x}$ ($x = 0.8$ and 1.0) is the two additional voltage steps at $y \approx 2.43$ and 1.55 (**Figure 3-11**), which appear as peaks in the corresponding derivative dV/dy curves (see the inset of **Figure 3-11** and **Figure 3-16**). This suggests that additional intermediate phases were present at those compositions. First-principles calculations were carried out to determine the probability of different intermediate phases for different fluorine contents. **Figure 3-17** shows a first-principles formation energy plot for $\text{Na}_y\text{V}_2(\text{PO}_4)_2\text{F}_3$ ($x = 1$) as a function of Na content. It was found that the stability at $y = 2.5$ and 1.5 was high compared to the formation energy plot of $\text{Na}_y(\text{VOPO}_4)_2\text{F}$ ($x = 0$) in my previous report.⁶⁷ The formation energies at $y = 2.5$ and 1.5 for $\text{Na}_y\text{V}_2(\text{PO}_4)_2\text{F}_3$ ($x = 1$) are both below the tie line at 0 K, implying the possibility of a stable intermediate phase at a finite temperature (denoted by circles in **Figure 3-17**). In contrast, $\text{Na}_y(\text{VOPO}_4)_2\text{F}$ ($x = 0$) showed formation energies well above the tie line at the same compositions. The significantly lower formation energies of $\text{Na}_y\text{V}_2(\text{PO}_4)_2\text{F}_3$ ($x = 1$) compared to those of $\text{Na}_y(\text{VOPO}_4)_2\text{F}$ ($x = 0$) at these compositions imply a greater probability of voltage steps at $y \approx 2.5$ and 1.5 in the $\text{Na}_y\text{V}_2(\text{PO}_4)_2\text{F}_3$ ($x = 1$) electrode at room temperature. Some Na configurations for $\text{Na}_y\text{V}_2(\text{PO}_4)_2\text{F}_3$ ($x = 1$) and $\text{Na}_y(\text{VOPO}_4)_2\text{F}$ ($x = 0$) are provided in **Figure 3-18** for both $y = 2.5$ and 1.5 .

The relative stability of intermediate phases at certain Na and F compositions is likely attributable to the type and strength of the $\text{Na}^+ - \text{Na}^+$ repulsion, which varied with the fluorine content in the $\text{Na}_y(\text{VO}_{1-x}\text{PO}_4)_2\text{F}_{1+2x}$ ($0 \leq x \leq 1$) electrodes. **Figure 3-19** shows the main type of $\text{Na}^+ - \text{Na}^+$ repulsion in the Na layer of $\text{Na}_3(\text{VO}_{1-x}$

$_{x}\text{PO}_4)_2\text{F}_{1+2x}$ (denoted by arrows). The repulsion among Na^+ ions inside the basic unit is primarily shielded by anions that lie at the center of the basic unit (denoted by black circles), whereas the center anion can be O^{2-} or F^- depending on x . Previous work has shown that the substitution of F^- ions takes place at the center anion.^{34,67} Because the shielding ability of less negative F^- ions is generally less effective than that of more negative O^{2-} ions, I believe that the intra-unit Na^+-Na^+ repulsion becomes stronger as x increases from 0 to 1. At $x = 0$, all the center positions are occupied by O^{2-} ions, and at $x = 1$, all are occupied by F^- ions. Thus, the stronger repulsion among Na^+ ions in $\text{Na}_y\text{V}_2(\text{PO}_4)_2\text{F}_3$ ($x = 1$) is believed to stabilize the Na in a triangular prism site (denoted by circles in **Figure 3-20**), which is the farthest from the other Na ions (see the first-principles calculations in **Figure 3-18** for the stable Na configuration).

Figure 3-21 shows a schematic representation of this new stable Na configuration within the basic unit, which minimizes the electrostatic repulsion among Na^+ ions. It was also found that the voltage step at $y \approx 2.0$ for $\text{Na}_y(\text{VO}_{1-x}\text{PO}_4)_2\text{F}_{1+2x}$ ($0 \leq x \leq 1$) increased with increasing x , suggesting a more stable intermediate phase at $y \approx 2.0$ in fluorine-rich samples, as shown in **Figure 3-22**. This is because samples with high x possess stronger intra-unit Na^+-Na^+ repulsion due to more intervening F^- ions with weaker shielding capability; therefore, the stable Na configuration that minimizes the Na^+-Na^+ repulsion becomes comparatively more important. However, exactly how the minimum formation energy at $y = 2.5$ and 1.5 could be below the tie lines for $x = 1.0$ is still unclear, because the different degree of shielding capability of O^{2-} and F^- ions is applied equally to all compositions of sodium (y). I believe that some particular Na-vacancy orderings (as shown in **Figure 3-21** and **Figure 3-18**) somehow could be

further stabilized at $x = 1.0$ as compared to $x = 0$, whose origin may be related to stronger inter-unit Na^+-Na^+ interactions at $x = 1.0$. The temperature-controlled experiment further confirmed that the appearance of the intermediate phases at certain Na contents arises due to the stabilization of Na-vacancy ordering. As the temperature increased, the thermal energy caused disorder of the Na and vacancies; thus, the Na-vacancy ordering became less visible. Electrochemical cycling performed at 60°C showed that the dV/dy peaks at $y \approx 2.5$ became less prominent with increasing temperature (see **Figure 3-23**), which originated from the disturbed Na-vacancy orderings due to thermal disordering.

The structural evolution of $\text{Na}_y(\text{VOPO}_4)_2\text{F}$ ($x = 0$) as a function of Na content (y) was investigated with ND and XRD, as shown in **Figure 3-24a** and **Figure 3-24b**, respectively. While the change in the diffraction patterns with different Na contents was not significant due to the small change in the structure, a two-phase reaction was detected in the region of $2.0 \leq y \leq 3.0$ for both ND and XRD patterns. The high-angle region of the ND patterns in **Figure 3-24a** (denoted by a dotted box) show that the peak at $\sim 111^\circ$ emerged as the peak at $\sim 109.5^\circ$ disappeared, which is typical for a two-phase reaction. Furthermore, the peak splitting at $\sim 28^\circ$ and $\sim 33^\circ$ in the XRD patterns (denoted by dotted circles in **Figure 3-24b**) clearly indicates a biphasic nature. On the other hand, signs of a biphasic reaction in the region of $1.0 \leq y \leq 2.0$ were difficult to identify, despite the two-phase plateau in the electrochemical profile. This observation is similar to the previous report for $\text{Na}_y(\text{VO}_{0.8}\text{PO}_4)_2\text{F}_{1.4}$ ($x = 0.2$).⁶⁷ One possible reason for the difficulty in identifying the phases is that the difference of two phases in the region is not big with negligible change in the structure, and they are mixed at the atomic level with the coherent interface.⁶⁷

Figure 3-25 shows the change in lattice parameters upon desodiation of $\text{Na}_y(\text{VOPO}_4)_2\text{F}$ ($x = 0$). With decreasing Na content, lattice parameter a decreased linearly, whereas lattice parameter c increased linearly. During the desodiation process, the contraction of vanadium octahedra ($\text{V}^{4+} \rightarrow \text{V}^{5+}$) led to the decrease in lattice parameter a , whereas larger electrostatic repulsion between O^{2-} layers due to an emptier intervening Na layer caused the increase in lattice parameter c . Similar structural evolutions were observed for other compositions of x .^{17,27,67,69} **Figure 3-26** shows the evolution of XRD patterns in the region of $2.0 \leq y \leq 3.0$ for the $\text{Na}_y\text{V}_2(\text{PO}_4)_2\text{F}_3$ ($x = 1$) electrode. Behavior typical of a two-phase mixture is evident by a sudden broadening of the (220) peak. Nevertheless, I did not observe additional two-phase reactions at $y \approx 2.43$ and $y \approx 1.55$ by diffraction; these reactions were suggested from the electrochemical profile and the first-principles calculations. However, it should be noted that the interaction between different basic units, including long-range Na-vacancy ordering, was responsible for the stability of the phases at $y \approx 2.43$ and $y \approx 1.55$, and is relatively weak. Thus, the phase identification at ambient temperature may be more difficult.

The $\text{Na}_y(\text{VOPO}_4)_2\text{F}$ ($x = 0$) electrode exhibited a remarkably small volume change of -2.2% over the full charge range ($1.0 \leq y \leq 3.0$), as shown in **Figure 3-25**. The volume changes were similar for $\text{Na}_y(\text{VO}_{1-x}\text{PO}_4)_2\text{F}_{1+2x}$ with various fluorine contents, implying that the small volume change with Na de/insertion is characteristic of this family of compounds: -2.9% for $\text{Na}_y(\text{VO}_{0.8}\text{PO}_4)_2\text{F}_{1.4}$ ($x = 0.2$; $0.88 \leq y \leq 3.0$),⁶⁷ -1.79% for $\text{Na}_y\text{V}_2(\text{PO}_4)_2\text{F}_3$ ($x = 1$; $1.0 \leq y \leq 3.0$),¹⁷ -2.12% for $\text{Na}_y(\text{VO}_{0.2}\text{PO}_4)_2\text{F}_{2.6}$ ($x = 0.8$; $1.0 \leq y \leq 3.0$), and -2.01% for $\text{Na}_y(\text{VO}_{0.5}\text{PO}_4)_2\text{F}_{2.0}$ ($x = 0.5$; $1.0 \leq y \leq 3.0$) (see **Figure 3-27** for $x = 0.8$ and 0.5). The exceptionally small volume change gives rise to excellent cyclability for this family of cathode

materials. **Figure 3-28** and **Figure 3-29** show that the capacity retention and Columbic efficiencies of the $\text{Na}_3(\text{VO}_{1-x}\text{PO}_4)_2\text{F}_{1+2x}$ ($x = 0.0, 0.2, 0.5, 0.8, \text{ and } 1.0$) electrodes were remarkably high. The discharge capacity of ~95% was well maintained for 150 cycles with high efficiency. The high voltage of ~4 V (vs. Na^+/Na) combined with the stable discharge capacity ($> 100 \text{ mAh g}^{-1}$) for all the electrodes in the family allows them to be categorized as a promising cathode group for NIBs. A relatively poor cycle stability was observed for $x = 0$, which agrees with the report by Sauvage *et al.*²⁷ The origin of this abnormal capacity fading for $x = 0$ is unclear for now.

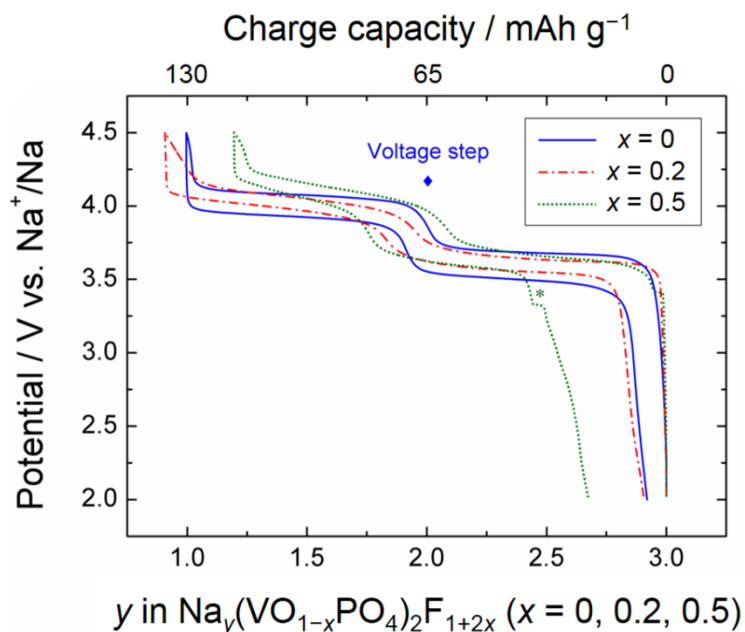


Figure 3-10. Voltage-composition curves of the $\text{Na}_y(\text{VO}_{1-x}\text{PO}_4)_2\text{F}_{1+2x}$ electrodes for $x = 0.0$ (blue), 0.2 (red), and 0.5 (green). The electrochemical cells were cycled at a $C/10$ rate with a voltage window of 2.0–4.5 V using the electrolyte of 1 M NaBF_4 in a mixture of EC and PC (1:1 v/v) at room temperature. Voltage steps are denoted by diamonds. The capacity from $\text{Na}_3\text{V}_2(\text{PO}_4)_3$ for $x = 0.5$ is denoted by an asterisk. Used with permission from [Y.-U. Park *et. al.*, *Adv. Funct. Mater.*, **24**, 4603-4614 (2014); DOI: 10.1002/adfm.201400561]. Copyright 2014 Wiley.

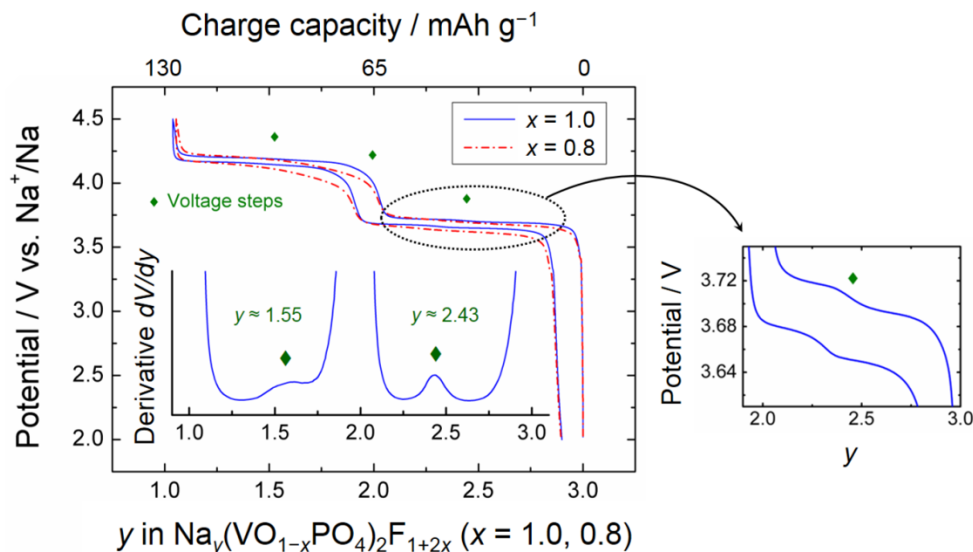


Figure 3-11. Voltage-composition curves of the $\text{Na}_y(\text{VO}_{1-x}\text{PO}_4)_2\text{F}_{1+2x}$ electrodes for $x = 0.8$ (red) and 1.0 (blue). The electrochemical cells were cycled at a $C/10$ rate with a voltage window of 2.0–4.5 V using the electrolyte of 1 M NaBF_4 in a mixture of EC and PC (1:1 v/v) at room temperature. Voltage steps are denoted by diamonds. The inset and right panel show a derivative dV/dy analysis and enlarged voltage-composition curves for $x = 1$, respectively. Used with permission from [Y.-U. Park *et. al.*, *Adv. Funct. Mater.*, **24**, 4603-4614 (2014); DOI: 10.1002/adfm.201400561]. Copyright 2014 Wiley.

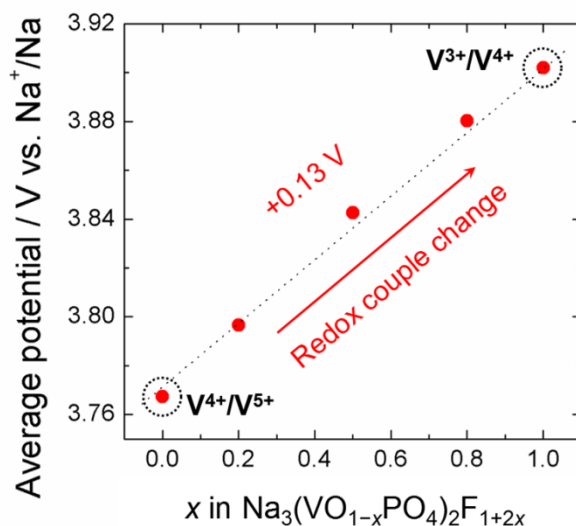


Figure 3-12. Change in average voltages of the $\text{Na}_y(\text{VO}_{1-x}\text{PO}_4)_2\text{F}_{1+2x}$ ($x = 0.0, 0.2, 0.5, 0.8, \text{ and } 1.0$) electrodes. The redox couple was changed from $\text{V}^{4+}/\text{V}^{5+}$ to $\text{V}^{3+}/\text{V}^{4+}$ when x increased from 0 to 1, accompanied by a voltage increment of ~ 0.13 V. The average voltages were calculated on the basis of the areas under the voltage-composition curves in **Figure 3-10** and **Figure 3-11**. Used with permission from [Y.-U. Park *et. al.*, *Adv. Funct. Mater.*, **24**, 4603-4614 (2014); DOI: 10.1002/adfm.201400561]. Copyright 2014 Wiley.

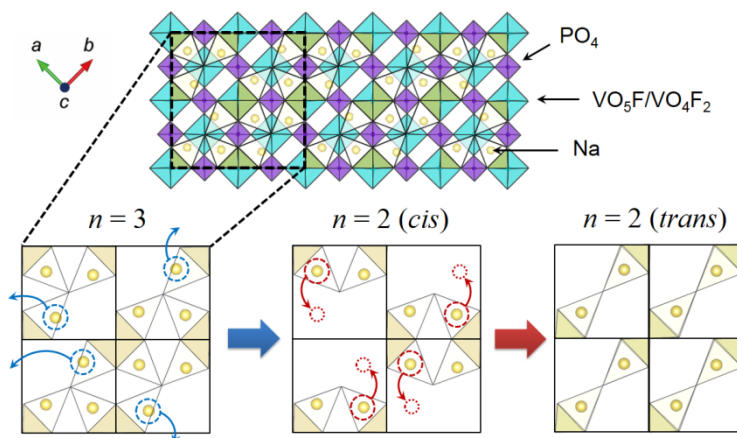


Figure 3-13. Evolution of Na-vacancy ordering in the $\text{Na}_y(\text{VO}_{1-x}\text{PO}_4)_2\text{F}_{1+2x}$ ($0 \leq x \leq 1$) electrodes from $y = 3.0$ to $y = 2.0$. The Na extraction process (denoted by blue arrows) and Na-vacancy re-ordering process (denoted by red arrows), as the pristine phase ($y = 3.0$) is transformed into the intermediate phase ($y = 2.0$), are schematically shown. Used with permission from [Y.-U. Park *et. al.*, *Adv. Funct. Mater.*, **24**, 4603-4614 (2014); DOI: 10.1002/adfm.201400561]. Copyright 2014 Wiley.

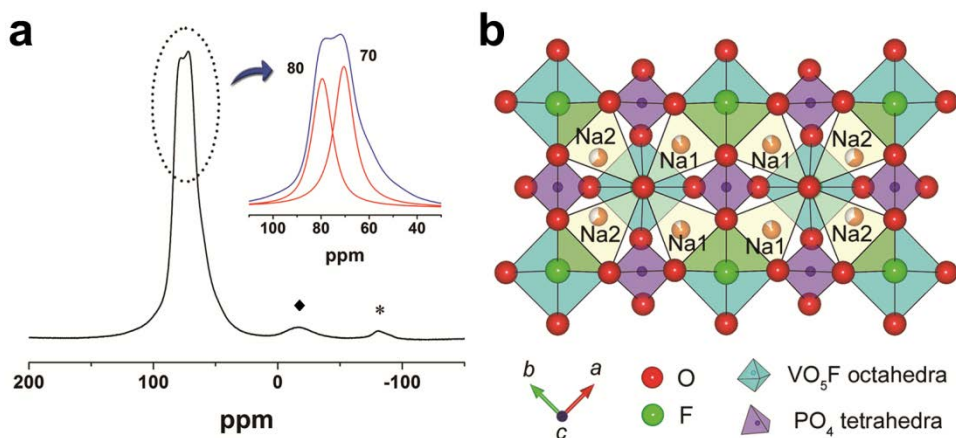


Figure 3-14. ^{23}Na MAS NMR study on Na-vacancy ordering in $\text{Na}_3(\text{VOPO}_4)_2\text{F}$ ($x = 0$) phase.

(a) ^{23}Na MAS NMR spectrum of $\text{Na}_3(\text{VOPO}_4)_2\text{F}$ ($x = 0$) at a MAS frequency of 17 kHz. The inset shows the result of spectral deconvolution for the main peak region. An isotropic peak denoted by a diamond (at ~ 10 ppm) may be from diamagnetic Na impurities.

(b) Projection along the c -axis for the crystal structure of $\text{Na}_3(\text{VOPO}_4)_2\text{F}$ ($x = 0$). Oxygen and fluorine ions are shown as red and green, respectively. VO_5F octahedra and PO_4 tetrahedra are shown as cyan and purple, respectively. The configuration of the Na1 (centered) and Na2 (off-centered) sites on the ab plane is also shown.

(*) Used with permission from [Y.-U. Park *et. al.*, *Adv. Funct. Mater.*, **24**, 4603-4614 (2014); DOI: 10.1002/adfm.201400561]. Copyright 2014 Wiley.

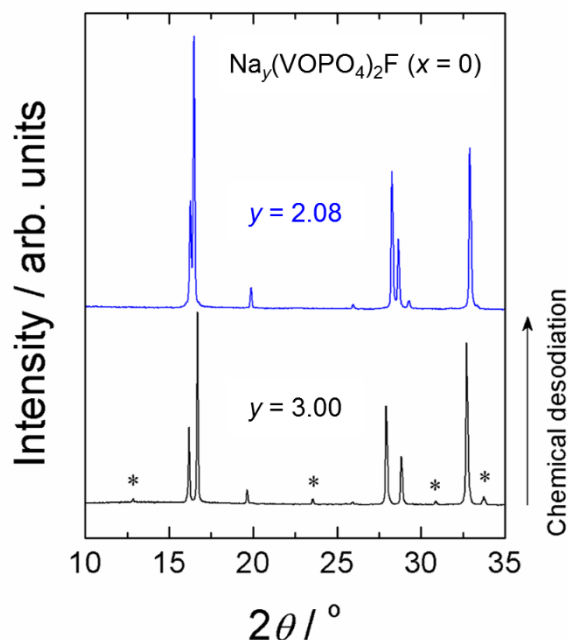


Figure 3-15. XRD patterns of $\text{Na}_y(\text{VOPO}_4)_2\text{F}$ powders for $y = 3.00$ and 2.08 .

Using the Rietveld refinement, I found that the former has a space group of $P4_2/mnm$ (No. 136), and the latter has a higher symmetry of $I4/mmm$ (No. 139). The reflections denoted by asterisks in the bottom spectrum are allowed only for $P4_2/mnm$; these superstructure peaks are forbidden for a higher symmetry of $I4/mmm$ (see the top spectrum). Used with permission from [Y.-U. Park *et. al.*, *Adv. Funct. Mater.*, **24**, 4603-4614 (2014); DOI: 10.1002/adfm.201400561]. Copyright 2014 Wiley.

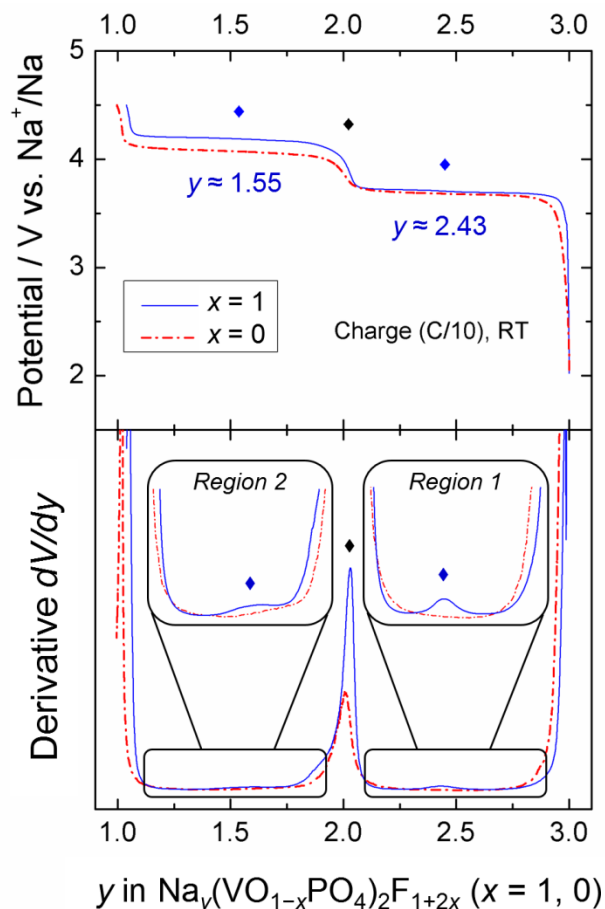


Figure 3-16. Derivative dV/dy analysis of the $\text{Na}_y(\text{VO}_{1-x}\text{PO}_4)_2\text{F}_{1+2x}$ electrodes for $x = 0$ (red) and $x = 1$ (blue). The top and bottom graphs show galvanostatic charge profiles and the corresponding derivative dV/dy curves, respectively. Black and blue diamonds denote the main ($y \approx 2.0$) and minor ($y \approx 2.43$ and 1.55) voltage steps, respectively. Regions 1 and 2 represent lower and higher voltage regions, respectively. Used with permission from [Y.-U. Park *et. al.*, *Adv. Funct. Mater.*, **24**, 4603-4614 (2014); DOI: 10.1002/adfm.201400561]. Copyright 2014 Wiley.

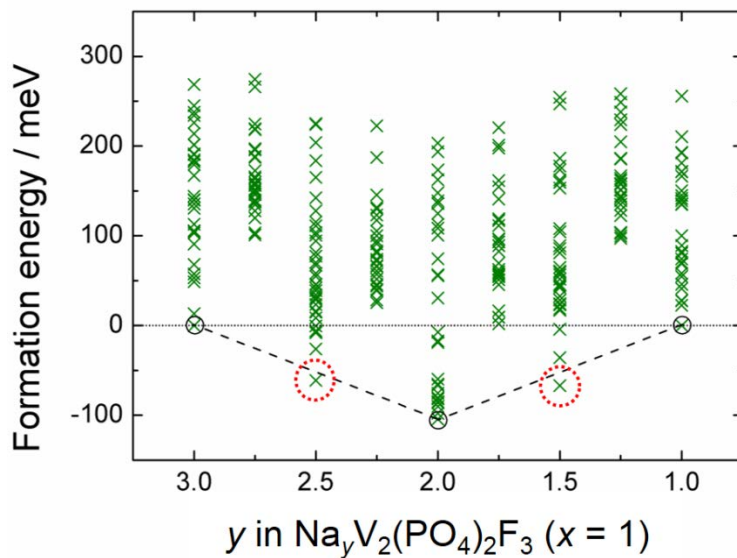


Figure 3-17. Formation energy curve of $\text{Na}_y\text{V}_2(\text{PO}_4)_2\text{F}_3$ ($x = 1$) from first-principles calculations. Used with permission from [Y.-U. Park *et. al.*, *Adv. Funct. Mater.*, **24**, 4603-4614 (2014); DOI: 10.1002/adfm.201400561]. Copyright 2014 Wiley.

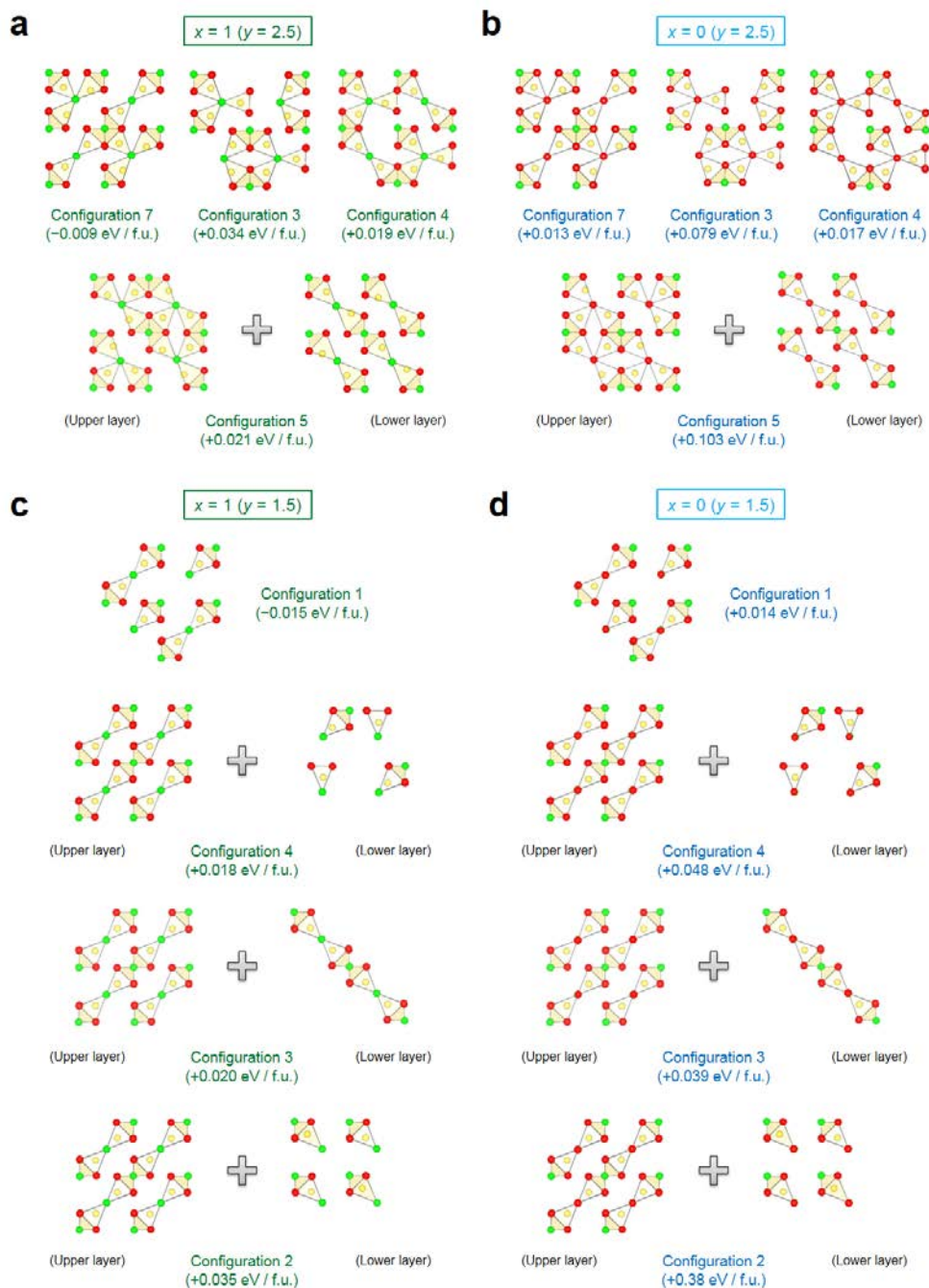


Figure 3-18. Calculated formation energies of some Na configurations for the

$\text{Na}_y(\text{VO}_{1-x}\text{PO}_4)_2\text{F}_{1+2x}$ system.

(a,b) Calculated formation energies of some Na configurations of two Na layers for (a) $x = 1$ (left) and (b) $x = 0$ (right) at the compositions of $y = 2.5$ for the $\text{Na}_y(\text{VO}_{1-x}\text{PO}_4)_2\text{F}_{1+2x}$ ($x = 1$ and 0) system. Only one Na layer is shown for each configuration, except for the case of the two Na layers having different Na configurations. The energies show the difference between the tie line (*i.e.*, a line between the lowest formation energies at $y = 3.0$ and 2.0) and the energy of each configuration.

(c,d) Calculated formation energies of some Na configurations of two Na layers for (c) $x = 1$ (left) and (d) $x = 0$ (right) at $y = 1.5$ in the $\text{Na}_y(\text{VO}_{1-x}\text{PO}_4)_2\text{F}_{1+2x}$ ($x = 1$ and 0) system. Only one Na layer is shown for each configuration, except for the case of the two Na layers having different Na configurations. The energies show the difference between the tie line (*i.e.*, a line between the lowest formation energies at $y = 2.0$ and 1.0) and the energy of each configuration.

(*) Used with permission from [Y.-U. Park *et. al.*, *Adv. Funct. Mater.*, **24**, 4603-4614 (2014); DOI: 10.1002/adfm.201400561]. Copyright 2014 Wiley.

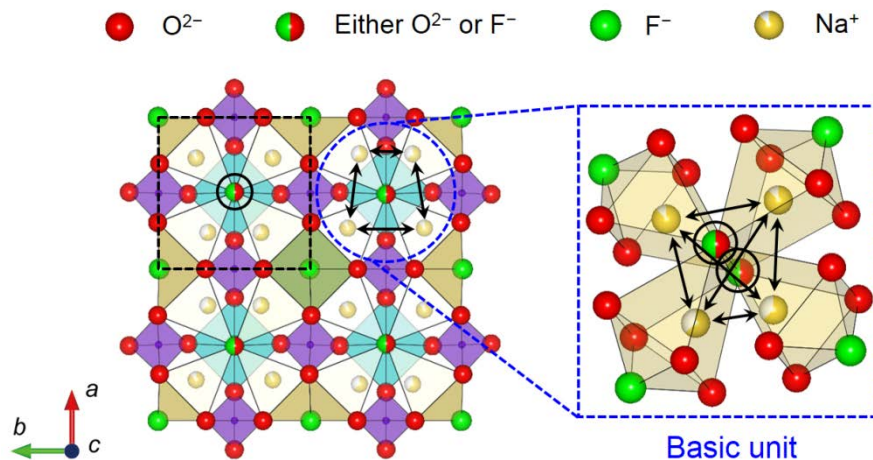


Figure 3-19. Intra-unit $\text{Na}^+ - \text{Na}^+$ repulsion in Na layer of $\text{Na}_3(\text{VO}_{1-x}\text{PO}_4)_2\text{F}_{1+2x}$ ($0 \leq x \leq 1$). The unit refers to a basic unit (denoted by a dashed box). Anions that lie at the center of the basic unit (denoted by black circles) are purely O^{2-} and F^- for $x = 0$ and 1, respectively. For other x , both O^{2-} and F^- ions can be found in the site with a certain probability depending on x . The right panel shows a slightly tilted representation of the shielding of the $\text{Na}^+ - \text{Na}^+$ repulsion by central O^{2-} or F^- ions in a basic unit. Used with permission from [Y.-U. Park *et. al.*, *Adv. Funct. Mater.*, **24**, 4603-4614 (2014); DOI: 10.1002/adfm.201400561]. Copyright 2014 Wiley.

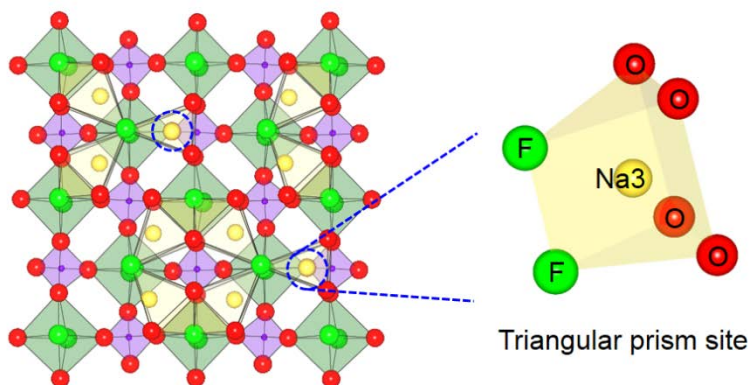


Figure 3-20. Na-vacancy configuration on the Na layer of $\text{Na}_y(\text{VO}_{1-x}\text{PO}_4)_2\text{F}_{1+2x}$ ($x = 1$; $y = 2.5$). The right panel shows the local environment for the Na3 site (denoted by circles); one Na^+ ion is surrounded by four O^{2-} and two F^- ions, forming a triangular prism site. Used with permission from [Y.-U. Park *et. al.*, *Adv. Funct. Mater.*, **24**, 4603-4614 (2014); DOI: 10.1002/adfm.201400561]. Copyright 2014 Wiley.

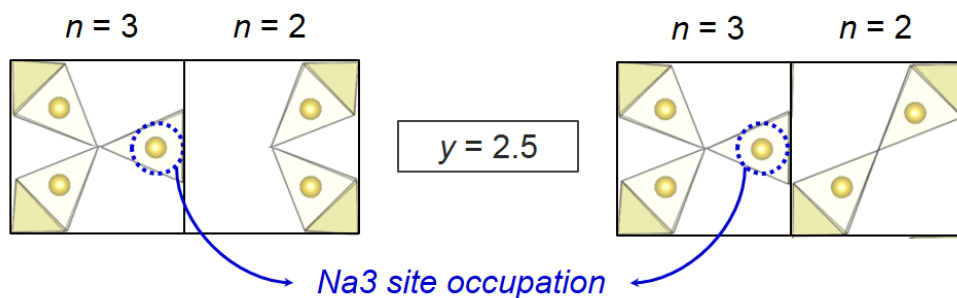


Figure 3-21. Two possible unit–unit Na configurations by Na3 site occupation at $y = 2.5$. Used with permission from [Y.-U. Park *et. al.*, *Adv. Funct. Mater.*, **24**, 4603-4614 (2014); DOI: 10.1002/adfm.201400561]. Copyright 2014 Wiley.

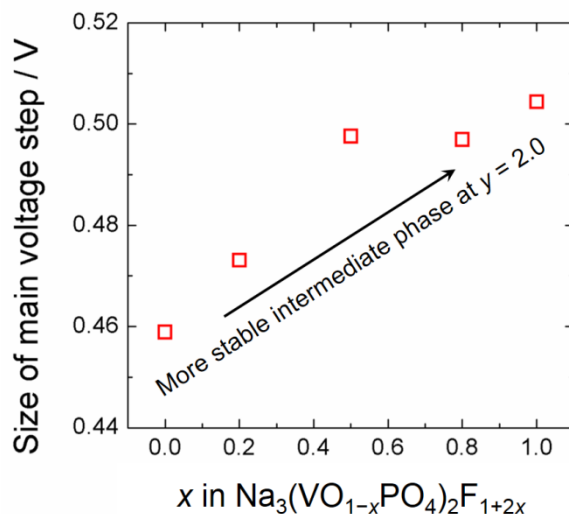
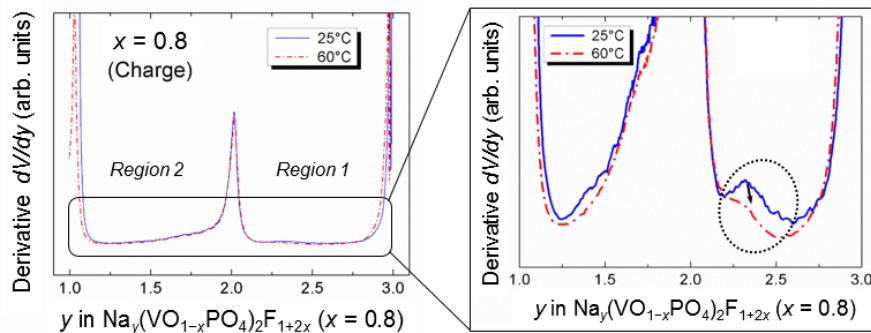


Figure 3-22. Size variation of the main voltage step at $y \approx 2.0$ for the $\text{Na}_y(\text{VO}_{1-x}\text{PO}_4)_2\text{F}_{1+2x}$ ($0 \leq x \leq 1$) electrodes with increasing fluorine content (x). The sizes of the main voltage steps at $y \approx 2.0$ were calculated by subtracting the average voltages of the higher voltage region from those of the lower voltage region for the $\text{Na}_y(\text{VO}_{1-x}\text{PO}_4)_2\text{F}_{1+2x}$ ($x = 0.0, 0.2, 0.5, 0.8$, and 1.0) electrodes. Used with permission from [Y.-U. Park *et. al.*, *Adv. Funct. Mater.*, **24**, 4603-4614 (2014); DOI: 10.1002/adfm.201400561]. Copyright 2014 Wiley.

a



b

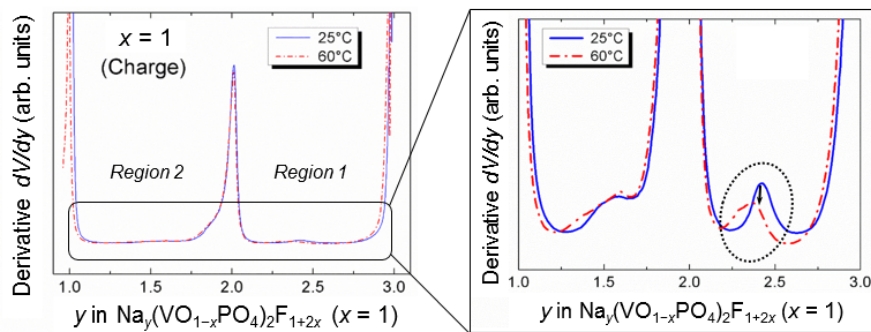


Figure 3-23. Derivative dV/dy curves for the first charge cycle of the $\text{Na}_y(\text{VO}_{1-x}\text{PO}_4)_2\text{F}_{1+2x}$ electrodes at 25°C and 60°C.

(a) $x = 0.8$ and (b) $x = 1$.

(*) Used with permission from [Y.-U. Park *et. al.*, *Adv. Funct. Mater.*, **24**, 4603-4614 (2014); DOI: 10.1002/adfm.201400561]. Copyright 2014 Wiley.

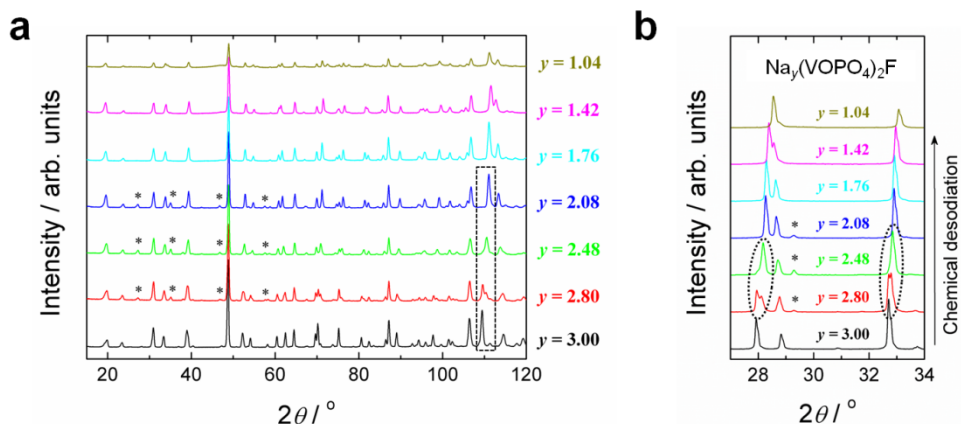


Figure 3-24. ND and XRD patterns of $\text{Na}_y(\text{VOPO}_4)_2\text{F}$ ($x = 0$; $1.0 \leq y \leq 3.0$) powders. Asterisks denote reflections of NaNO_3 , which was produced during the chemical desodiation process in acetonitrile (CH_3CN) using NO_2BF_4 as the oxidant.

(a) ND and (b) XRD patterns.

(*) Used with permission from [Y.-U. Park *et. al.*, *Adv. Funct. Mater.*, **24**, 4603-4614 (2014); DOI: 10.1002/adfm.201400561]. Copyright 2014 Wiley.

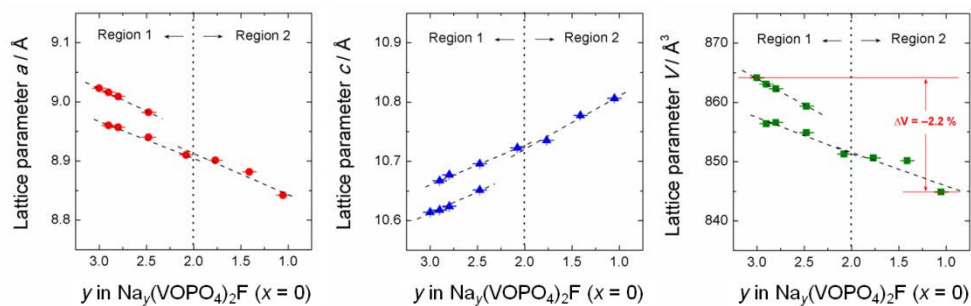


Figure 3-25. Lattice parameter changes with decreasing Na content (y) in $\text{Na}_y(\text{VOPO}_4)_2\text{F}$ ($x = 0$). Used with permission from [Y.-U. Park *et. al.*, *Adv. Funct. Mater.*, **24**, 4603-4614 (2014); DOI: 10.1002/adfm.201400561]. Copyright 2014 Wiley.

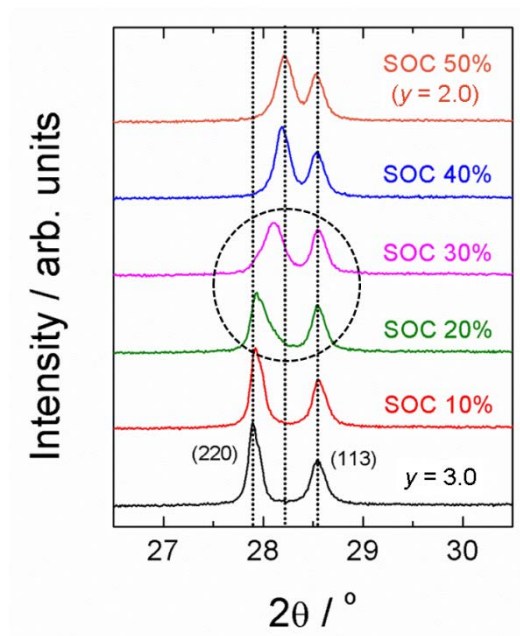


Figure 3-26. *Ex-situ* XRD patterns of the $\text{Na}_y\text{V}_2(\text{PO}_4)_2\text{F}_3$ ($x = 1$) electrode for the region of $2.0 \leq y \leq 3.0$. Used with permission from [Y.-U. Park *et. al.*, *Adv. Funct. Mater.*, **24**, 4603-4614 (2014); DOI: 10.1002/adfm.201400561]. Copyright 2014 Wiley.

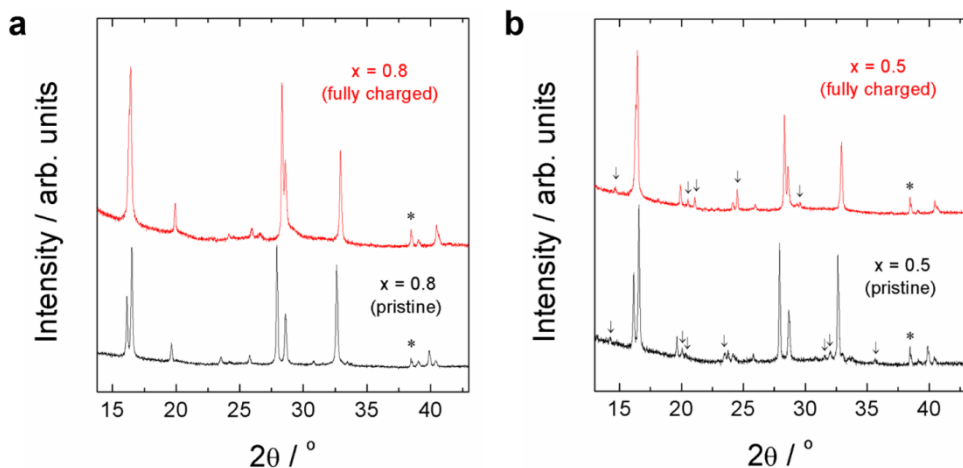


Figure 3-27. XRD patterns of fully charged states of the $\text{Na}_y(\text{VO}_{1-x}\text{PO}_4)_2\text{F}_{1+2x}$ electrodes ($x = 0.8$ and 0.5). (a) XRD patterns of the pristine state ($y = 3.0$, bottom) and the fully charged state ($y \approx 1.0$, top) of the $\text{Na}_y(\text{VO}_{0.2}\text{PO}_4)_2\text{F}_{2.6}$ ($x = 0.8$) electrode. The lattice parameters were $a = 9.0320(2) \text{ \AA}$, $c = 10.7220(3) \text{ \AA}$, $V = 874.66(4) \text{ \AA}^3$ ($x = 3.0$), and $a = 8.9133(6) \text{ \AA}$, $c = 10.7765(9) \text{ \AA}$, $V = 856.1(1) \text{ \AA}^3$ ($x \approx 1.0$); the volume change upon charge was -2.12% . (b) XRD patterns of the pristine state ($y = 3.0$, bottom) and the fully charged state ($y \approx 1.0$, top) of the $\text{Na}_y(\text{VO}_{0.5}\text{PO}_4)_2\text{F}_{2.0}$ ($x = 0.5$) electrode. The lattice parameters were $a = 9.0271(3) \text{ \AA}$, $c = 10.6811(5) \text{ \AA}$, $V = 870.38(6) \text{ \AA}^3$ ($x = 3.0$), and $a = 8.9033(7) \text{ \AA}$, $c = 10.760(1) \text{ \AA}$, $V = 852.9(1) \text{ \AA}^3$ ($x \approx 1.0$); the volume change upon charge was -2.01% . The fully charged samples were obtained by charging the electrochemical cells up to 4.5 V (vs. Na^+/Na) at a $C/10$ rate. Asterisks denote reflections from the aluminum foil of the electrode. Arrows denote reflections from an impurity phase of $\text{Na}_y\text{V}_2(\text{PO}_4)_3$ ($1 \leq y \leq 3$). Used with permission from [Y.-U. Park *et. al.*, *Adv. Funct. Mater.*, **24**, 4603-4614 (2014); DOI: 10.1002/adfm.201400561]. Copyright 2014 Wiley.

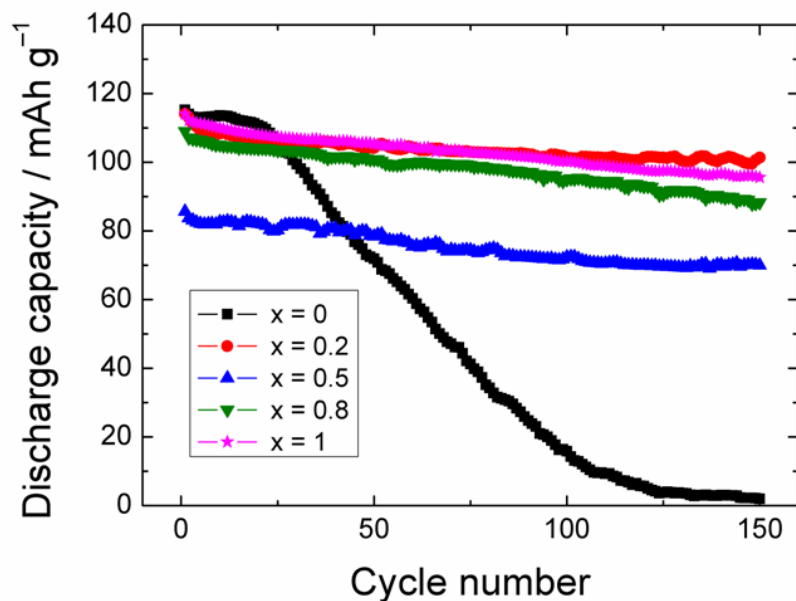


Figure 3-28. Variation in discharge capacity of the $\text{Na}_3(\text{VO}_{1-x}\text{PO}_4)_2\text{F}_{1+2x}$ ($x = 0.0, 0.2, 0.5, 0.8$, and 1.0) electrodes for 150 cycles. The electrochemical cells were cycled at a 1C rate with a voltage window of 2.0–4.5 V using the electrolyte of 1 M NaBF_4 in a mixture of EC and PC (1:1 v/v) at room temperature. Used with permission from [Y.-U. Park *et. al.*, *Adv. Funct. Mater.*, **24**, 4603-4614 (2014); DOI: 10.1002/adfm.201400561]. Copyright 2014 Wiley.

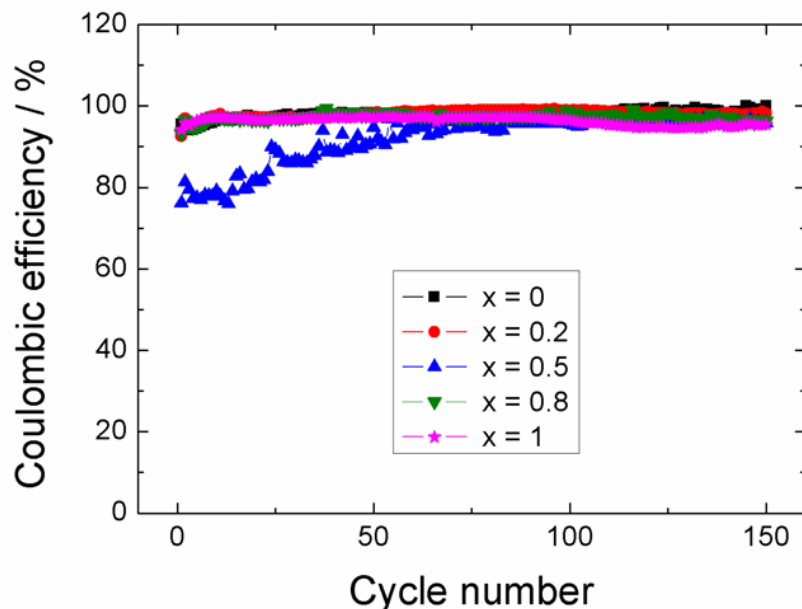


Figure 3-29. Variation in Coulombic efficiency of the $\text{Na}_3(\text{VO}_{1-x}\text{PO}_4)_2\text{F}_{1+2x}$ ($x = 0.0, 0.2, 0.5, 0.8,$ and 1.0) electrodes for 150 cycles. The electrochemical cells were cycled at a 1C rate with a voltage window of 2.0–4.5 V using the electrolyte of 1 M NaBF_4 in a mixture of EC and PC (1:1 v/v) at room temperature. Used with permission from [Y.-U. Park *et. al.*, *Adv. Funct. Mater.*, **24**, 4603-4614 (2014); DOI: 10.1002/adfm.201400561]. Copyright 2014 Wiley.

3.3.3. Possibility of Multi-Electron Transfer in $\text{Na}_y(\text{VO}_{1-x}\text{PO}_4)_2\text{F}_{1+2x}$ System.

A unique feature of $\text{Na}_y(\text{VO}_{1-x}\text{PO}_4)_2\text{F}_{1+2x}$ ($0 \leq x \leq 1$) is that its fluorine content can be tuned to utilize the multi-electron transfer of the vanadium redox reaction. **Figure 3-30** shows the voltage–composition curves of the $\text{Na}_y(\text{VO}_{1-x}\text{PO}_4)_2\text{F}_{1+2x}$ ($x = 0.0, 0.5, \text{ and } 1.0$) electrodes determined from first-principles calculations. The $\text{Na}_y(\text{VO}_{1-x}\text{PO}_4)_2\text{F}_{1+2x}$ series exhibited a similar profile as two Na^+ ions were extracted from the structure, but showed distinct behavior during the third Na^+ ion extraction. Interestingly, the size of the voltage step at $y = 1.0$ was much larger than that at $y = 2.0$ for all x . This is attributable to two main factors: the redox couple shift ($\text{V}^{3+}/\text{V}^{4+} \rightarrow \text{V}^{4+}/\text{V}^{5+}$ for $x = 0.5$ and 1.0 ; $\text{V}^{4+}/\text{V}^{5+} \rightarrow \text{V}^{5+}/\text{V}^{6+}$ for $x = 0$) and the presence of the stable intermediate phase at $y = 1.0$. For $x = 0$ (black line), it is noteworthy that the potential of the highest voltage plateau ($y \leq 1.0$) related to the $\text{V}^{5+}/\text{V}^{6+}$ redox couple is unusually high (*i.e.*, far above 5 V vs. Na^+/Na), which is due to the fact that vanadium ions are hard to be oxidized to the V^{6+} state. For samples with $x = 0$ or $x = 1$, both of these factors clearly increased the potential during extraction of the third Na^+ ion. However, for samples with mixed $\text{V}^{3+}/\text{V}^{4+}$ ions, an abrupt shift of the redox couple did not occur at $y = 1.0$. The mixed V^{3+} and V^{4+} ions continuously shifted the redox couple as y increased, as discussed before. This implies that the stability of the intermediate phase at $y = 1.0$ is solely responsible for the increased potential during the third Na^+ ion extraction in those cases. As a consequence, the predicted voltage for the third Na^+ ion extraction was notably lower at $x = 0.5$. Nevertheless, the potential for extracting the final, third Na^+ ion at $x = 0.5$ was greater than 4.5 V vs. Na^+/Na (denoted by a horizontal orange line in **Figure 3-30**), which is the onset potential for the decomposition of most Na electrolytes. Thus, reducing the voltage step at $y = 1.0$ or making the step

gentler so that some portion of the plateau remains below 4.5 V is expected to be important for utilizing the multi-electron transfer.

Interestingly, only the $\text{Na}_3(\text{V}^{3.8+}\text{O}_{0.8}\text{PO}_4)_2\text{F}_{1.4}$ ($x = 0.2$) sample showed the multi-electron transfer in the $\text{Na}_3(\text{VO}_{1-x}\text{PO}_4)_2\text{F}_{1+2x}$ ($0 \leq x \leq 1$) system (see **Figure 3-10**), which is attributable to two factors. First, the sample with $x = 0.2$ exhibited weaker $\text{Na}^+ - \text{Na}^+$ repulsion compared to the samples with $x = 0.8$ and 1.0. This is further evident by the much smaller voltage step at $y \approx 2.0$ (see **Figure 3-22**). Therefore, the former is expected to have a much wider solid-solution region near the voltage steps, allowing additional Na^+ ions to be extracted below 4.5 V (vs. Na^+/Na). This implies that the samples with intermediate fluorine contents (such as $x = 0.2$, 0.5, and 0.8) are more beneficial for multi-electron transfer. Second, the slightly different redox potentials of the two redox couples, $\text{V}^{3+}/\text{V}^{4+}$ and $\text{V}^{4+}/\text{V}^{5+}$, in mixed local environments can cause disorder in the operating voltage, which may make the voltage step at $y = 1.0$ gentler.

It is also possible to obtain a wider solid-solution region by substituting dopants in the Na layer to relieve the strong $\text{Na}^+ - \text{Na}^+$ repulsion. In fact, in my previous report, the $\text{Li}_{1.1}\text{Na}_{0.4}\text{VPO}_{4.8}\text{F}_{0.7}$ ($x = 0.2$) electrode showed a negligible voltage step due to the much lower $\text{Li}^+ - \text{Li}^+$ repulsion, and thereby showed multi-electron transfer.³⁴ For NIB applications, the replacement of Na^+ ions by a small amount of other cations, such as H^+ , Li^+ , K^+ , and Mg^{2+} ions, can be attempted. Furthermore, the substitution of other redox couples, such as Fe^{3+} , Ti^{3+} , and Cr^{3+} ions, may cause disorder and achieve multi-electron transfer.

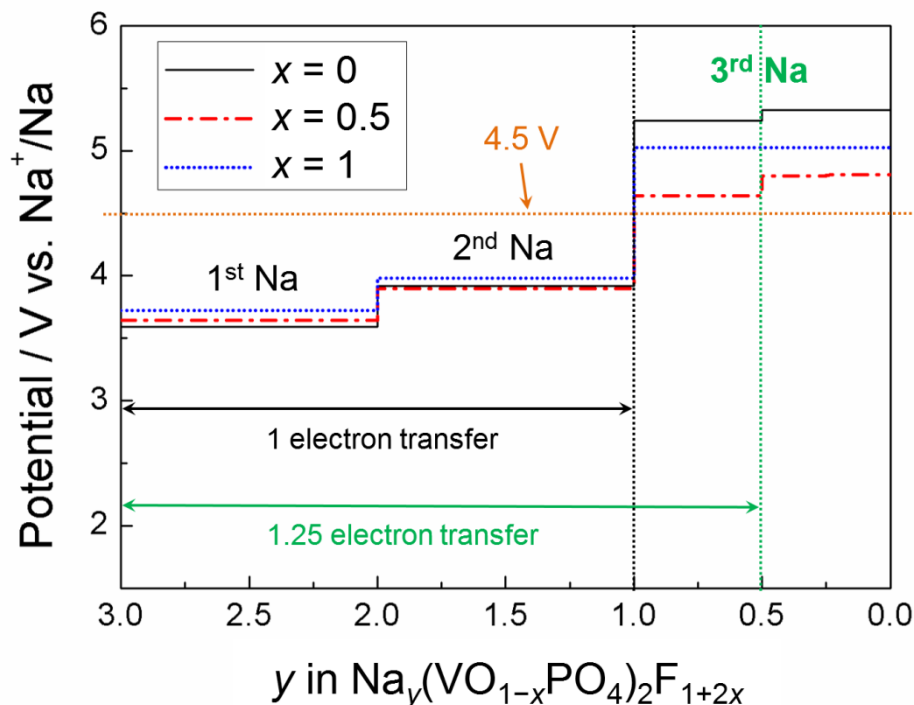


Figure 3-30. Voltage–composition curves for the $\text{Na}_y(\text{VO}_{1-x}\text{PO}_4)_2\text{F}_{1+2x}$ ($0 \leq x \leq 1$; $0 \leq y \leq 3$) electrodes from first-principles calculations. $x = 0$ (black), $x = 0.5$ (red), and $x = 1$ (blue). Vertical black and green lines denote one- and multi-electron transfer reactions, respectively. The horizontal orange line denotes 4.5 V (vs. Na^+/Na), above which the electrolyte starts to decompose. Used with permission from [Y.-U. Park *et. al.*, *Adv. Funct. Mater.*, **24**, 4603–4614 (2014); DOI: 10.1002/adfm.201400561]. Copyright 2014 Wiley.

3.4. Summary

In this chapter, I successfully synthesized, for the first time, a series of the isostructural $\text{Na}_3(\text{VO}_{1-x}\text{PO}_4)_2\text{F}_{1+2x}$ ($0 \leq x \leq 1$) compounds, in which the oxidation state of vanadium was altered by changing the fluorine content (x). The detailed electrochemical mechanisms of the $\text{Na}_y(\text{VO}_{1-x}\text{PO}_4)_2\text{F}_{1+2x}$ ($0 \leq x \leq 1$) electrodes were determined *via* a comparative study using a combined theoretical and experimental approach. The combination of different redox couples of $\text{V}^{3+}/\text{V}^{4+}$ or $\text{V}^{4+}/\text{V}^{5+}$, $\text{Na}^+ - \text{Na}^+$ ordering, and F/O distribution resulted in distinct voltage–composition curves and Na de/insertion mechanisms for the isostructural $\text{Na}_y(\text{VO}_{1-x}\text{PO}_4)_2\text{F}_{1+2x}$ family. I also found that all compositions in this system exhibited excellent electrochemical performance, attributable to the exceptionally small volume change upon cycling ($\sim 2\%$). The $\text{Na}_y(\text{VO}_{1-x}\text{PO}_4)_2\text{F}_{1+2x}$ electrodes also have one of the highest energy densities ($\sim 520 \text{ Wh kg}^{-1}$) among NIB cathodes with ultrahigh stability, which allows them to be categorized as a promising cathode group. I believe that the thorough understanding of this system will pave the way for the design of high-performance electrode materials for NIBs.

Chapter 4. Tailoring a Fluorophosphate as a 4 V Cathode for Li-Ion Batteries

(The essence of this chapter has been published in *Scientific Reports*. Reprinted from [Y.-U. Park *et. al.*, *Sci. Rep.*, **2**, 704 (2012); DOI: 10.1038/srep00704]. Because this paper has been distributed under a Creative Commons license (Attribution-Noncommercial 2.5), one may reuse the content of the paper for non-commercial/educational purposes without obtaining additional permission from Nature Publishing Group, providing that the author and the original source of publication are fully acknowledged.)

4.1. Introduction

Lithium-ion battery (LIB) is today's one of the most important energy storage systems especially in the portable electronics market. Moreover, it is about to broaden its territory toward electric vehicles (EVs) and plug-in hybrid electric vehicles (PHEVs).^{84,85} For large-scale applications, the problems of conventional cathode materials (e.g., high cost, severe environmental impact, poor safety, etc.) are one of the biggest obstacles. Recently, to say nothing of olivine phosphates,^{86,87} other polyanion-based compounds such as fluorophosphates,^{19,27,88-92} fluorosulfates,^{51,93} silicates,^{94,95} and pyrophosphates⁹⁶ have been vigorously studied as candidates for the next generation of positive electrodes. The electrochemical properties of these materials can be significantly changed by the type of polyanions and by how they are structured as building blocks. Various kinds of crystal structures with one-, two-, or three-dimensional diffusional pathways and tunable redox potentials originating from the different inductive effects of polyanions could provide the flexibility in developing novel cathode materials.^{19,27,51,86-98}

According to recent studies on the polyanion-based cathode materials,^{19,27,51,86-100} earlier works regarding sodium super ionic conductors (NASICONs) showed that the open framework of NASICONs was very advantageous for the fast diffusion of Na^+ and Li^+ ions; they performed well as an electrode material and even as a solid-state electrolyte.^{86,97,101-103} Even though its ionic conduction is fast, the heavy framework of typical NASICON-type materials results in a significantly lower energy density, making them practically less attractive as an electrode. The multivalent transition metals are expected to counterbalance this disadvantage, because they can allow more than one electron transfer upon lithiation and delithiation, leading to a higher energy density. Nazar group has attempted to use multivalent redox couples such as $\text{V}^{3+}/\text{V}^{5+}$ in NASICON framework or other structures, where the additional capacity from $\text{V}^{4+}/\text{V}^{5+}$ was only partially accessible even at slow current rates.^{90,98,99,104}

In this chapter, I focused on a vanadium-containing fluorophosphate compound with both a fast ion conducting framework and a multivalent transition metal (i.e., vanadium). Although its electrochemical performance is known to be poor,²⁷ sodium vanadium fluorophosphate, $\text{Na}_{1.5}\text{VPO}_5\text{F}_{0.5}$, was chosen as a starting material due to its fundamental advantages: (i) excess amount of mobile ions per transition metal (1.5 Na^+ ions for 1 vanadium ion), (ii) a multivalent vanadium ion (i.e., from V^{+3} to V^{+5}),¹⁰⁵ (iii) a fast ion conducting framework, (iv) high operating voltage (~ 3.8 V vs. Na^+/Na) originating from the large inductive effect of the $[\text{PO}_4\text{F}]^{4-}$ group, and (v) facile preparation of a Li-containing compound (*via* the ion-exchange reaction) which can be used as a cathode for Li-ion batteries. However, it was impossible to use more than one electron from the multivalent vanadium ion unless the initial oxidation state of vanadium in this material was +4.

In other words, although this material contains more than one Na^+ ion per transition metal, only one electron can participate in the electrochemical reaction *via* the $\text{V}^{4+}/\text{V}^{5+}$ redox couple, resulting in a low capacity ($\sim 130 \text{ mAh g}^{-1}$). If one further continues to use the vanadium redox reaction below +4, the structure can accommodate more Na^+ ions. Although this can increase the capacity a little bit, the operating voltage for this region should be too low to be used as a cathode. For this reason, this strategy was considered to be practically unacceptable. Instead, I attempted to change the atomic ratio of oxygen to fluorine in $\text{Na}_{1.5}\text{VPO}_5\text{F}_{0.5}$, maintaining the original crystal structure. Because the oxidation states of oxygen and fluorine ions are different (O^{2-} and F^- , respectively), the initial valence of the vanadium ion will vary with the O/F ratio in the material. Furthermore, if the polyanion group contains more F^- ions, the lower $\text{V}^{3+}/\text{V}^{4+}$ redox potential will be compensated with a higher inductive effect of fluorine, allowing a reasonably high average voltage. In this chapter, I will show that a novel lithium compound prepared *via chimie douce* ion-exchange reaction is a promising 4-V class cathode with a multivalent $\text{V}^{3+}/\text{V}^{5+}$ redox couple.

4.2. Experimental and Computational Details

4.2.1. Materials synthesis. A stoichiometric amount of V_2O_5 (Sigma-Aldrich, 99%) and $\text{NH}_4\text{H}_2\text{PO}_4$ (Sigma-Aldrich, 99%) was blended by high-energy ball-milling (HEBM) at 300 rpm over 24 hours. The mixture was then pelletized and heat-treated at 750°C for 4 hours in air to provide yellowish VOPO_4 (or V^{5+}PO_5) powder. A stoichiometric mixture of V_2O_5 and $\text{NH}_4\text{H}_2\text{PO}_4$, including 20 mol% Super P, was blended by HEBM at 300 rpm over 24 hours. Black VPO_4 powder was obtained by

pelletizing and heat-treating the mixture at 850°C for 2 hours under Ar atmosphere. The precursor combination used to synthesize $\text{Na}_{1.5}\text{VPO}_{5-\delta}\text{F}_{0.5+\delta}$ samples ($\delta = 0, 0.2$, and 1) was “ $(1-\delta)\text{V}^{5+}\text{PO}_5 + \delta\text{V}^{3+}\text{PO}_4 + (0.5+\delta)\text{NaF}$ (Sigma-Aldrich, 99%) + $[(1-\delta)/2]\text{Na}_2\text{CO}_3$ (Sigma-Aldrich, 99%)”. Blending was done by HEBM at 300 rpm for 24 hours; the resulting mixtures ($\delta = 0, 0.2$, and 1) were pelletized and sintered at 750°C for 1.5 hours under Ar flow to finally provide cyan $\text{Na}_{1.5}\text{VPO}_{5}\text{F}_{0.5}$, greenish $\text{Na}_{1.5}\text{VPO}_{4.8}\text{F}_{0.7}$, and black $\text{Na}_{1.5}\text{VPO}_{4}\text{F}_{1.5}$ powders.¹⁷ To prepare the isostructural lithium derivative of $\text{Na}_{1.5}\text{VPO}_{4.8}\text{F}_{0.7}$, I performed Na^+/Li^+ ion exchange in 1-hexanol (Sigma-Aldrich, 99%) at its boiling point (~160°C) under reflux. LiBr (Sigma-Aldrich, 99%) was used as the lithium source. An excess amount (10 times) of LiBr was added prior to the reaction, and the volume of the solvent (i.e., 1-hexanol) was adjusted to make a 5 M LiBr solution. After reacting for 5–17 hours, the product was rinsed, centrifuged several times, and then thoroughly dried to provide green-colored $\text{Li}_{1.1}\text{Na}_{0.4}\text{VPO}_{4.8}\text{F}_{0.7}$ powder. To prepare the fully delithiated version of the $\text{Li}_{1.1}\text{Na}_{0.4}\text{VPO}_{4.8}\text{F}_{0.7}$ powder, it was oxidized with stoichiometric amounts of NO_2BF_4 in acetonitrile solvent at 60°C. After reaction for 10 hours, the product was washed, centrifuged several times with the same solvent, and then completely dried in a vacuum oven at 70°C overnight, resulting in a yellowish $\text{Na}_{0.4}\text{VPO}_{4.8}\text{F}_{0.7}$ powder.

4.2.2. Electron microscopy and elemental analysis. Transmission electron microscopy (TEM) images were acquired using a Tecnai F20 (FEI, USA) at an accelerating voltage of 200 kV. Scanning electron microscopy (SEM) images were obtained using a SUPRA 55VP FE-SEM (Carl Zeiss, Germany) at an operating voltage of 2 kV. Compositional analysis was carried out simultaneously with SEM examination by using energy-dispersive X-ray spectroscopy (EDS) (X-Flash

spectrometer; Bruker, Germany) with a specified energy resolution of 127 eV at an operating voltage of 15 kV. For TEM observation, an EDAX/EDS system was used. All EDS measurements were repeated several times in different regions, and the observed values were averaged. The atomic ratios of lithium, sodium, vanadium, and phosphorus were more precisely determined by inductively coupled plasma (ICP) spectroscopy (Polyscan 60E; Thermo Jarrell Ash, USA). The carbon content of carbon-coated $\text{Li}_{1.1}\text{Na}_{0.4}\text{VPO}_{4.8}\text{F}_{0.7}$ was measured with a carbon-sulfur determinator (CS-800; ELTRA, Germany).

4.2.3. X-ray photoelectron spectroscopy (XPS). XPS spectra were obtained by electron spectroscopy for chemical analysis (ESCA) (Sigma Probe; Thermo VG Scientific, UK) with a pass energy of 30 eV and a step size of 0.1 eV. Binding energies were referenced to the C1s peak at 284.6 eV.

4.2.4. Diffraction. ND data were collected over a 2θ range of 0–180° with a step size of 0.05° and a wavelength of $\lambda = 1.83429 \text{ \AA}$ supplied by a Ge(331) single-crystal monochromator on a high-resolution powder diffractometer (HRPD) at the Hanaro facility of the Korea Atomic Energy Research Institute. XRD was carried out using an X-ray diffractometer (D8 Advance; Bruker, Germany) using Ni-filtered Cu-K α radiation ($\lambda = 1.5406 \text{ \AA}$) in the 2θ range of 10–80°. The room-temperature ND/XRD data were refined using the Rietveld method and Fullprof software.³⁵ Temperature-controlled XRD measurements were carried out under vacuum using an X-ray diffractometer (D/MAX-2500 diffractometer; Rigaku, Japan) with Cu-K θ radiation ($\lambda = 1.5406 \text{ \AA}$) and step scanning (0.01° s⁻¹) in the 2θ range of 10–60° with a scan speed of 2° min⁻¹. The heating rate was 5°C min⁻¹. Each measurement was taken after stabilizing at the desired temperature for ca. 3 min. Synchrotron powder XRD data were acquired at room temperature at the

beam line of BL02B2 in SPring-8 (Japan) with an average wavelength of ca. 0.9988 Å calibrated using the NIST silicon fine powder (SRM640d).

4.2.5. NMR and EPR spectroscopy. Solid-state ^6Li and ^{23}Na magic angle spinning (MAS) nuclear magnetic resonance (NMR) experiments were performed using a Bruker Avance 400 MHz 9.4 T Wide Bore spectrometer at Larmor frequencies of 58.9 and 105.8 MHz, respectively; all experiments were performed with a Bruker 4-mm probe at a MAS frequency of 15 kHz at room temperature. For the ^{23}Na MAS NMR measurements, all spectra were obtained using a 90° pulse of 1 μs and a recycle delay of 0.5 s. The ^6Li MAS NMR spectra were collected using a 90° pulse of 2 μs and a recycle delay of 1 s. The ^{23}Na and ^6Li NMR shifts were referenced to 0.1 M NaCl (0 ppm) and 1 M LiCl (0 ppm), respectively. EPR spectra were recorded using a JES-TE200 electron spin resonance spectrometer (JEOL, Japan) at room temperature with 4-mm quartz tubes. The magnetic field was varied from 2000 to 5000 G at a resonance frequency of 9.447 GHz.

4.2.6. Electrochemistry. To prepare the carbon-coated $\text{Li}_{1.1}\text{Na}_{0.4}\text{VPO}_{4.8}\text{F}_{0.7}$, the ion-exchanged $\text{Li}_{1.1}\text{Na}_{0.4}\text{VPO}_{4.8}\text{F}_{0.7}$ powders were mixed with carbon black *via* dry ball-milling with a ratio of 80 to 20 wt%. Then, the mixture was annealed at 450°C for 12 hours under an argon atmosphere to remove the residual solvent and enhance its crystallinity. For the electrochemical test, a slurry of 88 wt% carbon-coated $\text{Li}_{1.1}\text{Na}_{0.4}\text{VPO}_{4.8}\text{F}_{0.7}$ (70.4 wt% total active material), 2 wt% carbon black (19.6 wt% total carbon), and 10 wt% polyvinylidene fluoride (PVDF) dispersed in *N*-methyl-2-pyrrolidone (NMP) was prepared and cast on aluminium foil. The electrode was dried overnight at 70°C under vacuum. The loading of the active material on the electrode was ca. $5\text{--}6\text{ mg cm}^{-2}$. Electrochemical cells were assembled in an Ar-filled glove box into CR2016-type coin cells consisting of a counter electrode

(lithium metal), separator (Celgard 2400; Celgard, USA), and electrolyte (1 M LiPF_6 solution) in a mixture of ethyl carbonate/dimethyl carbonate (EC/DMC, 1:1 v/v). All the electrochemical tests were carried out using a WBCS 3000 potentiostat (WonAtech, Korea). For the galvanostatic intermittent titration technique (GITT) measurement, the electrochemical cells were rested for 2 hours after each hour-long charging or discharging at the C/20 rate (voltage window: 2.2–4.5 V) at 60°C. 1C corresponds to 156 mA g^{-1} . To acquire the charge curves for various C rates, the cells were cycled once at the rate of C/20 and then charged to 4.5 V at different rates. To obtain the discharge curves for various C rates, the cells were charged at the same rate of C/20 to 4.5 V and then discharged to 2.5 V at different rates. Unless otherwise noted, all cells were cycled between 2.5 and 4.5 V at room temperature.

4.2.7. Computational details. First-principles calculations were made using the Perdew–Burke–Ernzerhof exchange-correlation parameterization to density functional theory (DFT) with the spin-polarized generalized gradient approximation (GGA).³⁶ I used a plane-wave basis set and the projector-augmented wave (PAW) method as implemented in the Vienna *ab initio* simulation package (VASP).³⁷ The Hubbard parameters (GGA+U)³⁸ were added to correct the incomplete cancellation of the self-interaction of GGA. A U value of 5.0 eV (the on-site coulomb term) and J value of 1.0 eV (the exchange term) were used for the vanadium ions^{17,71} in the $\text{Na}_{1.5}\text{VPO}_5\text{F}_{0.5}$, $\text{LiNa}_{0.5}\text{VPO}_5\text{F}_{0.5}$, and $\text{Na}_{0.5}\text{VPO}_5\text{F}_{0.5}$ phases. Activation barriers for lithium and sodium diffusion in the two model systems of $\text{Na}_{1.5}\text{VPO}_5\text{F}_{0.5}$ and $\text{LiNa}_{0.5}\text{VPO}_5\text{F}_{0.5}$ were calculated using the nudged-elastic-band (NEB) method.¹⁰⁶ In those calculations, the Li^+ and Na^+ ions were allowed to move in $\text{Na}_{23/16}\text{VPO}_5\text{F}_{0.5}$ and $\text{Li}_{15/16}\text{Na}_{0.5}\text{VPO}_5\text{F}_{0.5}$. Seven replicas of the systems were

used as the starting points for the NEB method with linear interpolation between the initial and final states of the path. All lattice parameters were fixed at the $\text{Na}_{1.5}\text{VPO}_5\text{F}_{0.5}$ and $\text{LiNa}_{0.5}\text{VPO}_5\text{F}_{0.5}$ states, but all the internal degrees of freedom were relaxed during the NEB calculations.

4.3. Results and Discussion

4.3.1. Fluorination of the Pristine Na Phase of $\text{Na}_{1.5}\text{VPO}_5\text{F}_{0.5}$

The crystal structure of $\text{Na}_{1.5}\text{VPO}_5\text{F}_{0.5}$ could be described as a pseudo-layered framework where the alkali-metal and transition metal layers are repeated in an alternating manner along c axis (**Figure 4-1**). The structure consists of VO_5F octahedral and PO_4 tetrahedral units, where two VO_5F octahedra are connected by a bridging fluorine ion to form a $\text{V}_2\text{O}_{10}\text{F}$ bioctahedron.²⁷ These $\text{V}_2\text{O}_{10}\text{F}$ bioctahedral units are repeatedly connected in ab plane via PO_4 tetrahedra sharing oxygen atoms to thereby make an open framework with a layer-like spacing into which Na^+ ions can be inserted.

My synthesis strategy was to obtain an appropriate stoichiometric ratio of fluorine and oxygen in $\text{Na}_{1.5}\text{VPO}_5\text{F}_{0.5}$ so that the redox range of vanadium ions could be widened below +4 at a sufficiently high voltage. Starting from $\text{Na}_{1.5}\text{VPO}_5\text{F}_{0.5}$, I tried to increase the degree of fluorination (δ) in $\text{Na}_{1.5}\text{VPO}_{5-\delta}\text{F}_{0.5+\delta}$ by raising the fraction of the V^{3+} precursor (i.e., VPO_4) with a sufficient amount of fluorine-containing precursor (i.e., NaF). I found that V^{3+} ions prefer F^- ions as the anions constituting the $\text{V}_2\text{O}_{10-x}\text{F}_{1+x}$ bioctahedron than V^{4+} ions due to the charge balance. Thus, by tuning the ratio of V^{3+} to V^{4+} precursors, I successfully controlled

δ . The best degree of fluorination was $\delta = 0.2$.

To adjust the stoichiometric ratio of F and O in the structure, I systematically changed the precursor ratio in the synthesis. In other words, I increased δ (from zero to unity) in the reaction of “ $(1 - \delta)V^{5+}PO_5 + \delta V^{3+}PO_4 + (0.5 + \delta)NaF + [(1 - \delta)/2]Na_2CO_3$ ” to obtain a series of fluorinated $Na_{1.5}VPO_{5-\delta}F_{0.5+\delta}$ having different degrees of fluorine substitution. Use of $(V^{4+}O)_2P_2O_7$ instead of $V^{5+}PO_5$ always yielded the same result (even when $\delta = 0$), but I used $V^{5+}PO_5$ because the synthesis of the $(V^{4+}O)_2P_2O_7$ requires cost-ineffective inert atmosphere. For this reason, the “ V^{4+} precursor” means $V^{5+}PO_5$ rather than $(V^{4+}O)_2P_2O_7$. The corresponding cell parameters of each sample were obtained by full pattern matching of ND patterns. **Figure 4-2a** shows that lattice parameters of a product with $\delta = 0.2$ are in between those of non-fluorinated $Na_{1.5}VPO_5F_{0.5}$ ($\delta = 0$) and fully fluorinated $Na_{1.5}VPO_4F_{1.5}$ ($\delta = 1$), suggesting a solid-solution phase.

I tried to obtain more fluorinated samples ($\delta > 0.2$ in $Na_{1.5}VPO_{5-\delta}F_{0.5+\delta}$) by using a reaction of “ $0.7V^{5+}PO_5 + 0.3V^{3+}PO_4 + 0.8NaF + 0.35Na_2CO_3$ ” but failed to get a pure target phase (**Figure 4-2b**). Even though the main phase was the target phase ($Na_{1.5}VPO_{5-\delta}F_{0.5+\delta}$, no symbol), a considerable amount of impurity phases, such as $Na_3V_2(PO_4)_3$ (blue circles), V_2O_3 (green arrows), and VO_2 (orange asterisks), were detected. This means that, due to the solubility limit, I failed to obtain a pure solid-solution phase ($\delta = 0.3$) between $Na_{1.5}V^{4+}PO_5F_{0.5}$ and $Na_{1.5}V^{3+}PO_4F_{1.5}$ (target ratio = 7:3) using the stoichiometric combination of precursors. Therefore, I determined that $\delta = 0.2$ was the maximum fluorine content that would not generate second phases. Further substitution of fluorine resulted in a substantial fraction of impurity phases.

Finally, I experimentally determined the chemical compositions of three sodium phases having different degrees of fluorination ($\delta = 0, 0.2$, and 1) using inductively coupled plasma (ICP) spectroscopy and energy-dispersive X-ray spectroscopy (EDS) analyses. The contents (in wt%) of Na, V, and P were determined *via* ICP spectroscopy while those of anions (O and F) were carefully estimated by calculating O/V and F/V ratios from the EDS quantification results (see **Figure 4-2c**). From the two complementary quantification tools, I found that the average chemical compositions of the sodium phases were not considerably different from their theoretical compositions. Thus, (i) $\text{Na}_{1.47(\pm 0.02)}\text{V}_{1.00}\text{P}_{1.00(\pm 0.01)}\text{O}_{4.96(\pm 0.07)}\text{F}_{0.52(\pm 0.05)}$ for $\delta = 0$, (ii) $\text{Na}_{1.48(\pm 0.02)}\text{V}_{1.00}\text{P}_{1.00(\pm 0.01)}\text{O}_{4.78(\pm 0.06)}\text{F}_{0.74(\pm 0.04)}$ for $\delta = 0.2$, and (iii) $\text{Na}_{1.52(\pm 0.03)}\text{V}_{1.00}\text{P}_{1.00(\pm 0.01)}\text{O}_{3.95(\pm 0.08)}\text{F}_{1.54(\pm 0.07)}$ for $\delta = 1$.

The phase-pure $\text{Na}_{1.5}\text{VPO}_{5-\delta}\text{F}_{0.5+\delta}$ was successfully obtained, and all reflections in its ND pattern were completely indexed with a space group of $P4_2/mnm$, as shown in **Figure 4-3** (see **Table 4-1** and **Table 4-2** for details on the structural refinement). Elemental analysis of the micron-sized Na phase (inset of **Figure 4-3a**) by ICP and EDS experiments allowed me to confirm the detailed composition, i.e., $\text{Na}_{1.48(\pm 0.02)}\text{V}_{1.00}\text{P}_{1.00(\pm 0.01)}\text{O}_{4.78(\pm 0.06)}\text{F}_{0.74(\pm 0.04)}$, hereafter called $\text{Na}_{1.5}\text{VPO}_{4.8}\text{F}_{0.7}$ for convenience. Both the decreased O/V ratio and the increased F/V ratio suggested partial replacement of fluorine ions (F^-) for oxygen ions (O^{2-}), which led to a less negatively charged anion group in the structure.

XPS results suggested that the fluorine ions replaced those oxygen ions that lie in the two terminal positions of the $\text{V}_2\text{O}_{10}\text{F}$ bioctahedra. XPS is an effective tool to investigate the local state of element. One can compare either the local bonding or the oxidation state of a specific element in samples with relatively good accuracy.^{107,108} Phosphorus 2p binding energies of $\text{Na}_{1.5}\text{VPO}_{5}\text{F}_{0.5}$ and

$\text{Na}_{1.5}\text{VPO}_{4.8}\text{F}_{0.7}$ were same (132.6 eV) in the XPS spectra (**Figure 4-4**), which suggests that both have identical PO_4 tetrahedral environments.¹⁰⁹ While all other oxygen ions in the $\text{V}_2\text{O}_{10}\text{F}$ bioctahedra share corners of PO_4 tetrahedra, the two terminal oxygen ions are relatively unbound in the crystal. The invariance of phosphorus 2p binding energies for the PO_4 tetrahedra implies that the substitution of fluorine for one of the oxygen ions in PO_4 is quite unlikely.

By plotting unit cell volumes of two samples having extreme degrees of fluorination ($\delta = 0$ and 1) and a new sample ($\delta = 0.2$), I found a linear relationship between δ and cell volume (**Figure 4-2a**). This suggests that the new sample is a solid-solution phase between $\text{Na}_{1.5}\text{V}^{4+}\text{PO}_5\text{F}_{0.5}$ and $\text{Na}_{1.5}\text{V}^{3+}\text{PO}_4\text{F}_{1.5}$ with a ratio of 4:1.

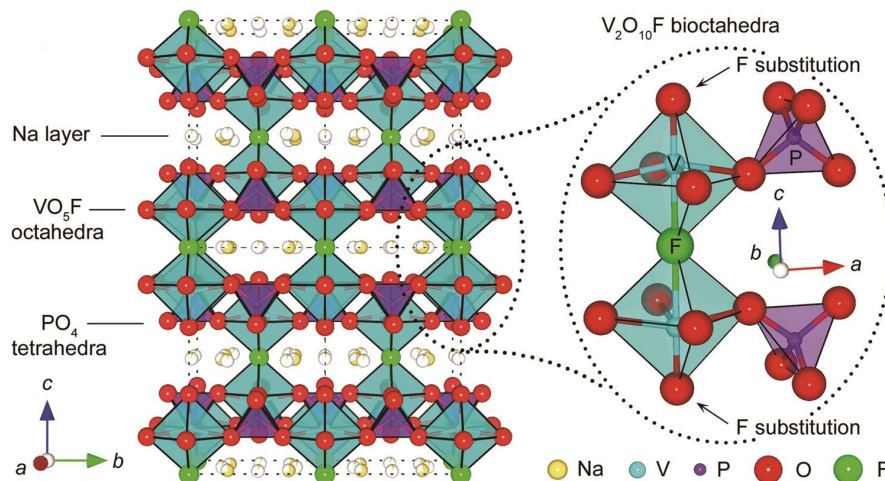


Figure 4-1. Crystal structure of the pristine Na phase ($\text{Na}_{1.5}\text{VPO}_5\text{F}_{0.5}$). The right inset shows $\text{V}_2\text{O}_{10}\text{F}$ bioctahedra with corner-sharing PO_4 tetrahedral units.

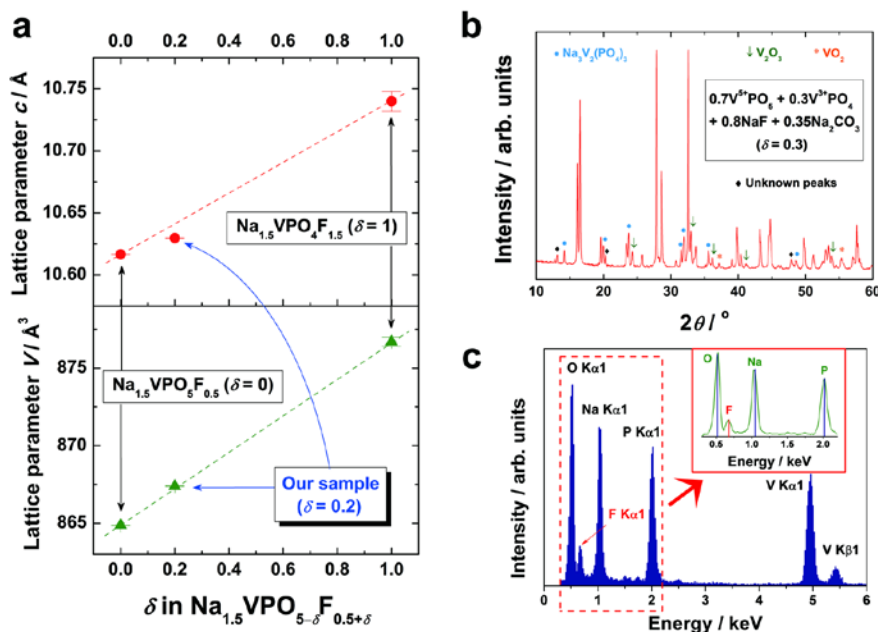


Figure 4-2. Search for the optimum fluorine substitution in $\text{Na}_{1.5}\text{VPO}_{5-\delta}\text{F}_{0.5+\delta}$.

(a) Variation in lattice parameter c and V of $\text{Na}_{1.5}\text{VPO}_5\text{F}_{0.5}$ ($\delta = 0$), $\text{Na}_{1.5}\text{VPO}_4\text{F}_{1.5}$ ($\delta = 1$), and a new sample ($\delta = 0.2$) determined from ND data. The cell parameters for each sample were calculated by performing the refinement (full pattern matching) with the space group $P4_2/mnm$. Lattice parameters of $\text{Na}_{1.5}\text{VPO}_5\text{F}_{0.5}$ ($P4_2/mnm$) were $a = b = 9.0257(1)$ Å, $c = 10.6166(2)$ Å, and $V = 864.87(2)$ Å³; lattice parameters of $\text{Na}_{1.5}\text{VPO}_4\text{F}_{1.5}$ ($P4_2/mnm$) were $a = b = 9.034(3)$ Å, $c = 10.740(8)$ Å, and $V = 876.7(3)$ Å³. (b) XRD pattern of the product after heat treatment (750°C, 1.5 hours, Ar) of the precursor combination of “ $0.7\text{V}^{5+}\text{PO}_5 + 0.3\text{V}^{3+}\text{PO}_4 + 0.8\text{NaF} + 0.35\text{Na}_2\text{CO}_3$ ($\delta = 0.3$)””. (c) An EDS spectrum of the single-crystalline $\text{Na}_{1.5}\text{VPO}_{4.8}\text{F}_{0.7}$ particle. The overall spectrum (0–6 keV) and an enlarged spectrum (0.3–2.2 keV, inset) show that the EDS peaks of all elements in the samples (Na, V, P, O, and F) are well separated. This probably makes the O and F quantification results from EDS spectra more reliable.

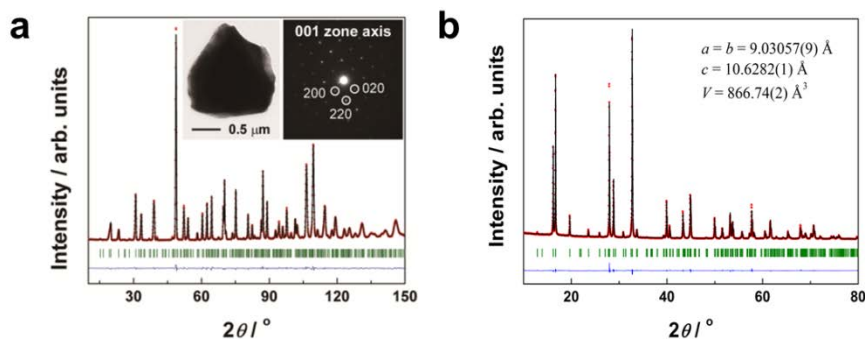


Figure 4-3. Structural characterization of the fluorinated $\text{Na}_{1.5}\text{VPO}_{4.8}\text{F}_{0.7}$.

(a) ND pattern of the fluorinated Na phase ($\text{Na}_{1.5}\text{VPO}_{4.8}\text{F}_{0.7}$) and Rietveld refinement with observed data points (red dots), calculated pattern (black line), difference curve (blue line), and Bragg positions (green bars); lattice parameters in the space group $P4_2/mnm$ were $a = b = 9.0332(1) \text{ \AA}$, $c = 10.6297(2) \text{ \AA}$, and $V = 867.37(2) \text{ \AA}^3$. The inset shows a bright-field transmission electron microscopy (TEM) image of a $\text{Na}_{1.5}\text{VPO}_{4.8}\text{F}_{0.7}$ particle (left) and its corresponding selected-area electron diffraction (SAED) pattern (right); most microcrystallites were single-crystalline (i.e., only spot patterns were detected).

(b) XRD pattern of $\text{Na}_{1.5}\text{VPO}_{4.8}\text{F}_{0.7}$ and its Rietveld refinement in the $P4_2/mnm$ space group; lattice parameters were $a = b = 9.03057(9) \text{ \AA}$, $c = 10.6282(1) \text{ \AA}$, and $V = 866.74(2) \text{ \AA}^3$.

Table 4-1. Lattice parameters and cell volumes for Na_{1.5}VPO_{4.8}F_{0.7}

<i>Space Group</i>	<i>P4₂/mnm</i>
<i>Cell parameters</i>	
<i>a</i> (Å)	9.0332(1)
<i>b</i> (Å)	9.0332(1)
<i>c</i> (Å)	10.6297(2)
<i>α</i> (°)	90(-)
<i>β</i> (°)	90(-)
<i>γ</i> (°)	90(-)
Volume (Å ³)	867.37(2)
<i>Reliability factors</i>	
<i>R_P</i> (%)	2.83
<i>R_I</i> (%)	3.20
<i>R_F</i> (%)	2.79

Table 4-2. Atomic positions for Na_{1.5}VPO_{4.8}F_{0.7}

<i>Label</i>	<i>Atom</i>	<i>Site</i>	<i>x</i>	<i>y</i>	<i>z</i>	<i>Occupancy</i>	<i>B_{iso}</i> (Å ²)
Na1	Na	8i	0.5110(4)	0.239(1)	0 (-)	0.88(1)	0.92(9)
Na2	Na	8i	0.8075(8)	0.0344(8)	0 (-)	0.62(1)	1.7(2)
V1	V	8j	0.2477(3)	0.2477(3)	0.19628(8)	1	0.74(3)
P1	P	4d	0 (-)	½ (-)	¼ (-)	1	0.16(3)
P2	P	4e	0 (-)	0 (-)	0.2561(5)	1	0.16(3)
O1	O	16k	0.0979(4)	0.4055(3)	0.1641(4)	1	0.17(5)
O2	O	8j	0.0954(4)	0.0954(4)	0.1686(5)	1	0.85(6)
O3	O	8j	0.4050(4)	0.4050(4)	0.1564(5)	1	0.85(6)
O4	O	8j	0.2470(4)	0.2470(4)	0.3548(1)	0.8	1.00(3)
F1	F	4f	0.2488(5)	0.2488(5)	0 (-)	1	0.25(4)
F2	F	8j	0.2470(4)	0.2470(4)	0.3548(1)	0.2	1.00(3)

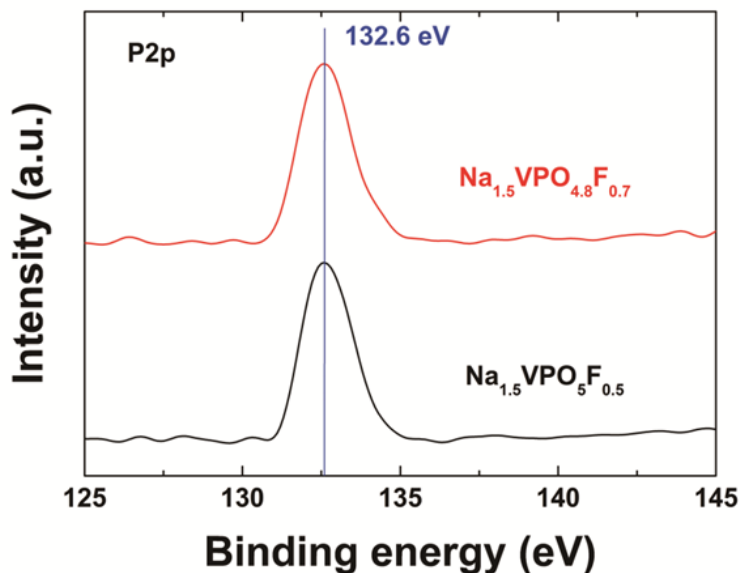


Figure 4-4. Comparison of P2p binding energies in XPS spectra of the pristine sodium phase ($\text{Na}_{1.5}\text{VPO}_5\text{F}_{0.5}$) and the fluorinated phase ($\text{Na}_{1.5}\text{VPO}_{4.8}\text{F}_{0.7}$). The identical XPS P2p binding energy implies that all phosphorus ions have the same local environment surrounded by four oxygen ions, i.e., PO_4 tetrahedral units.

4.3.2. Evidence for Reduced Oxidation State of Vanadium in $\text{Na}_{1.5}\text{VPO}_{4.8}\text{F}_{0.7}$

By tailoring the polyanion group from $[\text{PO}_5\text{F}_{0.5}]^{5.5-}$ to $[\text{PO}_{4.8}\text{F}_{0.7}]^{5.3-}$, I could effectively reduce the overall oxidation state of vanadium while maintaining structural integrity. ^{23}Na MAS NMR spectra of the three samples (**Figure 4-5a**) support my claim. The ^{23}Na MAS NMR spectrum of the new sample (middle; $\delta = 0.2$) shows two major Fermi contact shifts at 70 and 112 ppm, whereas the others exhibit a single Fermi contact shift (e.g., 71 ppm for $\text{Na}_{1.5}\text{V}^{4+}\text{PO}_5\text{F}_{0.5}$ and 136 ppm for $\text{Na}_{1.5}\text{V}^{3+}\text{PO}_4\text{F}_{1.5}$; this difference is explained by the fact that V^{3+} ions generally cause a more positive Fermi contact shift than V^{4+} ions by tens of ppm;^{80,81} see also **Figure 4-5b**). I believe that two paramagnetic sources (V^{4+} and V^{3+} ions) with different number of unpaired electrons are attributable to two dissimilar Fermi contact shifts (70 and 112 ppm), respectively, in the middle spectrum. The average oxidation state of vanadium in $\text{Na}_{1.5}\text{V}^{3.8+}\text{PO}_{4.8}\text{F}_{0.7}$ determined by the double titration method was about +3.8, which corresponds to that in a 4:1 mixture of V^{4+} and V^{3+} ions. This result is in good agreement with the observation that the intensity of the peak at 70 ppm was 3–4 times higher than that at 112 ppm in the ^{23}Na MAS NMR spectrum of $\text{Na}_{1.5}\text{V}^{3.8+}\text{PO}_{4.8}\text{F}_{0.7}$.

I used the double titration method¹¹⁰ to quantify the average oxidation state of vanadium ions in samples with high accuracy, whose experimental procedure is described in **Figure 4-6**. **Table 4-3** shows the average oxidation state of vanadium (AV) for various vanadium-containing compounds determined by the double titration method. The AV values of $\text{Na}_{1.5}\text{VPO}_5\text{F}_{0.5}$ and $\text{Na}_{1.5}\text{VPO}_4\text{F}_{1.5}$ were +4.07 and +2.99, respectively, and were very similar to the theoretical values (+4 and +3). The AV value of the new sample ($\text{Na}_{1.5}\text{VPO}_{4.8}\text{F}_{0.7}$) was ca. +3.8, suggesting that V^{3+} and V^{4+} ions are mixed in the crystal at a ratio of 1:4. Also, it is in good agreement

with the oxygen and fluorine quantification results. Additionally, AV values for other well-known vanadium-containing compounds (**Table 4-3**) were almost identical to their theoretical values, confirming the reliability of this method.

To further probe the substitution, EPR experiments were carried out on those three samples (**Figure 4-7a**). The EPR spectrum of $\text{Na}_{1.5}\text{V}^{4+}\text{PO}_5\text{F}_{0.5}$ was very intense, and the shape was in good agreement with a previous report.⁷¹ However, the EPR signal of $\text{Na}_{1.5}\text{V}^{3+}\text{PO}_4\text{F}_{1.5}$ was negligible, which can be explained by the fact that V^{3+} , a non-Kramer's ion with integral J in LS coupling,¹¹¹ is silent under conventional EPR experimental conditions.¹¹² On the contrary, the EPR spectrum of the new sample, $\text{Na}_{1.5}\text{V}^{3.8+}\text{PO}_{4.8}\text{F}_{0.7}$, showed a broad peak, unlike that of $\text{Na}_{1.5}\text{V}^{4+}\text{PO}_5\text{F}_{0.5}$ or $\text{Na}_{1.5}\text{V}^{3+}\text{PO}_4\text{F}_{1.5}$. It resembles the EPR spectra of $\text{Li}_x\text{V}_2(\text{PO}_4)_3$ phases ($x = 2.0$ and 2.5) in which V^{3+} and V^{4+} ions coexist (**Figure 4-7b**),¹¹³ suggesting the coexistence of V^{3+} and V^{4+} ions in the new sample ($\delta = 0.2$).

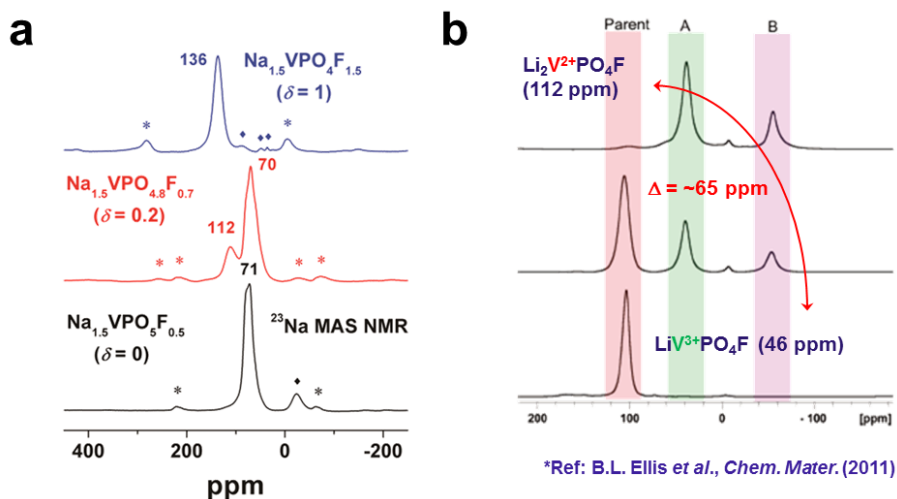


Figure 4-5. ^{23}Na and ^7Li MAS NMR spectra of vanadium fluorophosphates.

(a) ^{23}Na MAS NMR spectra of $\text{Na}_{1.5}\text{V}^{4+}\text{PO}_5\text{F}_{0.5}$ (bottom), $\text{Na}_{1.5}\text{V}^{3.8+}\text{PO}_{4.8}\text{F}_{0.7}$ (middle), and $\text{Na}_{1.5}\text{V}^{3+}\text{PO}_4\text{F}_{1.5}$ (top). Spinning sidebands are marked with asterisks. In contrast, the other Fermi contact shift was detected at 112 ppm instead of 136 ppm, implying that it arose from Na^+ ions whose nearest vanadium neighbors are partially V^{3+} ions. Note that the NMR shift originating from V^{3+} ions in $\text{Na}_{1.5}\text{V}^{3.8+}\text{PO}_{4.8}\text{F}_{0.7}$ (112 ppm in the middle spectrum) is considerably less positive than that of $\text{Na}_{1.5}\text{V}^{3+}\text{PO}_4\text{F}_{1.5}$ (136 ppm in the top spectrum). I believe that a homogeneous mixing of $\text{Na}_{1.5}\text{V}^{3+}\text{PO}_4\text{F}_{1.5}$ and $\text{Na}_{1.5}\text{V}^{4+}\text{PO}_5\text{F}_{0.5}$ phases prevented Na^+ ions from being surrounded solely by V^{3+} ions and lessened the net amount of spin density transferred to Na^+ ions (i.e., decreased Fermi contact shift). Small isotropic peaks (denoted as \blacklozenge) could not be assigned.

(b) ^7Li MAS NMR (40 kHz, 330 K) spectra of LiVPO_4F at various stages of lithiation. Reprinted with permission from reference ⁸¹. Copyright 2011 American Chemical Society.

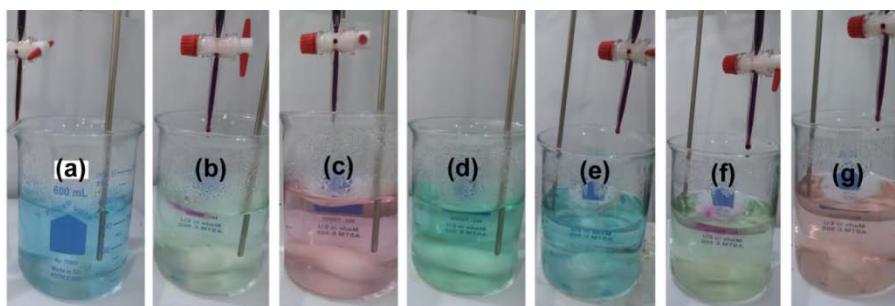
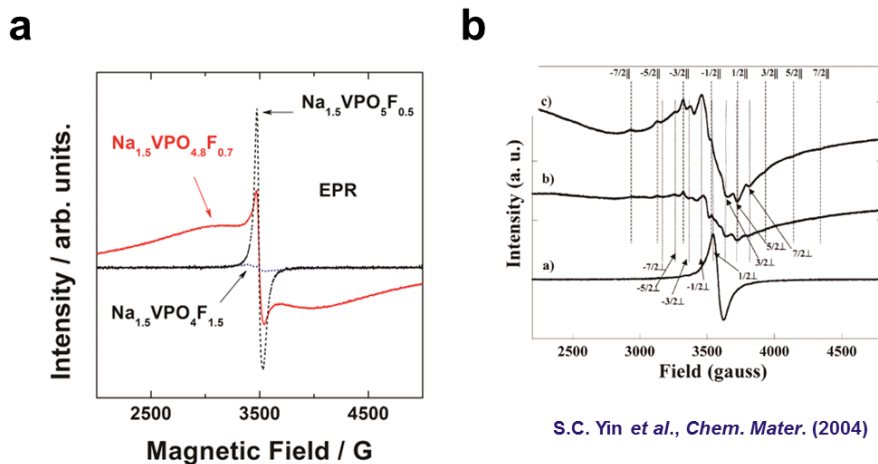


Figure 4-6. Photographs representing the experimental procedure of the double titration method. (a) Vanadium-containing compounds are completely dissociated or ionized in 2 M H_2SO_4 solution at 80°C . Colors of V^{3+} , V^{4+} , and V^{5+} ions in aqueous solution are generally known to be green, blue, and yellow, respectively. (b) The first titration with the 0.1 N KMnO_4 solution was not stopped until the overall color of the solution abruptly changed to purple (corresponding to complete oxidation of V^{x+} to V^{5+}). (c) The first titration was halted, and the total volume of the KMnO_4 solution consumed during the first titration (V_1) was measured. (d) An excess amount of $\text{FeSO}_4(\text{NH}_4)_2(\text{SO}_4) \cdot 6\text{H}_2\text{O}$ was added to the solution to reduce all V^{5+} ions to V^{4+} ions by the $\text{Fe}^{2+}/\text{Fe}^{3+}$ redox couple. (e) After the entire solution was cooled to room temperature, an excess amount of $(\text{NH}_4)_2\text{S}_2\text{O}_8$ was added to fully oxidize residual Fe^{2+} ions to Fe^{3+} ions for the accuracy of the second titration. (f) The second titration with the 0.1 N KMnO_4 solution was not stopped until the overall color of the solution abruptly changed to purple (corresponding to complete oxidation of V^{4+} to V^{5+}). (g) The second titration was halted, and the total volume of the KMnO_4 solution consumed during the second titration (V_2) was measured. Finally, the average oxidation state of vanadium (AV) was calculated by the equation “ $\text{AV} = 5 - V_1/V_2$ ”.

Table 4-3. Average oxidation state of vanadium (AV) for various vanadium-containing compounds determined by the double titration method

Sample	AV	Synthetic route
$\text{Na}_{1.5}\text{VPO}_4\text{F}_{1.5}$	+2.99	$\text{V}^{3+}\text{PO}_4 + 1.5\text{NaF}$ (750°C, 1.5 h, Ar)
$\text{Na}_{1.5}\text{VPO}_5\text{F}_{0.5}$	+4.07	$\text{V}^{5+}\text{PO}_5 + 0.5\text{NaF} + 0.5\text{Na}_2\text{CO}_3$ (750°C, 1.5 h, Ar)
$\text{Na}_{1.5}\text{VPO}_{4.8}\text{F}_{0.7}$ (a new sample)	+3.76	$0.8\text{V}^{5+}\text{PO}_5 + 0.2\text{V}^{3+}\text{PO}_4 + 0.7\text{NaF} + 0.4\text{Na}_2\text{CO}_3$ (750°C, 1.5 h, Ar)
$\text{Li}_3\text{V}_2(\text{PO}_4)_3$	+2.98	Reference ¹⁰²
V_2O_3	+2.97	Aldrich



S.C. Yin et al., *Chem. Mater.* (2004)

Figure 4-7. EPR spectra of sodium vanadium fluorophosphates and lithium vanadium phosphates.

(a) EPR spectra of $\text{Na}_{1.5}\text{V}^{4+}\text{PO}_5\text{F}_{0.5}$ (black dashed line), $\text{Na}_{1.5}\text{V}^{3.8+}\text{PO}_{4.8}\text{F}_{0.7}$ (red solid line), and $\text{Na}_{1.5}\text{V}^{3+}\text{PO}_4\text{F}_{1.5}$ (blue dotted line).

(b) EPR spectra of $\text{Li}_x\text{V}_2(\text{PO}_4)_3$ phases of a) $x = 3.0$, b) $x = 2.5$, and c) $x = 2.0$. Reprinted with permission from reference ¹¹³. Copyright 2004 American Chemical Society.

4.3.3. Na⁺/Li⁺ Ion-Exchange for Lithium Derivative of Na_{1.5}VPO_{4.8}F_{0.7}

Ion exchange is an effective way to synthesize a new metastable phase without causing much structural change to the pristine structure.^{102,103,114} Using a Na⁺/Li⁺ ion-exchange method, I successfully prepared an isostructural lithium derivative of Na_{1.5}VPO_{4.8}F_{0.7} (see **Table 4-4** for details). Several ion-exchange conditions were explored to optimize the degree of the process. Elemental analysis was carried out using ICP spectroscopy. All other products, except for the one prepared *via* the molten salt method, retained the initial structure. According to ICP elemental analysis, ~1.1 Na⁺ ions were replaced by Li⁺ ions without affecting the other elements; the overall composition was Li_{1.1}Na_{0.4}VPO_{4.8}F_{0.7}.

Important findings through various ion-exchange experiments in **Table 4-4** are as follows: (i) Ion-exchange conditions that are too mild (e.g., using ethanol or acetonitrile as the ionic conducting solvents) could substitute no more than 0.5 Li⁺ ions for Na⁺ ions. (ii) Too harsh conditions (e.g., LiCl/LiNO₃ molten salt) caused phase decomposition. (iii) Only the ion-exchange conditions using 1-hexanol with a reaction time of 6–17 hours yielded sufficient Na⁺/Li⁺ ion exchange (~1.1).

Detailed structural analysis of the new lithium phase was carried out using ND and ⁶Li and ²³Na NMR spectroscopies. All peaks of Li_{1.1}Na_{0.4}VPO_{4.8}F_{0.7} observed in the ND pattern (**Figure 4-8a**) could be indexed in the space group *P4₂/mnm*. All Miller indices (*hkl*) of the structure matched those of Na_{1.5}VPO_{4.8}F_{0.7}, indicating that the isostructural lithium derivative was obtained.

Na_{1.5}VPO_{4.8}F_{0.7} and Li_{1.1}Na_{0.4}VPO_{4.8}F_{0.7} particles had similar morphology, with sizes in the range of 1–5 μm (inset of **Figure 4-8a**). **Figure 4-8b** shows that the observed micron-sized crystallites were single crystals rather than agglomerates of

nanocrystals (see **Figure 4-9** for more TEM images). Bright-field TEM images (**Figure 4-9a, 4-9b, and 4-9c**) show that the particle sizes of $\text{Li}_{1.1}\text{Na}_{0.4}\text{VPO}_{4.8}\text{F}_{0.7}$ were in the micron range. Their respective SAED patterns (**Figure 4-9d, 4-9e, and 4-9f**) suggest that all of the microcrystallites were single crystals because only spot patterns rather than ring patterns were observed throughout a single particle. All of the spots in the SAED patterns could be indexed using the lattice parameters and (*hkl*) indices of $\text{Li}_{1.1}\text{Na}_{0.4}\text{VPO}_{4.8}\text{F}_{0.7}$ obtained from the refinement results of ND patterns, and each zone axis was determined by means of the Weiss zone law.

The ND pattern of $\text{Li}_{1.1}\text{Na}_{0.4}\text{VPO}_{4.8}\text{F}_{0.7}$ was successfully refined with the same space group ($P4_2/mnm$) as $\text{Na}_{1.5}\text{VPO}_{4.8}\text{F}_{0.7}$ (see **Table 4-5** and **Table 4-6** for details), with negligible change in the structure; an identical structure model (including the O4 and F2 sites) was used for both. Therefore, major structural changes were not observed during the ion-exchange process as previously reported.^{102,115} The atomic position and the atomic displacement parameter of vanadium were also determined from the XRD Rietveld refinement.

Supposing that the number of the Na^+ ions exchanged for Li^+ ions was 1.1 (per the ICP spectroscopy results), I investigated which site the newly introduced Li^+ ions preferred by refining the occupancies of the Li1/Na1 and Li2/Na2 sites (corresponding to the Na1 and Na2 sites in $\text{Na}_{1.5}\text{VPO}_{4.8}\text{F}_{0.7}$, respectively). The Li^+ ions seemed to strongly prefer the former to the latter, while the Na^+ ions were seldom located in the former. Hence, the Li1/Na1 site was fully occupied solely by Li^+ ions whereas the Li2/Na2 site was partially filled with both Li^+ and Na^+ ions.

Figure 4-10 shows the alkali metal layer in the *ab* plane with the local environments of the two kinds of sites. The configuration of the alkali ions

resembles the parent sodium phase (**Figure 4-11**), implying facile two-dimensional diffusion of mobile ions.

Using the theoretical molecular weight ($188.84 \text{ g mol}^{-1}$) calculated for the composition $\text{Li}_{1.1}\text{Na}_{0.4}\text{VPO}_{4.8}\text{F}_{0.7}$, its unit cell volume (843.24 \AA^3) obtained from the refinement, and the number of motifs per unit cell ($Z = 8$), I calculated a relatively low theoretical density of 3.0 g cm^{-3} for the material. This result implies that it has a more spacious structure than other conventional cathode materials (cf., 3.6 g cm^{-3} for LiFePO_4 and 5.1 g cm^{-3} for LiCoO_2).¹¹⁶

The local lithium environments in $\text{Li}_{1.1}\text{Na}_{0.4}\text{VPO}_{4.8}\text{F}_{0.7}$ were investigated by ^6Li and ^{23}Na MAS NMR (**Figure 4-12**). Most transition metal-containing positive electrode materials for lithium-ion batteries are paramagnetic, so isotropic shifts in their ^6Li MAS NMR spectra principally arise from Fermi contact interactions. This interaction causes a net electron spin around the lithium nuclei and hence leads to large hyperfine shifts.^{79,80} According to the Goodenough–Kanamori superexchange rules¹¹⁷ and their modified theory,⁷⁹ the amount of the net spins transferred from M t_{2g} or e_g orbitals (M = paramagnetic transition metals) to Li $2s$ orbitals *via* oxygen $2p$ orbitals is extremely sensitive to the spin transfer mechanism and the angles of the Li–O– M bonds, as well as to the coordination numbers or environments of M and the intervening oxygen.^{79,80,118,119}

The ^6Li MAS NMR spectrum (**Figure 4-12a**) suggests the existence of two types of local environments for lithium in the structure, reminiscent of the two kinds of sodium sites in the parent sodium phase. The signal at 25.5 ppm is significantly more intense than the signal at 0 ppm, indicating that one of two crystallographic sites for alkali ions is preferentially occupied by Li^+ ions. This preferential

occupation of Li^+ ions in one alkali-metal site is consistent with the ND refinement result and demonstrates that most Li^+ ions reside in the original Na1 site, while the Na2 sites remained mainly occupied by Na^+ ions.

The ^{23}Na MAS NMR spectrum of the ion-exchanged phase, $\text{Li}_{1.1}\text{Na}_{0.4}\text{VPO}_{4.8}\text{F}_{0.7}$, shows two different isotropic peaks at 30.3 and 93 ppm (**Figure 4-12b**), suggesting that two Fermi contact shifts originating from V^{4+} and V^{3+} ions still exist. In the pristine Na phase, a NMR shift of Na^+ ions around V^{4+} ions (70 ppm) and another shift of Na^+ ions around V^{3+} ions (112 ppm) in $\text{Na}_{1.5}\text{VPO}_{4.8}\text{F}_{0.7}$ were observed (see the middle spectrum in **Figure 4-5a**). However, the former (related to V^{4+} ions) in the lithium phase (30.3 ppm) was far more suppressed than the latter (related to V^{3+} ions) in the lithium phase (93 ppm), implying that Na^+ ions around V^{4+} ions in the original sodium phase more actively participated in the ion-exchange process than those around V^{3+} ions. In other words, most Li^+ ions in the lithium phase probably exist around V^{4+} ions, which can explain the absence of another minor peak having a more positive isotropic shift (related to V^{3+} ions) in the ^6Li MAS NMR spectrum of the lithium phase.

The ^{23}Na NMR shifts were different for the lithium phase and the parent sodium phase because the NMR shifts for my paramagnetic samples were mainly governed by the Fermi contact interaction. For $\text{Na}_{1.5}\text{VPO}_{4.8}\text{F}_{0.7}$ and $\text{Li}_{1.1}\text{Na}_{0.4}\text{VPO}_{4.8}\text{F}_{0.7}$, each Na^+ ion receives electron spins from four adjacent vanadium ions via O 2p (or F 2p) orbitals, and the transferred net spin densities lead to a large sodium hyperfine shift. Various possible Na 3s – O 2p – V t_{2g} and Na 3s – F 2p – V t_{2g} interactions are schematically shown in **Figure 4-13**. In $\text{Li}_{1.1}\text{Na}_{0.4}\text{VPO}_{4.8}\text{F}_{0.7}$, hyperfine shifts originating from Na^+ ions around V^{4+} and V^{3+} ions were 30.3 and 93 ppm, respectively (**Figure 4-12b**), while those in $\text{Na}_{1.5}\text{VPO}_{4.8}\text{F}_{0.7}$ were 70 and 112 ppm,

respectively (the middle spectrum in **Figure 4-5a**). Less-positive shift values for the lithium phase arose from the smaller net electron spin density near a sodium nucleus being transferred from the paramagnetic $V^{4+} (t_{2g}^1 e_g^0)$ and $V^{3+} (t_{2g}^2 e_g^0)$ ions via O 2p or F 2p orbitals.^{79,80} Assuming that the sodium and lithium phases have a similar degree of mixing uniformity between V^{4+} and V^{3+} ions, I believe that the fewer transferred spins are attributable to a larger deviation from 90° of the Na–O(F)–V angles in the lithium phase.^{79,80}

The thermal phase stability of $Li_{1.1}Na_{0.4}VPO_{4.8}F_{0.7}$ was evaluated by temperature-controlled XRD (**Figure 4-14**). Metastable phases obtained from low-temperature *Chimie Douce* routes are often susceptible to thermal degradation upon slight heat treatment. However, it was found that the $Li_{1.1}Na_{0.4}VPO_{4.8}F_{0.7}$ phase was thermally stable up to 550°C, which indicates that various low-temperature synthetic techniques, such as ionothermal processes,^{51,93,120,121} can be applied to the synthesis of $Li_{1.1}Na_{0.4}VPO_{4.8}F_{0.7}$.

Table 4-4. Comparison of the degree of Na⁺/Li⁺ ion-exchange (i.e., the exchanged amount) for a variety of experimental conditions

<i>Solvent</i>	<i>Reaction temp. (°C)</i>	<i>Reaction time (h)</i>	<i>Lithium source</i>	<i>Li</i>	<i>Na</i>	<i>V</i>	<i>P</i>
Ethanol	70	17	LiBr	0	1.5	1.0	1.0
Acetonitrile	85	17	LiBr	0.5	1.0	1.0	1.0
1-hexanol	160	6–17	LiBr	1.1	0.4	1.0	1.0
LiCl/LiNO ₃ molten salt	280	5	LiCl/LiNO ₃	Phase decomposition			

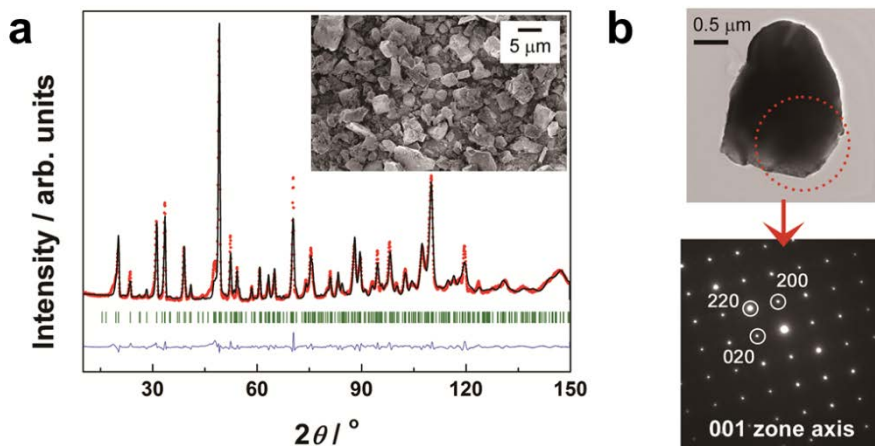


Figure 4-8. Material characterization of the ion-exchanged $\text{Li}_{1.1}\text{Na}_{0.4}\text{VPO}_{4.8}\text{F}_{0.7}$.

(a) ND pattern of $\text{Li}_{1.1}\text{Na}_{0.4}\text{VPO}_{4.8}\text{F}_{0.7}$ and its Rietveld refinement in the $P4_2/mnm$ space group with observed data points (red dots), calculated pattern (black line), difference curve (blue line), and Bragg positions (green bars); lattice parameters are $a = b = 8.9836(6) \text{ \AA}$, $c = 10.4483(8) \text{ \AA}$, and $V = 843.24(9) \text{ \AA}^3$. The unit cell volume was significantly reduced from $867.37(2) \text{ \AA}^3$ for $\text{Na}_{1.5}\text{VPO}_{4.8}\text{F}_{0.7}$ to $843.24(9) \text{ \AA}^3$ for the new lithium phase because of the smaller ionic radius of Li^+ ion. The inset shows a scanning electron microscopy (SEM) image (magnification: $\times 5,000$).

(b) A bright-field TEM image of a micron-sized particle (top) and its corresponding SAED pattern (bottom).

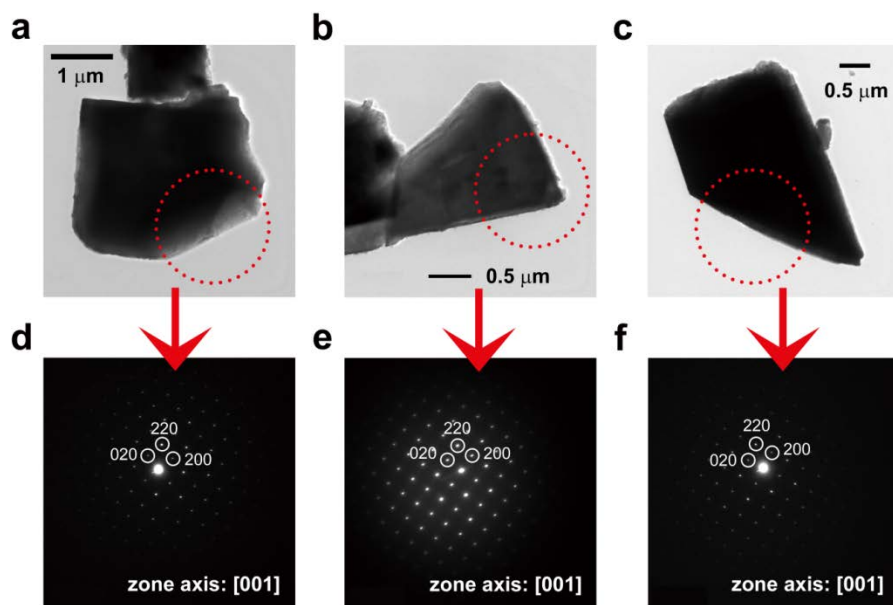


Figure 4-9. TEM study for $\text{Li}_{1.1}\text{Na}_{0.4}\text{VPO}_{4.8}\text{F}_{0.7}$. (a–c) Bright-field TEM images and (d–f) the corresponding SAED patterns of $\text{Li}_{1.1}\text{Na}_{0.4}\text{VPO}_{4.8}\text{F}_{0.7}$.

Table 4-5. Lattice parameters and cell volumes for $\text{Li}_{1.1}\text{Na}_{0.4}\text{VPO}_{4.8}\text{F}_{0.7}$

<i>Space Group</i>	<i>$P4_2/mnm$</i>
<i>Cell parameters</i>	
<i>a</i> (Å)	8.9836(6)
<i>b</i> (Å)	8.9836(6)
<i>c</i> (Å)	10.4483(8)
\angle (°)	90(-)
\angle (°)	90(-)
\angle (°)	90(-)
Volume (Å ³)	843.24(9)
<i>Reliability factors</i>	
<i>R_P</i> (%)	5.31
<i>R_I</i> (%)	8.17
<i>R_F</i> (%)	5.39

Table 4-6. Atomic positions for $\text{Li}_{1.1}\text{Na}_{0.4}\text{VPO}_{4.8}\text{F}_{0.7}$

<i>Label</i>	<i>Atom</i>	<i>Site</i>	<i>x</i>	<i>y</i>	<i>z</i>	<i>Occupancy</i>
Li1	Li	8i	0.462(2)	0.258(3)	0 (-)	0.968(9)
Na1	Na	8i	0.462(2)	0.258(3)	0 (-)	0.032(9)
Li2	Li	8i	0.722(7)	0.021(8)	0 (-)	0.134(9)
Na2	Na	8i	0.722(7)	0.021(8)	0 (-)	0.366(9)
V1	V	8j	0.248(2)	0.248(2)	0.2028(4)	1
P1	P	4d	0 (-)	½ (-)	¼ (-)	1
P2	P	4e	0 (-)	0 (-)	0.259(2)	1
O1	O	16k	0.097(2)	0.408(2)	0.159(2)	1
O2	O	8j	0.095(3)	0.095(3)	0.167(3)	1
O3	O	8j	0.397(3)	0.397(3)	0.142(4)	1
O4	O	8j	0.241(3)	0.241(3)	0.3508(9)	0.8
F1	F	4f	0.256(3)	0.256(3)	0 (-)	1
F2	F	8j	0.241(3)	0.241(3)	0.3508(9)	0.2

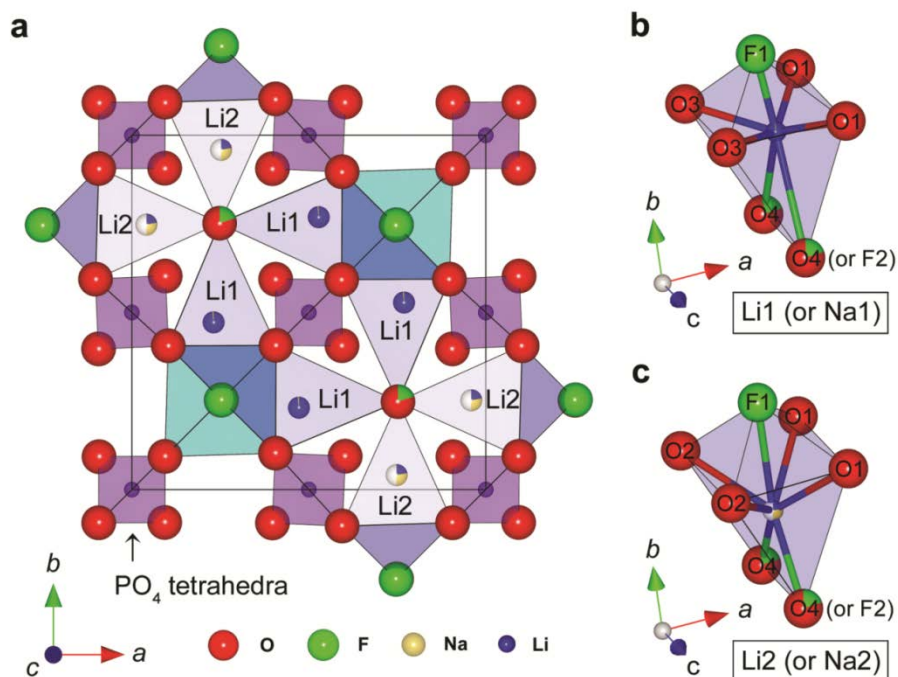


Figure 4-10. Local environments of Li and Na sites in $\text{Li}_{1.1}\text{Na}_{0.4}\text{VPO}_{4.8}\text{F}_{0.7}$.

(a) Configuration of Li^+ and Na^+ ions in the *ab* plane in $\text{Li}_{1.1}\text{Na}_{0.4}\text{VPO}_{4.8}\text{F}_{0.7}$ and the corresponding local environments of (b) Li1 (or Na1) and (c) Li2 (or Na2) sites drawn based on the refinement results. Li, Na, P, O, and F atoms are shown in blue, yellow, purple, red, and green, respectively. Partially occupied sites (Li/Na) are denoted as multicolored spheres. The relative amounts of blue and yellow areas in each site indicate the extent of occupancy by Li^+ and Na^+ ions, respectively. White regions denote the vacancy fraction.

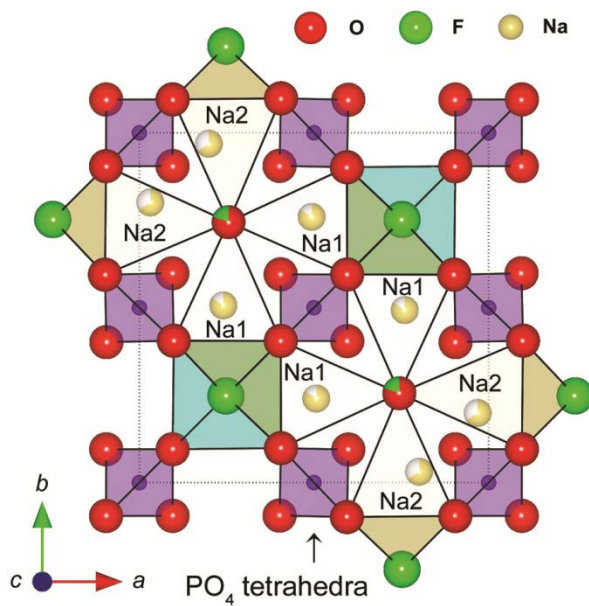


Figure 4-11. The configuration of Na^+ ions on ab plane in $\text{Na}_{1.5}\text{VPO}_{4.8}\text{F}_{0.7}$. The white regions in the Na sites denote the vacancy fraction.

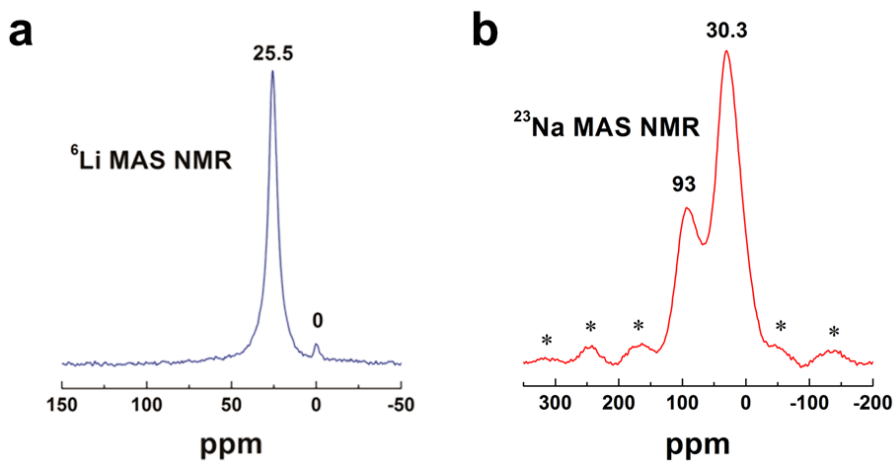


Figure 4-12. ${}^6\text{Li}$ and ${}^{23}\text{Na}$ MAS NMR spectra of $\text{Li}_{1.1}\text{Na}_{0.4}\text{VPO}_{4.8}\text{F}_{0.7}$.

(a) ${}^6\text{Li}$ MAS NMR spectrum of $\text{Li}_{1.1}\text{Na}_{0.4}\text{VPO}_{4.8}\text{F}_{0.7}$. Two isotropic shifts at 25.5 ppm and 0 ppm were observed.

(b) ${}^{23}\text{Na}$ MAS NMR spectrum of $\text{Li}_{1.1}\text{Na}_{0.4}\text{VPO}_{4.8}\text{F}_{0.7}$ at a MAS spinning speed of 15 kHz. Spinning sidebands are marked with asterisks and the NMR shifts were referenced to 0.1 M NaCl (0 ppm).

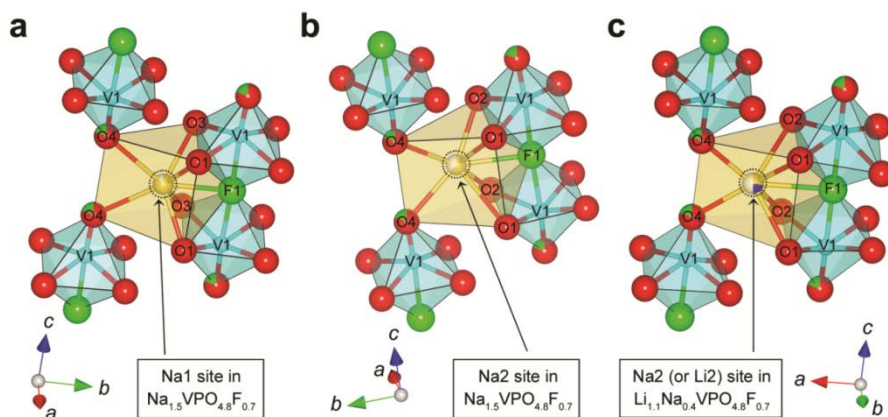


Figure 4-13. Schematic representation for several types of Na 3s – O 2p (F 2p) – V t_{2g} interactions in $\text{Na}_{1.5}\text{VPO}_{4.8}\text{F}_{0.7}$ and $\text{Li}_{1.1}\text{Na}_{0.4}\text{VPO}_{4.8}\text{F}_{0.7}$.

- (a) Na 3s – O 2p (F 2p) – V t_{2g} interactions for Na1 site in $\text{Na}_{1.5}\text{VPO}_{4.8}\text{F}_{0.7}$.
- (b) Na 3s – O 2p (F 2p) – V t_{2g} interactions for Na2 site in $\text{Na}_{1.5}\text{VPO}_{4.8}\text{F}_{0.7}$.
- (c) Na 3s – O 2p (F 2p) – V t_{2g} interactions for Na2/Li2 site in $\text{Li}_{1.1}\text{Na}_{0.4}\text{VPO}_{4.8}\text{F}_{0.7}$.

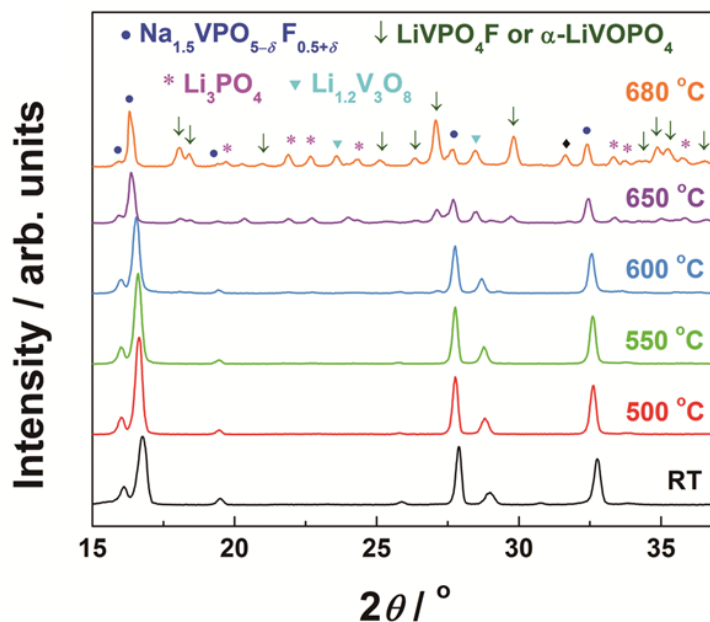


Figure 4-14. Temperature-controlled XRD patterns of $\text{Li}_{1.1}\text{Na}_{0.4}\text{VPO}_{4.8}\text{F}_{0.7}$. Increasing temperature above 600°C triggered phase separation into a sodium phase ($\text{Na}_{1.5}\text{VPO}_{5-\delta}\text{F}_{0.5+\delta}$) and lithium phase (favorite LiVPO_4F or triclinic α - LiVOPO_4). This suggests that sodium and lithium phases crystallize in different structures having dissimilar stoichiometries in the “Na(Li)–V–P–O–F” system under conventional high-temperature synthesis conditions. A reflection denoted as ♦ could not be identified.

4.3.4. Electrochemical Properties of $\text{Li}_{1.1}\text{Na}_{0.4}\text{VPO}_{4.8}\text{F}_{0.7}$

The electrochemical properties of $\text{Li}_{1.1}\text{Na}_{0.4}\text{VPO}_{4.8}\text{F}_{0.7}$ were examined in a Li cell. The quasi-equilibrium profile obtained by the galvanostatic intermittent titration technique (GITT) at 60°C shown in **Figure 4-15** exhibited an average voltage of ~3.95 V. The low-current charge and discharge via the GITT mode exhibited a low polarization and yielded a capacity approaching the theoretical capacity for $\text{Li}_{1.1}\text{Na}_{0.4}\text{VPO}_{4.8}\text{F}_{0.7}$, 156 mAh g⁻¹ (equivalent to insertion/deinsertion of 1.1 Li⁺ ions per formula unit). This clearly indicates more than one lithium ion contributes to the capacity through the widened V^{3.8+}/V⁵⁺ redox reaction achieved by tailoring the pristine $\text{Na}_{1.5}\text{VPO}_5\text{F}_{0.5}$. The $\text{Na}_{1.5}\text{V}^{4+}\text{PO}_5\text{F}_{0.5}$ electrode and its lithium derivative ($\text{LiNa}_{0.5}\text{V}^{4+}\text{PO}_5\text{F}_{0.5}$) with a V⁴⁺/V⁵⁺ redox couple can theoretically deliver only 130 mAh g⁻¹ and 141 mAh g⁻¹, respectively. Tailoring the pristine fluorophosphate material as the 4 V electrode with the capacity of 156 mAh g⁻¹ makes this material a strong alternative to other cathode materials: LiCoO_2 (4 V, ca. 160 mAh g⁻¹),¹²² LiFePO_4 (3.45 V, ca. 170 mAh g⁻¹),¹²³ LiMn_2O_4 (4 V, ca. 120 mAh g⁻¹),¹²⁴ and $\text{LiNi}_{0.5}\text{Mn}_{1.5}\text{O}_4$ (4.7 V, ca. 130 mAh g⁻¹).¹²⁵

Galvanostatic cycling at a rate of C/20 (**Figure 4-16a**) could deliver ~140 mAh g⁻¹ reversibly without a noticeable change in the shape of the charge/discharge profile. At a faster rate of 1C, about 87% of the theoretical capacity of $\text{Li}_{1.1}\text{Na}_{0.4}\text{VPO}_{4.8}\text{F}_{0.7}$ could be retained after the first cycle. After 100 full charge–discharge cycles at 1C at room temperature, no significant capacity loss (96%) occurred, as shown in the bottom panel of **Figure 4-16b**. Moreover, the cyclability at 60°C was even better: 98% of the initial capacity was sustained after 100 cycles (top panel of **Figure 4-16b**). The excellent cycle stability at elevated temperatures presents a clear advantage over its strongest competitor as a 4 V cathode material,

the spinel LiMn_2O_4 , which typically suffers from poor cycle performance at elevated temperatures due to severe manganese dissolution.¹²⁶ The outstanding cyclability of $\text{Li}_{1.1}\text{Na}_{0.4}\text{VPO}_{4.8}\text{F}_{0.7}$, irrespective of the operating temperature, implies high structural stability of the host framework.

Exceptionally high rate capability could be achieved for both charging and discharging of the $\text{Li}_{1.1}\text{Na}_{0.4}\text{VPO}_{4.8}\text{F}_{0.7}$ electrode (**Figure 4-17**). At the 10C rate, more than 115 mAh g^{-1} could still be achieved. A capacity of ca. 100 mAh g^{-1} was obtained at the 25C rate. Moreover, similar capacities can be charged at the same current densities. This fast-charging capability is quite impressive given that the upper bound of the voltage window is 4.5 V, which is only ca. 0.5 V above the equilibrium voltage. Also, micron-sized particles (inset of **Figure 4-8a**) were able to provide very good power. Such a high rate capability had never been reported for any fluorophosphate-based electrodes to date, making $\text{Li}_{1.1}\text{Na}_{0.4}\text{VPO}_{4.8}\text{F}_{0.7}$ a promising candidate as a high-power cathode.

The unexpected capacity retention (see **Figure 4-16b**) is probably due to the small difference in the cell volumes between lithiated and delithiated phases. The unit cell volumes of the pristine $\text{Li}_{1.1}\text{Na}_{0.4}\text{VPO}_{4.8}\text{F}_{0.7}$ and $\text{Na}_{0.4}\text{VPO}_{4.8}\text{F}_{0.7}$ (i.e., fully charged state) calculated from XRD experiments revealed that the change in volume between the two is ca. 0.7% (see **Figure 4-18** and **Table 4-7**). This unusually small volume change of $\text{Li}_{1.1}\text{Na}_{0.4}\text{VPO}_{4.8}\text{F}_{0.7}$ upon cycling is comparable to the lowest volume change reported for triplite $\text{Li}(\text{Fe}_{1-\delta}\text{Mn}_\delta)\text{SO}_4\text{F}$ (ca. 0.6%).⁹³

First-principles structure calculations also confirmed the small volume difference between two simple models of $\text{LiNa}_{0.5}\text{VPO}_5\text{F}_{0.5}$ and $\text{Na}_{0.5}\text{VPO}_5\text{F}_{0.5}$. Due to various difficulties in the calculations for fluorine-substituted compositions (e.g.,

unaffordable computational costs due to oversized supercells, too many possible configurations of oxygen and fluorine ions), similar but simpler systems (i.e., those having smaller supercells and containing fewer atoms in the anions with several arrangements) were examined. Specifically, simpler compositions ($\text{Na}_{1.5}\text{VPO}_5\text{F}_{0.5}$, $\text{LiNa}_{0.5}\text{VPO}_5\text{F}_{0.5}$, and $\text{Na}_{0.5}\text{VPO}_5\text{F}_{0.5}$) were used instead of $\text{Na}_{1.5}\text{VPO}_{4.8}\text{F}_{0.7}$, $\text{Li}_{1.1}\text{Na}_{0.4}\text{VPO}_{4.8}\text{F}_{0.7}$, and $\text{Na}_{0.4}\text{VPO}_{4.8}\text{F}_{0.7}$. I believe that the calculations for these slightly different compositions will still allow us to arrive at reasonable conclusions. From first-principles, various Na/Vacancy and Li/Na/Vacancy configurations were calculated to determine the ground-state structures of $\text{Na}_{1.5}\text{VPO}_5\text{F}_{0.5}$ and $\text{LiNa}_{0.5}\text{VPO}_5\text{F}_{0.5}$, respectively. The reported crystal structure of $\text{Na}_{1.5}\text{VPO}_5\text{F}_{0.5}$ was used as the starting point for the calculations.²⁷ Then, the ground-state structure of $\text{Na}_{0.5}\text{VPO}_5\text{F}_{0.5}$ was chosen by eliminating the more energetically unfavorable Na^+ ions in $\text{Na}_{1.5}\text{VPO}_5\text{F}_{0.5}$. Their ground-state structures are illustrated in **Figure 4-19** with the corresponding configurations of alkali ions. All lattice parameters of $\text{Na}_{1.5}\text{VPO}_5\text{F}_{0.5}$, $\text{LiNa}_{0.5}\text{VPO}_5\text{F}_{0.5}$, and $\text{Na}_{0.5}\text{VPO}_5\text{F}_{0.5}$ were predicted *via* first-principles calculations using the most energetically stable structures (at 0 K). Their lattice parameters are shown for the space group $P4_2/mnm$ in **Table 4-8**. The volume change between the charged and discharged states ($\Delta V_{\text{chg.-dchg.}}$) was estimated by comparing their cell volumes. For example, the volume changes of $\text{Na}_{1.5}\text{VPO}_5\text{F}_{0.5}$ and $\text{LiNa}_{0.5}\text{VPO}_5\text{F}_{0.5}$ during charging/discharging were calculated by dividing the differences from the predicted cell volume of $\text{Na}_{0.5}\text{VPO}_5\text{F}_{0.5}$ (the structure in which one Na^+ or Li^+ ion per formula unit is extracted from each initial structure) by pristine volumes. While $\text{Na}_{1.5}\text{VPO}_5\text{F}_{0.5}$ showed a volume change of 3.1%, $\text{LiNa}_{0.5}\text{VPO}_5\text{F}_{0.5}$ exhibited a very small volume difference (0.4%) between the charged and discharged states, which could explain its excellent cyclability.

The structural investigation of $\text{Li}_{1.1}\text{Na}_{0.4}\text{VPO}_{4.8}\text{F}_{0.7}$ after 100 cycles at a rate of 1C showed no change in the XRD pattern (see **Figure 4-20**), implying good structural stability during charge/discharge. From EDS analysis, I found that the Na/V ratio of a pristine electrode (0.399 ± 0.017) was almost identical to that of the 100th discharged electrode (0.391 ± 0.021). This implies that Na^+ ions are immobile in the structure and do not significantly affect the structural evolution upon cycling.

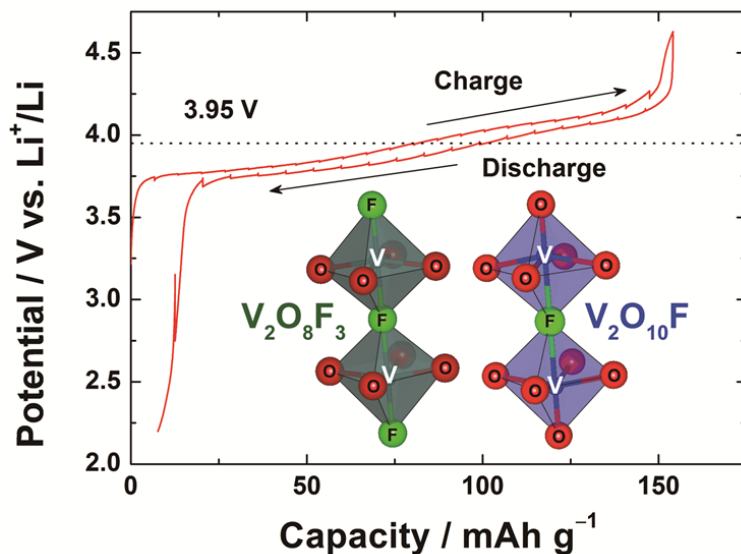


Figure 4-15. GITT curve during charge and discharge of $\text{Li}_{1.1}\text{Na}_{0.4}\text{VPO}_{4.8}\text{F}_{0.7}$ at 60°C . Note that no clear separation was observed between redox potentials of $\text{V}^{3+}/\text{V}^{4+}$ and $\text{V}^{4+}/\text{V}^{5+}$ in this material. In fact, the redox potential of $\text{V}^{3+}/\text{V}^{4+}$ in $\text{V}_2\text{O}_8\text{F}_3$ of $\text{Na}_{1.5}\text{V}^{3+}\text{PO}_4\text{F}_{1.5}$ (left inset) is ~ 3.9 V vs. Na^+/Na (ref. ¹⁷) and that of $\text{V}^{4+}/\text{V}^{5+}$ in $\text{V}_2\text{O}_{10}\text{F}$ of $\text{Na}_{1.5}\text{V}^{4+}\text{PO}_5\text{F}_{0.5}$ (right inset) is ca. 3.8 V vs. Na^+/Na (ref. ²⁷). I believe that the larger inductive effect in the $\text{V}_2\text{O}_8\text{F}_3$ biotetrahedron having more fluorine atoms increased the redox potential of $\text{V}^{3+}/\text{V}^{4+}$ up to that of $\text{V}^{4+}/\text{V}^{5+}$.

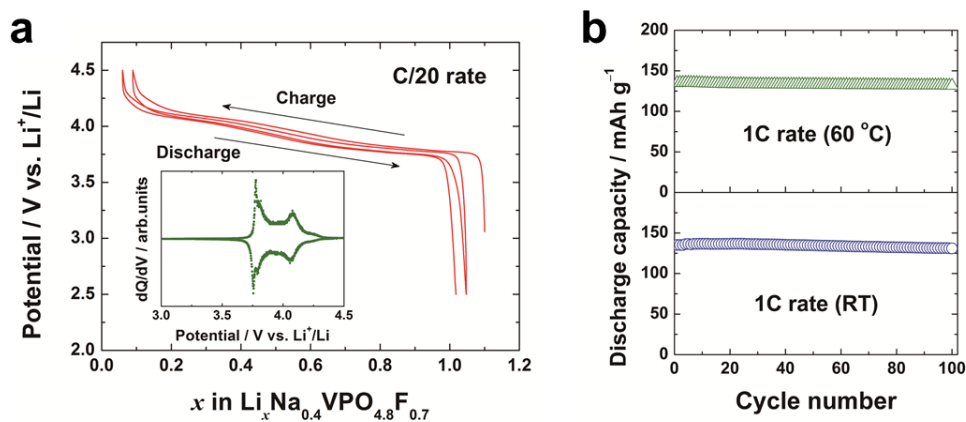


Figure 4-16. Charge/discharge curves and cyclability of $\text{Li}_{1.1}\text{Na}_{0.4}\text{VPO}_{4.8}\text{F}_{0.7}$.

- (a) Galvanostatic charge/discharge curves for the first two cycles at the C/20 rate. 1C corresponds to 156 mA g^{-1} . The inset shows the corresponding dQ/dV curve. Two major peaks were reversibly detected at ca. 3.8 and 4.1 V.
- (b) Cyclability over 100 cycles of galvanostatic charge/discharge at the 1C rate at room temperature (bottom) and at an elevated temperature of 60°C (top).

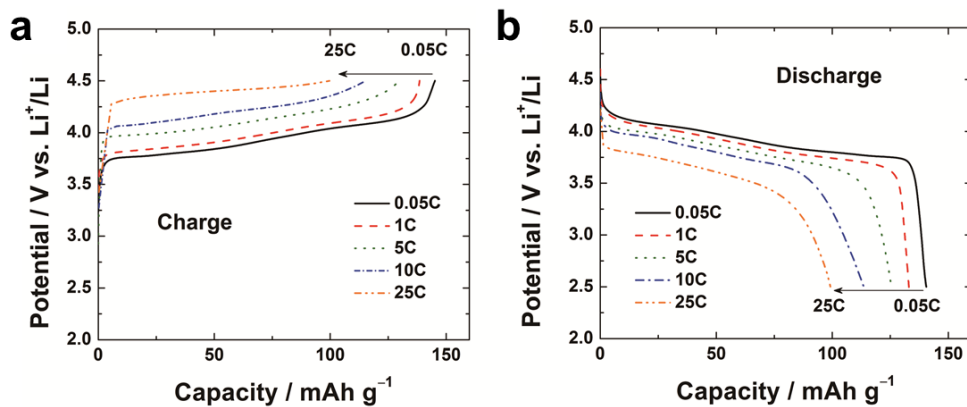


Figure 4-17. Rate capability of the $\text{Li}_{1.1}\text{Na}_{0.4}\text{VPO}_{4.8}\text{F}_{0.7}$ electrode.

(a) The charge curves for various C rates.

(b) The discharge curves for various C rates.

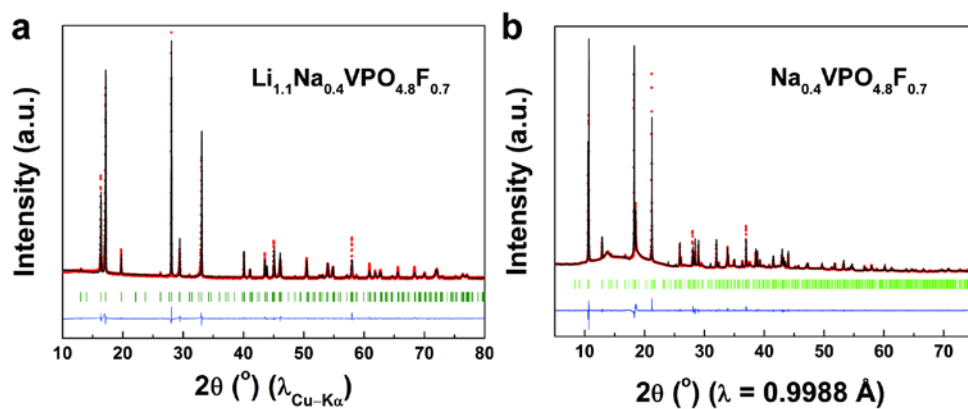


Figure 4-18. XRD patterns of the lithium phase and fully delithiated phase.

(a) An X-ray powder diffraction pattern ($\lambda_{\text{Cu-K}\alpha}$) and the Rietveld refinement of $\text{Li}_{1.1}\text{Na}_{0.4}\text{VPO}_{4.8}\text{F}_{0.7}$.

(b) A synchrotron XRD pattern and the Rietveld refinement of $\text{Na}_{0.4}\text{VPO}_{4.8}\text{F}_{0.7}$ with observed data points (red dots), calculated pattern (black line), difference curve (blue line), and Bragg positions (green bars).

Table 4-7. Lattice parameters of $\text{Li}_{1.1}\text{Na}_{0.4}\text{VPO}_{4.8}\text{F}_{0.7}$ and $\text{Na}_{0.4}\text{VPO}_{4.8}\text{F}_{0.7}$

<i>Composition</i>	<i>a (Å)</i>	<i>c (Å)</i>	<i>Cell Volume (Å³)</i>
$\text{Li}_{1.1}\text{Na}_{0.4}\text{VPO}_{4.8}\text{F}_{0.7}$	8.9881(3)	10.4483(6)	844.08(6)
$\text{Na}_{0.4}\text{VPO}_{4.8}\text{F}_{0.7}$	8.8980(2)	10.7326(3)	849.75(3)

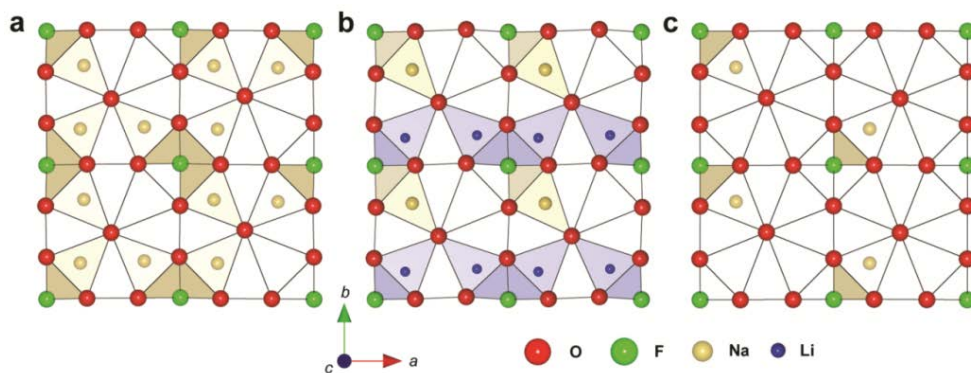


Figure 4-19. Ground-state structures for the lattice parameter calculations.

(a) Ground-state structure of $\text{Na}_{1.5}\text{VPO}_5\text{F}_{0.5}$.

(b) Ground-state structure of $\text{LiNa}_{0.5}\text{VPO}_5\text{F}_{0.5}$.

(c) Ground-state structure of $\text{Na}_{0.5}\text{VPO}_5\text{F}_{0.5}$.

Table 4-8. Lattice parameters predicted by first-principles calculations

<i>Composition</i>	<i>a</i> (Å)	<i>c</i> (Å)	<i>Cell Volume</i> (Å ³)	$\Delta V_{chg.-dchg.}$
Na _{1.5} VPO ₅ F _{0.5}	9.04	10.38	848	3.1 %
LiNa _{0.5} VPO ₅ F _{0.5}	8.99	10.20	825	0.4 %
Na _{0.5} VPO ₅ F _{0.5}	8.82	10.55	822	-

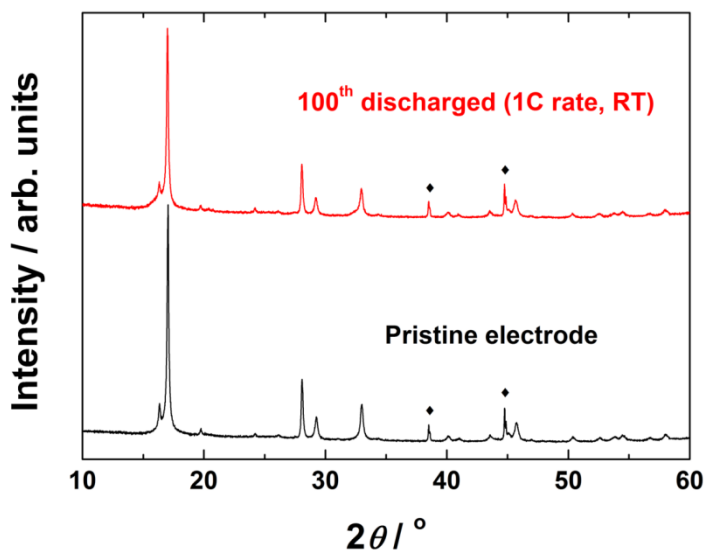


Figure 4-20. XRD patterns of the $\text{Li}_{1.1}\text{Na}_{0.4}\text{VPO}_{4.8}\text{F}_{0.7}$ electrode in the pristine and 100th discharged states. Top red line shows XRD pattern of the electrode in the discharged state after 100 cycles with a 1C cycling rate at room temperature. The bottom black line shows XRD pattern of the pristine electrode for comparison. Reflections from aluminum foil are denoted as ◆.

4.3.5. The Origin of the Fast Charging and Discharging

The high rate capability of $\text{Li}_{1.1}\text{Na}_{0.4}\text{VPO}_{4.8}\text{F}_{0.7}$ (see **Figure 4-17**) is attributable to fast Li^+ ion transport in the open crystal lattice possessing two-dimensional diffusional pathways in the *ab* plane: Li^+ ions can hop along the ring-shaped route (path 1, circular cyan arrows in **Figure 4-21**) or across the ring (path 2, straight red arrows in **Figure 4-21**). Using NEB method,¹⁰⁶ the diffusion kinetics of alkali ions for the two plausible diffusion paths (i.e., path 1 and path 2) with activation energies (E_a) was estimated. Two models of $\text{Na}_{1.5}\text{VPO}_5\text{F}_{0.5}$ and $\text{LiNa}_{0.5}\text{VPO}_5\text{F}_{0.5}$ were introduced to examine the transport property of Na^+ ions and Li^+ ions in the isostructural $\text{Na}_{1.5}\text{VPO}_{4.8}\text{F}_{0.7}$ and $\text{Li}_{1.1}\text{Na}_{0.4}\text{VPO}_{4.8}\text{F}_{0.7}$, respectively.

For NEB calculation, the initial configurations of the alkali ions in $\text{Na}_{1.5}\text{VPO}_5\text{F}_{0.5}$ and $\text{LiNa}_{0.5}\text{VPO}_5\text{F}_{0.5}$ were chosen (**Figure 4-22**). These configurations have similar environments for alkali ion hopping in the initial and final states. The energies of these configurations are ~30 meV per formula unit higher than those of the ground-state structures (see **Figure 4-19a** and **Figure 4-19b**). Since these small energy differences can be easily overcome with thermal energy at room temperature (ca. 25 meV), I believe that the initial configurations are suitable representations for alkali ion diffusion in $\text{Na}_{1.5}\text{VPO}_5\text{F}_{0.5}$ and $\text{LiNa}_{0.5}\text{VPO}_5\text{F}_{0.5}$.

Two types of diffusion pathways exist for alkali ions in $\text{Na}_{1.5}\text{VPO}_5\text{F}_{0.5}$ and $\text{LiNa}_{0.5}\text{VPO}_5\text{F}_{0.5}$. Path 1 follows a ring-shaped route and path 2 crosses the ring (**Figure 4-21**). **Figure 4-23** shows the trajectories and the corresponding activation energies for sodium and lithium hopping in diffusion path 1 in $\text{Na}_{1.5}\text{VPO}_5\text{F}_{0.5}$ and $\text{LiNa}_{0.5}\text{VPO}_5\text{F}_{0.5}$ predicted by the NEB method. It was found that a negligible E_a value at a similar scale of thermal energy at room temperature (ca. 25 meV) exists

for both the Na^+ and Li^+ ions along path 1 (see **Figure 4-23b** and **Figure 4-23d**). This implies unusually fast motion of these ions in the closed-loop ring pattern of the *ab* plane.

Nevertheless, to escape or be reinserted into the material, the ions should be capable of crossing among ring patterns through path 2. The E_a values of diffusion path 2 for the Na^+ ions in $\text{Na}_{1.5}\text{VPO}_5\text{F}_{0.5}$ and Li^+ ions in $\text{LiNa}_{0.5}\text{VPO}_5\text{F}_{0.5}$ were estimated at 310 and 200 meV (see **Figure 4-24**), respectively. The Li^+ ion trajectory along path 2 is quite different from that of Na^+ . The Na^+ ions, whose site energy strongly affects the activation barrier, migrate with a sinusoidal motion (**Figure 4-24a**) along path 2 due to the small intermediate space in the middle of the path. On the contrary, the Li^+ ions travel in a nearly straight line (**Figure 4-24c**). The energy trajectory in **Figure 4-24d** indicates metastability at the intermediate space. This is because the presence of Na^+ ions in the structure provides a larger empty space for the Li^+ ions.

Since the extraction of Na^+ or Li^+ ions should involve both path 1 and path 2, the diffusion kinetics is rate-limited by the activation barrier for path 2. The activation barrier of Li^+ ion hopping is significantly lower than that for Na^+ . This is probably because the residual Na^+ maintains a somewhat larger framework, which is beneficial for Li^+ ion diffusion in the lithium phase. The activation barrier for Li^+ ion hopping of $\text{Li}_{1.1}\text{Na}_{0.4}\text{VPO}_{4.8}\text{F}_{0.7}$ (200 meV) is even lower than that of LiCoO_2 (~250 meV),^{55,127} which gives an estimated diffusivity a few times greater than that for LiCoO_2 . I believe that this is due to the smaller size of Li^+ ions compared to Na^+ ions, as well as the presence of partially-filled alkali-metal sites in the framework.

The diffusion coefficient or diffusion constant, D , can be expressed by the following equation:

$$D = a^2 \nu^* e^{-E_a/k_B T}$$

where a is the jump distance, ν^* is the jump frequency, E_a is the activation barrier for lithium diffusion, and k_B is the Boltzmann constant.¹²⁸ Assuming that ν^* is ca. 10^{12} Hz, which is within the range of phonon frequencies, and a is approximately 5 Å, corresponding to the distance of a hop along path 2, the diffusion constants of $\text{Na}_{1.5}\text{VPO}_5\text{F}_{0.5}$ and $\text{LiNa}_{0.5}\text{VPO}_5\text{F}_{0.5}$ can be approximated as 10^{-8} and 10^{-6} $\text{cm}^2 \text{s}^{-1}$, respectively, at room temperature. Assuming the same pre-exponential factor of diffusivity, lithium diffusivity in $\text{LiNa}_{0.5}\text{VPO}_5\text{F}_{0.5}$ is expected to be one order of magnitude greater than the diffusion coefficients of conventional cathode materials.

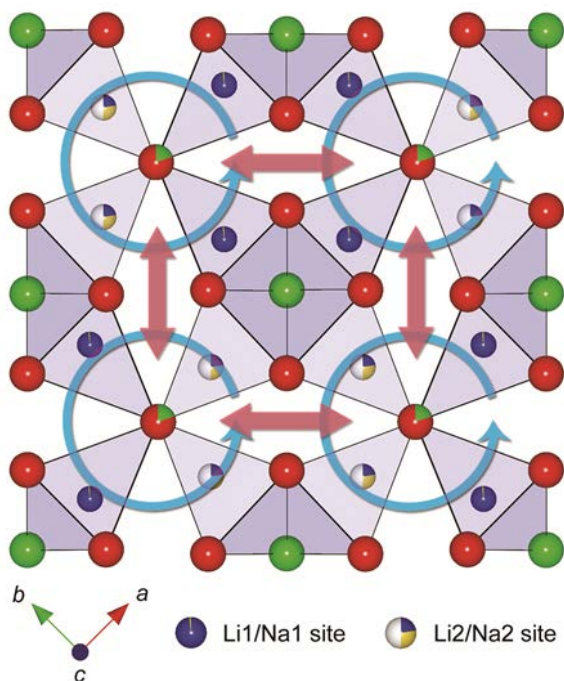


Figure 4-21. Top view (ab plane) of the alkali metal layer in $\text{Li}_{1.1}\text{Na}_{0.4}\text{VPO}_{4.8}\text{F}_{0.7}$.

This scheme shows two types of diffusion paths for Li^+ ions (indicated by arrows). This illustration was based on the refinement results. Li, Na, O, and F atoms are represented in blue, yellow, red, and green, respectively.

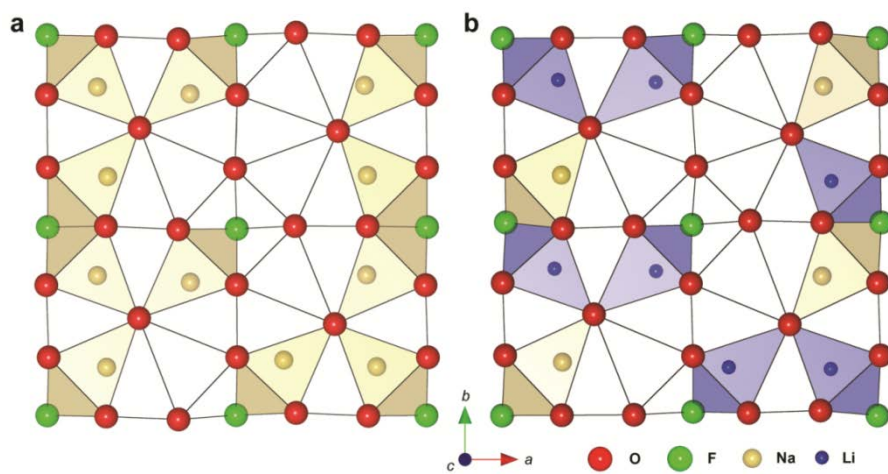


Figure 4-22. Initial configurations of alkali ions for the NEB calculations.

(a) Na configuration in $\text{Na}_{1.5}\text{VPO}_5\text{F}_{0.5}$.

(b) Li/Na configuration in $\text{LiNa}_{0.5}\text{VPO}_5\text{F}_{0.5}$.

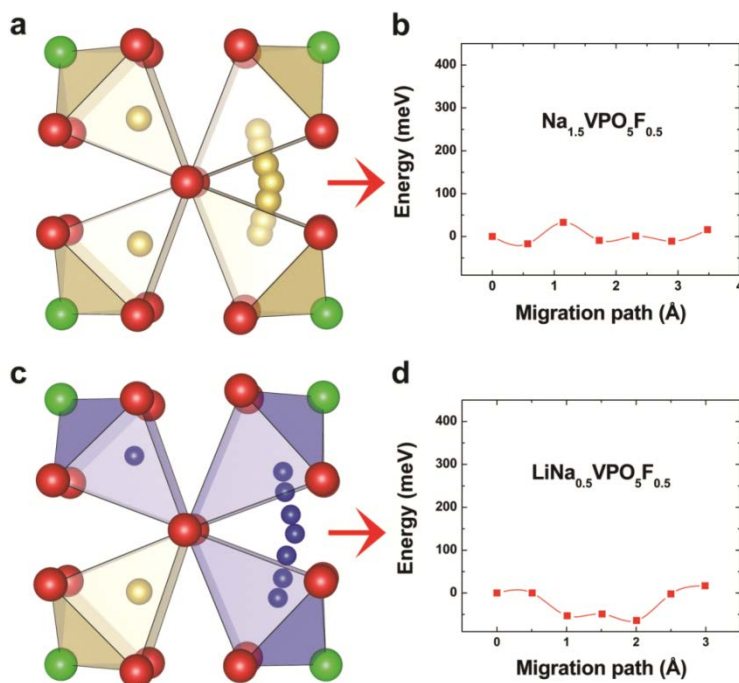


Figure 4-23. NEB calculations for path 1 in $\text{Na}_{1.5}\text{VPO}_5\text{F}_{0.5}$ and $\text{LiNa}_{0.5}\text{VPO}_5\text{F}_{0.5}$.

(a) Trajectories and (b) corresponding activation barriers for Na hopping for diffusion path 1 in $\text{Na}_{1.5}\text{VPO}_5\text{F}_{0.5}$ as predicted by the NEB method.

(c) Trajectories and (d) corresponding activation barriers for Li hopping for diffusion path 1 in $\text{LiNa}_{0.5}\text{VPO}_5\text{F}_{0.5}$ as predicted by the NEB method.

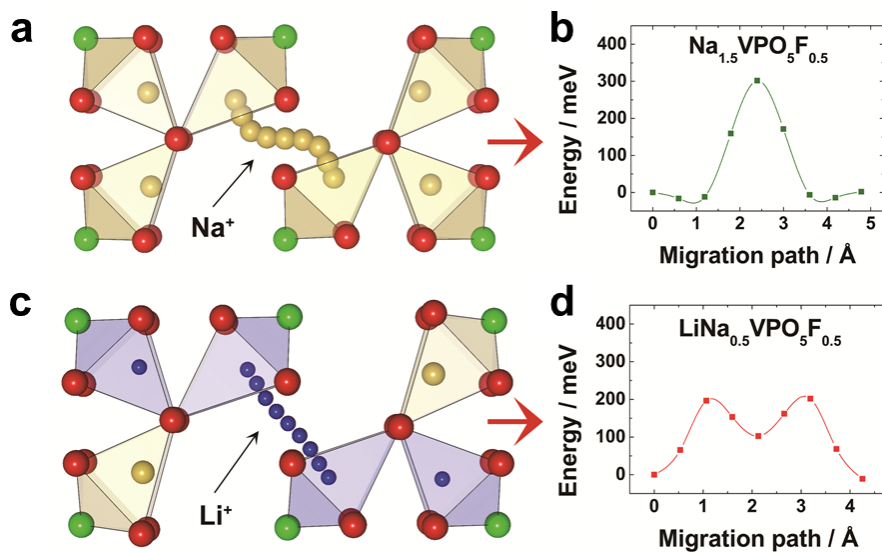


Figure 4-24. NEB calculations for path 2 in Na_{1.5}VPO₅F_{0.5} and LiNa_{0.5}VPO₅F_{0.5}.

(a) Trajectories and (b) corresponding activation barriers for Na hopping for diffusion path 2 in Na_{1.5}VPO₅F_{0.5} as predicted by the NEB method.

(c) Trajectories and (d) corresponding activation barriers for Li hopping for diffusion path 2 in LiNa_{0.5}VPO₅F_{0.5} as predicted by the NEB method.

4.4. Summary

In this chapter, a novel fluorophosphate-based electrode material having high energy and power capability with outstanding cycle stability was developed by tailoring a polyanion compound having an open framework. Once the synthesis of the electrode becomes optimized on the basis of cost, $\text{Li}_{1.1}\text{Na}_{0.4}\text{VPO}_{4.8}\text{F}_{0.7}$ will become a serious contender as a commercial electrode. The capacity of 156 mAh g^{-1} with a voltage of 4 V is comparable to other competitor cathode materials. The performance of this material even exceeds that of the recently discovered triplite $\text{Li}(\text{Fe}_{1-\delta}\text{Mn}_{\delta})\text{SO}_4\text{F}$, which can deliver a theoretical capacity of 146 mAh g^{-1} with 3.90 V. Additionally, this material has excellent cycle stability and rate capability. The discovery of this new electrode material is particularly important because its energy density was tuned by tailoring the polyanion groups in the structure to widen the redox reaction range of the redox center. Such design flexibility broadens the scope for further investigation of polyanion-based compounds as frameworks for new cathode materials and offers exciting opportunities for the development of new compounds.

Chapter 5. Conclusion

This dissertation is mainly about designing a variety of promising cathode materials for both Na and Li ion batteries. Starting material for new cathode materials was chosen with a guideline to obtain high specific capacity and operating voltage. To enhance the specific capacity, I focused on multivalent transition metals capable of providing more than one electron per formula unit. For example, vanadium ions can have various oxidation states (+2, +3, +4, and +5). Therefore, multi-electron redox reactions can take place in some vanadium-containing compounds, leading to a higher capacity compared to one-electron redox reaction. To increase operating voltage, I focused on polyanion compounds because the strong inductive effect of polyanion group can increase redox potential of redox couple. For this reason, I selected $\text{Na}_{1.5}\text{VOPO}_4\text{F}_{0.5}$ with both vanadium redox couple and polyanion group of $[\text{PO}_4\text{F}]^{4-}$ as a starting material for a high-energy cathode material. Furthermore, $\text{Na}_{1.5}\text{VOPO}_4\text{F}_{0.5}$ belongs to the NASICON-type compounds in which fast Na^+ ion conduction is possible. Maintaining the advantages of $\text{Na}_{1.5}\text{VOPO}_4\text{F}_{0.5}$, I tried to prepare new cathode materials with improved electrochemical properties.

In the first part of this dissertation, by tailoring anion group, I successfully transformed the existing $\text{Na}_{1.5}\text{VOPO}_4\text{F}_{0.5}$ into a novel $\text{Na}_{1.5}\text{VPO}_{4.8}\text{F}_{0.7}$ cathode with outstanding electrochemical performance for Na-ion batteries. The average voltage of fluorine-substituted $\text{Na}_{1.5}\text{VPO}_{4.8}\text{F}_{0.7}$ cathode was as high as ~ 3.8 V (vs. Na^+/Na), and the tailored $\text{V}^{3.8+}/\text{V}^{5+}$ redox couple provided more than one-electron during charging. The theoretical energy density of the $\text{Na}_{1.5}\text{VPO}_{4.8}\text{F}_{0.7}$ cathode was close to 600 Wh kg^{-1} that was one of the largest values among other cathode materials for

Na-ion batteries. The cycle life of the material was outstanding: ~95% and ~84% of the initial capacity were retained for 100 cycles and extended 500 cycles, respectively. Based on *ex situ* XRD data of this electrode, the volume change of the material during charge/discharge was as low as 2.9% which was lower than any other cathode materials for Na-ion battery. This exceptionally low volume change is likely to be related to the outstanding cyclability of the $\text{Na}_{1.5}\text{VPO}_{4.8}\text{F}_{0.7}$ cathode. From first-principle calculations, it was found that the $\text{Na}_{1.5}\text{VPO}_{4.8}\text{F}_{0.7}$ cathode had two-dimensional diffusion pathways on the Na layer, which enabled excellent rate capability.

In the second part, I explored a wider anion composition range starting from $\text{Na}_{1.5}\text{VPO}_{4.8}\text{F}_{0.7}$ compound which I discovered in the first chapter. I succeeded in preparing a series of the isostructural $\text{Na}_3(\text{VO}_{1-x}\text{PO}_4)_2\text{F}_{1+2x}$ ($0 \leq x \leq 1$) compounds, for the first time. From XANES and ^{23}Na MAS NMR, I found that the oxidation state of vanadium ion varied with the fluorine content (x) and that V^{3+} and V^{4+} ions were uniformly mixed in the crystal structure. By using a combined theoretical and experimental approach, I discovered the detailed electrochemical mechanisms of the $\text{Na}_y(\text{VO}_{1-x}\text{PO}_4)_2\text{F}_{1+2x}$ ($0 \leq x \leq 1$) electrodes. Furthermore, I explained the reason why voltage–composition curves of the $\text{Na}_y(\text{VO}_{1-x}\text{PO}_4)_2\text{F}_{1+2x}$ electrodes varied with the F content in terms of $\text{Na}^+ - \text{Na}^+$ ordering, F/O distribution, and different redox couples of $\text{V}^{3+}/\text{V}^{4+}$ or $\text{V}^{4+}/\text{V}^{5+}$. Moreover, I disclosed Na de/insertion mechanisms for the isostructural $\text{Na}_y(\text{VO}_{1-x}\text{PO}_4)_2\text{F}_{1+2x}$ family. It was found that all compositions in this system could act as high-performance cathodes for Na-ion batteries. All of them showed exceptionally small volume changes upon cycling (~2%), responsible for the excellent cyclability. This newly found $\text{Na}_y(\text{VO}_{1-x}\text{PO}_4)_2\text{F}_{1+2x}$ cathode group has one of the highest energy densities (~520 Wh kg^{-1}) among NIB cathodes with

excellent cycle life. For this reason, I believe that $\text{Na}_y(\text{VO}_{1-x}\text{PO}_4)_2\text{F}_{1+2x}$ electrodes can be categorized as a promising cathode group.

In the final part, I have transformed a routine sodium compound into a promising fluorophosphate-based cathode material for lithium-ion batteries. It should be noted that modifying polyanion groups to a significant extent while keeping the original structure intact is quite challenging, since the polyanion groups are often structural units of the crystal framework. Substantial substitution results in destruction of the original structure or the precipitation of a new phase. Here, tuning of the oxidation states of transition metals and their redox potentials was achieved by substantial ionic substitution in a polyanion group within a crystal structure. This tuning was crucial to enhancing its energy density as an electrode. The oxidation states of transition metals in the inorganic compounds may also be tuned by aliovalent cation doping.⁸⁷ However, in order to lower the initial oxidation state of V^{4+} in $\text{Na}_{1.5}\text{VPO}_5\text{F}_{0.5}$ via the aliovalent cation doping, elements having the valence of +5 or more need to be doped (or substituted) by substantial amounts. However, such cations are usually rare, unstable, or toxic (e.g., Cr^{6+} , Mn^{6+} , Nb^{5+} , Ta^{5+} , etc.). Also, those cations need to be strongly electronegative enough to reduce the valence of vanadium ion from +4 to +3 and electrochemically active at similar potential not to sacrifice the gravimetric capacity. Therefore, the fluorination replacing O^{2-} ions by F^- ions was a rational alternative. It is noteworthy that the modification of polyanion groups alters not only the oxidation states of transition metals but also their redox potentials by affecting on the degree of the inductive effect.

Despite a lot of advantages of vanadium-based fluorophosphates as a cathode material for NIB and LIB, it should be mentioned that this material group also has some weak points. From an industrial point of view, vanadium is still expensive

compared to iron or manganese, and its price is not that stable. Furthermore, the synthesis of fluorophosphates can be more difficult than layered oxides or simple phosphates due to multiple processing steps. This may increase the processing cost, making fluorophosphates less attractive. Low electronic conductivity of NAISCON compounds is another obstacle. To utilize an electronically insulating material as a battery electrode, additional processing steps such as carbon-coating and/or nano-sizing are essential. I believe that these steps can reduce volumetric capacity of the electrode as well as increase the price of final product.

In my opinion, $\text{Li}_z\text{Na}_{1.5-z}(\text{VO}_{1-x}\text{PO}_4)_2\text{F}_{1+2x}$ compounds have room for further improvement in terms of energy density and power capability. First of all, one can attempt to replace Li^+ and Na^+ ions by other alkali-metal ions such as H^+ , K^+ , and Mg^{2+} ions. This substitution may affect the strength of $\text{Na}^+\text{-Na}^+$ repulsion and thereby modify the voltage-composition profile. This modification can increase the specific capacity by enabling multi-electron redox reaction. To utilize the voltage region higher than 4.5 V (vs. Na^+/Na), all solid-state battery whose solid-electrolyte is stable above 4.5 V can be attempted. If one exploits the full voltage range of the $\text{Li}_z\text{Na}_{1.5-z}(\text{VO}_{1-x}\text{PO}_4)_2\text{F}_{1+2x}$ electrodes, an energy density higher than 700 Wh kg^{-1} can be achieved.

References

- (1) Kim, S.-W.; Seo, D.-H.; Ma, X.; Ceder, G.; Kang, K. *Adv. Energy Mater.* **2012**, 2, 710.
- (2) Palomares, V.; Serras, P.; Villaluenga, I.; Hueso, K. B.; Carretero-Gonzalez, J.; Rojo, T. *Energy Environ. Sci.* **2012**, 5, 5884.
- (3) Hong, S. Y.; Kim, Y.; Park, Y.; Choi, A.; Choi, N.-S.; Lee, K. T. *Energy Environ. Sci.* **2013**, 6, 2067.
- (4) Pan, H.; Hu, Y.-S.; Chen, L. *Energy Environ. Sci.* **2013**, 6, 2338.
- (5) Ellis, B. L.; Nazar, L. F. *Curr. Opin. Solid State Mater. Sci.* **2012**, 16, 168.
- (6) Slater, M. D.; Kim, D.; Lee, E.; Johnson, C. S. *Adv. Funct. Mater.* **2013**, 23, 947.
- (7) Palomares, V.; Casas-Cabanas, M.; Castillo-Martinez, E.; Han, M. H.; Rojo, T. *Energy Environ. Sci.* **2013**, 6, 2312.
- (8) Yabuuchi, N.; Kajiyama, M.; Iwatate, J.; Nishikawa, H.; Hitomi, S.; Okuyama, R.; Usui, R.; Yamada, Y.; Komaba, S. *Nat. Mater.* **2012**, 11, 512.
- (9) Komaba, S.; Murata, W.; Ishikawa, T.; Yabuuchi, N.; Ozeki, T.; Nakayama, T.; Ogata, A.; Gotoh, K.; Fujiwara, K. *Adv. Funct. Mater.* **2011**, 21, 3859.
- (10) Ponrouch, A.; Marchante, E.; Courty, M.; Tarascon, J.-M.; Palacin, M. R. *Energy Environ. Sci.* **2012**, 5, 8572.
- (11) Berthelot, R.; Carlier, D.; Delmas, C. *Nat. Mater.* **2011**, 10, 74.
- (12) Ding, J. J.; Zhou, Y. N.; Sun, Q.; Yu, X. Q.; Yang, X. Q.; Fu, Z. W. *Electrochimica Acta* **2013**, 87, 388.
- (13) Guignard, M.; Didier, C.; Darriet, J.; Bordet, P.; Elkaïm, E.; Delmas, C. *Nat. Mater.* **2013**, 12, 74.
- (14) Yabuuchi, N.; Yano, M.; Yoshida, H.; Kuze, S.; Komaba, S. *J. Electrochem. Soc.* **2013**, 160, A3131.
- (15) Jian, Z.; Han, W.; Lu, X.; Yang, H.; Hu, Y.-S.; Zhou, J.; Zhou, Z.; Li, J.; Chen, W.; Chen, D.; Chen, L. *Adv. Energy Mater.* **2013**, 3, 156.
- (16) Vassilaras, P.; Ma, X.; Li, X.; Ceder, G. *J. Electrochem. Soc.* **2013**, 160, A207.
- (17) Shakoor, R. A.; Seo, D.-H.; Kim, H.; Park, Y.-U.; Kim, J.; Kim, S.-W.; Gwon, H.; Lee, S.; Kang, K. *J. Mater. Chem.* **2012**, 22, 20535.
- (18) Gover, R. K. B.; Bryan, A.; Burns, P.; Barker, J. *Solid State Ionics* **2006**, 177, 1495.
- (19) Barker, J.; Gover, R. K. B.; Burns, P.; Bryan, A. J. *Electrochem. Solid-State Lett.* **2006**, 9, A190.
- (20) Barpanda, P.; Ye, T.; Nishimura, S.-i.; Chung, S.-C.; Yamada, Y.; Okubo, M.; Zhou, H.; Yamada, A. *Electrochem. Commun.* **2012**, 24, 116.
- (21) Casas-Cabanas, M.; Roddatis, V. V.; Saurel, D.; Kubiak, P.; Carretero-Gonzalez, J.; Palomares, V.; Serras, P.; Rojo, T. *J. Mater. Chem.* **2012**, 22, 17421.
- (22) Kawabe, Y.; Yabuuchi, N.; Kajiyama, M.; Fukuhara, N.; Inamasu, T.; Okuyama, R.; Nakai, I.; Komaba, S. *Electrochem. Commun.* **2011**, 13, 1225.
- (23) Kim, H.; Shakoor, R. A.; Park, C.; Lim, S. Y.; Kim, J.-S.; Jo, Y. N.; Cho, W.; Miyasaka, K.; Kahraman, R.; Jung, Y.; Choi, J. W. *Adv. Funct. Mater.* **2013**, 23, 1147.

- (24) Moreau, P.; Guyomard, D.; Gaubicher, J.; Boucher, F. *Chem. Mater.* **2010**, *22*, 4126.
- (25) Oh, S.-M.; Myung, S.-T.; Hassoun, J.; Scrosati, B.; Sun, Y.-K. *Electrochem. Commun.* **2012**, *22*, 149.
- (26) Saravanan, K.; Mason, C. W.; Rudola, A.; Wong, K. H.; Balaya, P. *Adv. Energy Mater.* **2013**, *3*, 444.
- (27) Sauvage, F.; Quarez, E.; Tarascon, J. M.; Baudrin, E. *Solid State Sciences* **2006**, *8*, 1215.
- (28) Ellis, B. L.; Makahnouk, W. R. M.; Rowan-Weetaluktuk, W. N.; Ryan, D. H.; Nazar, L. F. *Chem. Mater.* **2009**, *22*, 1059.
- (29) Sakaushi, K.; Hosono, E.; Nickerl, G.; Gemming, T.; Zhou, H.; Kaskel, S.; Eckert, J. *Nat. Commun.* **2013**, *4*, 1485.
- (30) Sakaushi, K.; Nickerl, G.; Wisser, F. M.; Nishio-Hamane, D.; Hosono, E.; Zhou, H.; Kaskel, S.; Eckert, J. *Angewandte Chemie International Edition* **2012**, *51*, 7850.
- (31) Padhi, A. K.; Nanjundaswamy, K. S.; Masquelier, C.; Goodenough, J. B. *J. Electrochem. Soc.* **1997**, *144*, 2581.
- (32) Nanjundaswamy, K. S.; Padhi, A. K.; Goodenough, J. B.; Okada, S.; Ohtsuka, H.; Arai, H.; Yamaki, J. *Solid State Ionics* **1996**, *92*, 1.
- (33) Whittingham, M. S. *Chem. Rev.* **2004**, *104*, 4271.
- (34) Park, Y.-U.; Seo, D.-H.; Kim, B.; Hong, K.-P.; Kim, H.; Lee, S.; Shakoar, R. A.; Miyasaka, K.; Tarascon, J.-M.; Kang, K. *Sci. Rep.* **2012**, *2*.
- (35) Roisnel, T.; Rodríguez-Carvajal, J. *Mater. Sci. Forum* **2001**, *378-381*, 118.
- (36) Perdew, J. P.; Burke, K.; Ernzerhof, M. *Phys. Rev. Lett.* **1996**, *77*, 3865.
- (37) Kresse, G.; Furthmüller, J. *Comp. Mater. Sci.* **1996**, *6*, 15.
- (38) Anisimov, V. I.; Zaanen, J.; Andersen, O. K. *Phys. Rev. B* **1991**, *44*, 943.
- (39) Van der Ven, A.; Thomas, J. C.; Xu, Q.; Bhattacharya, J. *Mathematics and Computers in Simulation* **2010**, *80*, 1393.
- (40) Van der Ven, A.; Thomas, J. C.; Xu, Q.; Swoboda, B.; Morgan, D. *Phys. Rev. B* **2008**, *78*, 104306.
- (41) Henkelman, G.; Uberuaga, B. P.; Jonsson, H. *The Journal of Chemical Physics* **2000**, *113*, 9901.
- (42) Sale, M.; Avdeev, M. *J. Appl. Crystallogr.* **2012**, *45*, 1054.
- (43) Momma, K.; Izumi, F. *J. Appl. Crystallogr.* **2008**, *41*, 653.
- (44) Meng, Y. S.; Hinuma, Y.; Ceder, G. *J. Chem. Phys.* **2008**, *128*, 104708.
- (45) Wong, J.; Lytle, F. W.; Messmer, R. P.; Maylotte, D. H. *Phys. Rev. B* **1984**, *30*, 5596.
- (46) Yoon, J.; Muhammad, S.; Jang, D.; Sivakumar, N.; Kim, J.; Jang, W.-H.; Lee, Y.-S.; Park, Y.-U.; Kang, K.; Yoon, W.-S. *J. Alloys Compd.* **2013**, *569*, 76.
- (47) Kim, H.; Park, I.; Seo, D.-H.; Lee, S.; Kim, S.-W.; Kwon, W. J.; Park, Y.-U.; Kim, C. S.; Jeon, S.; Kang, K. *J. Am. Chem. Soc.* **2012**, *134*, 10369.
- (48) Sun, Y.; Zhao, L.; Pan, H.; Lu, X.; Gu, L.; Hu, Y.-S.; Li, H.; Armand, M.; Ikuhara, Y.; Chen, L.; Huang, X. *Nat. Commun.* **2013**, *4*, 1870.
- (49) Wang, L.; Lu, Y.; Liu, J.; Xu, M.; Cheng, J.; Zhang, D.; Goodenough, J. B. *Angewandte Chemie International Edition* **2013**, *52*, 1964.
- (50) Delacourt, C.; Laffont, L.; Bouchet, R.; Wurm, C.; Leriche, J.-B.; Morcrette, M.; Tarascon, J.-M.; Masquelier, C. *J. Electrochem. Soc.* **2005**, *152*, A913.

- (51) Recham, N.; Chotard, J.-N.; Dupont, L.; Delacourt, C.; Walker, W.; Armand, M.; Tarascon, J.-M. *Nat. Mater.* **2009**, *9*, 68.
- (52) Bohnke, O.; Ronchetti, S.; Mazza, D. *Solid State Ionics* **1999**, *122*, 127.
- (53) Sadaoka, Y.; Matsuguchi, M.; Sakai, Y.; Nakayama, S. *Journal of Materials Science* **1989**, *24*, 1299.
- (54) Chen, C. H.; Vaughey, J. T.; Jansen, A. N.; Dees, D. W.; Kahaian, A. J.; Goacher, T.; Thackeray, M. M. *J. Electrochem. Soc.* **2001**, *148*, A102.
- (55) Kang, K.; Ceder, G. *Phys. Rev. B* **2006**, *74*, 094105.
- (56) Malik, R.; Burch, D.; Bazant, M.; Ceder, G. *Nano Letters* **2010**, *10*, 4123.
- (57) Kang, K.; Meng, Y. S.; Bréger, J.; Grey, C. P.; Ceder, G. *Science* **2006**, *311*, 977.
- (58) Porter, D. A.; Easterling, K. E. *Phase transformations in metals and alloys*; CRC Press, 1992.
- (59) Park, K.-Y.; Hong, J.; Kim, J.; Park, Y.-U.; Kim, H.; Seo, D.-H.; Kim, S.-W.; Choi, J.-W.; Kang, K. *J. Electrochem. Soc.* **2013**, *160*, A444.
- (60) Tang, M.; Belak, J. F.; Dorr, M. R. *The Journal of Physical Chemistry C* **2011**, *115*, 4922.
- (61) Wang, Y.; Yu, X.; Xu, S.; Bai, J.; Xiao, R.; Hu, Y.-S.; Li, H.; Yang, X.-Q.; Chen, L.; Huang, X. *Nat. Commun.* **2013**, *4*.
- (62) Chihara, K.; Kitajou, A.; Gocheva, I. D.; Okada, S.; Yamaki, J.-i. *J. Power Sources* **2013**, *227*, 80.
- (63) Kim, H.; Park, I.; Lee, S.; Kim, H.; Park, K.-Y.; Park, Y.-U.; Kim, H.; Kim, J.; Lim, H.-D.; Yoon, W.-S.; Kang, K. *Chem. Mater.* **2013**.
- (64) Liu, Z.-m.; Wang, X.-y.; Wang, Y.; Tang, A.-p.; Yang, S.-y.; He, L.-f. *Transactions of Nonferrous Metals Society of China* **2008**, *18*, 346.
- (65) Xu, M.; Wang, L.; Zhao, X.; Song, J.; Xie, H.; Lu, Y.; Goodenough, J. B. *Phys. Chem. Chem. Phys.* **2013**, *15*, 13032.
- (66) Zhuo, H.; Wang, X.; Tang, A.; Liu, Z.; Gamboa, S.; Sebastian, P. J. *J. Power Sources* **2006**, *160*, 698.
- (67) Park, Y.-U.; Seo, D. H.; Kwon, H.-S.; Kim, B.; Kim, J.; Kim, H.; Kim, I.; Yoo, H.-I.; Kang, K. *J. Am. Chem. Soc.* **2013**, *135*, 13870.
- (68) Serras, P.; Palomares, V.; Goni, A.; Gil de Muro, I.; Kubiak, P.; Lezama, L.; Rojo, T. *J. Mater. Chem.* **2012**, *22*, 22301.
- (69) Serras, P.; Palomares, V.; Alonso, J.; Sharma, N.; López del Amo, J. M.; Kubiak, P.; Fdez-Gubieda, M. L.; Rojo, T. *Chem. Mater.* **2013**.
- (70) Serras, P.; Palomares, V.; Goñi, A.; Kubiak, P.; Rojo, T. *J. Power Sources* **2013**, *241*, 56.
- (71) Tsirlin, A. A.; Nath, R.; Abakumov, A. M.; Furukawa, Y.; Johnston, D. C.; Hemmida, M.; Krug von Nidda, H. A.; Loidl, A.; Geibel, C.; Rosner, H. *Phys. Rev. B* **2011**, *84*, 014429.
- (72) Barker, J.; Saidi, M. Y.; Swoyer, J. L. *Electrochem. Solid-State Lett.* **2003**, *6*, A1.
- (73) Jiang, T.; Chen, G.; Li, A.; Wang, C.; Wei, Y. *J. Alloys Compd.* **2009**, *478*, 604.
- (74) Le Meins, J. M.; Crosnier-Lopez, M. P.; Hemon-Ribaud, A.; Courbion, G. *J. Solid State Chem.* **1999**, *148*, 260.
- (75) Toukmaji, A. Y.; Board Jr, J. A. *Comput. Phys. Commun.* **1996**, *95*, 73.

- (76) Zavalij, P. Y.; Whittingham, M. S. *Acta Crystallogr. B* **1999**, *55*, 627.
- (77) Baur, W. *Acta Crystallographica Section B: Structural Crystallography and Crystal Chemistry* **1974**, *30*, 1195.
- (78) Cabana, J.; Shirakawa, J.; Chen, G.; Richardson, T. J.; Grey, C. P. *Chem. Mater.* **2010**, *22*, 1249.
- (79) Carlier, D.; Menetrier, M.; Grey, C. P.; Delmas, C.; Ceder, G. *Phys. Rev. B* **2003**, *67*, 174103.
- (80) Grey, C. P.; Dupré, N. *Chem. Rev.* **2004**, *104*, 4493.
- (81) Ellis, B. L.; Ramesh, T. N.; Davis, L. J. M.; Goward, G. R.; Nazar, L. F. *Chem. Mater.* **2011**, *23*, 5138.
- (82) Cullity, B. D.; Stock, S. R. *Elements of X-ray Diffraction*; Prentice hall Upper Saddle River, NJ, 2001; Vol. 3.
- (83) Bard, A. J.; Faulkner, L. R. *Electrochemical methods: fundamentals and applications*; Wiley New York, 1980; Vol. 2.
- (84) Tarascon, J.-M.; Armand, M. *Nature* **2001**, *414*, 359.
- (85) Armand, M.; Tarascon, J. M. *Nature* **2008**, *451*, 652.
- (86) Padhi, A. K.; Nanjundaswamy, K.; Goodenough, J. B. d. *J. Electrochem. Soc.* **1997**, *144*, 1188.
- (87) Chung, S.-Y.; Bloking, J. T.; Chiang, Y.-M. *Nat. Mater.* **2002**, *1*, 123.
- (88) Ellis, B.; Makahnouk, W.; Makimura, Y.; Toghill, K.; Nazar, L. *Nat. Mater.* **2007**, *6*, 749.
- (89) Barker, J.; Saidi, M.; Swoyer, J. *J. Electrochem. Soc.* **2003**, *150*, A1394.
- (90) Makimura, Y.; Cahill, L.; Iriyama, Y.; Goward, G.; Nazar, L. *Chem. Mater.* **2008**, *20*, 4240.
- (91) Barker, J.; Saidi, M. Y.; Swoyer, J.; Google Patents: 2002.
- (92) Recham, N.; Chotard, J.-N.; Jumas, J.-C.; Laffont, L.; Armand, M.; Tarascon, J.-M. *Chem. Mater.* **2009**, *22*, 1142.
- (93) Barpanda, P.; Ati, M.; Melot, B. C.; Rousse, G.; Chotard, J.-N.; Doublet, M.-L.; Sougrati, M. T.; Corr, S.; Jumas, J.-C.; Tarascon, J.-M. *Nat. Mater.* **2011**, *10*, 772.
- (94) Nytén, A.; Abouimrane, A.; Armand, M.; Gustafsson, T.; Thomas, J. O. *Electrochem. Commun.* **2005**, *7*, 156.
- (95) Dominko, R.; Bele, M.; Gaberscek, M.; Meden, A.; Remskar, M.; Jamnik, J. *Electrochem. Commun.* **2006**, *8*, 217.
- (96) Nishimura, S.-i.; Nakamura, M.; Natsui, R.; Yamada, A. *J. Am. Chem. Soc.* **2010**, *132*, 13596.
- (97) Nanjundaswamy, K.; Padhi, A.; Goodenough, J.; Okada, S.; Ohtsuka, H.; Arai, H.; Yamaki, J. *Solid State Ionics* **1996**, *92*, 1.
- (98) Gaubicher, J.; Wurm, C.; Goward, G.; Masquelier, C.; Nazar, L. *Chem. Mater.* **2000**, *12*, 3240.
- (99) Yin, S.-C.; Grondy, H.; Strobel, P.; Anne, M.; Nazar, L. *J. Am. Chem. Soc.* **2003**, *125*, 10402.
- (100) Ellis, B. L.; Lee, K. T.; Nazar, L. F. *Chem. Mater.* **2010**, *22*, 691.
- (101) Aono, H.; Imanaka, N.; Adachi, G.-y. *Accounts of chemical research* **1994**, *27*, 265.
- (102) Cushing, B. L.; Goodenough, J. B. *J. Solid State Chem.* **2001**, *162*, 176.
- (103) Goodenough, J.; Hong, H.-P.; Kafalas, J. *Materials Research Bulletin* **1976**, *11*, 203.
- (104) Huang, H.; Yin, S. C.; Kerr, T.; Taylor, N.; Nazar, L. F. *Adv. Mater.*

- 2002**, *14*, 1525.
- (105) Huggins, R. *Advanced batteries: materials science aspects*; Springer, 2008.
- (106) Meng, Y. S.; Arroyo-de Dompablo, M. E. *Energy Environ. Sci.* **2009**, *2*, 589.
- (107) Bocquet, A.; Mizokawa, T.; Saitoh, T.; Namatame, H.; Fujimori, A. *Phys. Rev. B* **1992**, *46*, 3771.
- (108) Silversmit, G.; Depla, D.; Poelman, H.; Marin, G. B.; De Gryse, R. *Journal of Electron Spectroscopy and Related Phenomena* **2004**, *135*, 167.
- (109) Šalkus, T.; Kežionis, A.; Kazakevičius, E.; Dindune, A.; Kanepe, Z.; Ronis, J.; Bohnke, O.; Kazlauskienė, V.; Miškinis, J.; Lelis, M. *Phase Transitions* **2010**, *83*, 581.
- (110) Hodnett, B.; Permanne, P.; Delmon, B. *Applied Catalysis* **1983**, *6*, 231.
- (111) Poole, C. P.; Farach, H. A. *The theory of magnetic resonance*; Wiley-Interscience New York, 1972.
- (112) Slebodnick, C.; Hamstra, B. J.; Pecoraro, V. L. In *Metal Sites in Proteins and Models*; Springer: 1997, p 51.
- (113) Yin, S.-C.; Strobel, P.; Grondy, H.; Nazar, L. *Chem. Mater.* **2004**, *16*, 1456.
- (114) England, W.; Goodenough, J.; Wiseman, P. J. *Solid State Chem.* **1983**, *49*, 289.
- (115) Clearfield, A. *Chem. Rev.* **1988**, *88*, 125.
- (116) Li, Z.; Zhang, D.; Yang, F. *Journal of materials science* **2009**, *44*, 2435.
- (117) Goodenough, J. B. *Magnetism and chemical bond*, Interscience publishers, 1963.
- (118) Lee, Y. J.; Grey, C. P. *Chem. Mater.* **2000**, *12*, 3871.
- (119) Pan, C.; Lee, Y. J.; Ammundsen, B.; Clare, P. *Chem. Mater.* **2002**, *14*, 2289.
- (120) Tripathi, R.; Popov, G.; Ellis, B. L.; Huq, A.; Nazar, L. *Energy Environ. Sci.* **2012**, *5*, 6238.
- (121) Tarascon, J.-M.; Recham, N.; Armand, M.; Chotard, J.-N.; Barpanda, P.; Walker, W.; Dupont, L. *Chem. Mater.* **2009**, *22*, 724.
- (122) Cho, J.; Kim, Y. J.; Kim, T. J.; Park, B. *Angewandte Chemie* **2001**, *113*, 3471.
- (123) Huang, H.; Yin, S.-C.; Nazar, L. s. *Electrochem. Solid-State Lett.* **2001**, *4*, A170.
- (124) Kim, D. K.; Muralidharan, P.; Lee, H.-W.; Ruffo, R.; Yang, Y.; Chan, C. K.; Peng, H.; Huggins, R. A.; Cui, Y. *Nano letters* **2008**, *8*, 3948.
- (125) Lazarraga, M.; Pascual, L.; Gadjov, H.; Kovacheva, D.; Petrov, K.; Amarilla, J.; Rojas, R.; Martin-Luengo, M.; Rojo, J. J. *Mater. Chem.* **2004**, *14*, 1640.
- (126) Xia, Y.; Zhou, Y.; Yoshio, M. *J. Electrochem. Soc.* **1997**, *144*, 2593.
- (127) Van der Ven, A.; Ceder, G.; Asta, M.; Tepesch, P. *Phys. Rev. B* **2001**, *64*, 184307.
- (128) Shewmon, P. *The Minerals, Metals & Materials Society, Diffusion in Solids. Second Edition.(Retroactive Coverage)(United States)*, 1989 **1989**, 246.

논문초록

리튬 및 소듐 이온 배터리를 불화인산염 양극물질 연구

Park, Young-Uk

Department of Materials Science and Engineering
The Graduate School
Seoul National University

대규모 전기에너지 저장장치는 신재생에너지의 효율적인 사용에 필수적이다. 대규모 에너지 저장장치를 실제로 구축하기 위해서는 값싸고 오래가는 배터리 기술이 필요하다. 이러한 측면에서 상온에서 구동되는 소듐 이온 배터리가 값싼 대안으로 최근 재조명되고 있다. 지구상에 풍부한 원소인 소듐(Na)은 리튬에 비해 훨씬 싸기 때문에, 신재생에너지 시장에서 많은 양의 물질을 필요로 할 경우 이점을 가진다. 하지만 에너지밀도와 장기간 안정성과 같은 문제들이 먼저 해결되어야 한다. 두 번째 장에서는 소듐 배터리를 새로운 양극물질인 $\text{Na}_{1.5}\text{VPO}_{4.8}\text{F}_{0.7}$ 을 소개한다. 이 신물질은 600 Wh kg^{-1} 에 달하는 높은 에너지 밀도를 가지는데, 이것은 불소치환을 통해 조절된 바나듐 산화환원쌍($\text{V}^{3.8+}/\text{V}^{5+}$)의 다전자 산화환원반응($1.2 e^-$) 및 높은 전압($\sim 3.8 \text{ V vs. Na}^+/\text{Na}$)에서 기인한다. 또한 100 사이클 동안 95%의 용량이 유지되는 우수한 수명특성을 보였는데, 이것은 충/방전 중 생기는 부피변화(2.9%)가 작기 때문이다. 이 물질은 열린 결정구조와 2차원의 소듐 확산 경로를 가지기 때문에 소듐 이온이 구조 내에서 쉽게 이동 가능하며, 그 결과 뛰어난 출력특성을 얻을 수 있었다.

세 번째 장에서는 일련의 $\text{Na}_3(\text{VO}_{1-x}\text{PO}_4)_2\text{F}_{1+2x}$ ($0 \leq x \leq 1$) 화합물들을 최초로 합성에 성공하였으며, 이 물질들이 소듐 이온 배터리를 위한 하나의 고성능 양극물질 그룹으로 분류될 수 있다는 것을 밝혔다. $\text{Na}_3(\text{VO}_{1-x}\text{PO}_4)_2\text{F}_{1+2x}$ 계열 물질들은 모두 높은 에너지밀도와 우수한 수명특성을 보였다. 하지만 산화환원 반응은 조성에 따라 상이했다. 이 현상을 더 깊이 연구하기 위해서 제일원리계산과 실험을 통해 $\text{Na}_3(\text{VOPO}_4)_2\text{F}$ and $\text{Na}_3\text{V}_2(\text{PO}_4)_2\text{F}_3$ 의

다양한 고용체에 대한 자세한 구조분석 및 전기화학분석을 실시하였다. 그 결과, $\text{Na}_y(\text{VO}_{1-x}\text{PO}_4)_2\text{F}_{1+2x}$ 전극에서 $\text{V}^{3+}/\text{V}^{4+}/\text{V}^{5+}$ 산화환원반응, Na^+-Na^+ 상호작용, 소듐 이온 삽입/탈리 기구 등이 서로 어떻게 연관되어 있는지를 명확히 규명하였다.

리튬 이온 배터리는 현재 휴대용 전자기기에 널리 사용되고 있으며, 전기자동차에도 적용되려 하고 있다. 하지만 새롭게 부상하는 전기자동차 시장에서 리튬 이온 배터리가 살아남기 위해서는 빠른 충전 능력, 장기간의 사이클 안정성, 높은 에너지밀도가 모두 요구된다. 네 번째 장에서는 새로운 층상형 리튬 바나듐 불화인산염 화합물인 $\text{Li}_{1.1}\text{Na}_{0.4}\text{VPO}_{4.8}\text{F}_{0.7}$ 을 우수한 리튬 배터리 양극으로 소개한다. 이 신물질은 2차원적인 리튬 확산 경로를 가지며, 4 V의 높은 전압에서 약 1.1개의 리튬 이온의 가역적 삽입/탈리가 가능하다. 이 물질의 비용량은 약 156 mAh g^{-1} 이며, 그 결과 624 Wh kg^{-1} 의 높은 에너지밀도를 가진다. 또한 60°C 및 상온 조건에서 100 사이클 후에 각각 98% 및 96%의 용량이 유지되었다. 뿐만 아니라 입자 크기가 상당히 큼($\sim \mu\text{m}$)에도 불구하고 우수한 출력특성을 보였다. 적절한 나노 공정을 사용하면 출력특성을 한층 더 향상시킬 수 있을 것이다.

주요어 : 소듐 이온 배터리, 리튬 이온 배터리, 양극물질, 불화인산염, 다전자 산화환원반응, 이온교환반응

학 번 : 2011-30785